LARGE SIGNALS IN SWITCHING CONVERTERS

Thesis by

Robert W. Erickson

In Partial Fulfillment of the Requirements

for the Degree of

Doctor of Philosophy

California Institute of Technology

Pasadena, California

1983

(Submitted November 8, 1982)

to my parents,

Robert, Sr. and Pearlie,

and to my wife, Linda

ACKNOWLEDGMENTS

ABSTRACT

The behavior of switching converters under large-signal conditions is modelled and analyzed. Two major problems are of interest: the reduction of the distortion which occurs in switching amplifiers, and the stabilization of switching regulators for all transients which are expected to occur.

In Part 1, a large-signal model is described which predicts the simple harmonic distortion generated inherently by switched-mode amplifiers. The causes of this distortion are identified, and relatively simple design techniques for its reduction to an acceptable level are presented. A particularly attractive feature of the method is the ability to compute harmonic magnitude and phase using linear circuit models and Bode plots.

The method is extended to account for intermodulation distortion. Additional effects not described by the model are also discussed, including crossover distortion and bandwidth limitations.

Although in its simplest form the buck converter is inherently linear, considerable distortion may arise when it is preceded by an input filter. This problem is solved as an example of the usefulness and circuit-oriented nature of the method.

In Part 2, a large-signal switching regulator model is derived, and prominent features of the transient response are determined. In particular, the various regions of operation are identified in the state plane, analytical expressions are found for the equilibrium points of the system, and computer-generated transient waveforms are obtained.

As an example, a boost regulator is investigated, and is found to be stable for small signals but unstable for large transients. Approximate analytical expressions are found for the waveforms and salient features of the response, and a number of ways of obtaining global stability are discussed.

Experimental evidence is presented to verify both the distortion and stability analyses.

TABLE OF CONTENTS

PART 1

DISTORTION IN SWITCHING AMPLIFIERS

CHAPTER 1

INTRODUCTION

Switching converters are finding increasing application as motor controllers, transducer drivers, servo amplifiers, uninterruptible power supplies, and low-distortion (unity power factor) ac-to-dc power supplies. In these applications, the converter must reproduce a control signal at high power levels with reasonable accuracy and efficiency. Because of their theoretical 100% efficiency, switching converters would appear to be much better suited for these applications than conventional class B amplifiers. However, the inherent nonlinearity in these converters poses an obstacle to both their analysis and design. In particular, it is possible for nonlinearities to cause the appearance of large, previously unexpected and mysterious amounts of low and mid-frequency distortion. The analysis of this distortion in a design-oriented manner is the subject of the first part of this thesis.

The technology for the implementation of switching power supplies is currently at a high level and continues to develop. Since both switching power supplies and switching amplifiers fall into the general category of "switched-mode power converters", it is natural to attempt to adapt this technology to the realization of a power amplifier. Indeed, in many instances this may be done with only a few major modifications [9,10]. However, there is one fundamental difference between the amplifier and the power supply: the amplifier must

reproduce continual large-signal variations of a control signal, whereas the power supply need only regulate a dc output against the occasional external perturbations which may occur. Consequently, additional requirements on the large-signal bandwidth and linearity of a switching amplifier exist which must be satisfied before acceptable performance can be attained.

It is of interest, therefore, to identify the various aspects of the general switching amplifier which degrade its large-signal performance. Chapter 6 contains a discussion of some of these distortion processes, including slew-rate limiting, crossover distortion, component nonidealities, and the generation of high frequency switching ripple. These problems must all be resolved before a linear switching amplifier is realized. However, the most fundamental source of distortion arises from the switching process itself. It is well-known that the dc characteristics of many of the basic converter topologies are nonlinear. For example, the dc line-to-output gain of the boost converter is $1/(1 - D)$ where D = duty ratio. In these cases, one expects low-frequency harmonic distortion to be generated even by the ideal converter stage. Furthermore, since inductors and capacitors are intrinsic to the converter, one might suspect that the nonlinearities depend on the frequency of excitation. It is well-known that the small-signal response contains frequency-dependent terms [1,2]; it follows that the large-signal response should vary with the frequency of excitation also. It is shown here that the harmonic distortion is indeed a function of frequency.
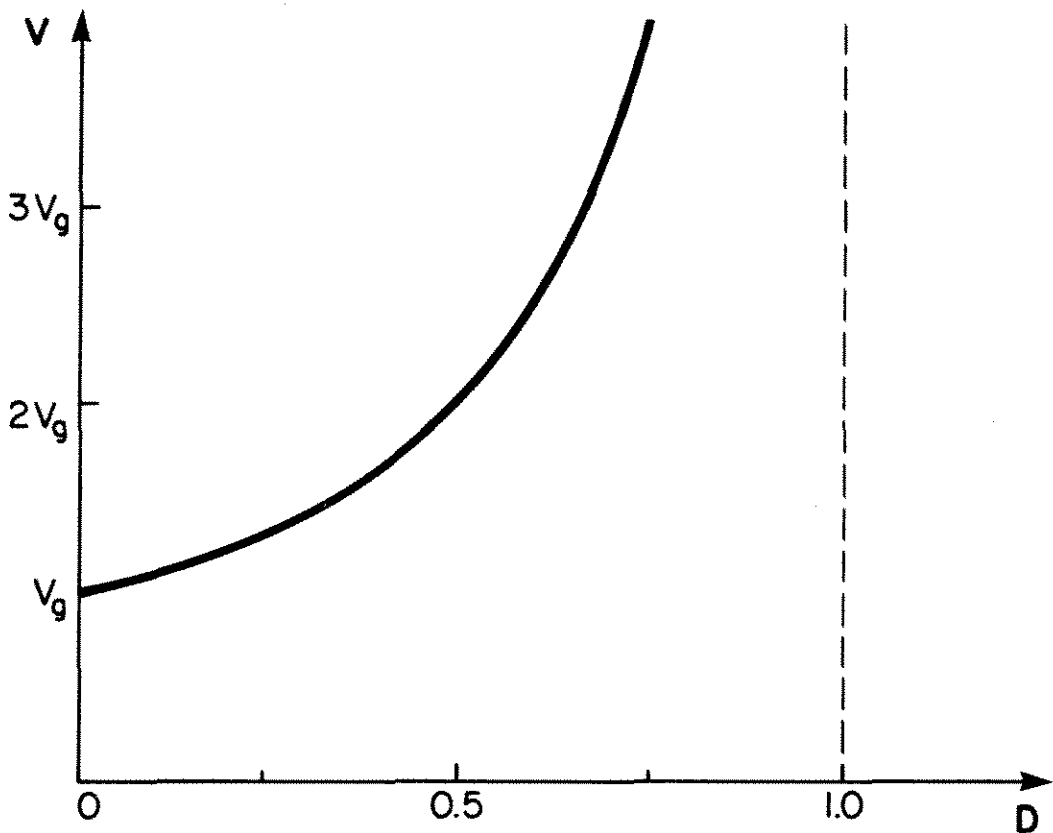
Fig. 1.1.   *Dc characteristics of the boost converter: the output voltage V is a nonlinear function of the control signal D.*

Moreover, the peak level of distortion may occur not at dc, but rather at some midband frequency. Two extreme examples of this are given in Chapter 5, where the distortion generated by two types of buck amplifier with input filter is analyzed. In these cases, the dc gain curve is completely linear, yet harmonic distortion occurs when ac excitation is present! Apparently a dc distortion analysis is not sufficient; ac effects must be accounted for also.

The conclusion is that a large-signal ac model is required for the design of a switching amplifier. From such a model, it should be possible to calculate the various harmonics which appear at the output, to determine their dependence on the various circuit element values,

and then if possible to design an amplifier which is sufficiently linear for a given application. A large-signal model of this type is derived in Chapter 3 which predicts simple harmonic distortion. The outcome of the method is a series of *linear circuit models*, one for each component of the output. Hence, standard linear circuit analysis techniques may be used to find the amplitude and phase of each harmonic; no complicated nonlinear differential equations need be solved by the engineer. The result is a useful design-oriented procedure for the reduction of the distortion inherent in switching amplifiers to an acceptable level.

The procedure is extended in Chapter 4 to the situation where two inputs are present. Intermodulation distortion may occur in this case. Two different types of buck amplifier with input filter are analyzed as design examples in Chapter 5. It is found that the distortion in the configurations considered may be reduced to an arbitrarily low level if the output impedance of the input filter is sufficiently small. This illustrates the concrete, quantitative, design-oriented nature of the method.

Experimental evidence is presented in Chapter 7. As might be expected, it was necessary to augment the standard small-signal measurement techniques used for switching power supplies with linear amplifier distortion measurement methods. First, the result of the design procedure in Chapter 5 is verified. Next, it is shown that the method is capable of predicting the actual time-domain output waveforms. Thus, the method is verified in two distinct ways. The entire procedure is summarized in Chapter 8.

CHAPTER 2

AN INTRODUCTION TO SWITCHING AMPLIFIERS

2.1 Introduction

This chapter contains a brief review of the basic principles of switched-mode conversion and amplification and an introduction to the nonlinear processes involved. In the first section, some typical circuits are examined. First, the four basic converter topologies are discussed, and a number of ways of modifying them to obtain four-quadrant amplifiers are shown. This is followed by a review of some of the ac applications of switching converters which have been recently proposed. In the second section, the basic properties of the ideal switching amplifier are described. In particular, it is found that the ideal switching amplifier is inherently nonlinear. The distortion processes are modelled, and a strategy is formulated for the analysis and design of low-distortion amplifiers.

2.2 Review of Topologies and Applications

The basic dc-to-dc converter topologies, from which all amplifiers discussed in this thesis are derived, are shown in Fig. 2.1. Each configuration converts a dc input voltage V_g to some dc output voltage V, supplying power to a load R. A switch repetitively connects reactive elements between the input and output, first storing energy in the reactor when the switch is in position 1, then discharging the
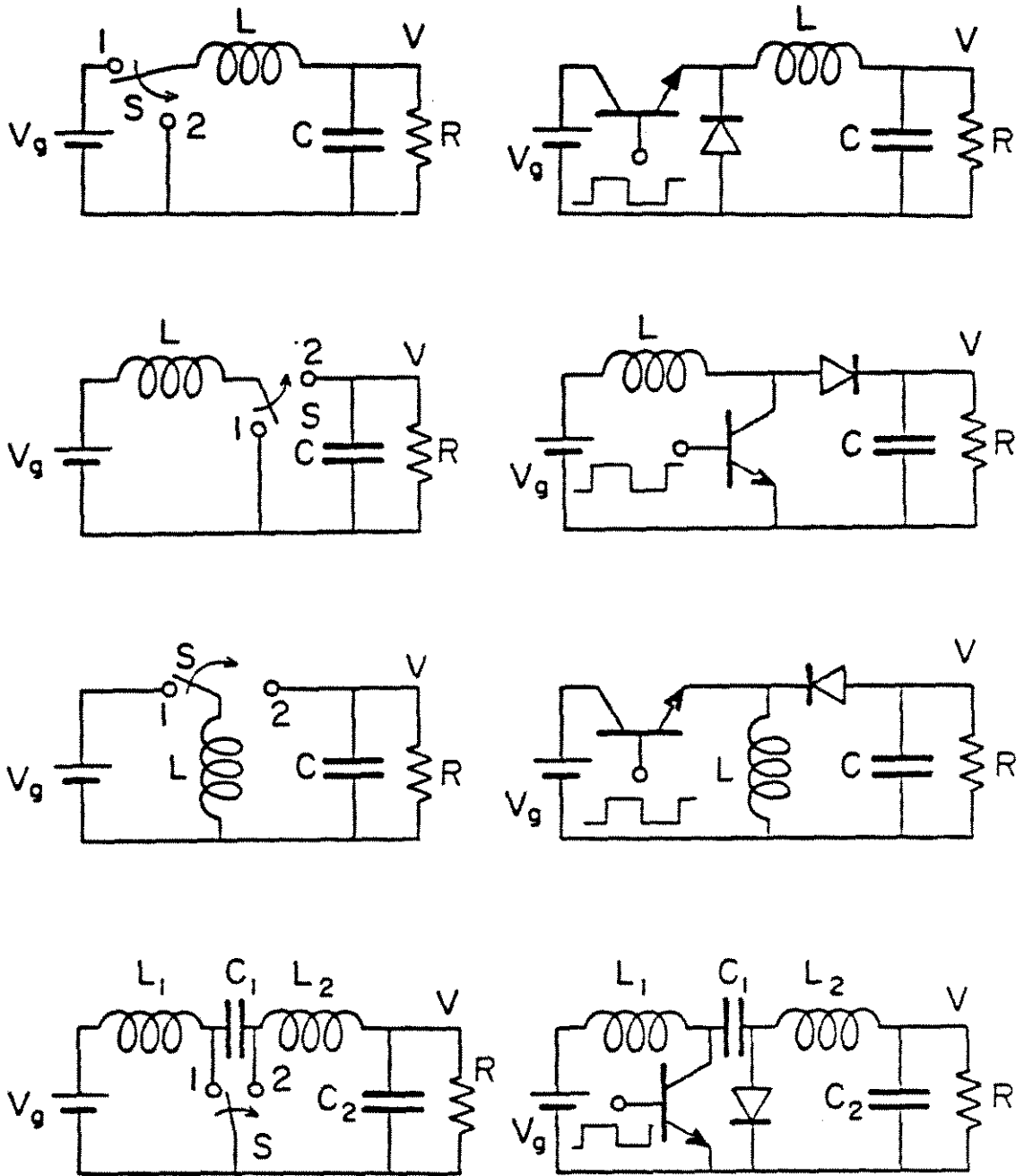
Fig. 2.1. Four basic dc-to-dc switching converters: Buck, Boost, Buck-Boost, and Ćuk. The ideal switch is usually implemented with a single transistor and diode as shown.
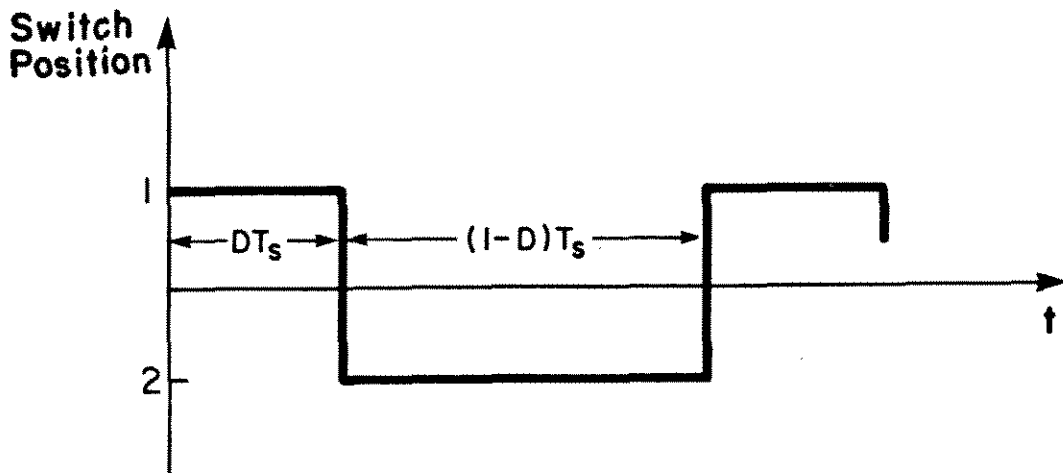
Fig. 2.2. *The switch changes repetitively between position 1, during interval DT_s, and position 2, during interval $(1-D)T_s$, where T_s is the switching period and D is the duty ratio.*

energy to the output when the switch is in position 2. The output

voltage may be controlled by proper variation of the relative amounts

of time which the switch spends in the two positions; this suggests

the use of these converters as dc amplifiers. Furthermore, since no

dissipative components are required, the efficiency of these converters

may approach 100%. Consequently, they are well-suited for power

applications.

The conversion ratios $M(D) = V/V_g$ for the basic converters are

given in Fig. 2.3. The buck converter steps the voltage down, and

the conversion ratio $M(D) = D$ is a linear function of D. The boost

converter steps up the voltage. The conversion ratio for this

converter is $M(D) = 1/(1 - D)$, a nonlinear function of D. The buck-

boost and Ćuk [2,14,15,16,17,18] converters both invert the voltage and

may either step up or step down. The conversion ratio for these

converters is $M(D) = -D/(1 - D)$, again a nonlinear function of D.

These converters are only capable of producing output voltages and

currents of one polarity; hence, they find application where a dc

(a)

(b)

(c)
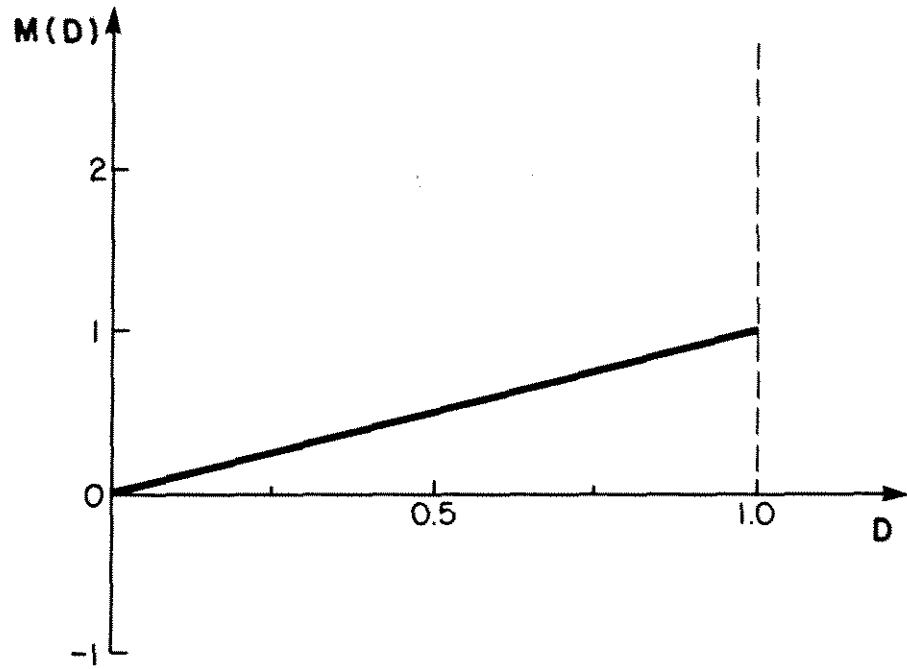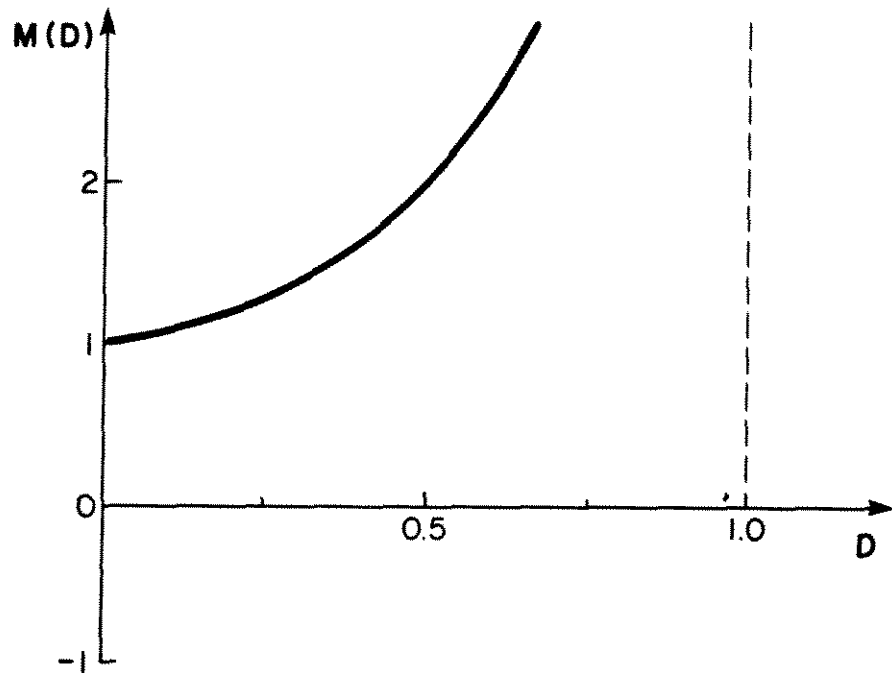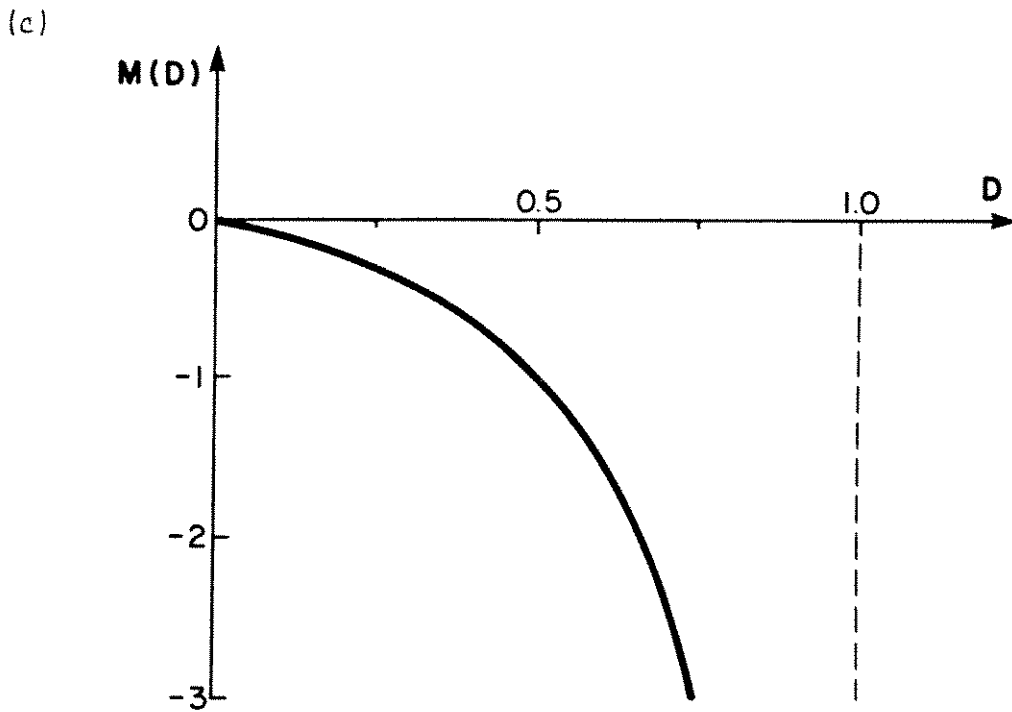
Fig. 2.3.   Conversion ratios M(D) for the basic converters of Fig.
2.1:   (a) M(D) = D for the buck converter; (b) M(D) = 1/(1-D)
for the boost converter; (c) M(D) = -D/(1-D) for the
buck-boost and Čuk converters.

output is required, principally as regulated dc power supplies.

A number of configurations have been suggested [9,10,12,19] for

dc-to-ac applications. These circuits require a power input voltage of

positive polarity, but can produce output voltages and currents of

either polarity. As a result, they are useful in ac power amplifier

applications.

Three of the many possible switching amplifier configurations are

shown in Fig. 2.4 a, b, c, and a complete open-loop system is shown in

(a)
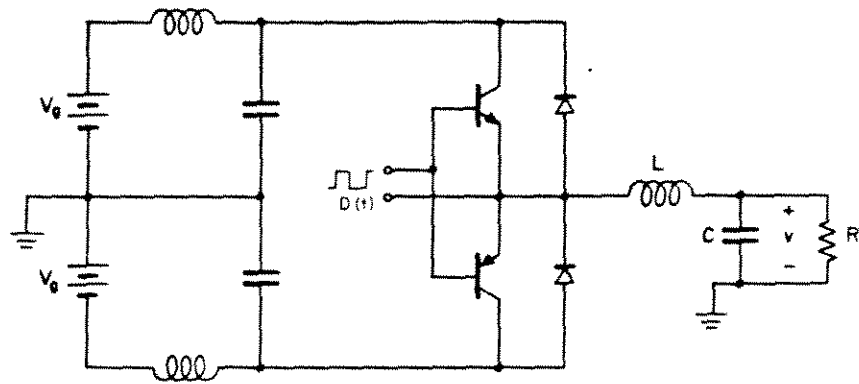
(b)
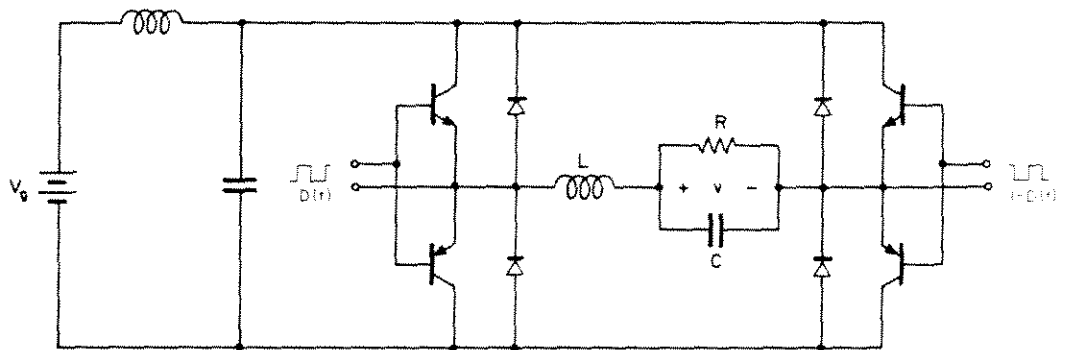
(c)
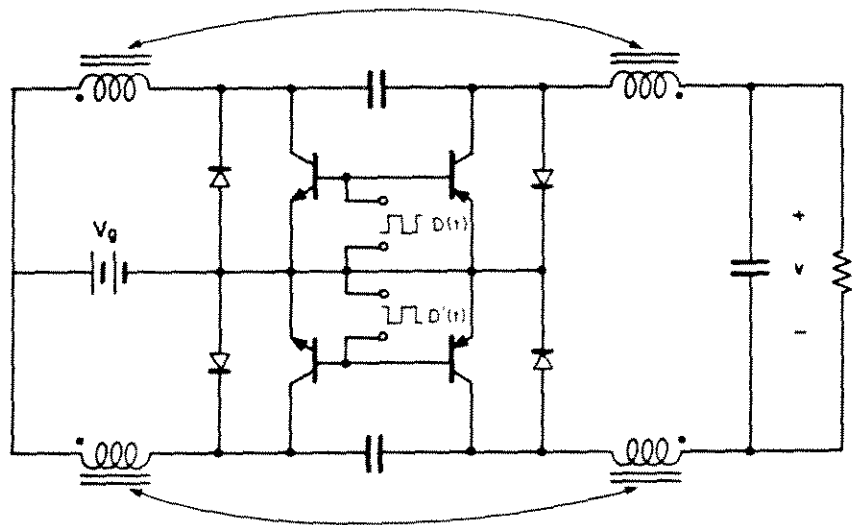
(d)
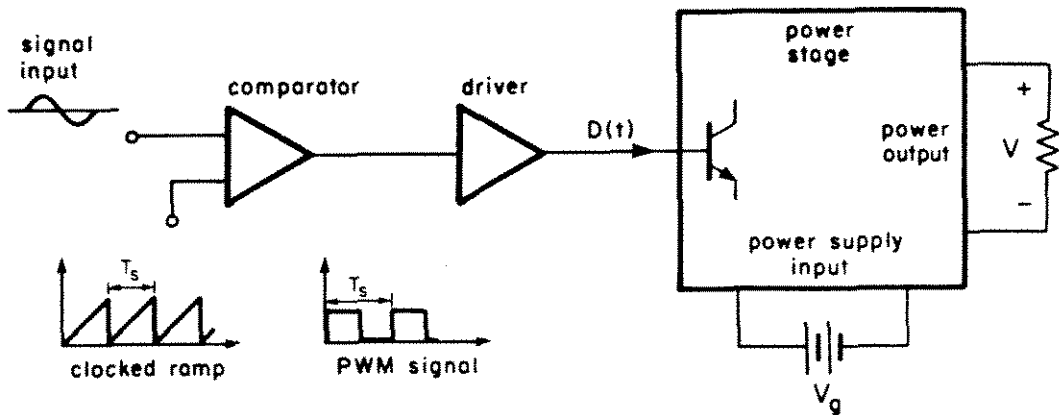
Fig. 2.4. Typical switching amplifier configurations: (a) buck amplifier with input filters; (b) bridge amplifier with input filter; (c) Ćuk amplifier; (d) the complete open-loop system.

Fig. 2.4d. The first (Fig. 2.4a) is a buck-derived converter with the load referred to ground. Both positive and negative power supplies are required, and two input filters are needed to smooth the pulsating input current which is generated. An alternative buck-derived amplifier is based on the bridge configuration and is given in Fig. 2.4b. In this case, only one supply and input filter is required; however, the load is no longer referenced to ground. The third configuration consists of a parallel connection of two two-quadrant amplifiers; a version based on the Ćuk converter is shown in Fig. 2.4c [9,20]. It too requires only one power supply at the expense of a floating load. The entire open-loop amplifier system is shown in Fig. 2.4d. It consists of a comparator and clocked ramp which perform the pulse-width modulation function, a driver which interfaces the comparator to the power switches, and the power stage itself.
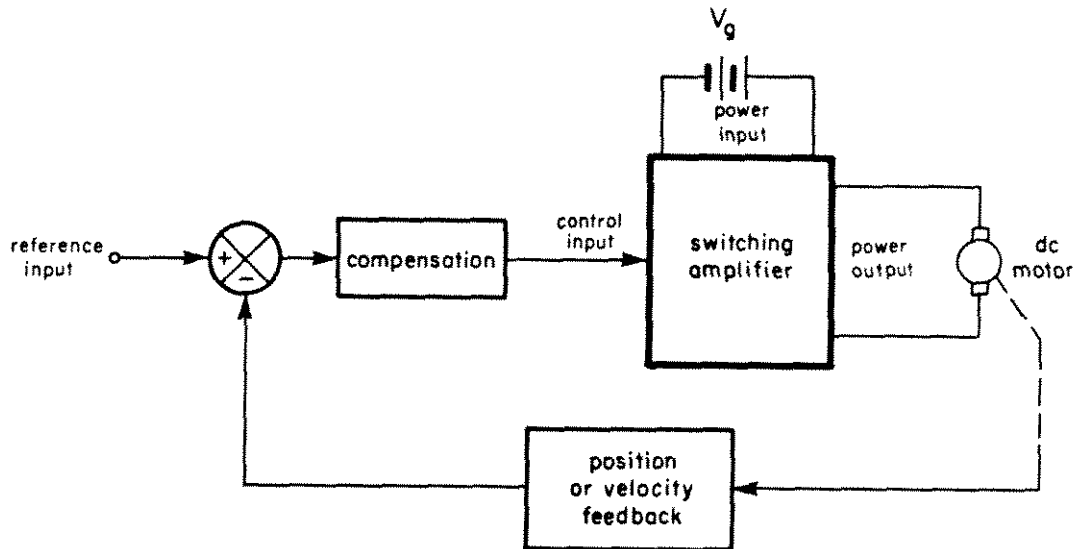
Fig. 2.5.   The application of a switching amplifier to drive a dc
motor in a servo system.

A number of authors have considered the use of switching converters

as servo amplifiers.   In [21], the idea of using a bridge amplifier

to drive a dc motor was introduced.   Later papers considered the use of

regenerative braking in such a system [22], the design of the feedback

loop [23], and the effects of dead time on the linearity of the

amplifier [24].   Another paper contained a detailed description of the

design of the entire switching servo system [25].   In light of the low

bandwidth requirements of most servo amplifiers, this is an application

for which switching amplifiers are well-suited since switching

transistors and diodes capable of operating at the kilowatt power

level and 20 kHz switching frequency are widely available today.

Another application which has received some attention is as a ringing-tone generator in telephone systems [26,27,28,29]. Here, it is necessary to produce programmable low-frequency sine waves at 100W power levels.

Switching converters have been suggested for the variable speed drive of induction motors [30,31,32]. Three-phase (or polyphase) sine waves of adjustable frequency and magnitude must be supplied to the motor at high power levels. A one-horsepower system of the type illustrated in Fig. 2.6 has been demonstrated [30]. One dc-to-dc converter is used per phase to produce a properly phased sinusoid with dc offset. This dc offset is cancelled by differential connection of the motor across the three outputs. The same technique can be applied to other areas, such as a unity power factor battery charger or uninterruptible power supply [30].
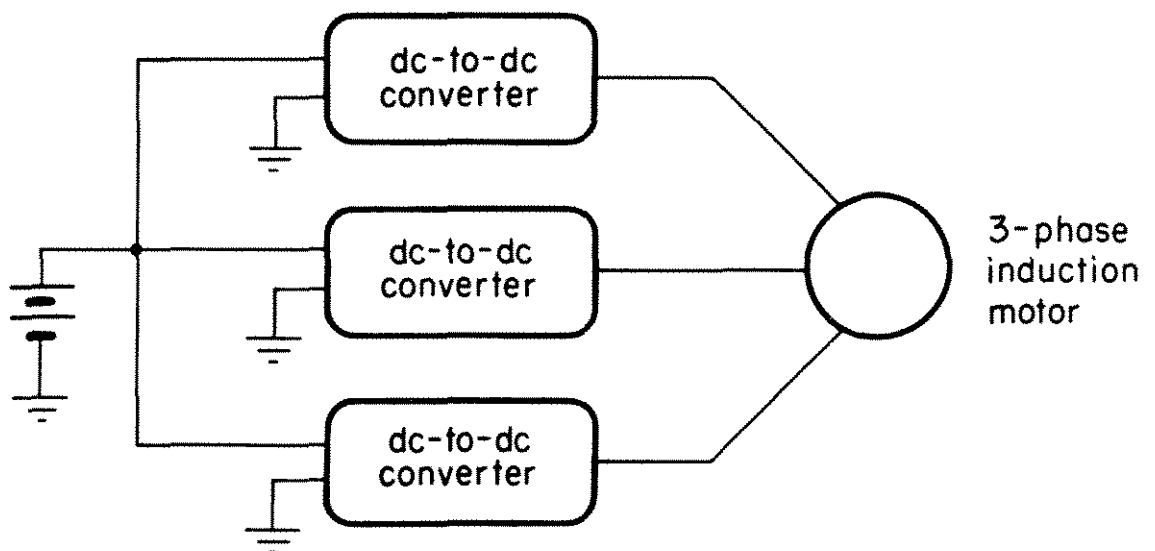
Fig. 2.6. The use of switching converters for the variable-speed drive of three phase induction motors [30]. One dc-to-dc converter is used per phase.

Yet another application is in the processing of 60 Hz power. Switching converters have been proposed as active power bandpass filters [33], solid-state transformers with adjustable turns ratios [34], power frequency converters [35], and dc-to-ac inverters for solar arrays [36,37,38,39]. Here, power is efficiently processed in ways which were not practical previously.

The most demanding application is as a high fidelity audio amplifier. Although its high efficiency makes the switching audio amplifier attractive at power levels of hundreds of watts, the high linearity and bandwidth required of such amplifiers makes their design very difficult. The design and analysis of audio switching amplifiers for dc and small signals is considered in [9,10].

It is apparent that many applications exist for switching amplifiers. In each of these, some of the voltages and currents in the converter must contain large-signal ac components. As a result, the nonlinearities in the system become significant. In the next section, the fundamental large-signal behavior of switching converters is examined.

2.3 An Elementary Nonlinear Model

In this section, the basic properties of the ideal switching amplifier are reviewed, and it is pointed out that this device is inherently nonlinear. A number of examples are given which illustrate the types of distortion that can occur. Experimentally obtained waveforms are presented which verify the existence of this distortion, and a strategy is formulated for the analysis and design of low-distortion switching amplifier systems.
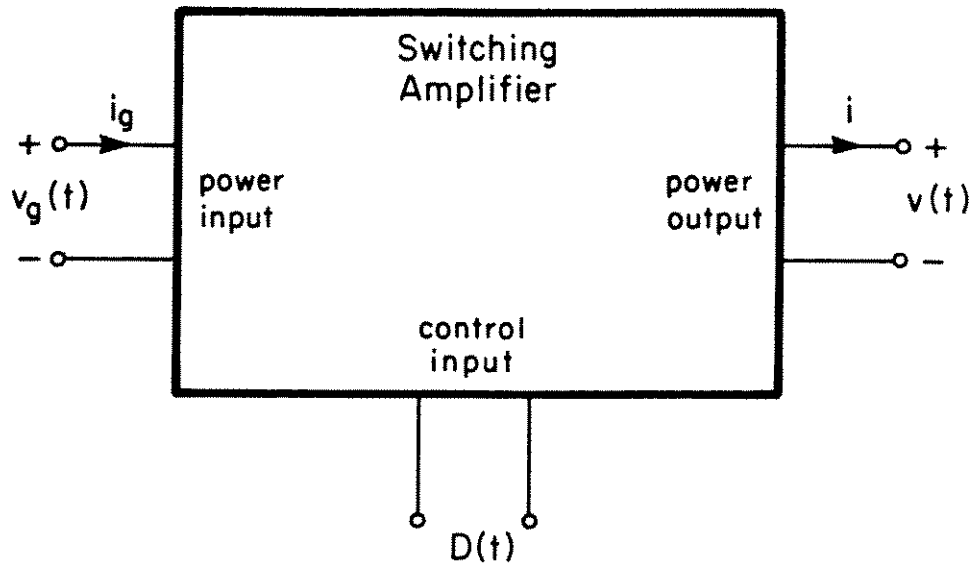
Fig. 2.7. *The basic switching amplifier is a three-port device: it contains a control input, a power input, and a power output.*

The basic switching amplifier is a three-port device, as shown in Fig. 2.7. It contains a power input, a power output, and a control input. The input power is processed as specified by the control input and then it is output to the load. Ideally, these functions are performed with 100% efficiency; therefore, if the ideal amplifier contains no storage elements, then the instantaneous input power and output power are equal:

$$v_g i_g = v \, i \qquad (2.1)$$

In general, the voltage is tranformed by some conversion ratio $M(D)$:

$$v = M(D) \, v_g \qquad (2.2)$$

Equations (2.1) and (2.2) suggest that the ideal switching amplifier possesses the properties of an ideal "dc transformer" [1,2,7,17,40,41], with "turns ratio" $M(D)$, as shown in Fig. 2.8. Note that, even though
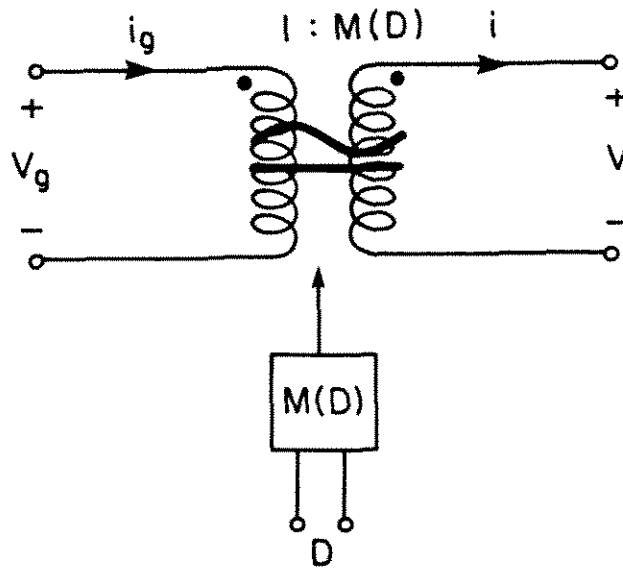
Fig. 2.8.   The ideal switching amplifier possesses the properties of
a "dc transformer" with controllable turns ratio M(D).

a real transformer cannot process dc power, the symbol in Fig. 2.8 can

nonetheless be defined to work at dc and hence correctly model the ideal

switching amplifier.

It is apparent that the ideal switching amplifier is inherently

a nonlinear device, for two reasons. First, the transformer ratio

M(D) may not be a linear function of D. Second, the transformer ratio

may be time-varying, causing the multiplication of two time-varying

signals, as described by Eq. (2.2). Examples of these two processes

are given below.

The transformer ratio of the boost converter is

$$M(D) = 1/(1 - D) \qquad\qquad (2.3)$$

Hence, M(D) is a nonlinear function of D. Consider the idealized boost

converter of Fig. 2.9. The output is given by

$$v(t) = V_g \, M(D(t)) = V_g/(1 - D(t)) \tag{2.4}$$

Since V_g is constant in this example, the multiplication process does not generate additional harmonics. In consequence, the harmonics which appear can be ascribed to the nonlinearity of M(D). For example, with sinusoidal control input

$$D(t) = D_0 + \varepsilon \sin \omega t \tag{2.5}$$

the power output is given by

$$v(t) = \frac{V_g}{1 - D_0 - \varepsilon \sin \omega t} \tag{2.6}$$

or,

$$v(t) = \frac{V_g}{D_0'} \left(1 + \frac{\varepsilon}{D_0'} \sin \omega t + \left(\frac{\varepsilon}{D_0'}\right)^2 \sin^2 \omega t + \ldots\right) \tag{2.7}$$

where $D_0' = 1 - D_0$, valid for $\varepsilon < D_0'$

which contains both even and odd harmonics.

$$M(D) = \frac{1}{1-D}$$

$$0 \leq D \leq 1$$
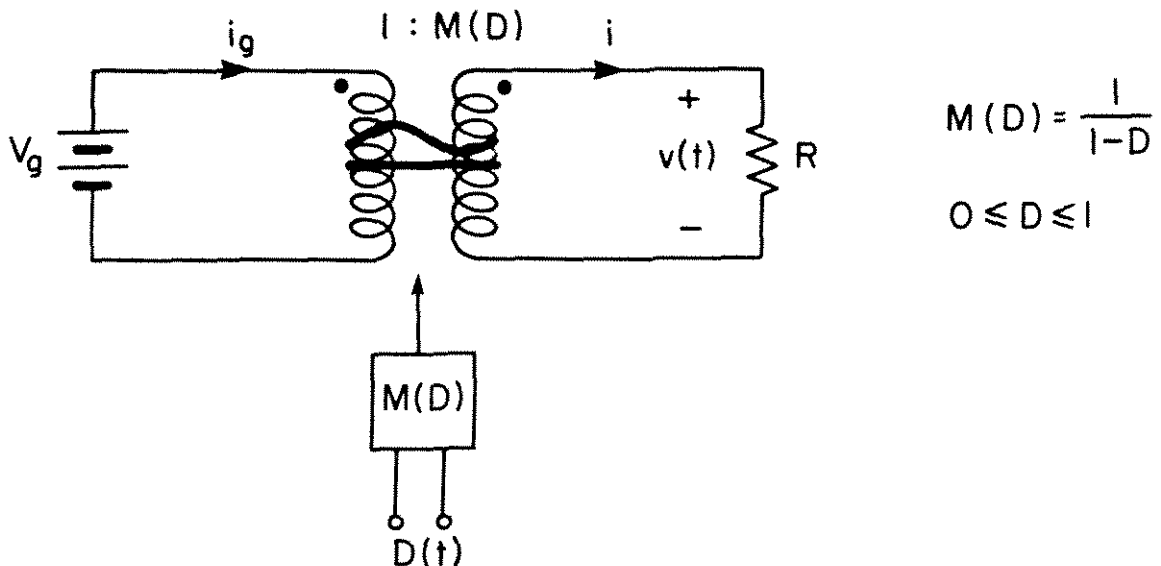
Fig. 2.9. *Idealized boost converter example. The conversion ratio M(D) is a nonlinear function of the control signal D(t).*

In this example, the form of the nonlinearity is very simple: it is a single-input, single-output block containing a nonlinear dc gain. Hence, this idealized system is easily analyzed. Unfortunately, real-life boost converters are considerably more complicated. As shown by example in the next chapter, the storage elements intrinsic to the boost converter cause the distortion to vary with frequency; as a result, the analysis above is only valid at dc.

The multiplication process generates a different type of distortion. As an example, consider the idealized buck converter of Fig. 2.10. Here the transformer ratio is a linear function of the control input; as a result, no harmonics are generated by the $M(D)$ block. However, since both $v_g(t)$ and $D(t)$ are time-varying, the multiplication process does generate harmonics. For example, if
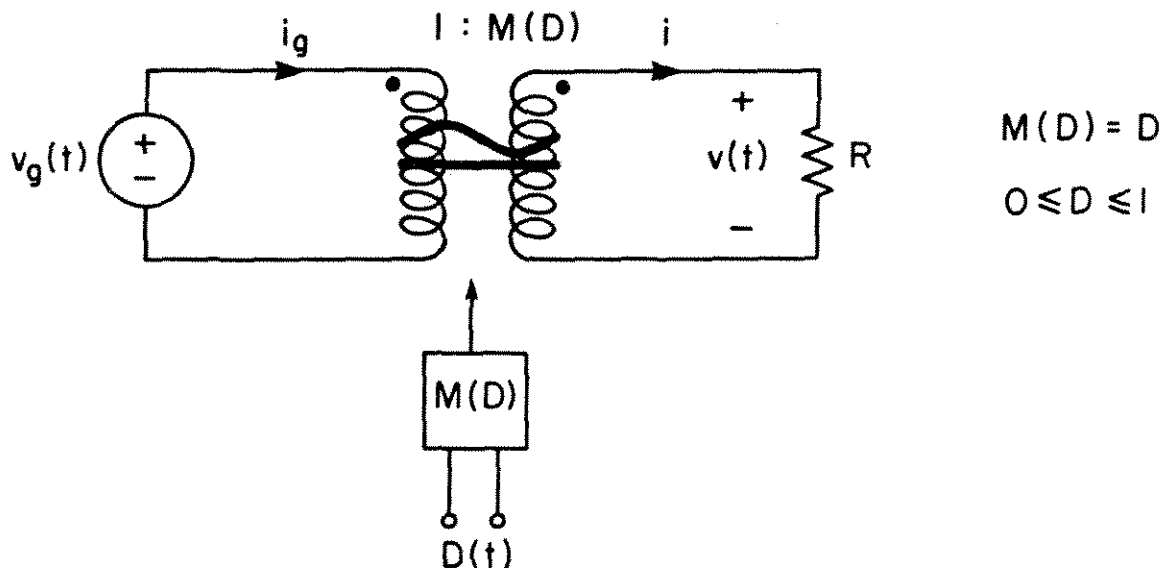
Fig. 2.10. Idealized buck converter example. Although the conversion ratio $M(D)$ is a linear function of the control signal $D(t)$, harmonics nonetheless appear at the output because the power input $v_g(t)$ and control inputs $D(t)$ are both time varying.

$$v_g(t) = A \sin \omega t \qquad\qquad (2.8)$$

$$D(t) = D_0 + \epsilon \sin \omega t \qquad\qquad (2.9)$$

then the output $v(t)$ contains dc and second harmonic components:

$$v(t) = D_0 A \sin \omega t + \frac{1}{2} \epsilon A (1 + \sin 2 \omega t) \qquad\qquad (2.10)$$

Although this multiplication process can be used to advantage in some ac-to-dc and ac-to-ac systems, in most cases it is a source of undesired harmonics.

A more complicated system occurs when external circuit elements are added. A typical dc-to-ac application is shown in Fig. 2.11. The presence of the inductor causes the input to the transformer, v_1, to vary even though V_g is constant. As a result, the multiplication process generates distortion. Furthermore, since reactive elements are present, nonlinear differential equations occur which can be very
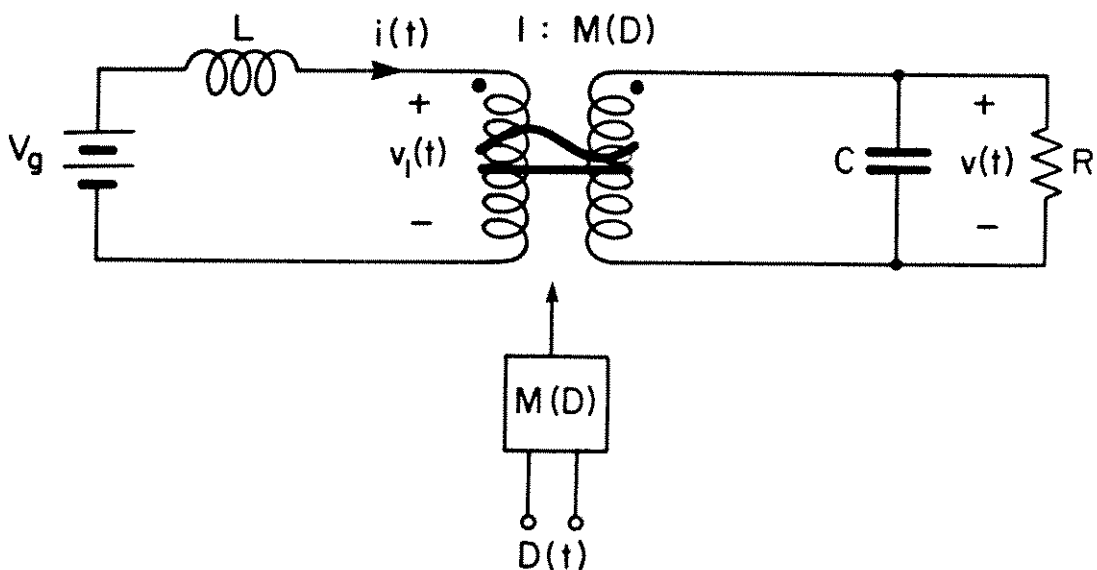
Fig. 2.11. The addition of external reactive elements results in a nonlinear dynamical system.

difficult to solve. For the example in Fig. 2.11, one obtains

$$L \frac{d\ i(t)}{dt} = V_g - v(t)/M(D(t))$$

$$(2.11)$$

$$C \frac{d\ v(t)}{dt} = i(t)/M(D(t)) - v(t)/R$$

It is apparent that the output voltage v(t) is a nonlinear function of the control input D(t), and that the level of distortion may vary with the frequency of excitation. Hence, embedding an ideal switching amplifier in a larger system can significantly complicate the distortion problem.

A more concrete example is the bridge amplifier of Fig. 2.12. An input filter is included to smooth the pulsating input current which is generated. The ac large-signal model can be found; it is given by Fig. 2.13. It can be seen that the presence of L_f causes the input to the transformer, v_s, to vary even though V_g is constant. Hence, again, the multiplication process generates distortion. The exact shape of the distorted waveform depends on the interaction of the input filter, transformer, and output filter; it should vary with frequency since the filters contain reactive elements.
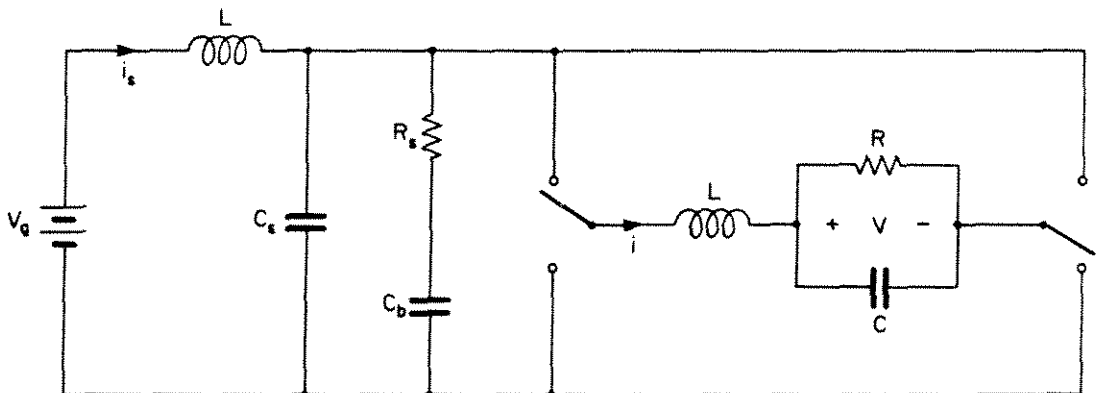
Fig. 2.12. Bridge amplifier with input filter which generates distortion.
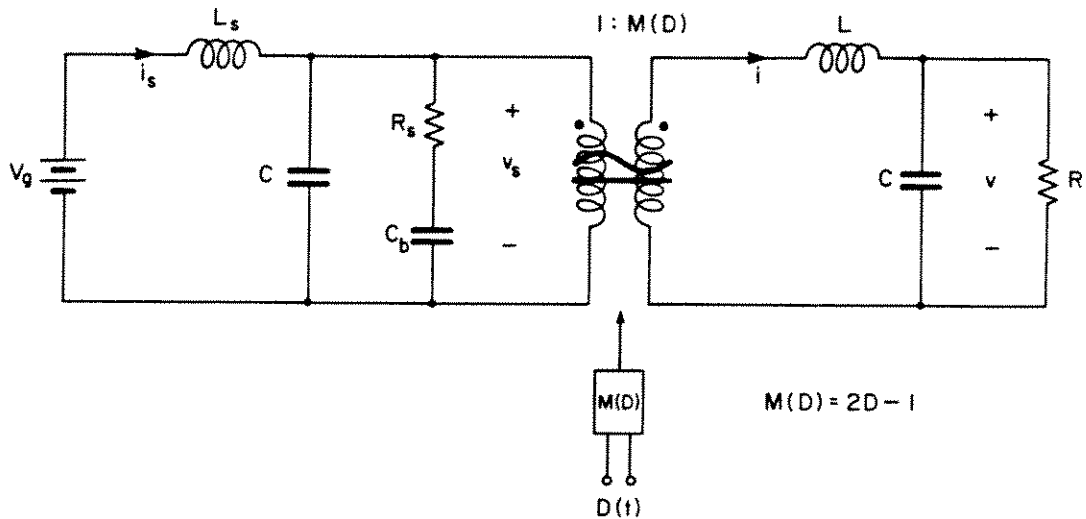
Fig. 2.13. Nonlinear model for the bridge amplifier with input filter example.

A bridge amplifier was constructed and excited sinusoidally:

$$D(t) = 0.5 + 0.25 \sin \omega t \qquad\qquad (2.12)$$

The resulting output is shown in Fig. 2.14 for 100 Hz, 300 Hz, and 750 Hz excitations. A moderate amount of distortion occurs at 100 Hz, the distortion is large at 300 Hz, but the distortion is relatively small at 750 Hz. Obviously, the relative magnitude of distortion and the shape of the output waveform change with frequency. Furthermore, the peak distortion level appears to occur in the vicinity of 300 Hz, rather than at dc. In consequence, a dc distortion analysis is insufficient; ac effects must be considered. This behavior is typical of many switching amplifiers.
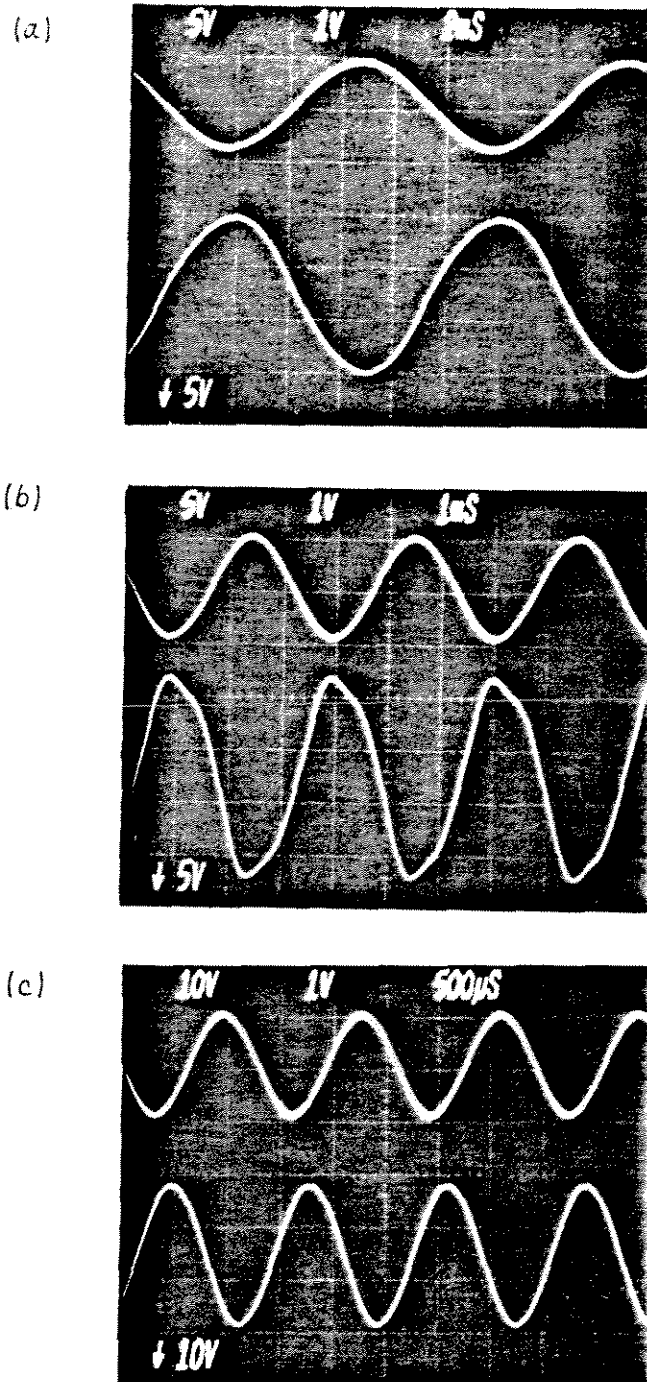
Fig. 2.14. An example of the nonlinear response inherent in switching amplifiers: output waveforms of an open-loop bridge amplifier with sinusoidal excitation. (a) the output is moderately distorted at 100Hz. (b) the output is very distorted at 300Hz. (c) the distortion is comparatively small at 750Hz. The distortion is obviously a function of frequency.

We have seen that the "ideal" switching amplifier possesses the properties of an idealized dc transformer, with turns ratio adjustable via a control signal. It is inherently a nonlinear device, and this can cause distortion problems when large signals are present. Practical switching amplifiers contain reactive components which can interact with the nonlinear transformer element, causing frequency-dependent distortion. The operating environment of the amplifier may contain additional impedances which can also interact with the switching amplifier. Thus, the ideal first-order properties of switching amplifiers can lead to intricately distorted large-signal output waveforms.

How should this problem be analyzed? A typical problem may contain many reactive elements, and hence become quite complicated. In light of this, it is apparent that if a result is to be useful, it should be design-oriented. Hence, we would prefer to draw linear circuit models, Bode plots, etc., which yield insight into the distortion processes and provide an efficient procedure for the reduction of distortion to an acceptable level. For example, one would like to draw a Bode plot similar to Fig. 2.9 which describes the amplitude and phase of each harmonic as a function of frequency. It would then be a straightforward matter to choose component values which meet the specifications.

Unfortunately, the above techniques were developed for linear systems, so it appears impossible to analyze nonlinear phenomena such as distortion in this way. Apparently, one must resort to the solution of the nonlinear differential equations which describe the system, a hopeless task. The remainder of Part I describes a procedure which
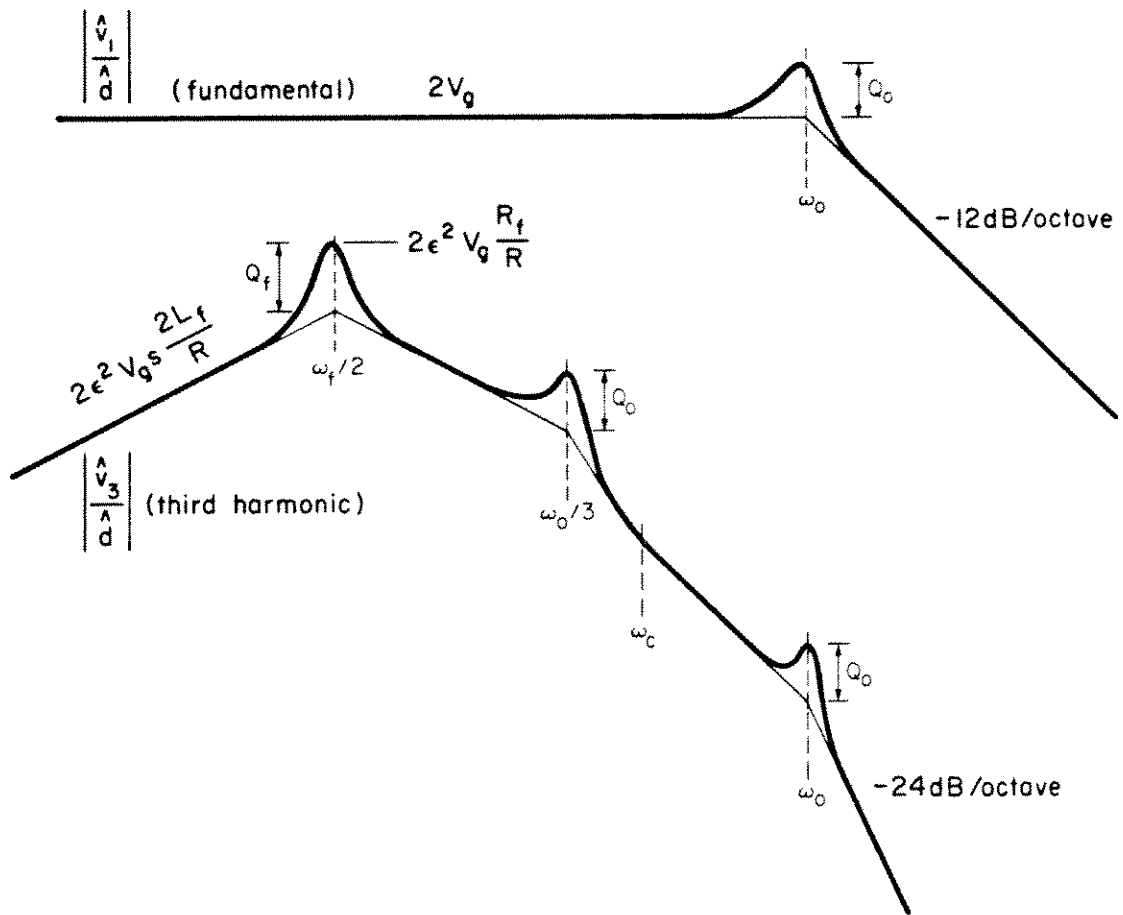
Fig. 2.15. The goal of the distortion analysis: magnitude vs. frequency plots of the dominant components of the output waveform. All salient features are labelled, and the dependence of the distortion on the various circuit elements is apparent.

avoids this problem. Rather than solving the nonlinear differential equations in exact closed form, an approximate series solution is sought. In most cases, the first few terms of this series yield an accurate approximation of the output waveforms. The result of the procedure, described in the next chapter, is a series of *linear* circuit models, which may be solved using standard techniques, yielding the approximate amplitude and phase of each harmonic. The objective of a design-oriented method for the prediction and reduction of the distortion inherent in switching amplifiers is then realized.

CHAPTER 3

ANALYSIS — SIMPLE HARMONIC DISTORTION

3.1 Introduction

In this chapter, the model described in the previous section is rigorously derived, and a step-by-step procedure is given for the construction of this model for any switching amplifier. Only variations in duty ratio are considered here, although the same techniques could be applied to variations in other quantities such as the line voltage V_g if desired. The method used is a generalization of the small-signal continuous-mode state-space averaging technique [1,2] to include large signals. The nonlinear averaged state equations which describe the converter are defined and then solved by use of a series expansion. An additional assumption is then made which allows the neglect of the higher-order terms in the expansion for each harmonic. One may then construct a series of *linear circuit models*, one for each harmonic, which may be solved to yield the approximate magnitude and phase of every harmonic component in the output.

3.2 Series Expansion of State Vector

The first step is the formulation of the state-space descriptions of the system during the two switched intervals. During each interval, the system may be described by a set of linear differential equations:

$$K \frac{d\underline{x}(t)}{dt} = A_1 \underline{x}(t) + B_1 \underline{u} \quad \text{during interval } DT_s \quad\quad (3.1)$$

$$K \frac{d\underline{x}(t)}{dt} = A_2 \underline{x}(t) + B_2 \underline{u} \quad \text{during interval } D'T_s \quad\quad (3.2)$$

where D = duty ratio, $D' \triangleq 1 - D$.

T_s = period of one complete switching cycle.

K is a matrix usually containing values of L and C.

$\underline{x}$ is a state vector, usually comprised of capacitance voltages and inductance currents.

$\underline{u}$ is a vector of independent sources.

These equations may be solved exactly; however, the subsequent analysis is greatly simplified if the usual state-space averaging approximations [1,2] are made. Specifically, if the converter natural frequencies are all well below the switching frequency, then Eqs. (3.1) and (3.2) above have approximately linear solutions. This is indeed the case in well-designed converters, in which the switching ripple is small. An additional consequence of this condition is that one may neglect the sampling process inherent in all pulse-width modulators. In other words, the actual discrete-time system may be transformed into a continuous-time system with negligible loss of accuracy in the open-loop transfer functions of the power amplifier. This is an important step because it allows us to employ a frequency-domain approach in our distortion analysis. Otherwise, we could not speak of

a harmonic series at all.

The result of these approximations is the following nonlinear state equation:

$$K \frac{d\underline{x}(t)}{dt} = [D(t)A_1 + D'(t)A_2]\underline{x}(t) + [D(t)B_1 + D'(t)B_2]\underline{u} \qquad (3.3)$$

This equation is nonlinear because the input $D(t)$ and the state vector $\underline{x}(t)$ appear multiplied together. A general closed-form solution is not known, and would probably be useless anyway.

The alternative is to find a series expansion of the solution. To do so, one requires a parameter for expansion. The logical choice when calculating simple harmonic distortion is the amplitude of the input sine wave. Therefore, define

$$D(t) = D_0 + \hat{d}(t) \qquad (3.4)$$

$$D_0' = 1 - D_0$$

$$\hat{d}(t) = \text{ac input to system}$$

For the analysis of simple harmonic distortion, one assumes that the input is a sine wave:

$$\hat{d}(t) = \epsilon \sin \omega t \qquad (3.5)$$

$$\epsilon = \text{amplitude of the sinusoidal input}$$

Note that, since $0 \le D(t) \le 1$, $\epsilon \le 1/2$

It is convenient in the subsequent analysis to display the dependence of $\hat{d}$ on ϵ explicitly; hence define

$$\epsilon \, d'(t) = \hat{d}(t) \tag{3.6}$$

Thus $d'(t) = \sin \omega t$

A suitable parameter for expansion, therefore, is ϵ. We will perform a "straightforward expansion" [3,4], writing the state vector as an infinite series. The hope is that convergence will be rapid and only the first few terms will be significant. Hence, let

$$\underline{x}(t) = \underline{x}_0 + \epsilon \underline{x}_1(t) + \epsilon^2 \underline{x}_2(t) + \epsilon^3 \underline{x}_3(t) + \ldots \tag{3.7}$$

Substitution of Eqs. (3.4) - (3.7) into Eq. (3.3) yields

$$K \frac{d}{dt} [\underline{x}_0 + \epsilon \underline{x}_1 + \epsilon^2 \underline{x}_2 + \ldots] =$$

$$[(D_0 + \epsilon d')A_1 + (D_0' - \epsilon d')A_2] [\underline{x}_0 + \epsilon \underline{x}_1 + \epsilon^2 \underline{x}_2 + \ldots]$$

$$+ [(D_0 + \epsilon d')B_1 + (D_0' - \epsilon d')B_2]\underline{u} \tag{3.8}$$

The individual components of the state vector $\underline{x}_i(t)$ may now be found by equating like powers of ϵ:

to order ϵ^0

$$K \frac{d}{dt} \underline{x}_0 = \underline{0} = [D_0 A_1 + D_0' A_2]\underline{x}_0 + [D_0 B_1 + D_0' B_2]\underline{u}$$

$$\underline{x}_0 = - A^{-1}B\underline{u} \tag{3.9}$$

where $A = D_0 A_1 + D_0' A_2$, $B = D_0 B_1 + D_0' B_2$

$\underline{x}_0$ is the quiescent (dc) operating point. It has the same values as when calculated using the small-signal state-space averaging method [1,2].

to order ε^1

$$K \frac{d}{dt} \underline{x}_1(t) = A\underline{x}_1 + \underline{c} \, d \tag{3.10}$$

where $\underline{c} = (A_1 - A_2)\underline{x}_0 + (B_1 - B_2)\underline{u}$

$\underline{x}_1$ is the dominant linear component of the state vector. It is the ac quantity calculated by the small-signal state-space averaging method. Note that $\underline{c}d$ is the linear forcing term.

to order ε^2

$$K \frac{d}{dt} \underline{x}_2(t) = A\underline{x}_2 + [A_1 - A_2]\underline{x}_1(t)d(t) \tag{3.11}$$

This is the second order system. Note that it is a *linear* differential equation. $[A_1 - A_2]\underline{x}_1 d$ is the forcing term. If the order ε^1 system has been solved, then the forcing term may be evaluated. The linear differential equation (3.11) is then solved to find $\underline{x}_2(t)$.

to order ε^n

$$K \frac{d}{dt} \underline{x}_n(t) = A\underline{x}_n + [A_1 - A_2]\underline{x}_{n-1}(t) \, d(t), \quad n > 1 \tag{3.12}$$

This is the nth order system. Again note that is is *linear*. Knowing $\underline{x}_{n-1}(t)$ and $d(t)$, one may easily calculate the forcing term

$[A_1 - A_2]\underline{x}_{n-1}(t)$ $\tilde{d}(t)$. The solution of the linear differential equation (3.12) then yields $\underline{x}_n(t)$.

Thus, one obtains a linear system at each order of ε. The solution of these systems is relatively straightforward since no nonlinear differential equations need be solved. However, it remains to put these equations in a form more accessible to the electrical engineer. This may be done by reconstructing equivalent circuit models for the state equations at each order of ε, as in the next section.

3.3 Linear Circuit Models

In the above analysis a series of linear systems was derived which describes the waveforms present at each state. No small-signal assumption was made; hence, the method is valid for large signals and predicts harmonic distortion. However, this series of linear systems is so far merely a collection of equations. It is desirable to find a more illuminating form for the design of a switching amplifier. Namely, we would like to find some type of *circuit model* which describes the harmonic distortion generated, yet retains the desirable linear properties of the above mathematical representations. This can easily be done; one merely reconstructs the linear circuits described by the above state equations at each order of ε. This is done below for the example of the boost converter in Fig. 3.1.
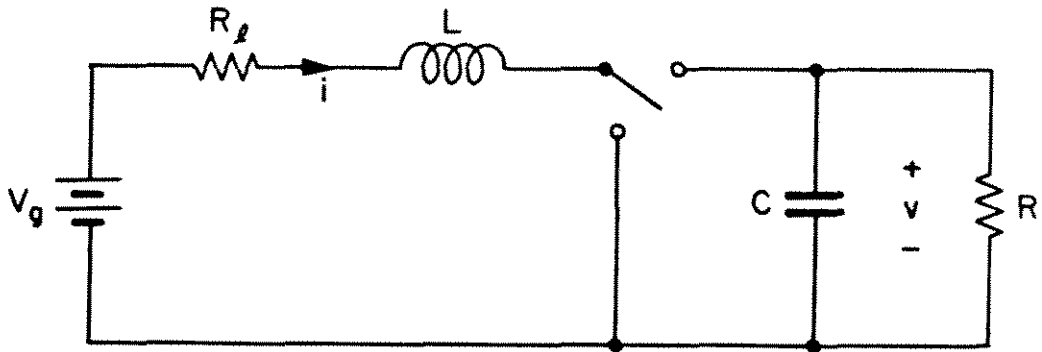
Fig. 3.1. Simple boost converter example.

to order ϵ^0

Upon evaluation of Eq. (3.9) for the boost example, one obtains

$$
\begin{bmatrix} 0 \\ \\ 0 \end{bmatrix} = \begin{bmatrix} -R_\ell & -D_0' \\ \\ D_0' & -\frac{1}{R} \end{bmatrix} \begin{bmatrix} i_0 \\ \\ v_0 \end{bmatrix} + \begin{bmatrix} 1 \\ \\ 0 \end{bmatrix} V_g \tag{3.13}
$$

The corresponding circuit is Fig. 3.2. After circuit manipulation, one obtains Fig. 3.3. This is the usual dc model. It is also the zero-order term in our large-signal expansion. One may solve for the nominal quantities i_0 and v_0, taking into account parasitic elements such as R_ℓ if desired.
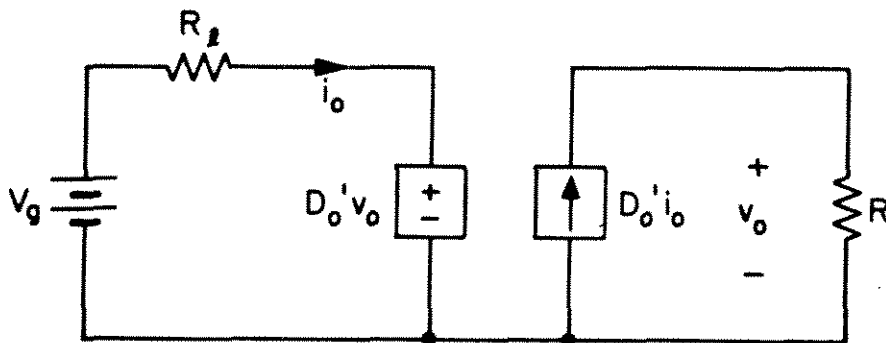
Fig. 3.2. Circuit which models the dc (quiescent) conditions in the boost example.
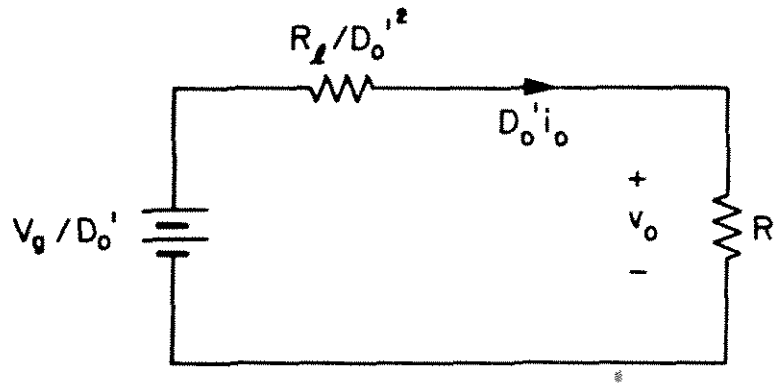
Fig. 3.3. Simplification of the dc model of Fig. 3.2.

to order ϵ^1.

Evaluation of Eq. (3.10) yields

$$\begin{bmatrix} L & 0 \\ & \\ 0 & C \end{bmatrix} \frac{d}{dt} \begin{bmatrix} i_1 \\ \\ v_1 \end{bmatrix} = \begin{bmatrix} -R_\ell & -D_0' \\ & \\ D_0' & -\frac{1}{R} \end{bmatrix} \begin{bmatrix} i_1 \\ \\ v_1 \end{bmatrix} + \begin{bmatrix} 0 & 1 \\ & \\ -1 & 0 \end{bmatrix} \begin{bmatrix} i_0 \\ \\ v_0 \end{bmatrix} d$$

(3.14)

The corresponding circuit is given in Fig. 3.4. This is the usual small signal model which accounts for duty ratio variations but not variations in V_g or other independent sources.
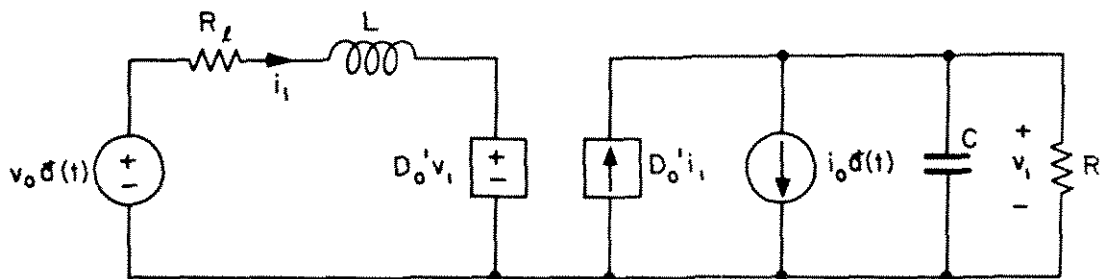
Fig. 3.4. Circuit which models the first-order (fundamental) components in the boost example.

It is also the first-order term in our large-signal expansion. One may solve for first-order variations in state quantities (i.e., i_1 and v_1). In general, these are all sinusoids at the fundamental frequency ω but with different amplitudes and phase offsets:

$$d(t) = \sin \omega t$$

$$v_1(t) = \left| \frac{v_1}{d} \right| \sin\left(\omega t + \left/ \frac{v_1}{d} \right.\right)$$

$$i_1(t) = \left| \frac{i_1}{d} \right| \sin\left(\omega t + \left/ \frac{i_1}{d} \right.\right) \tag{3.15}$$

with

$$\underline{x}_1(t) = \begin{bmatrix} i_1(t) \\ v_1(t) \end{bmatrix}$$

<u>to order ε^2</u>

Upon evaluation of Eq. (3.11), one obtains

$$\begin{bmatrix} L & 0 \\ 0 & C \end{bmatrix} \frac{d}{dt} \begin{bmatrix} i_2 \\ v_2 \end{bmatrix} = \begin{bmatrix} -R_\ell & -D_0' \\ D_0' & -\frac{1}{R} \end{bmatrix} \begin{bmatrix} i_2 \\ v_2 \end{bmatrix} + \begin{bmatrix} 0 & 1 \\ -1 & 0 \end{bmatrix} \begin{bmatrix} i_1 \\ v_1 \end{bmatrix} d \tag{3.16}$$

The corresponding circuit is shown in Fig. 3.5. This is the first new result of the present analysis. Note the similarity with the first-order model; only the independent generators differ. This system is *linear*, yet it yields information about second-order *nonlinearities*
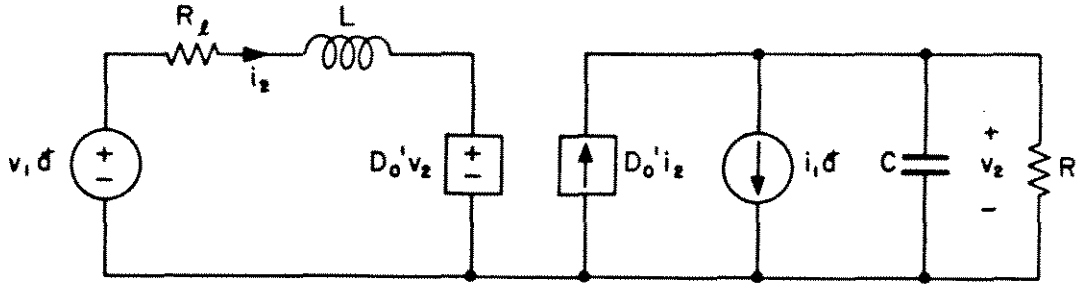
Fig. 3.5.   Circuit which models the second-order (dc and second harmonic) components in the boost example.

of the power amplifier.   In particular, one may calculate the approximate magnitude of the second harmonic using this model.

Note that, since the circuit elements are connected in the same way, the poles of the second-order system will be the same as the poles of the first-order system.   However, the amplitudes and phasings of the generators are not the same, so the zeroes will in general be different.   If the first-order model has been solved, then the quantities $v_1(t)d(t)$ and $i_1(t)d(t)$ are known and are of the form

$$v_1\, d = \left|\frac{v_1}{d}\right| \sin\left(\omega t + \angle\frac{v_1}{d}\right)\, \sin(\omega t)$$

$$i_1\, d = \left|\frac{i_1}{d}\right| \sin\left(\omega t + \angle\frac{i_1}{d}\right)\, \sin(\omega t)$$

(3.17)

which involves the product of two sinusoids.   The application of a trigonometric identity yields

$$v_1\, d = v_{10} + v_{12}(t)$$

$$i_1\, d = i_{10} + i_{12}(t)$$

(3.18)

$$\underline{x}_2(t) = \underline{x}_{20} + \underline{x}_{22}(t)$$

where

$$v_{10} = -\frac{1}{2} \left| \frac{v_1}{a} \right| \sin \left(\angle \frac{v_1}{a} - \frac{\pi}{2} \right)$$

$$v_{12} = \frac{1}{2} \left| \frac{v_1}{a} \right| \sin \left(2\omega t + \angle \frac{v_1}{a} - \frac{\pi}{2} \right)$$

$$i_{10} = -\frac{1}{2} \left| \frac{i_1}{a} \right| \sin \left(\angle \frac{i_1}{a} - \frac{\pi}{2} \right)$$

$$i_{12} = \frac{1}{2} \left| \frac{i_1}{a} \right| \sin \left(2\omega t + \angle \frac{i_1}{a} - \frac{\pi}{2} \right)$$

$\underline{x}_{20}$ = the resulting dc component of $\underline{x}_2(t)$

$\underline{x}_{22}(t)$ = the resulting second harmonic component of $\underline{x}_2(t)$.

Define

$$\underline{x}_{12}(t) = \begin{bmatrix} i_{12}(t) \\ v_{12}(t) \end{bmatrix}, \quad \underline{x}_{10} = \begin{bmatrix} i_{10}(t) \\ v_{10}(t) \end{bmatrix} \tag{3.19}$$

Note that

$$\underline{x}_{12}(t) = \frac{1}{2} \underline{x}_1 \left(2t - \frac{\pi}{2\omega} \right)$$

$$\underline{x}_{10}(t) = -\frac{1}{2} \underline{x}_1 \left(-\frac{\pi}{2\omega} \right) \tag{3.20}$$
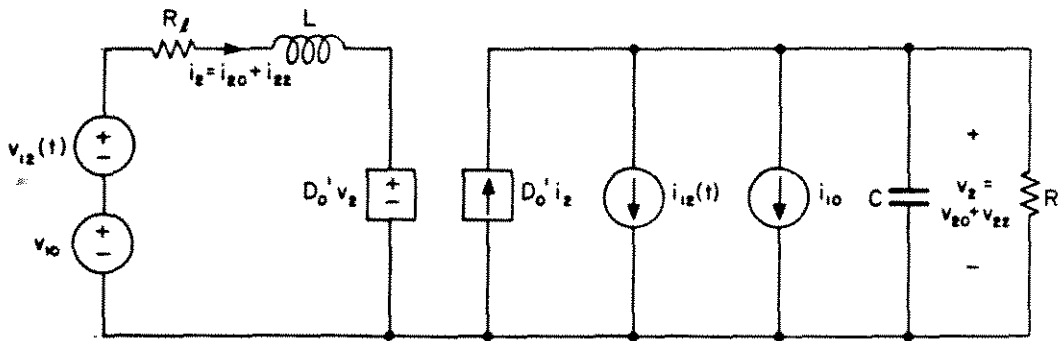
Fig. 3.6. *The first step in the simplification of the second-order model: split the nonlinear generators into their dc components (V_{10} and i_{10}) and second harmonic components (V_{12} and i_{12}).*

Thus, the nonlinear generators in Fig. 3.5 may be resolved into their dc components v_{10} and i_{10}, and their second harmonic components v_{12} and i_{12}, as in Fig. 3.6. Furthermore, since the resulting second-order system is linear, the principle of linear superposition holds; in consequence, the dc and second harmonic components may be solved separately as in Fig. 3.7.
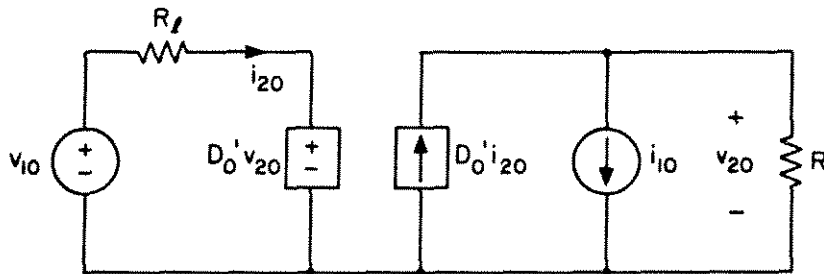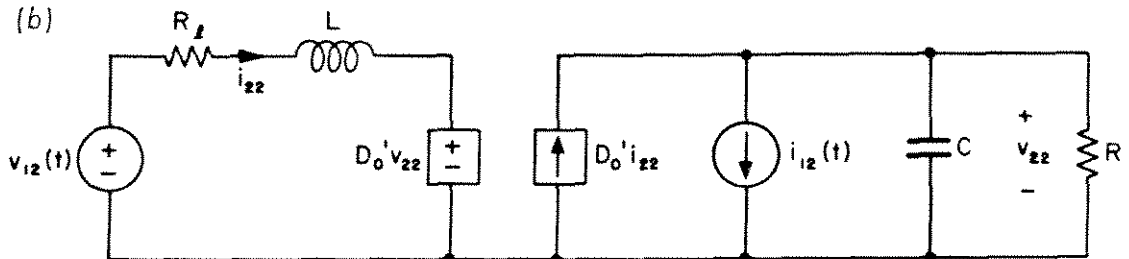
Fig. 3.7. *The second step in the simplification of the second order model: with the use of linear superposition, calculate the dc components (a) and second harmonic components (b) separately.*
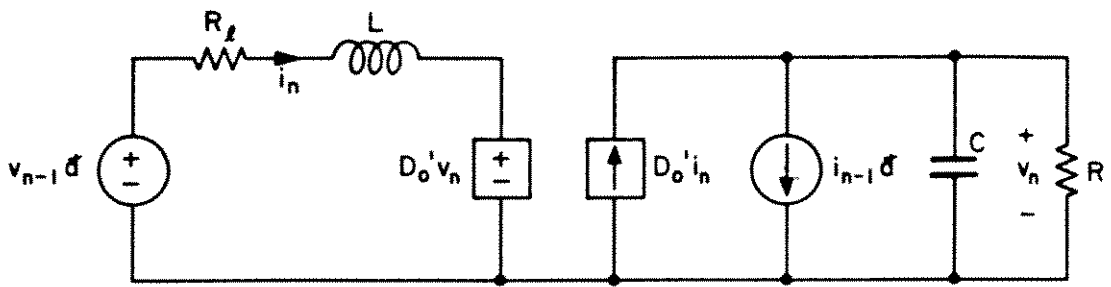
Fig. 3.8. Circuit which models the n-th order (n ≥ 2) components in the boost example.

to order ε^n.

Evaluation of Eq. (3.12) yields

$$
\begin{bmatrix} L & 0 \\ 0 & C \end{bmatrix} \frac{d}{dt} \begin{bmatrix} i_n \\ v_n \end{bmatrix} = \begin{bmatrix} -R_\ell & i_n \\ D_0' & v_n \end{bmatrix} + \begin{bmatrix} 0 & 1 \\ -1 & 0 \end{bmatrix} \begin{bmatrix} i_{n-1} \\ v_{n-1} \end{bmatrix} \vec{\alpha} \tag{3.21}
$$

The corresponding circuit model is given in Fig. 3.8. In general, the n-th-order model is of the same form as the second-order model; only the subscripts are changed. The amplitude and phase of v_n and i_n depend on the amplitude and phase of v_{n-1} and i_{n-1}, as well as the circuit elements. The circuit topology and element values remain the same, independent of n. The nth order circuit model yields information about nth order nonlinearities of the system; in particular, one may calculate the approximate magnitude and phase of the nth harmonic using this model.

If the order ϵ^{n-1} model, has been solved, then the quantities $v_{n-1}(t)$ $\bar{d}(t)$ and $i_{n-1}(t)$ $\bar{d}(t)$ are known. In general, $v_{n-1}(t)$ and $i_{n-1}(t)$ contain even harmonics of frequencies 0, 2ω, 4ω, ... $(n-1)\omega$ for n odd, or odd harmonics of frequencies ω, 3ω, 5ω, ... $(n-1)\omega$ for n even. Hence, the generators in the order ϵ^n model contain terms of the form

$$\sin((k-1)\omega t + \phi)\,\sin(\omega t) = \frac{1}{2}\sin(k\omega t + \phi - \frac{\pi}{2}) - \frac{1}{2}\sin((k-2)\omega t + \phi - \frac{\pi}{2})$$

$$k = \begin{cases} 0,\ 2,\ 4,\ \ldots\ n & \text{for n even} \\ 1,\ 3,\ 5,\ \ldots\ n & \text{for n odd} \end{cases} \tag{3.22}$$

In other words, the n-th order system contains even harmonics for n even and odd harmonics for n odd, as summarized in Table 3.1.

The n-th order system may now be solved by the same procedure used for the second-order system. The generators are first resolved into their different frequency components, as in Fig. 3.9. Linear superposition is then employed to calculate each component separately, as in Fig. 3.10.

Thus, by adapting the small-signal state-space averaging method to include large signals, one may analyze the simple harmonic distortion generated by a switching amplifier. The method employs the key state-space averaging approximations which require the converter natural frequencies to be well below the switching frequency. However, the small signal approximation is not used; instead, a series expansion of the state vector is made. The result is a series of *linear* equations which may be solved consecutively, yielding the amplitude and phase of any harmonic component of the output. Moreover, a series of *linear circuit models* may be reconstructed from these equations which yield additional insight into the operation of the

frequency   order

component ε^0 ε^1 ε^2 ε^3 ε^4 ε^5

dc $\underline{x}_0$ $\underline{x}_{20}$ $\underline{x}_{40}$

ω $\underline{x}_1$ $\underline{x}_{31}$ $\underline{x}_{51}$

2ω $\underline{x}_{22}$ $\underline{x}_{42}$

3ω $\underline{x}_{33}$ $\underline{x}_{53}$

4ω $\underline{x}_{44}$

5ω $\underline{x}_{55}$
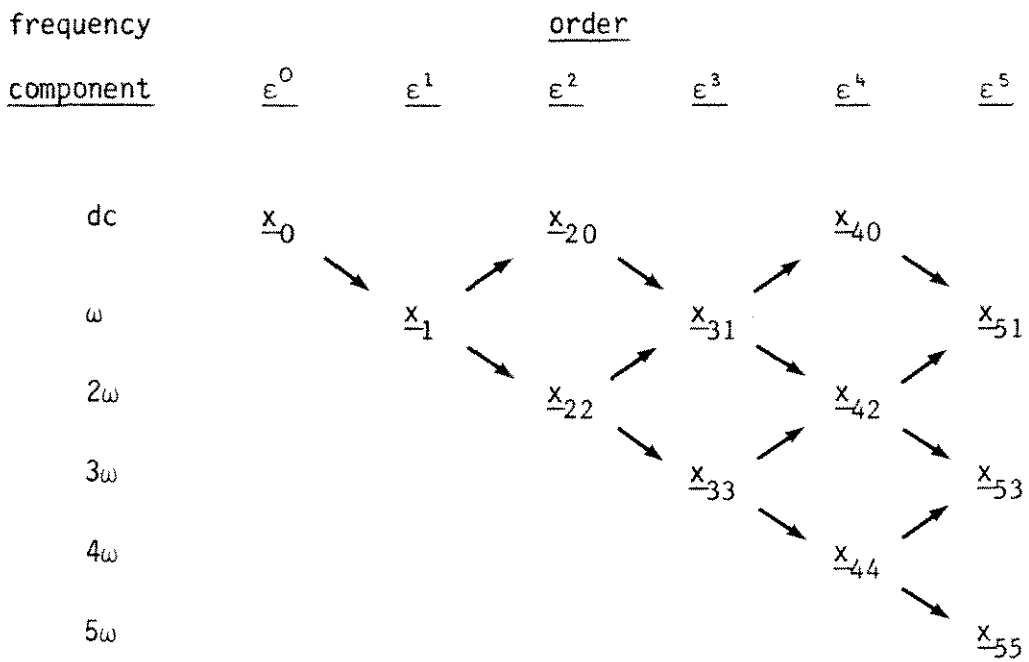
Table 3.1. Summary of the frequency components present in the order ε^n model, and their dependence on the components present in the order ε^{n-1} model.
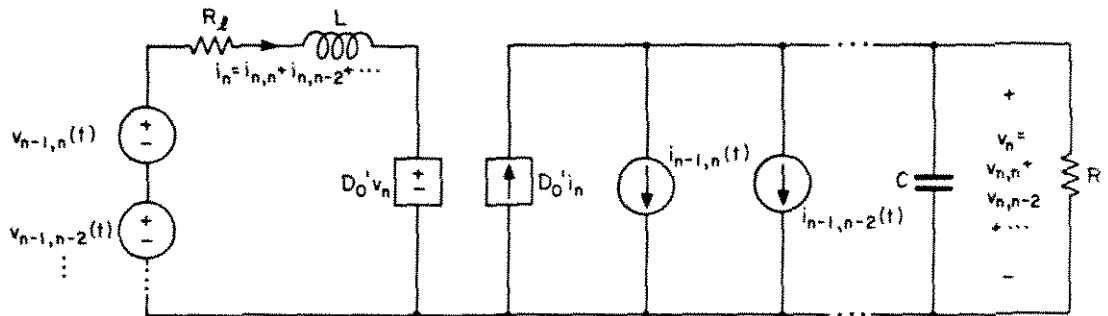
Fig. 3.9.   The first step in the simplification of the n-th order model: resolve the nonlinear generators into their various harmonic components.
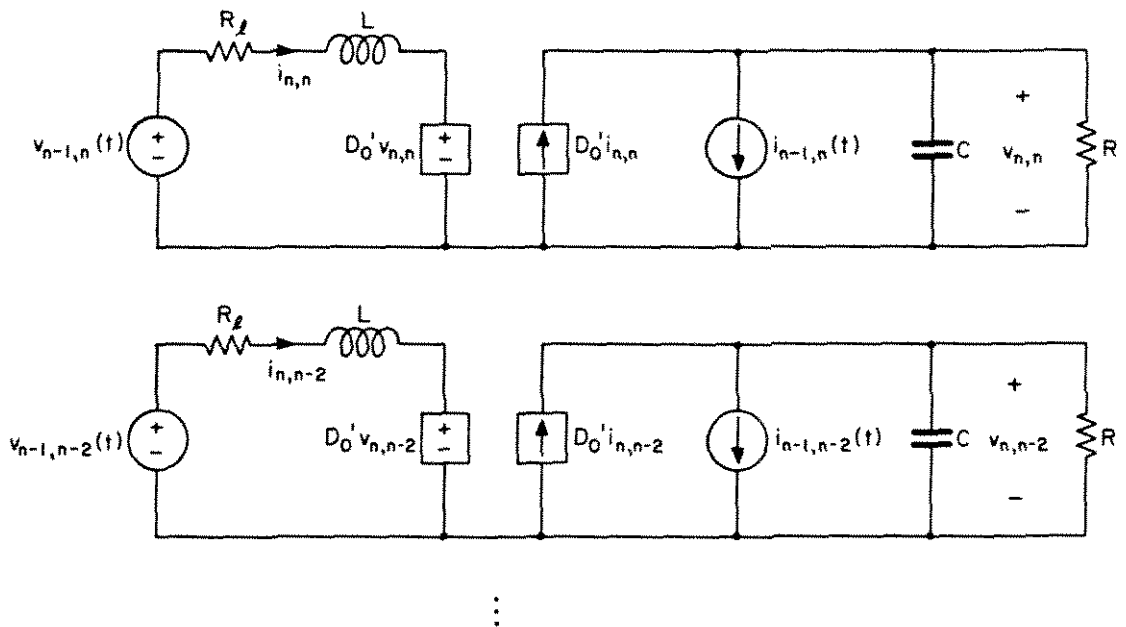
Fig. 3.10.   The second step in the simplification of the n-th order model: with the use of linear superposition, calculate each harmonic component separately.

circuit. Standard linear circuit analysis techniques may then be used.

The method as it stands to this point requires the solution of the circuit model at each order in the series separately. For example, to estimate the second harmonic, one must first evaluate the zero-order circuit at dc. The solutions for $\underline{x}_0$ obtained are then inserted into the first-order circuit model, and it is evaluated at the fundamental frequency. These first-order solutions ($\underline{x}_1$) are next inserted into the second-order circuit model and it is solved at the second-harmonic frequency, yielding the desired solution $\underline{x}_2$. Then, to order ε^2, the total solution for $\underline{x}(t)$ given by Eq. (3.7) is

$$\underline{x}_0 + \varepsilon\underline{x}_1(t) + \varepsilon^2\underline{x}_2(t).$$

Needless to say, this procedure may become tedious for orders of ε larger than two or three. In the next section, we will see how to translate the frequency of the nth-order model down to the fundamental, thus allowing the evaluation of the entire series of circuit models to be done at the fundamental frequency. In addition, we will approximate the series solution for each harmonic by its lowest-order term. The series of models may then be combined into one large circuit model and solved in one step.

3.4 An Additional Simplification

As stated previously, the objective of this analysis is to obtain expressions for the magnitude of the various harmonic distortion components as a function of frequency. In particular, it is desired to draw Bode plots for each harmonic, as in Fig. 2.15. Note that all salient features of the response are labeled; in consequence, the dependence of each harmonic on the element values in the system is apparent, and the result is design-oriented.

Since the result of the analysis in Sections 3.2 and 3.3 is a series of linear circuit models, most of the useful techniques of linear circuit theory may be applied, including the derivation of sinusoidal transfer functions and the construction of Bode plots. However, there is one complication which arises owing to the necessity of evaluating each circuit model at a different frequency: the resulting "transfer functions" must be evaluated partially at the fundamental frequency, partially at the second harmonic frequency, and so on. For example, the order ε^3 third-harmonic component of the output of the bridge amplifier in Fig. 2.4b may be found by application of this method; the result is

$$\left| v_3 \right| = 2\varepsilon^3 \, V_g \, \frac{\left| Z_s(s) \right|_{s \,=\, 2j\omega}}{\left| Z_i(s) \right|_{s \,=\, j\omega}} \, \left| H(s) \right|_{s \,=\, 3j\omega} \tag{3.23}$$

where $Z_s(s)$, $Z_i(s)$, and $H(s)$ are various impedances and transfer functions in the amplifier. Note that $Z_i(s)$ is evaluated at the fundamental frequency, $Z_s(s)$ at the second harmonic, and $H(s)$ at the

third harmonic. Thus, even though the intermediate models at each order of ε are linear, the complete model is not entirely linear and expressions for the harmonics such as Eq. (3.23) are not evaluated at a single frequency. It is desirable to eliminate this remaining nonlinearity from the model; all sinusoidal transfer functions would then be evaluated completely at the fundamental frequency.

It is also desired to approximate each harmonic by its lowest-order term. For example, the fundamental component of the state vector is

$$\varepsilon \underline{x}_1(t) + \varepsilon^3 \underline{x}_{31}(t) + \varepsilon^5 \underline{x}_{51}(t) + \dots \tag{3.24}$$

If this series converges rapidly enough, then it may be approximated by its lowest-order term, $\varepsilon \underline{x}_1(t)$. A similar argument holds for all other harmonics, with the result that the n-th harmonic is approximated by $\varepsilon^n \underline{x}_{nn}(t)$. This is summarized in Table 3.2. The analysis is greatly simplified with this approximation.

It now becomes a straightforward matter to modify the model so that it is evaluated entirely at the fundamental frequency; one merely shifts the frequency of each higher-order model by an appropriate amount. The mechanics of this frequency shift involve the substitution of effective vectors $\hat{\underline{x}}_n$ for the n-th-order state vectors $\underline{x}_{nn}$ defined previously. These effective vectors $\hat{\underline{x}}_n$ have the same magnitude as their counterparts $\underline{x}_{nn}$, but are evaluated at the fundamental frequency instead of at the n-th harmonic. One may thus solve the resulting linear circuit models using standard techniques at the fundamental

frequency component	order					
	ε^0	ε^1	ε^2	ε^3	ε^4	ε^5
dc	$\underline{x}_0$					
ω		$\underline{x}_1$				
2ω			$\underline{x}_{22}$			
3ω				$\underline{x}_{33}$		
4ω					$\underline{x}_{44}$	
5ω						$\underline{x}_{55}$

Table 3.2. Summary of the frequency components present in the approximate model. Each harmonic is approximated by its lowest-order term.

frequency, yet find the amplitude and phase of each harmonic.

The differential equations which describe $\underline{x}_1(t)$ and $\underline{x}_{22}(t)$ are as follows:

$$\underline{0} = A \, \underline{x}_0 + B\underline{u} \tag{3.25a}$$

$$K \frac{d}{dt} \underline{x}_1(t) = A \, \underline{x}_1(t) + \underline{c} \, \bar{d}(t) \tag{3.25b}$$

$$K \frac{d}{dt} \underline{x}_{22}(t) = A \, \underline{x}_{22}(t) + [A_1 - A_2] \cdot \underline{x}_{12}(t)$$

$$= A \, \underline{x}_{22}(t) + \frac{1}{2} [A_1 - A_2] \, \underline{x}_1 \, (2t - \frac{\pi}{2\omega}) \tag{3.25c}$$

This follows from Eqs. (3.9-3.11) and (3.20). We now shift the frequency of $\underline{x}_{22}(t)$ by performing the substitution

$$\hat{\underline{x}}_1(t) = \varepsilon \underline{x}_1(t)$$

$$\hat{\underline{x}}_2(t) = \varepsilon^2 \underline{x}_{22}(\frac{1}{2}(t + \frac{\pi}{2\omega})) \tag{3.26}$$

Eqs. (3.25 abc) then become

$$\underline{0} = A\underline{x}_0 + B\underline{u} \tag{3.27a}$$

$$K \frac{d}{dt} \hat{\underline{x}}_1(t) = A\hat{\underline{x}}_1(t) + \underline{c} \, \hat{d}(t) \tag{3.27b}$$

$$2K \frac{d}{dt} \hat{\underline{x}}_2(t) = A\hat{\underline{x}}_2(t) + \frac{\varepsilon}{2} [A_1 - A_2] \, \hat{\underline{x}}_1(t) \tag{3.27c}$$

Note that $\hat{\underline{x}}_2(t)$ now contains components only at the fundamental

frequency, but with the same amplitude as the second harmonic component

of $\varepsilon^2\underline{x}_2(t)$. The phase is also the same, except it is shifted by -90°.

The approximate amplitude and phase of the fundamental are found by

evaluating Eq. (3.27b) at the fundamental frequency. The amplitude and

phase of the second harmonic are found by evaluating Eq. (3.27c) at

the fundamental frequency also; at the end of the analysis we simply

note that the amplitude of the second harmonic is the same as the

magnitude of $\hat{\underline{x}}_2(t)$, and the phase differs by -90°.

The result may easily be generalized to the higher order case:

$\underline{x}_n$ contains harmonics 1,3,5,...n for odd and 0,2,4,...n for n even.

All harmonics are usually negligible except for the nth, defined by

$$\hat{\underline{x}}_n(t) = \varepsilon^n\underline{x}_{nn}(\frac{1}{n}(t + \frac{(n-1)\pi}{2\omega}))$$
(3.28)

Again, this is usually a good approximation since the components we

neglect are of higher order than the dominant component which is kept.

If desired, an extension of this procedure may be used to calculate

the extra correction terms due to these additional harmonics.

Insertion of Eq. (3.28) into Eq. (3.12) yields

$$nK\frac{d}{dt}\hat{\underline{x}}_n(t) = A\hat{\underline{x}}_n(t) + \frac{\varepsilon}{2}(A_1 - A_2)\hat{\underline{x}}_{n-1}(t)$$
(3.29)

$\hat{\underline{x}}_n$ has the same amplitude as the dominant component of the nth

harmonic. Its phase differs by $-(n-1)90^\circ$.

The higher-order circuit model corresponding to Eqs. (3.27b), (3.27c), and (3.29) for our boost example now becomes Fig. 3.11. The complete set of linear state equations which describes the dominant component of each harmonic is given below:

$$\underline{0} = A \, \underline{x}_0 + B\underline{u}$$

$$K \frac{d}{dt} \hat{\underline{x}}_1 = A \, \hat{\underline{x}}_1 + [(A_1 - A_2)\underline{x}_0 + (B_1 - B_2)\underline{u}] \, \hat{d}$$

$$2K \frac{d}{dt} \hat{\underline{x}}_2 = A \, \hat{\underline{x}}_2 + \frac{\varepsilon}{2} (A_1 - A_2) \, \hat{\underline{x}}_1$$

$$3K \frac{d}{dt} \hat{\underline{x}}_3 = A \, \hat{\underline{x}}_3 + \frac{\varepsilon}{2} (A_1 - A_2) \, \hat{\underline{x}}_2$$

$$\vdots$$

$$nK \frac{d}{dt} \hat{\underline{x}}_n = A \, \hat{\underline{x}}_n + \frac{\varepsilon}{2} (A_1 - A_2) \, \hat{\underline{x}}_{n-1} \qquad\qquad (3.30)$$

Thus by considering only the element component of each harmonic and by shifting the frequency of the harmonics (i.e., the higher-order models) down to the fundamental frequency, a *completely linear* set of differential equations is derived which predicts the simple harmonic distortion inherent in switching amplifiers. Linear circuit models such as Fig. 3.11 may now be constructed and then solved using standard phasor techniques, evaluated at the fundamental frequency. Bode plots may be drawn for each harmonic, and design criteria found for the reduction of this distortion to an acceptable level. An example of this procedure is given in Chapter 5.
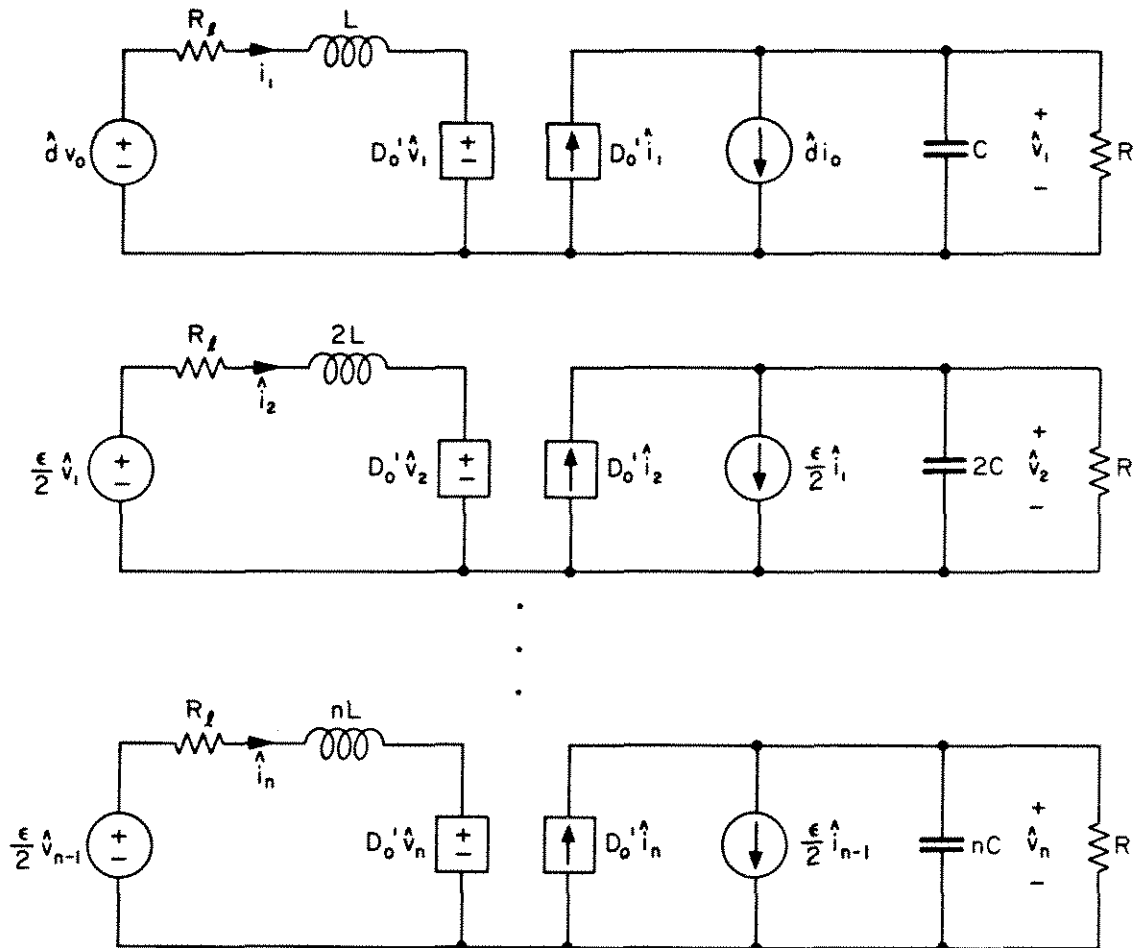
Fig. 3.11a.
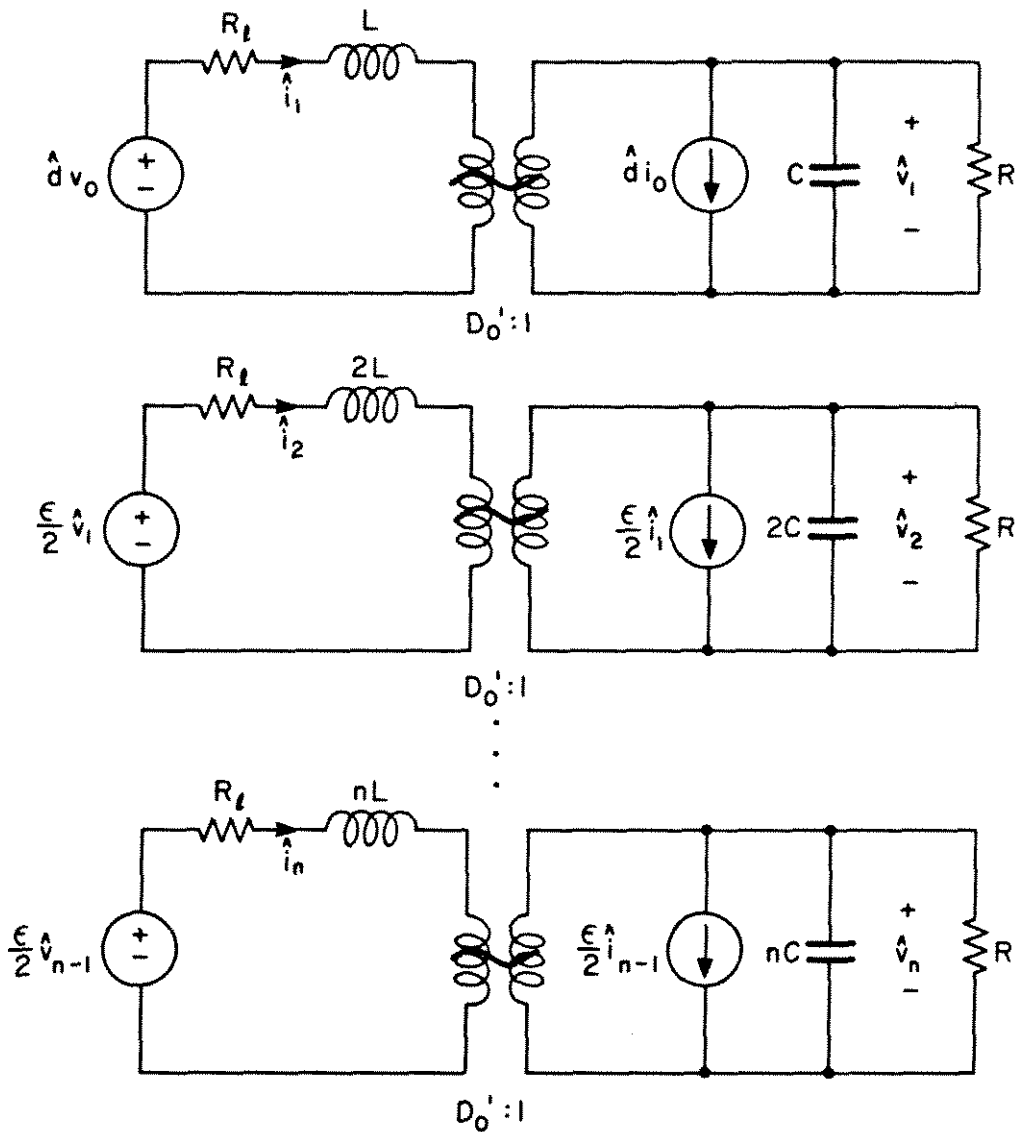
Fig. 3.11b.

Fig. 3.11. The result of the simplification process: (a) a series of linear circuit models, evaluated at the fundamental frequency, which approximate the amplitude and phase of the fundamental, second harmonic, and n-th harmonic components; (b) an equivalent representation, with the dependent generators replaced by ideal transformers.

3.5 Discussion

Upon inspection of Fig. 3.11, one observes the following
qualitative features. First, an extra set of states is added for each
higher order calculated. However, because of the structure of
Eq. (3.30) it is a simple matter to construct these higher-order models.
The topology of each model is the same, but the L's and C's are
multiplied by n. As a result, the natural frequencies (poles) merely
shift down in frequency by a factor of n; the associated Q-factors
remain the same. Thus, the poles may be drawn by inspection if the
first-order response is known. However, the zeroes change and may not
be drawn as easily.

These features may be explained as follows: Combination of
Eqs. (3.3) and (3.4) yields

$$K \frac{d\underline{x}(t)}{dt} = A\underline{x}(t) + B\underline{u} + \varepsilon(B_1-B_2)\underline{u}\tilde{d}(t) + \underbrace{(A_1-A_2)\underline{x}(t)\varepsilon\tilde{d}(t)}_{\text{nonlinear term}} \qquad (3.31)$$

The nonlinear term has the form $(A_1 - A_2)\underline{x}(t)\varepsilon\tilde{d}(t)$. If this term is
small in magnitude, then the differential equation is nearly linear and
hence we expect distortion to be small. The converse also applies:
if the nonlinear term is large, we expect to have a large amount of
distortion.

One way to make the nonlinear term large is to make $\varepsilon\tilde{d}(t)$ large.
In other words, increasing the input amplitude ε tends to increase the
amount of harmonics at the output: dc asymptotes increase.

Another way to increase the nonlinear term is to increase $(A_1 - A_2)\underline{x}(t)$. Thus, a resonance which causes $\underline{x}(t)$ to be large will probably result in increased harmonics. Likewise, the poles of the first-order system should also appear in all higher-order systems.

Harmonics are also affected by the L-C filter. Hence, the poles of the first-order system occur shifted down an octave in the second-order system, down a factor of three in the third-order system, etc. This accounts for the extra set of poles added at each higher-order system.

The phasings and positions of the generators account for the zeroes. For example, if the generators are scaled and phased just right, a null could occur (i.e., resonant zeroes). So the zeroes of the higher-order models are not as closely related to the first-order model as are the poles.

As an example of the behavior predicted by the model, the functions $\hat{v}_1/\hat{d}$, $\hat{v}_2/\hat{d}$, and $\hat{v}_3/\hat{d}$ are plotted in Fig. 3.12 for the boost converter example of Fig. 3.13. Also, the locations of the poles and zeroes for this example are summarized in Table 3.3.

It can be seen that the fundamental response contains the familiar two poles and one right-half-plane zero of the small-signal transfer function [1,2]. This is expected because all fundamental-frequency terms of higher order have been neglected.

The "second harmonic response", $\hat{v}_2/\hat{d}$, contains four poles and two zeroes. Note that the peak second harmonic distortion occurs around 700 Hz rather than at dc. A dc distortion analysis would give
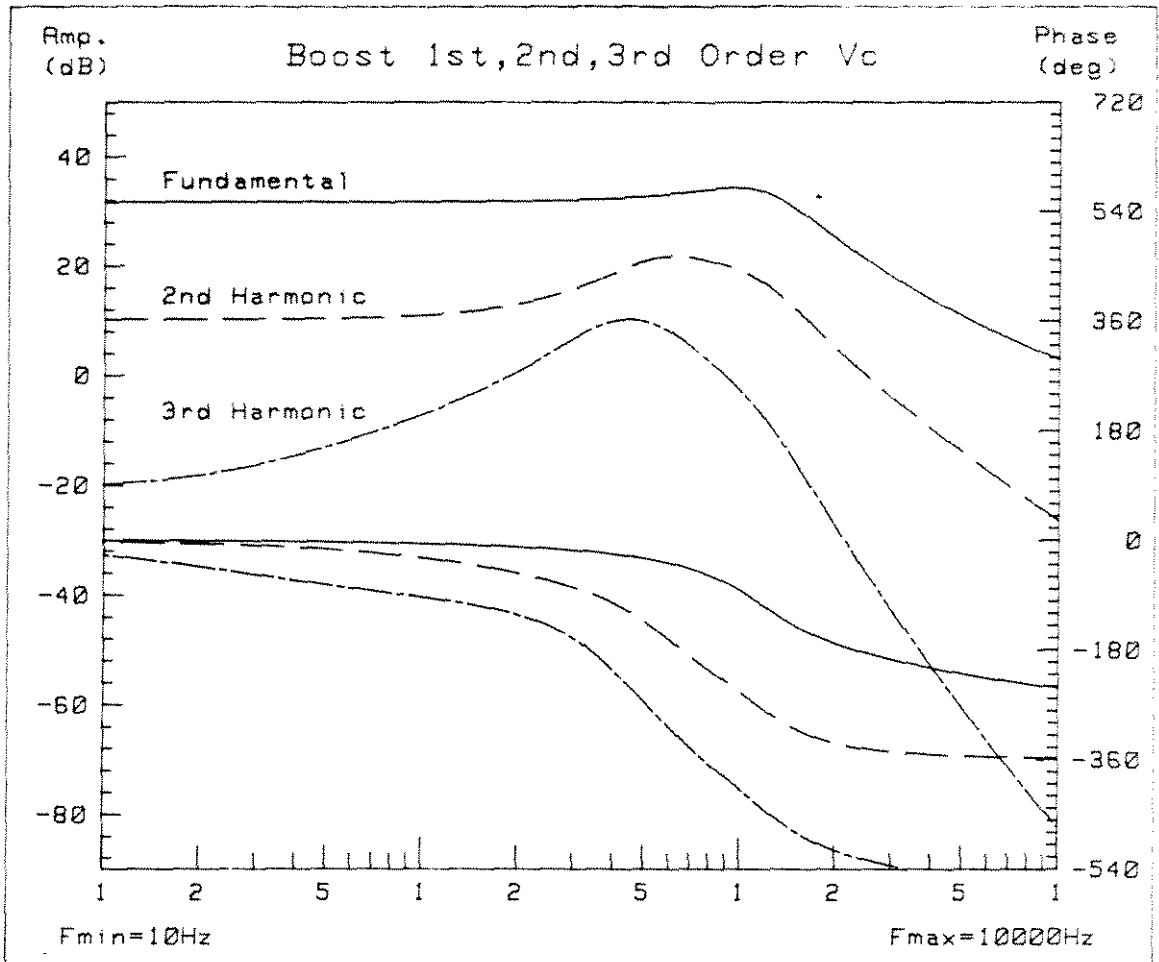
Fig. 3.12. Predicted frequency dependence of the fundamental, second, and third harmonic components $\hat{v}_1$, $\hat{v}_2$, and $\hat{v}_3$, for the boost converter example. The phase shift of $-(n-1)90^\circ$ is not yet accounted for.
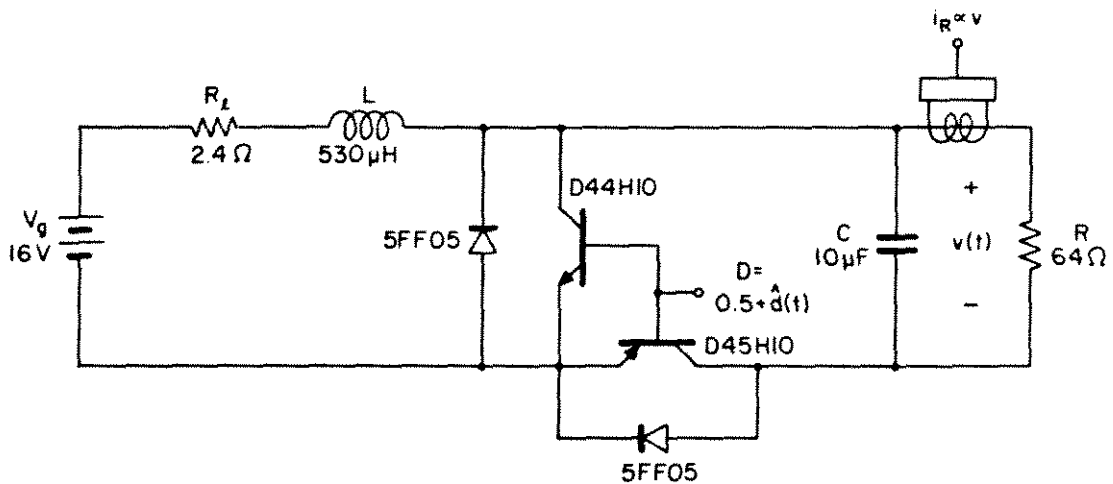
Fig. 3.13. Component values used in the theoretical predictions of Fig. 3.12.

	Poles	Zeroes
$\dfrac{\hat{v}_1}{\hat{d}}$	two poles at 1.17 kHz with Q of 1.2	RHP zero at 4.1 kHz
$\dfrac{\hat{v}_2}{\hat{d}}$	two poles at 1.17 kHz with Q of 1.2	RHP zero at 264 Hz
	two poles at 586 Hz with Q of 1.2	LHP zero at 1.25 kHz
$\dfrac{\hat{v}_3}{\hat{d}}$	two poles at 1.17 kHz with Q of 1.2	RHP zero at 23.5 Hz
	two poles at 586 Hz with Q of 1.2	LHP zero at 600 Hz
	two poles at 391 Hz with Q of 1.2	RHP zero at 8.3 kHz

Table 3.3. Salient features of $\dfrac{\hat{v}_1}{\hat{d}}$, $\dfrac{\hat{v}_2}{\hat{d}}$, $\dfrac{\hat{v}_3}{\hat{d}}$

predictions approximately 6 dB too low at 700 Hz.

The "third harmonic response", $\hat{v}_3/\hat{d}$, contains six poles and three zeroes. Note that the first zero occurs at 23.5 Hz, a factor of 50 lower in frequency than the small-signal system poles! Hence for this example, a dc analysis correctly predicts the third harmonic amplitude only for fundamental frequencies less than the 1/50 of the small-signal poles. Furthermore, the peak occurs in the vicinity of 400 Hz at approximately 24 dB above the dc value. It is clear from this example that (1) a dc distortion analysis is not sufficient for the prediction of peak simple harmonic distortion levels, and (2) harmonic distortion components may change significantly in amplitude over frequencies where the fundamental response is flat. Hence, it is incorrect to assume that a dc distortion analysis is valid for all frequencies where the small-signal response is at its dc asymptote.

For completeness, it should be noted that straightforward expansions of the type used in Eq. (3.7) may diverge, or may converge so slowly that they are useless. This is a well-known phenomenon [3,4,5] and indicates that a different type of approximation method must be used. As an example of this behavior, the model was evaluated for a boost converter with two different sets of circuit element values and duty ratio excitation.

The first circuit considered is the same boost converter used in Fig. 3.13. All components to order ε^7 were calculated for a duty ratio excitation of amplitude $\varepsilon = .15$ and frequency 300 Hz. The result is given in Table 3.4. It can be seen that the series converges

Order	Harmonic	Amplitude(volts)	Phase(degrees)	
1	1	3.23	-17	$\epsilon = .15$
2	2	.518	-154	$f = 300$ Hz
3	1	.0791	-91	$V_g = 16$ V
3	3	.126	-324	$R = 64\ \Omega$
4	2	.0359	88	$R_\ell = 2.4\ \Omega$
4	4	.0374	-171	$L = 530\ \mu$H
5	1	.00535	142	$C = 10\ \mu$F
5	3	.0163	-134	$D_0 = .5$
5	5	.0102	-406	
6	2	.00351	-87	
6	4	.00608	-383	
6	6	.00240	-295	
7	1	.000505	-33	
7	3	.00179	-354	
7	5	.00183	-286	
7	7	.000504	-552	

Table 3.4. Boost example #1. Amplitude and phase of all components of the output (capacitor voltage) to order ϵ^7. Dc terms are not included.

Order	Harmonic	Amplitude(volts)	Phase(degrees)
1	1	58.1	-108
2	2	14.3	-18
3	1	74.9	-29
3	3	3.10	-288
4	2	18.9	56
4	4	.669	-199
5	1	91.4	39
5	3	4.19	-218
5	5	.146	-469
6	2	23.2	-237
6	4	.924	-132
6	6	.0323	-379
7	1	114	113
7	3	5.16	-151
7	5	.206	-405
7	7	.00722	-649
8	2	28.6	-163
8	4	1.14	-425
8	6	.0465	-317
8	8	.00163	-559
.	.	.	.
.	.	.	.
.	.	.	.

$\varepsilon = .3$

$f = 2500$ Hz

$V_g = 20$ V

$R = 100\ \Omega$

$R_\ell = .05\ \Omega$

$L = 300\ \mu H$

$C = 5\ \mu F$

$D_0 = .4$

Table 3.5.

Table 3.5 continued

Order	Harmonic	Amplitude(volts)	Phase(degrees)
27	1	1090	101
27	3	50.4	-163
27	5	1.92	-417
27	7	.0770	-678
27	9	.00337	-572
27	11	.000139	-830

Table 3.5. Boost Example #2. Amplitude and phase of various
components of the output (capacitor voltage), as predicted
by the straightforward expansion method. Dc terms are
not included.

rapidly, the system is well-behaved, and that the approximation of the n-th harmonic by $\varepsilon^n \underline{x}_{nn}(t)$, as noted in Section 3.4, is valid. The method gives very good results in this case.

The second circuit considered is also a boost converter, but with different circuit element values and duty ratio excitation. The values are chosen such that the system exhibits a resonant response (the small-signal model predicts two complex poles at 2467 Hz with a Q of 4.5), and the system is driven with hard excitation near resonance. All components to order ε^{27} were calculated and are summarized in Table 3.5. The series diverges for this example! The reason for this divergence is known as the "problem of small divisors" [4]. If desired, another technique such as the Krylov-Bogoliubov method [4,5,44,45,46] may be used here in place of the straightforward expansion. However, practical switching amplifiers normally must exhibit a well-damped and reasonably linear response. The straight-forward expansion converges rapidly for such systems and is preferred because of the circuit-oriented nature of the result.

3.6 Step-by-Step Summary of the Procedure

For reference, the procedure for constructing circuit models of the form in Fig. 3.11 is summarized here:

1. Using Kirchoff's laws, find the state equations of the system, first during switching interval DT_s then during interval $D'T_s$. Write the state equations in the following matrix form:

$$K \frac{dx(t)}{dt} = A_1 \underline{x}(t) + B_1 \underline{u} \qquad \text{during } DT_s$$

$$K \frac{dx(t)}{dt} = A_2 \underline{x}(t) + B_2 \underline{u} \qquad \text{during } D'T_s \tag{3.32}$$

2. Evaluate the matrices A, B, and $(A_1 - A_2)$, where

$$A = D_0 A_1 + D_0' A_2$$

$$B = D_0 B_1 + D_0' B_2 \tag{3.33}$$

3. Write out the zero-order, first-order, and nth-order set of state equations which describe the dominant component of each harmonic present, as follows:

$$\underline{0} = A\underline{x}_0 + B\underline{u}$$

$$K \frac{d}{dt} \hat{\underline{x}}_1 = A\hat{\underline{x}}_1 + [(A_1 - A_2)\underline{x}_0 + (B_1 - B_2)\underline{u}] \, \hat{d} \tag{3.34}$$

$$nK \frac{d}{dt} \hat{\underline{x}}_n = A\hat{\underline{x}}_n + \frac{\varepsilon}{2} (A_1 - A_2) \hat{\underline{x}}_{n-1} \, , \, n \geq 2$$

4. Reconstruct circuit models which satisfy the loop and node equations of Eq. (3.34). These circuit models may now be manipulated as desired. $\underline{x}_0$ is the nominal (dc) value of the state vector. $\hat{\underline{x}}_1$ is the first-order (linear) component of the state vector. $\hat{\underline{x}}_n$ is an effective vector, evaluated at the fundamental frequency ω, whose amplitude is the same as the

dominant component of the nth harmonic ($n \geq 2$). The phase of $\hat{\underline{x}}_n$ differs from the phase of the nth harmonic by $-(n-1)90°$. $\hat{\underline{x}}_n$ may be evaluated using linear techniques in the same way that $\hat{\underline{x}}_1$ is evaluated.

CHAPTER 4

AN EXTENSION — INTERMODULATION DISTORTION

4.1 Introduction

The previous chapter considered the simple harmonic distortion
which occurs when the duty ratio is modulated by a single sine wave.
This is the most basic measure of the nonlinearity of a system and in
many applications such as a variable speed ac motor drive or
uninterruptible power supply, where the system is only intended to
produce a single sine wave, it is sufficient.

In general, however, the nonlinearity may produce other
objectionable forms of distortion when the input to the system is more
complicated, and a number of methods have been devised to measure the
distortion produced by an amplifier under more general conditions. The
most widely known of these is called intermodulation distortion, which
refers to the distortion produced when not one but two sine waves at
different frequencies are injected into the system simultaneously. In
general, these two sine waves may both be injected through the duty
ratio, or one may enter the system through the duty ratio and one from
an independent source such as the line voltage. Only the former case
will be considered here.

By generalization of the method of the previous chapter, one
obtains a series expansion for the state vector when two sine waves
are injected into the system. A completely linear set of state

equations occurs at each order; hence, linear techniques may be used to calculate each component of the intermodulation distortion. In particular, linear circuit models may be drawn which result in a design procedure more easily accessible to the engineer.

4.2 Mathematical Description

The basic nonlinear differential equation which describes the system is given by Eq. (3.3), repeated here for conveniences:

$$K \frac{d\underline{x}(t)}{dt} = [D(t)A_1 + D'(t)A_2]\underline{x}(t) + [D(t)B_1 + D'(t)B_2]\underline{u} \qquad (4.1)$$

The duty ratio is now to be modulated by two independent sine waves instead of one. Hence, define

$$D(t) = D_0 + \hat{d}_1(t) + \hat{d}_2(t) \qquad (4.2)$$

where D_0 = nominal duty ratio

$$\hat{d}_1(t) = \epsilon_1 \sin\omega_1 t$$

$$\hat{d}_2(t) = \epsilon_2 \sin\omega_2 t \qquad (4.3)$$

ϵ_1 = amplitude of the first sinusoidinal input

ϵ_2 = amplitude of the second sinusoidinal input

It is convenient in the subsequent analysis to display the dependence of $\hat{d}_1$ and $\hat{d}_2$ on ϵ_1 and ϵ_2 explicitly, as follows:

$$\hat{d}_1(t) = \varepsilon_1 \, \bar{d}_1(t)$$

$$\hat{d}_2(t) = \varepsilon_2 \, \bar{d}_2(t) \tag{4.4}$$

Thus

$$\bar{d}_1(t) = \sin\omega_1 t$$

$$\bar{d}_2(t) = \sin\omega_2 t \tag{4.5}$$

Our expansion will therefore involve two amplitude parameters, ε_1 and ε_2. As before, we will perform a "straightforward expansion", writing the state vector $\underline{x}(t)$ as an infinite series. Since there are now two parameters for expansion, we obtain an infinite series in each parameter, corresponding to the simple harmonic distortion generated separately by each input, plus cross multiplication terms corresponding to the intermodulation distortion. Hence, let

$$\underline{x}(t) = \underline{x}_0 + \varepsilon_1\underline{x}_1 + \varepsilon_2\underline{x}_2 + \varepsilon_1{}^2\underline{x}_{11} + \varepsilon_1\varepsilon_2\underline{x}_{12}$$

$$+ \varepsilon_2{}^2\underline{x}_{22} + \varepsilon_1{}^3\underline{x}_{111} + \varepsilon_1{}^2\varepsilon_2\underline{x}_{112} + \varepsilon_1\varepsilon_2{}^2\underline{x}_{122}$$

$$+ \varepsilon_2{}^3\underline{x}_{222} \cdots \tag{4.6}$$

Insertion of Eqs. (4.2) and (4.6) into the basic state equations (4.1) yields

$$K \frac{d}{dt} [\underline{x}_0 + \epsilon_1 \underline{x}_1 + \epsilon_2 \underline{x}_2 + \epsilon_1^2 \underline{x}_{11} + \epsilon_1 \epsilon_2 \underline{x}_{12} + \epsilon_2^2 \underline{x}_{22} + \ldots]$$

$$= [(D_0 + \epsilon_1 \bar{a}_1 + \epsilon_2 \bar{a}_2)A_1 + (D_0' - \epsilon_1 \bar{a}_1 - \epsilon_2 \bar{a}_2)A_2]$$

$$[\underline{x}_0 + \epsilon_1 \underline{x}_1 + \epsilon_2 \underline{x}_2 + \ldots]$$

$$+ [(D_0 + \epsilon_1 \bar{a}_1 + \epsilon_2 \bar{a}_2)B_1 + (D_0' - \epsilon_1 \bar{a}_1 - \epsilon_2 \bar{a}_2)B_2]\underline{u} \qquad (4.7)$$

The individual components of the state vector may now be found by equating like powers of ϵ_1 and ϵ_2. The zero-order equation does not differ from the simple harmonic case; it is given by Eq. (3.9).

to first order

$$K \frac{d}{dt} \underline{x}_1(t) = A\underline{x}_1 + \underline{c}\bar{a}_1 \qquad (4.8a)$$

$$K \frac{d}{dt} \underline{x}_2(t) = A\underline{x}_2 + \underline{c}\bar{a}_2 \qquad (4.8b)$$

where $\underline{c} = (A_1 - A_2)\underline{x}_0 + (B_1 - B_2)\underline{u}$

$\underline{x}_1$ and $\underline{x}_2$ are the first-order linear components of the state vector occurring at the fundamental frequencies ω_1 and ω_2 respectively.

to second order

$$K \frac{d}{dt} \underline{x}_{11}(t) = A\underline{x}_{11} + [A_1 - A_2]\underline{x}_1 \bar{a}_1 \qquad (4.9a)$$

$$K \frac{d}{dt} \underline{x}_{12}(t) = A\underline{x}_{12} + [A_1 - A_2](\underline{x}_1 \bar{a}_2 + \underline{x}_2 \bar{a}_1) \qquad (4.9b)$$

$$K \frac{d}{dt} \underline{x}_{22}(t) = A\underline{x}_{22} + [A_1 - A_2]\underline{x}_2 \vec{a}_2 \qquad (4.9c)$$

$\underline{x}_{11}$ and $\underline{x}_{22}$ are the components of the state vector containing the second-order harmonics of $\vec{a}_1$ and $\vec{a}_2$ respectively. These quantities may be calculated separately using the simple harmonic distortion analysis method of Chapter 3. However, $\underline{x}_{12}$ is the second-order cross multiplication term and is the first new result of this section. It contains components at the sum and difference frequencies $\omega_1 + \omega_2$ and $\omega_1 - \omega_2$. Again, note that Eqs. (4.9) are linear; if the first-order systems have been solved, then the forcing terms $[A_1 - A_2]\underline{x}_i \vec{a}_j$ may be evaluated. The linear differential equations above are then solved using standard techniques to find the second-order terms.

to third order

$$K \frac{d}{dt} \underline{x}_{111}(t) = A\underline{x}_{111} + [A_1 - A_2]\underline{x}_{11}\vec{a}_1 \qquad (4.10a)$$

$$K \frac{d}{dt} \underline{x}_{112}(t) = A\underline{x}_{112} + [A_1 - A_2](\underline{x}_{11}\vec{a}_2 + \underline{x}_{12}\vec{a}_1) \qquad (4.10b)$$

$$K \frac{d}{dt} \underline{x}_{122}(t) = A\underline{x}_{122} + [A_1 - A_2](\underline{x}_{22}\vec{a}_1 + \underline{x}_{12}\vec{a}_2) \qquad (4.10c)$$

$$K \frac{d}{dt} \underline{x}_{222}(t) = A\underline{x}_{222} + [A_1 - A_2]\underline{x}_{22}\vec{a}_2 \qquad (4.10d)$$

$\underline{x}_{111}$ and $\underline{x}_{222}$ are the components of the state vector containing the third-order harmonics of $\vec{a}_1$ and $\vec{a}_2$ respectively, and may be calculated separately using the simple harmonic distortion analysis method of Chapter 3. $\underline{x}_{112}$ and $\underline{x}_{122}$ are the third-order cross multiplication

terms containing components at ω_1, ω_2, $2\omega_1 \pm \omega_2$, and $2\omega_2 \pm \omega_1$. Having solved the second order systems, the forcing terms $[A_1 - A_2]\underline{x}_i \sigma_j$ may be evaluated, and then the above linear equations may be solved.

The process may be continued ad nauseum. At each order of approximation, linear differential equations are obtained describing various components of the state vector. Two of these components are always the simple harmonic distortion terms occurring at multiples of ω_1 or ω_2; the remainder are intermodulation distortion terms occurring at the various sum and difference frequencies. Thus for the case when the input consists of two independent sine waves, the original nonlinear differential equation has been reduced to a series of linear equations describing each component of the state vector $\underline{x}(t)$. To obtain further insight into the distortion processes inherent in the system, we will next reconstruct linear circuit models which describe the intermodulation distortion components that appear.

4.3 Linear Circuit Models

As in Chapter 3.3, it is desirable to reconstruct linear circuit models which describe the intermodulation terms that arise. This can again be done; the result for the intermodulation terms is the same as the result for simple harmonic distortion with the exception of the generators in the model. Namely, the topology does not change, but the nonlinear generators introduce signals at sum and difference frequencies instead of at simple multiples of the fundamental. This is done below for the same boost converter example in Fig. 3.1.

The zero- and first-order models were found in Section 3.3; they are given by Figs. 3.2 and 3.4.

to second order

Eq. (4.9b) describes the second-order (order $\varepsilon_1\varepsilon_2$) intermodulation distortion which arises. For the boost example, this equation becomes

$$
\begin{bmatrix} L & 0 \\ \\ 0 & C \end{bmatrix} \frac{d}{dt} \begin{bmatrix} i_{12} \\ \\ v_{12} \end{bmatrix} = \begin{bmatrix} -R_\ell & -D_0' \\ \\ D_0' & -1/R \end{bmatrix} \begin{bmatrix} i_{12} \\ \\ v_{12} \end{bmatrix}
$$
$$
+ \begin{bmatrix} 0 & 1 \\ \\ -1 & 0 \end{bmatrix} \begin{bmatrix} i_1\tilde{d}_2 + i_2\tilde{d}_1 \\ \\ v_1\tilde{d}_2 + v_2\tilde{d}_1 \end{bmatrix}
$$

(4.11)

The circuit which corresponds to Eq. (4.11) is given in Fig. 4.1. It is *linear*, yet it describes the *nonlinear* order $(\varepsilon_1\varepsilon_2)$ intermodulation terms which arise. Having calculated v_1, v_2, i_1, and i_2 from the first-order model, one may evaluate the nonlinear generators $v_1\tilde{d}_2$, $v_2\tilde{d}_1$, $i_1\tilde{d}_2$, and $i_2\tilde{d}_1$. These generators contain components at frequencies $\omega_1 + \omega_2$ and $\omega_1 - \omega_2$. One then solves the linear circuit of Fig. 4.1, yielding $v_{12}(t)$ and $i_{12}(t)$.
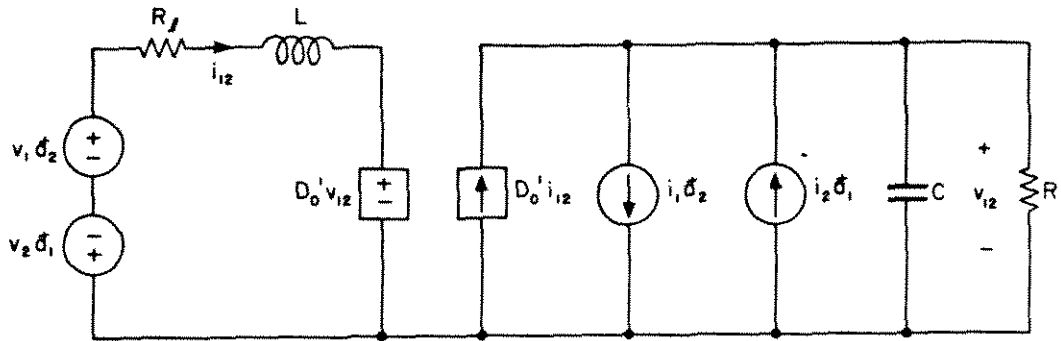
Fig. 4.1. Circuit which models the order $\epsilon_1\epsilon_2$ intermodulation components in the boost example.

to third order

Eqs. (4.10b) and (4.10c) describe the third-order (order $\epsilon_1^2\epsilon_2$ and $\epsilon_1\epsilon_2^2$) intermodulation distortion which arises. For the boost example, one obtains

$$
\begin{bmatrix} L & 0 \\ \\ 0 & C \end{bmatrix} \frac{d}{dt} \begin{bmatrix} i_{112} \\ \\ v_{112} \end{bmatrix} = \begin{bmatrix} -R_\ell & -D_0' \\ \\ D_0' & -1/R \end{bmatrix}
$$

$$
+ \begin{bmatrix} 0 & 1 \\ \\ -1 & 0 \end{bmatrix} \begin{bmatrix} i_{11}d_2 + i_{12}d_1 \\ \\ v_{11}d_2 + v_{12}d_1 \end{bmatrix}
\tag{4.12}
$$

$$
\begin{bmatrix} L & 0 \\ & \\ 0 & C \end{bmatrix} \frac{d}{dt} \begin{bmatrix} i_{122} \\ & \\ v_{122} \end{bmatrix} = \begin{bmatrix} -R_\ell & -D_0' \\ & \\ D_0' & -1/R \end{bmatrix} \begin{bmatrix} i_{122} \\ & \\ v_{122} \end{bmatrix}
$$

$$
+ \begin{bmatrix} 0 & 1 \\ & \\ -1 & 0 \end{bmatrix} \begin{bmatrix} i_{22}d_1 + i_{12}d_2 \\ & \\ v_{22}d_1 + v_{12}d_2 \end{bmatrix}
$$

$$(4.13)$$
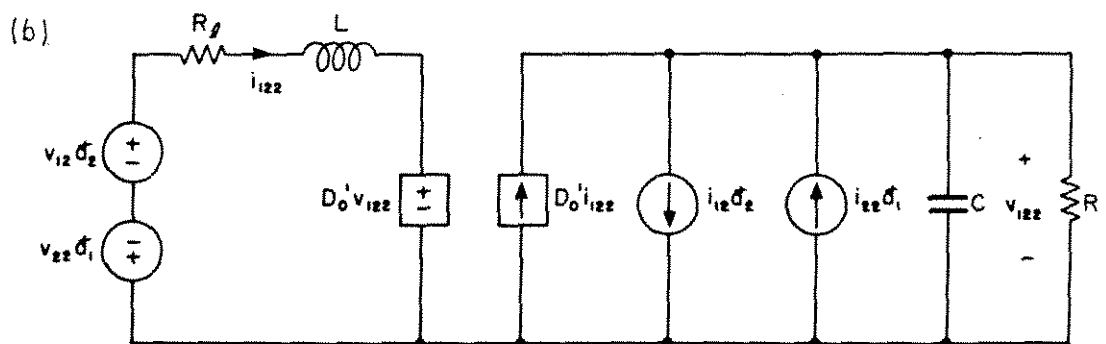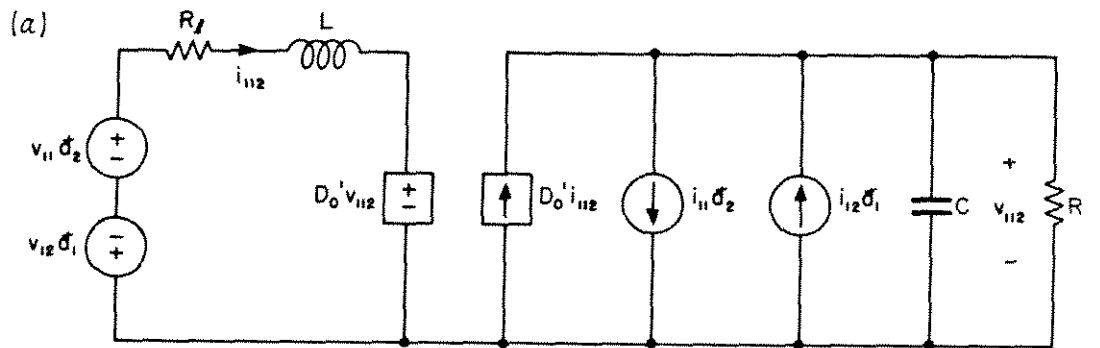
Fig. 4.2. Circuits which model the order $\epsilon_1^2\epsilon_2$ (a) and order $\epsilon_1\epsilon_2^2$ (b) intermodulation components in the boost example.

The circuits which correspond are given in Fig. 4.2. They are linear, yet describe the nonlinear order $\epsilon_1^2\epsilon_2$ (Fig. 4.2a) and order $\epsilon_1\epsilon_2^2$ (Fig. 4.2b) intermodulation distortion which arises. Having calculated i_{11}, i_{12}, i_{22}, v_{11}, v_{12}, and v_{22} from the second order systems, one may evaluate the nonlinear generator terms. These generators contain components of frequencies ω_1, ω_2, $2\omega_1 \pm \omega_2$, and $2\omega_2 \pm \omega_1$. One then solves the linear circuits of Fig. 4.2, yielding i_{112}, i_{122}, v_{112}, and v_{122}.

Thus, by a simple extension of the technique of Chapter 3, intermodulation distortion may be modelled. In particular, one considers the case where the duty ratio is modulated by two independent sine waves. One expects the resulting circuit waveforms to contain the harmonics of both sine waves, plus additional terms resulting from interactions between the two which represent the intermodulation distortion. Therefore, the state vector is expanded in a more complicated form which includes these extra terms. The result of the analysis is a series of linear circuit models which may be solved using standard techniques, yielding the magnitude and phase of each component of the output. The engineer may then gain insight into the distortion processes and the means for linearization of his amplifier.

CHAPTER 5

DESIGN EXAMPLES: DISTORTION IN BUCK AMPLIFIERS

5.1 Introduction

In this chapter the usefulness and design-oriented nature of the
modelling approach is demonstrated by two examples. First, a bridge-
configuration buck-type amplifier with input filter is analyzed. The
circuit models are given, and simple design criteria are found for the
reduction of the simple harmonic distortion to an acceptably low level.
In addition, it is shown that only odd harmonics appear at the output
of this configuration, while only even harmonics appear in the input
filter. Next, a simple buck converter with input filter is analyzed,
and is found to generate both even and odd harmonics at its output.
The operation of this converter is considerably more complicated than
the bridge; as a result, more sophisticated design techniques must be
used to avoid becoming inundated with algebra and losing all physical
insight into the operation of the circuit. A useful technique is
described, which has general application to other configurations. The
result for this second example is a set of approximate design criteria
similar to the results for the first example; these criteria may be
used to reduce the simple harmonic distortion which appears to an
acceptably low level.

5.2 Existence of Distortion in Buck Amplifiers

It may at first seem surprising that a buck-type configuration would inherently produce any distortion at all. Indeed, the simple ideal buck converter of Fig. 5.1 is completely linear if high-frequency switching ripple is neglected. The large-signal gain is given by Eq. (5.1).

$$\frac{\hat{v}(s)}{\hat{d}(s)} = V_g \, H(s) \qquad \text{valid for large signals} \qquad (5.1)$$

where $H(s)$ is the transfer function of the low-pass filter. Thus, the only harmonics expected to appear at the output are those resulting from nonidealities in the pulse-width modulator, switch, or other components.

The addition of line source impedance, however, results in the generation of distortion by the power stage itself, rather than by switch or PWM nonidealities. For example, if the source impedance is
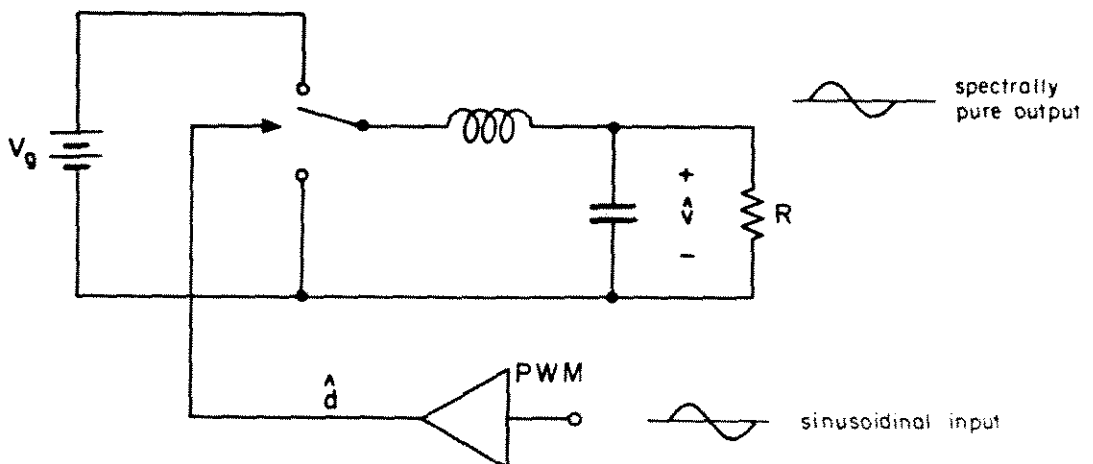
Fig. 5.1. *Simple, ideal buck converter which generates no low-frequency distortion.*

(a)

(b)
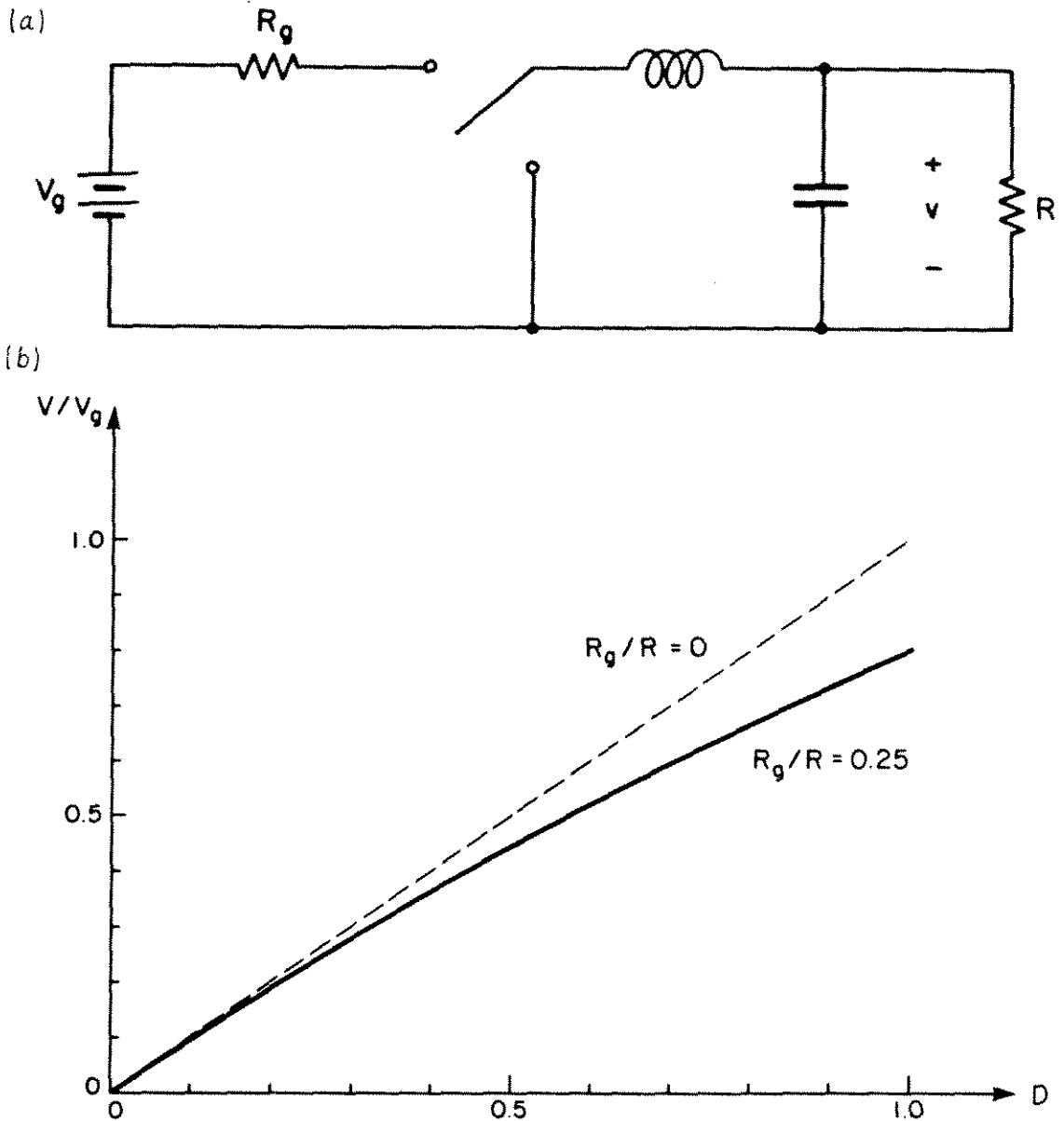
Fig. 5.2.   The addition of resistive source impedance results in the
generation of distortion in buck converters: (a) schematic;
(b) deviation of the resulting dc gain curve (solid line)
from the ideal case (dashed line).

purely resistive as in Fig. 5.2a, then the dc steady-state gain

characteristic becomes

$$\frac{V}{V_g} = D \; \frac{R}{R + DR_g}$$

(5.2)

This function is plotted in Fig. 5.2b. It is a nonlinear function of

D; therefore it is clear that distortion occurs at dc and probably also

at higher frequencies. Eq. (5.1) is not valid for this system with

large signals.

On the other hand, suppose the source impedance of V_g is

non-dissipative? In particular, consider the addition of an L-C

input filter containing no resistive elements, as in Fig. 5.3a. Since

L_f and C_f are purely reactive components, they do not affect the dc

steady-state gain of the system. The dc transfer function of this

(a)

(b)
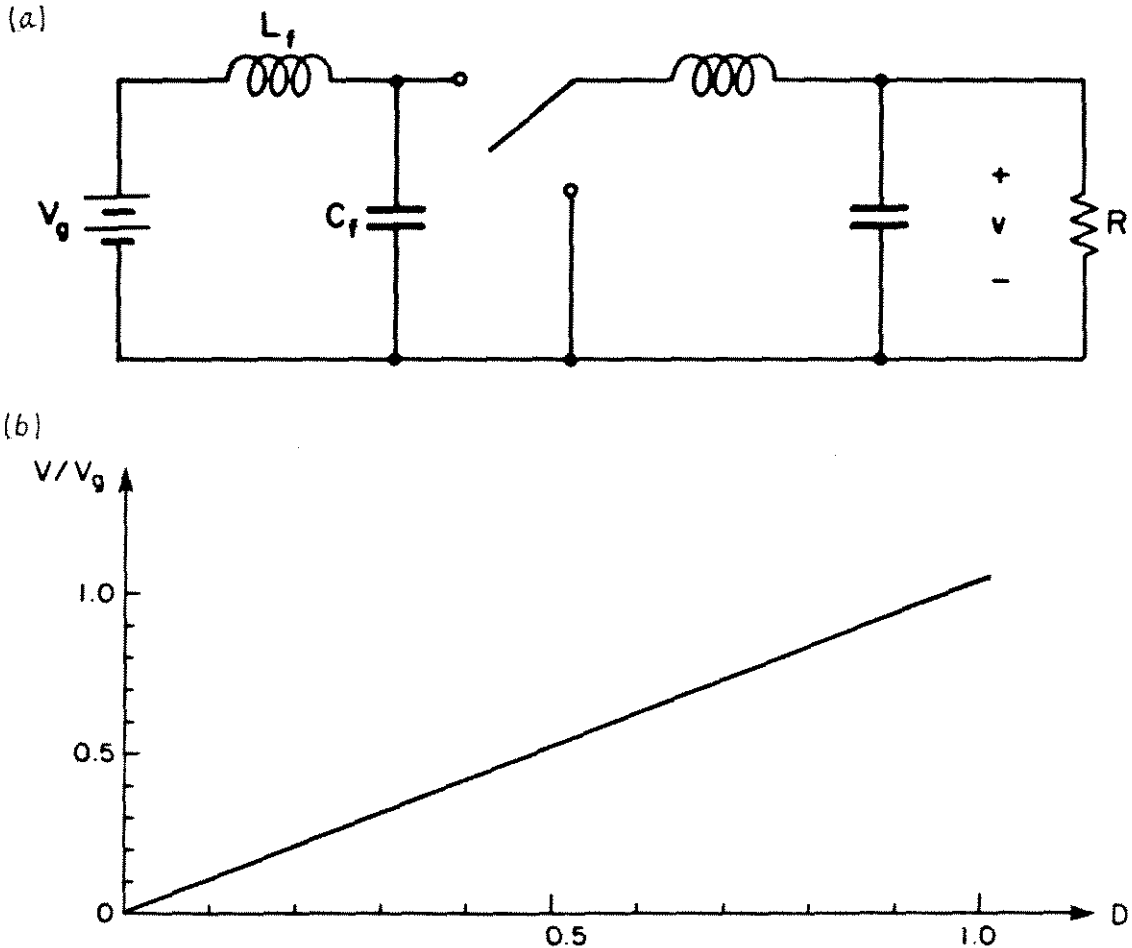
Fig. 5.3.   The addition of purely reactive source impedance has no
effect on the dc gain of buck converters; nonetheless,
ac signals are distorted: (a) schematic; (b) linear dc
gain characteristics.

system is therefore linear, as given below and plotted in Fig. 5.3b.

$$V = DV_g \tag{5.3}$$

But is there distortion? At dc, $\left|Z_g\right| = 0$. However, for ac, $\left|Z_g\right| \neq 0$ and as a result there is indeed distortion. The nonlinearity inherent in the buck converter of Fig. 5.3a affects ac signals but not the dc gain.

Thus, even a buck converter may generate harmonic distortion if source impedance in series with V_g exists. In practice, this impedance may arise in a number of ways. The addition of an L-C input filter results in a circuit similar to Fig. 5.3, and the discussion above holds. A similar case occurs when V_g is a switching power supply, and the L-C filter is actually the equivalent output impedance of the power supply. A third example is the inclusion of switch ON-state resistances, as when MOSFETs are employed as the switching devices. An equivalent circuit similar to Fig. 5.2 then occurs, and distortion is again generated.

These sources of distortion can never be completely eliminated in practice. The design problem is therefore to choose component values in a way that the resulting distortion is acceptably small.
To accomplish this, one must first develop an understanding of how the distortion depends on the various components. This involves finding the circuit models described in Chapter 3 and drawing Bode plots of the predicted distortion. One may then see the steps necessary for the reduction of the harmonic distortion to an acceptable level. This procedure is carried out in the following example.

(a)

(b)

$D_o = 0.5$
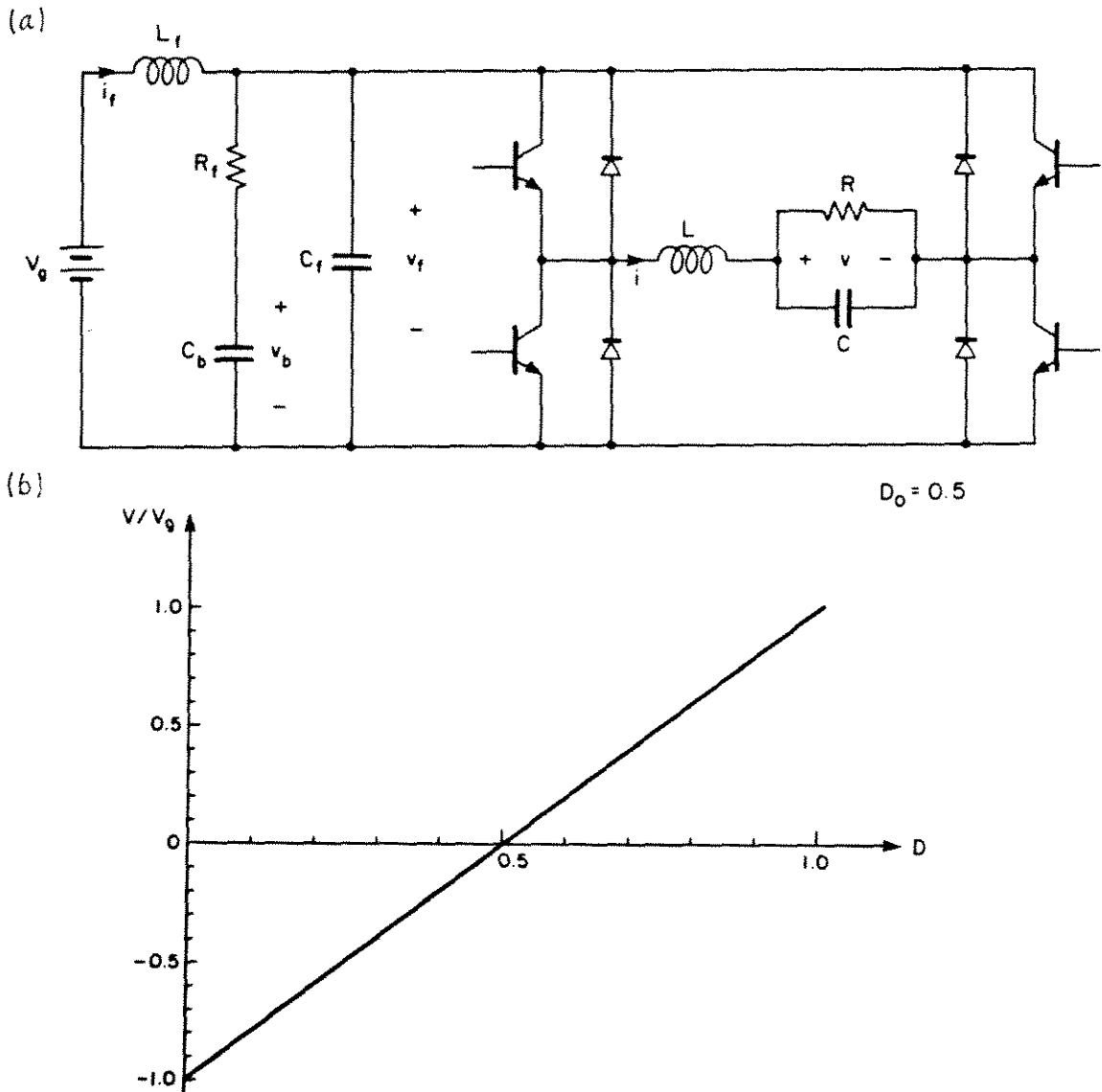
Fig. 5.4.   Bridge amplifier with input filter example: (a) schematic; (b) linear dc gain curve.

5.3 Bridge-type Buck Amplifier with Input Filter

The first example is a bridge-configuration amplifier with a single input filter, as shown in Fig. 5.4a. The dc gain, neglecting the saturation drops of the switches, is given in Fig. 5.4b; it is completely linear. Nonetheless, harmonic distortion appears across the load when the system is excited by ac. To analyze this system, one first constructs the corresponding circuit models following the

step-by-step procedure of Section 3.6.

With the assumption of ideal switches and neglect of parasitics, the vectors and matrices in the state-space description of the system (i.e., the loop and node equations written in matrix form as defined in Eq. (5.4)) are as follows:

$$\underline{x} = \begin{bmatrix} i_f \\ i \\ v_f \\ v_b \\ v \end{bmatrix} \qquad \underline{u} = \begin{bmatrix} V_g \end{bmatrix} \qquad B_1 = B_2 = \begin{bmatrix} 1 \\ 0 \\ 0 \\ 0 \\ 0 \end{bmatrix} \qquad (5.4)$$

$$K = \begin{bmatrix} L_f & 0 & 0 & 0 & 0 \\ 0 & L & 0 & 0 & 0 \\ 0 & 0 & C_f & 0 & 0 \\ 0 & 0 & 0 & C_b & 0 \\ 0 & 0 & 0 & 0 & C \end{bmatrix}$$

$$A_1 = \begin{bmatrix} 0 & 0 & -1 & 0 & 0 \\ 0 & 0 & 1 & 0 & -1 \\ 1 & -1 & -1/R_f & 1/R_f & 0 \\ 0 & 0 & 1/R_f & -1/R_f & 0 \\ 0 & 1 & 0 & 0 & -1/R \end{bmatrix}$$

$$A_2 = \begin{bmatrix} 0 & 0 & -1 & 0 & 0 \\ 0 & 0 & -1 & 0 & -1 \\ 1 & 1 & -1/R_f & 1/R_f & 0 \\ 0 & 0 & 1/R_f & -1/R_f & 0 \\ 0 & 1 & 0 & 0 & -1/R \end{bmatrix}$$

Next, the matrices A, B, and $(A_1 - A_2)$ are evaluated:

$$A = D_0 A_1 + D_0' A_2 = \begin{bmatrix} 0 & 0 & -1 & 0 & 0 \\ 0 & 0 & 0 & 0 & -1 \\ 1 & 0 & -1/R_f & 1/R_f & 0 \\ 0 & 0 & 1/R_f & -1/R_f & 0 \\ 0 & 1 & 0 & 0 & -1/R \end{bmatrix} \text{ at } D_0 = 0.5$$

$$B = D_0 B_1 + D_0' B_2 = \begin{bmatrix} 1 \\ 0 \\ 0 \\ 0 \\ 0 \end{bmatrix} \tag{5.5}$$

$$A_1 - A_2 = \begin{bmatrix} 0 & 0 & 0 & 0 & 0 \\ 0 & 0 & 2 & 0 & 0 \\ 0 & -2 & 0 & 0 & 0 \\ 0 & 0 & 0 & 0 & 0 \\ 0 & 0 & 0 & 0 & 0 \end{bmatrix}$$

Now the zero-, first-, and n-th-order set of state equations which describe the dominant component of each harmonic may be written: The dc (zero-order) equation is:

$$\begin{bmatrix} 0 \\ 0 \\ 0 \\ 0 \\ 0 \end{bmatrix} = \begin{bmatrix} 0 & 0 & -1 & 0 & 0 \\ 0 & 0 & 0 & 0 & -1 \\ 1 & 0 & -1/R_f & 1/R_f & 0 \\ 0 & 0 & 1/R_f & -1/R_f & 0 \\ 0 & 1 & 0 & 0 & -1/R \end{bmatrix} \begin{bmatrix} i_{f0} \\ i_0 \\ v_{f0} \\ v_{b0} \\ v_0 \end{bmatrix} + \begin{bmatrix} 1 \\ 0 \\ 0 \\ 0 \\ 0 \end{bmatrix} V_g$$

$$\underline{0} \quad = \qquad\qquad A \qquad\qquad\qquad \underline{x}_0 \quad + \quad B \quad \underline{u}$$
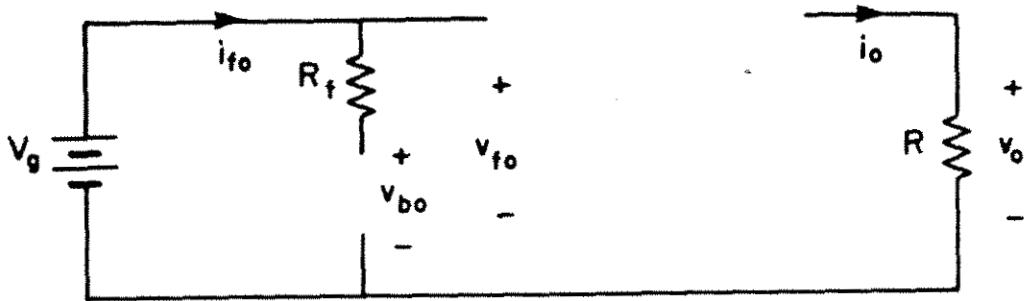
Fig. 5.5. Dc circuit model from which quiescent conditions are calculated.

The circuit model which corresponds to this equation is Fig. 5.5. The solution is given by Eq. (5.7) below.

$$\underline{x}_0 = \begin{bmatrix} 0 \\ 0 \\ V_g \\ V_g \\ 0 \end{bmatrix} \qquad (5.7)$$

The first order equation is

$$
\begin{bmatrix} L_f\ \dot{\hat{i}}_{f1} \\ L\ \dot{\hat{i}}_{1} \\ C_f\ \dot{\hat{v}}_{f1} \\ C_b\ \dot{\hat{v}}_{b1} \\ C\ \dot{\hat{v}}_{1} \end{bmatrix} = \begin{bmatrix} 0 & 0 & -1 & 0 & 0 \\ 0 & 0 & 0 & 0 & -1 \\ 1 & 0 & -1/R_f & 1/R_f & 0 \\ 0 & 0 & 1/R_f & -1/R_f & 0 \\ 0 & 1 & 0 & 0 & -1/R \end{bmatrix} \begin{bmatrix} \hat{i}_{f1} \\ \hat{i}_{1} \\ \hat{v}_{f1} \\ \hat{v}_{b1} \\ \hat{v}_{1} \end{bmatrix}
$$

$$
K\dot{\hat{\underline{x}}}_1 \qquad = \qquad\qquad A \qquad\qquad\qquad \dot{\hat{\underline{x}}}_1
$$

$$
+ \begin{bmatrix} 0 \\ 2V_g \\ 0 \\ 0 \\ 0 \end{bmatrix} \hat{d} \qquad\qquad\qquad (5.8)
$$

$$
+ \quad \underline{c} \quad\ \hat{d}
$$
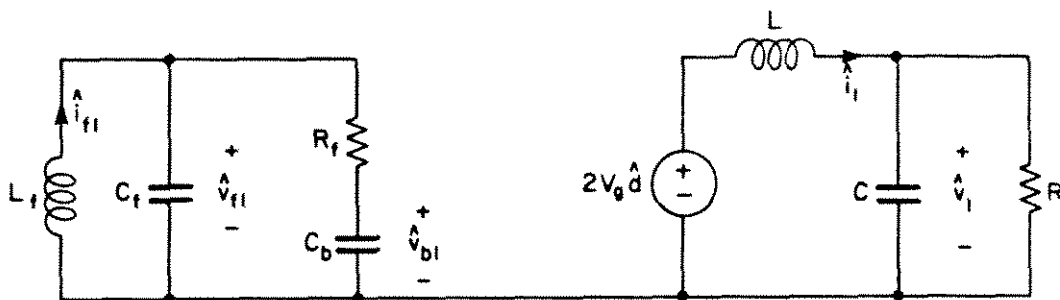
Fig. 5.6. *Circuit which models the first-order (fundamental) components in the bridge amplifier.*

Eq. (5.8) is the system of loop and node equations describing the first-order (linear) circuit model. The circuit model may be reconstructed from these equations; the result is Fig. 5.6. Note that the states of the input filter are not excited in the first-order model; the only generator in the system drives the output filter states only. In consequence, no fundamental appears in the input filter.

The n-th-order ($n \geq 2$) equation describing the dominant component of the n-th harmonic is given in Eq. (5.9).

$$
\begin{bmatrix}
nL_f\ \dot{\hat{i}}_{fn} \\[2ex]
nL\ \dot{\hat{i}}_n \\[2ex]
nC_f\ \dot{\hat{v}}_{fn} \\[2ex]
nC_b\ \dot{\hat{v}}_{bn} \\[2ex]
nC\ \dot{\hat{v}}_n
\end{bmatrix}
=
\begin{bmatrix}
0 & 0 & -1 & 0 & 0 \\[2ex]
0 & 0 & 0 & 0 & -1 \\[2ex]
1 & 0 & -1/R_f & 1/R_f & 0 \\[2ex]
0 & 0 & 1/R_f & -1/R_f & 0 \\[2ex]
0 & 1 & 0 & 0 & -1/R
\end{bmatrix}
\begin{bmatrix}
\hat{i}_{fn} \\[2ex]
\hat{i}_n \\[2ex]
\hat{v}_{fn} \\[2ex]
\hat{v}_{bn} \\[2ex]
\hat{v}_n
\end{bmatrix}
$$

$$
nK\ \dot{\hat{\underline{x}}}_n \qquad = \qquad\qquad\qquad A \qquad\qquad\qquad \hat{\underline{x}}_n
$$

$$+ \begin{bmatrix} 0 \\ \epsilon \hat{v}_{fn-1} \\ -\epsilon \hat{i}_{n-1} \\ 0 \\ 0 \end{bmatrix} \tag{5.9}$$

$$+ \quad \frac{\epsilon}{2} (A_1 - A_2) \hat{x}_{n-1}$$

This is the system of loop and node equations describing the circuit model for the dominant component of the n-th harmonic. The corresponding model may be reconstructed from these equations; the result is shown in Fig. 5.7 for the second harmonic, the third harmonic, and the n-th harmonic.

A number of features may be noted from Figs. 5.6 and 5.7. First, the basic topologies of the first- and n-th-order models are the same; the states are connected together the same way in each case. However, the generators are not necessarily the same at each order of n. Second, the values of the reactive components are multiplied by n. These properties hold for the general converter and are a consequence of the modelling method, as described in Chapter 3.5.

The nature of the distortion in the amplifier now becomes apparent. In the first-order model, Fig. 5.6, the input filter states are not excited. Therefore, no fundamental appears in the input filter, and the quantities $\hat{i}_{f1}$, $\hat{v}_{f1}$, and $\hat{v}_{b1}$ are zero. As a result, no second harmonic appears in the output filter or across the load, since the
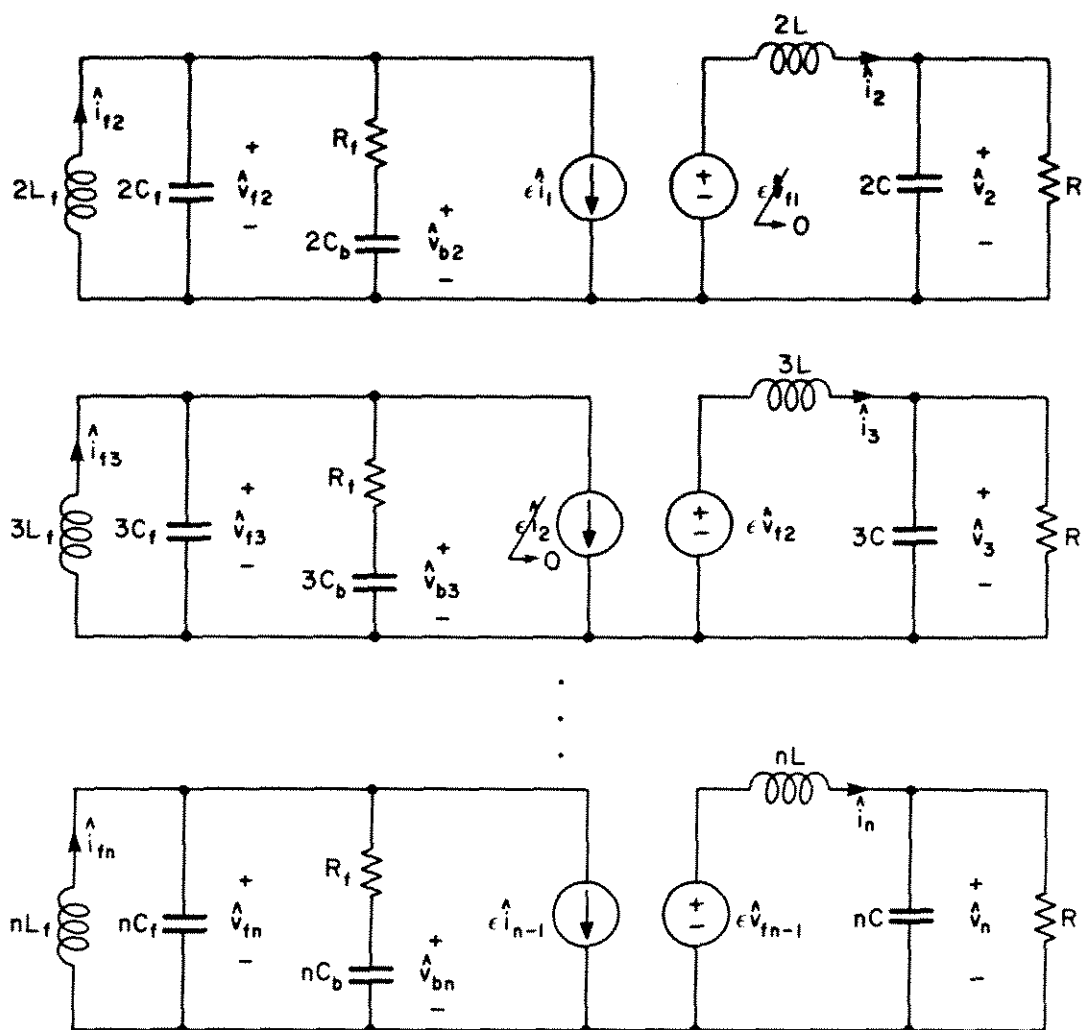
Fig. 5.7. *Circuit models which approximate the amplitude and phase of the second, third, and n-th harmonic components in the bridge amplifier.*

generator $\varepsilon\hat{v}_{f1}$ exciting the output filter in the second-order model at the top of Fig. 5.7 is zero. However, the input filter contains a second-harmonic component owing to the presence of the $\varepsilon\hat{i}_1$ generator in the second-order model. The fundamental in the output filter inductor current $\hat{i}_1$ excites a second harmonic in the input filter.

In the third harmonic model, the input filter states again are not excited since $\hat{i}_2 = 0$ (no second harmonic is present in the output filter inductor current). However, the output filter contains a third

harmonic component owing to the presence of the $\epsilon\hat{v}_{f2}$ generator in the third harmonic model. The second harmonic across the input filter capacitor C_f excites a third harmonic in the output filter and hence across the load.

The process described above continues for all of the higher-order models. Variations in the output filter inductor current $\hat{i}_n$ excite harmonics in the input filter states, and variations in the input filter capacitor voltage $\hat{v}_{fn}$ excite harmonics in the output filter states and across the load. The result of the process is the presence of even harmonics in the input filter and odd harmonics in the output filter and load.

It is a fairly simple matter to calculate the magnitude and phase of the harmonics predicted by the model. First, the circuit models of Figs. 5.6 and 5.7 are simplified as in Fig. 5.8, eliminating the states not excited. Second, the following definitions are made:

$Z_{in}(s)$ = input impedance of the output filter in the n-th order model.

$Z_{sn}(s)$ = output impedance of the input filter in the n-th order model.

$H_n(s)$ = transfer function of the output filter in the n-th order model.

The duty-ratio-to-n-th-order-output response may then easily be evaluated. The result is,

$$\frac{\hat{v}_n(s)}{\hat{d}(s)} = \begin{cases} 0, & n \text{ even} \\ \\ 2\epsilon^{n-1} V_g \dfrac{Z_{s2} Z_{s4} \cdots Z_{sn-1}}{Z_{i1} Z_{i3} \cdots Z_{in-2}} H_n(s), & n \text{ odd} \end{cases} \quad (5.10)$$

$$\frac{\hat{i}_1}{\hat{d}} = \frac{2V_g}{Z_{i1}(s)}$$

$$\frac{\hat{v}_{f2}}{\hat{i}_1} = \epsilon Z_{s2}(s)$$

$$\frac{\hat{i}_3}{\hat{v}_{f2}} = \frac{\epsilon}{Z_{i3}(s)}$$
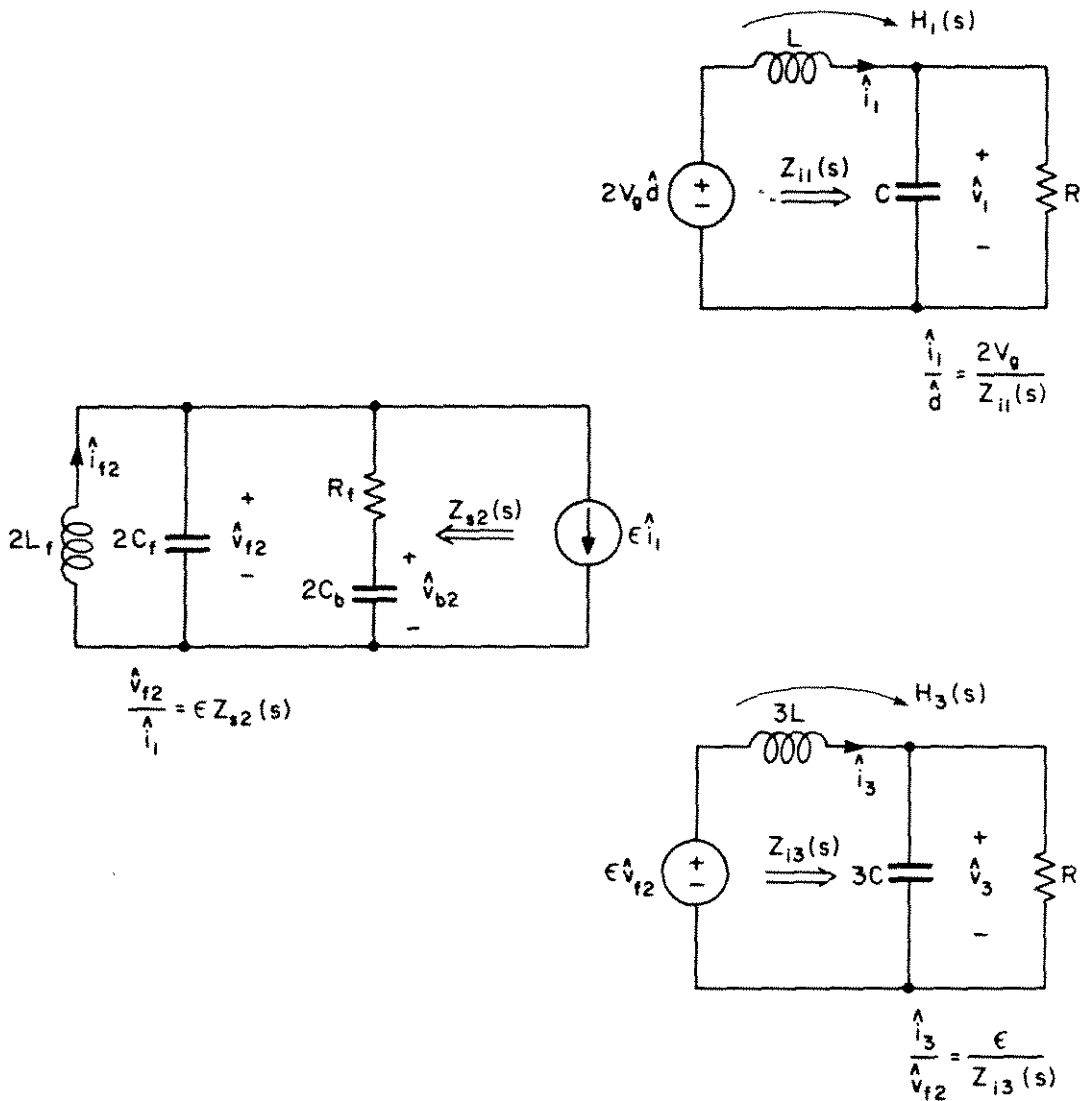
Fig. 5.8. Simplified models from which the "transfer functions" $\hat{v}_1/\hat{d}$ and $\hat{v}_3/\hat{d}$ are calculated.

The steps necessary for the reduction of the distribution to an acceptable level are now apparent. By designing $\left| Z_{sn+1}(s) \right| \ll \left| Z_{in}(s) \right|$, the resulting distortion may be made as low as desired. This may involve choosing larger, more expensive values of L_f, C_f and C_b however; therefore, it is advantageous to design the smallest input filter which meets the distortion specifications. An efficient design procedure thus involves the specification of reasonable distortion limits, followed by the intelligent choice of $Z_{sn+1}(s)$ and $Z_{in}(s)$.

The quantities $Z_{sn}(s)$, $Z_{in}(s)$, and $H_n(s)$ are each a function of frequency, and it is of interest to examine typical frequency dependencies to determine peak distortion levels and the frequency ranges over which they occur. Bode plots of these quantities are constructed in Fig. 5.9 for the case when C_b is large. From these plots it is a straightforward matter to construct the fundamental and third-harmonic responses, plotted in Fig. 5.10 for the case where $\omega_f < \omega_c < \omega_0$. Note that the third harmonic response has a zero at dc. Thus, as noted before there is indeed no third harmonic distortion at dc. However, for ac a significant third harmonic response may exist.

One now proceeds to design the input filter such that $\left| Z_{s2} \right|$ is sufficiently lower than $\left| Z_{i1} \right|$, thereby ensuring that the harmonic response given by Eq. (5.10) is acceptably low. It can be seen from Fig. 5.10 that the peak third harmonic response occurs at one-half of the input filter resonant frequency for the case drawn. The magnitude at this point is $2\varepsilon^2 V_g R_f / R$. This peak may be lowered by proper input filter design, generally involving increased damping of the input filter (i.e., by decreasing the value of R_f). The problem of properly designing an input filter under small-signal conditions has been considered elsewhere [6,7,8], and many of the results are applicable here. In particular, the corner frequencies $\omega_f/2$ and ω_0 should be well separated in order to avoid excessive peaking in the third-harmonic response. Next, the amount of damping necessary to reduce the third harmonic to an acceptable level is determined. Optimal values of R_f and C_b may be calculated [7], thereby avoiding the use of excessively large values of blocking capacitance for C_b. The result is the reduction of the transfer functions of the harmonics given by Eq. (5.10), thereby producing a satisfactorily linear amplifier.

$$|H_n(s)| \qquad 0 \text{ dB}$$

$$Q_0 = R\sqrt{C/L}, \quad \omega_0 = 1/\sqrt{LC}$$

$$\omega_c = \frac{1}{RC}$$

$$\frac{1}{s^2 n^2 LC}$$

$$\omega_0/n$$

$$|Z_{in}(s)| \qquad R$$

$$\frac{1}{snC} \qquad snL$$

$$\omega_c/n$$

$$\omega_0/n$$

$$|Z_{sn}(s)|$$

$$snL_f \qquad \omega_f/n \qquad \frac{1}{snC_f}$$

$$\omega_f = 1/\sqrt{L_f C_f}$$

$$Q_f = R_f\sqrt{C_f/L_f}$$

(assuming C_b large)
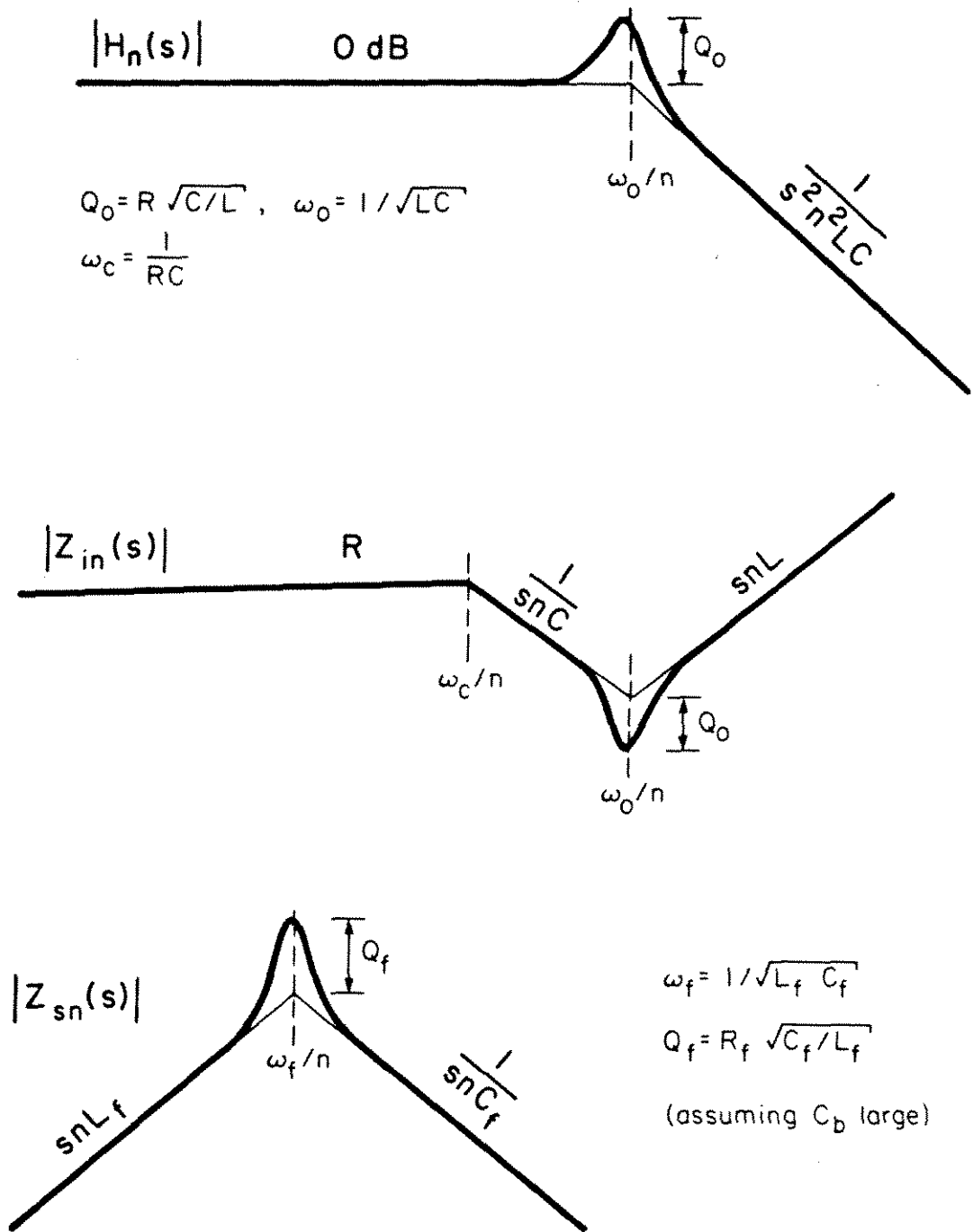
Fig. 5.9. Typical frequency dependencies of the relevant quantities $|Z_{sn}|$, $|Z_{in}|$, and $|H_n|$. The criterion $|Z_{s\,n+1}| \ll |Z_{in}|$ is well-satisfied in a low-distortion amplifier.

$\left|\dfrac{\hat{v}_1}{\hat{d}}\right|$ (fundamental) $2V_g$

Q_o

ω_o

-12dB/octave

$2\epsilon^2 V_g \dfrac{R_f}{R}$

Q_f

$2\epsilon^2 V_g s \dfrac{2L_f}{R}$

$\omega_f/2$

$\left|\dfrac{\hat{v}_3}{\hat{d}}\right|$ (third harmonic)

Q_o

$\omega_o/3$

ω_c

Q_o

ω_o

-24dB/octave
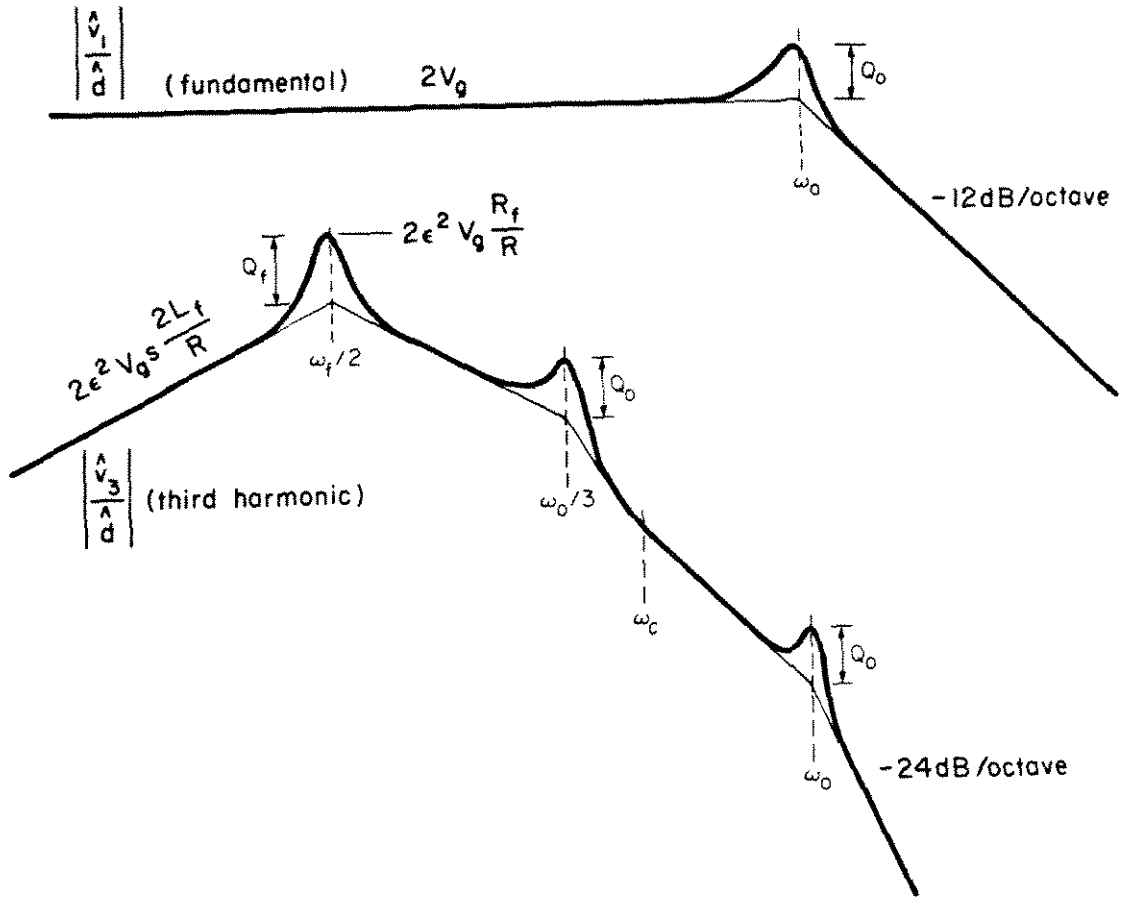
Fig. 5.10. Typical frequency dependence of the fundamental response $|\hat{v}_1/\hat{d}|$ and third harmonic response $|\hat{v}_3/\hat{d}|$.

Thus, a bridge-configuration buck amplifier with input filter produces odd harmonics across its output. This circuit may be modelled, analyzed, and designed using the method of Chapter 3. Application of this procedure may result in a set of Bode plots describing the dependence of the various distortion components upon each circuit element. The steps necessary to reduce this distortion to an acceptable level then become apparent. For this example, it is necessary to design $|Z_{s2}|$ sufficiently smaller than $|Z_{i1}|$. This may be done by proper choice of the various poles and Q-factors of the system.
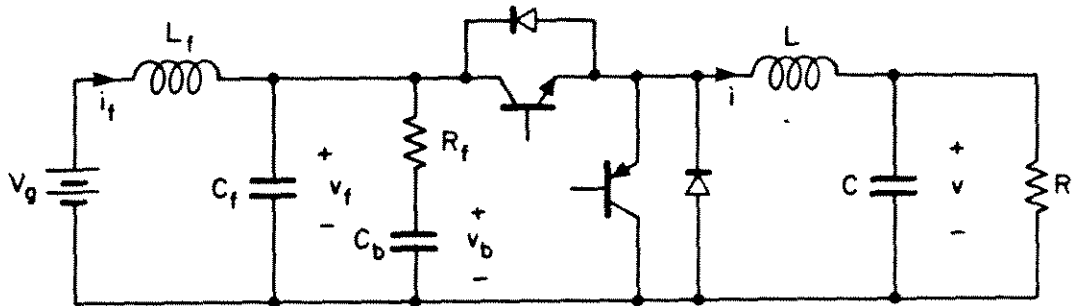
Fig. 5.11. Simple buck amplifier with input filter.

5.4 Single-Ended Buck Converter with Input Filter

As a second example, the simple buck converter with input filter
of Fig. 5.11 is analyzed. The operation of this circuit differs
substantially from that of the previous example. Owing to the
increased interaction between the input filter and the output filter,
even harmonics appear at the output in addition to the odd harmonics
which occur in the bridge. As a result of this interaction, this
circuit is more difficult to analyze and design; the transfer
functions become very large and complicated. To obtain more lucid
results, some additional analytical techniques are useful. One such
technique is given here, which involves the solution of the difference
equation describing the states $\hat{\underline{x}}_n(s)$ of the n-th order model in terms
of $\hat{\underline{x}}_{n-1}(s)$. The result is a set of approximate design equations
similar to the bridge example. Again, it is necessary to design $\left| Z_{s2} \right|$
sufficiently smaller than $\left| Z_{i1} \right|$, and this is done by the proper choice
of the various poles and Q-factors of the system.

Again, the first step in the analysis of this system is the construction of the corresponding circuit models, following the step-by-step procedure of Section 3.6. The first-order state equations are

$$
\frac{d}{dt}
\begin{bmatrix}
L_f & \hat{i}_{f1} \\
L & \hat{i}_1 \\
C_f & \hat{v}_{f1} \\
C_b & \hat{v}_{b1} \\
C & \hat{v}_1
\end{bmatrix}
=
\begin{bmatrix}
0 & 0 & -1 & 0 & 0 \\
0 & 0 & D & 0 & -1 \\
1 & -D & -1/R_f & 1/R_f & 0 \\
0 & 0 & 1/R_f & -1/R_f & 0 \\
0 & 1 & 0 & 0 & -1/R
\end{bmatrix}
\begin{bmatrix}
\hat{i}_{f1} \\
\hat{i}_1 \\
\hat{v}_{f1} \\
\hat{v}_{b1} \\
\hat{v}_1
\end{bmatrix}
$$

$$
K\dot{\hat{\underline{x}}}_1 \qquad = \qquad\qquad A \qquad\qquad\qquad \hat{\underline{x}}_1
$$

$$
+
\begin{bmatrix}
0 \\
v_{f0} \\
-i_0 \\
0 \\
0
\end{bmatrix}
\hat{d}
\qquad\qquad\qquad (5.11)
$$

$$
+ \quad \underline{c} \qquad \hat{d}
$$
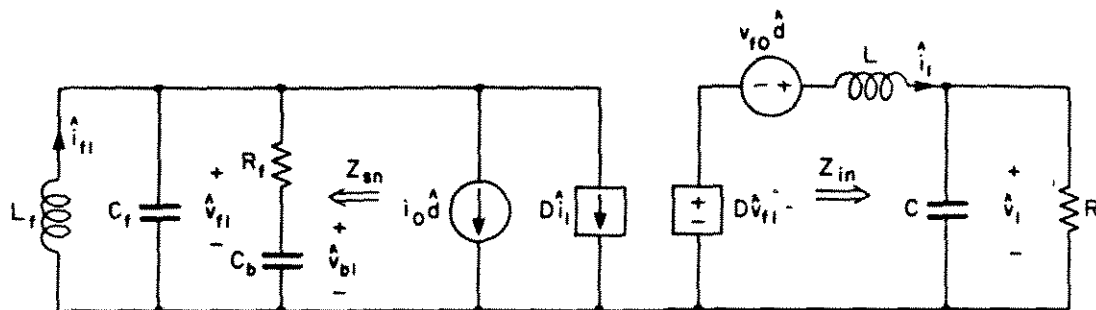
Fig. 5.12. Circuit which models the first-order (fundamental) components in the buck example.

The first-order circuit model which satisfies these loop and node equations is given in Fig. 5.12. This is the usual small-signal model. Note the presence of the $\hat{Di}_1$ and $\hat{Dv}_{f1}$ generators; these lead to first-order interactions between the input filter and the output filter states. Consequently, all states of the system are excited to first order, and fundamental appears in the input filter.

The n-th-order ($n \geq 2$) equations describing the dominant component of the n-th-harmonic are given in Eq. (5.12).

$$\frac{d}{dt}\begin{bmatrix} nL_f\,\hat{i}_{fn} \\ nL\,\hat{i}_n \\ nC_f\,\hat{v}_{fn} \\ nC_b\,\hat{v}_{bn} \\ nC\,\hat{v}_n \end{bmatrix} = \begin{bmatrix} 0 & 0 & -1 & 0 & 0 \\ 0 & 0 & D & 0 & -1 \\ 1 & -D & -1/R_f & 1/R_f & 0 \\ 0 & 0 & 1/R_f & -1/R_f & 0 \\ 0 & 1 & 0 & 0 & -1/R \end{bmatrix} \begin{bmatrix} \hat{i}_{fn} \\ \hat{i}_n \\ \hat{v}_{fn} \\ \hat{v}_{bn} \\ \hat{v}_n \end{bmatrix}$$

$$n\dot{K}\hat{\underline{x}}_n \qquad = \qquad A \qquad\qquad \hat{\underline{x}}_n$$

$$+ \begin{bmatrix} 0 \\ \frac{\epsilon}{2}\,\hat{v}_{fn-1} \\ -\frac{\epsilon}{2}\,\hat{i}_{n-1} \\ 0 \\ 0 \end{bmatrix} \tag{5.12}$$

$$+ \quad \frac{\epsilon}{2}\,(A_1 - A_2)\hat{\underline{x}}_{n-1}$$

The n-th-order circuit model which corresponds to Eq. (5.12) is given in Fig. 5.13. Again, owing to the presence of the $D\hat{i}_n$ and $D\dot{\hat{v}}_{fn}$ generators, there is n-th-order interaction between the input and output filters and hence both even and odd harmonics appear in each state.
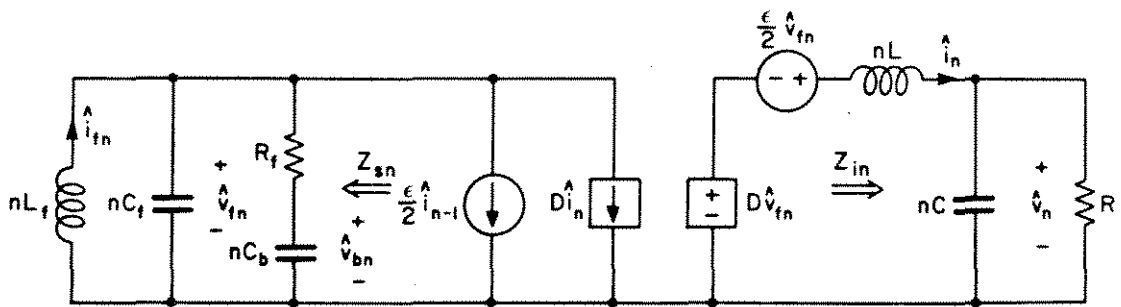
Fig. 5.13. *Circuit model which approximates the amplitude and phase of the n-th harmonic components ($n \geq 2$) in the buck example.*

This interaction complicates the analysis and design of the amplifier. As a result, the straightforward solution of the various transfer functions is an almost hopeless task. An alternative is the employment of the following artifices:

First, it is recognized that each model may be partitioned into three sections: the input filter, the output filter, and the generators. This is illustrated in Fig. 5.14 for the first-order model, the second-order model, and the n-th-order model. The loop and
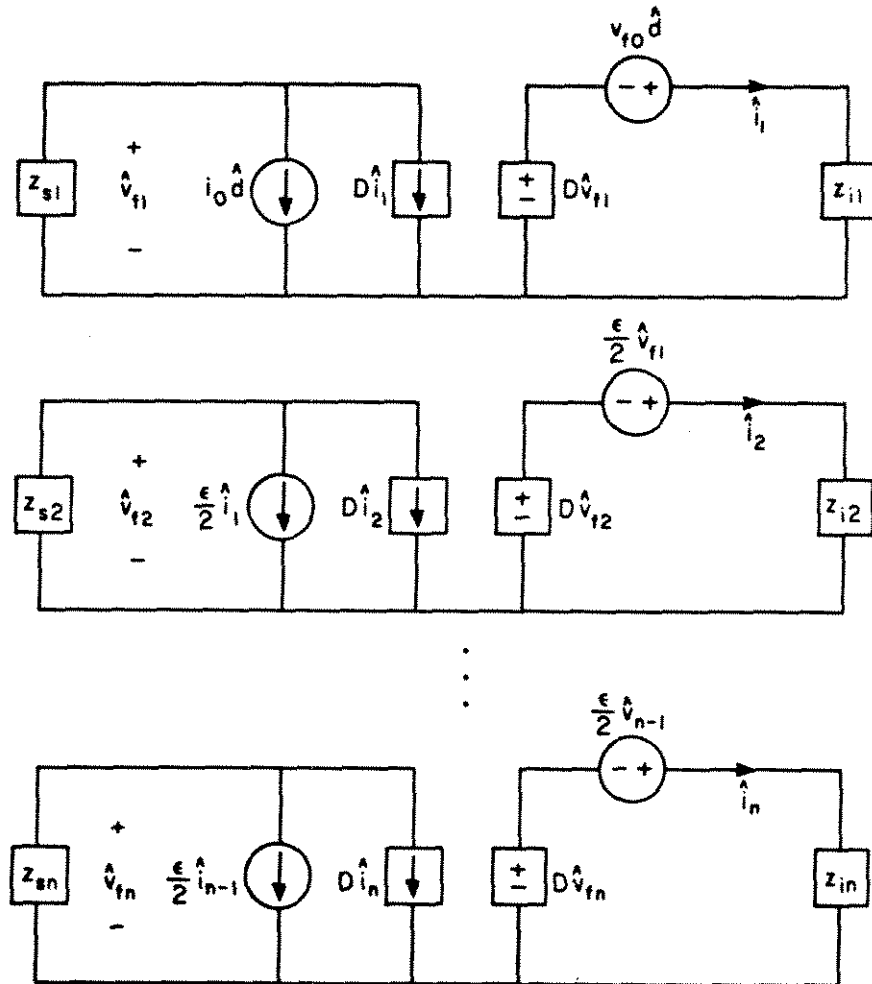
Fig. 5.14. The analysis is simplified when the models are partitioned into three sections: the input filter impedance Z_s, the output filter impedance Z_i, and the generators, shown above for the fundamental, second harmonic, and n-th harmonic models.

node equations may now be rewritten in a more compact form.   In the
first-order model,

$$\frac{\hat{v}_{f1}}{Z_{s1}} + D\hat{i}_1 = - i_0\hat{d}$$

$$-D\hat{v}_{f1} + Z_{i1}\hat{i}_1 = v_{f0}\hat{d}$$

(5.13)

Eq. (5.13) may be expressed in matrix form:

$$\Psi_1 \underline{\xi}_1 = \underline{n}\,\hat{d}$$

(5.14)

where $\qquad \Psi_1 = \begin{bmatrix} 1/Z_{s1} & D \\ -D & Z_{i1} \end{bmatrix}$

$$\underline{\xi}_1 = \begin{bmatrix} \hat{v}_{f1} \\ \hat{i}_1 \end{bmatrix} \qquad \underline{n} = \begin{bmatrix} -i_0 \\ v_{f0} \end{bmatrix}$$

The n-th-order model ($n \geq 2$) is similar; the loop and node equations
are given below.

$$\frac{\hat{v}_{fn}}{Z_{sn}} + D\hat{i}_n = - \frac{\varepsilon}{2}\,\hat{i}_{n-1}$$

$$-D\hat{v}_{fn} + Z_{in}\,\hat{i}_n = \frac{\varepsilon}{2}\,\hat{v}_{fn-1}$$

(5.15)

Eqs. (5.15) may also be expressed in matrix form:

$$\Psi_n \, \underline{\xi}_n = \frac{\varepsilon}{2} \, \Gamma \, \underline{\xi}_{n-1} \qquad (5.16)$$

where

$$\Psi_n = \begin{bmatrix} 1/Z_{sn} & D \\ \\ -D & Z_{in} \end{bmatrix}$$

$$\Gamma = \begin{bmatrix} 0 & -1 \\ \\ 1 & 0 \end{bmatrix}$$

$$\underline{\xi}_n = \begin{bmatrix} \hat{v}_{fn} \\ \\ \hat{i}_n \end{bmatrix}$$

Hence,

$$\underline{\xi}_n = \frac{\varepsilon}{2} \, \Psi_n^{-1} \, \Gamma \, \underline{\xi}_{n-1} = \left(\frac{\varepsilon}{2}\right)^{n-1} (\Psi_n^{-1}\Gamma)(\Psi_{n-1}^{-1}\Gamma) \cdots (\Psi_2^{-1}\Gamma) \, \Psi_1^{-1} \underline{n} \, \hat{d}$$

$$(5.17)$$

Since Ψ_n is of dimension 2, its inverse is easily computed, and the product $\Psi_n^{-1}\Gamma$ is then found:

$$\Psi_n^{-1} \, \Gamma = \frac{Z_{sn}}{Z_{in}} \quad \frac{1}{1 + D^2 Z_{sn}/Z_{in}} \begin{bmatrix} -D & -Z_{in} \\ \\ 1/Z_{sn} & -D \end{bmatrix} \qquad (5.18)$$

One may now evaluate Eq. (5.18) to find analytical expressions for $\underline{\xi}_n$ and hence for $\hat{v}_{fn}$ and $\hat{i}_n$. It is then a simple matter to compute other quantities such as the n-th-order component of the output, $\hat{v}_n$. The result for the first-order system is

$$\frac{\hat{v}_1}{\hat{d}} = V_g \, H_1(s) \, \frac{1 - D^2 Z_{s1}/R}{1 + D^2 Z_{s1}/Z_{i1}} \tag{5.19}$$

where $H_1(s)$ is the transfer function of the first-order output filter:

$$H_1(s) = \frac{1}{1 + sL/R + s^2 LC} \tag{5.20}$$

This is the small-signal result discussed in [6,7]. Note that if the inequalities

$$D^2 Z_{s1} < < R$$

$$D^2 Z_{s1} < < Z_{i1} \tag{5.21}$$

are well satisfied, then Eq. (5.19) reduces to

$$\frac{\hat{v}_1}{\hat{d}} \simeq V_g \, H_1(s) \tag{5.22}$$

This is the small-signal transfer function obtained for the buck converter with no input filter. In other words, the input filter has

negligible effect on the small-signal duty-ratio-to-output transfer function if the inequalities of Eq. (5.21) are satisfied.

The solution for the dominant component of the second harmonic is

$$\frac{\hat{v}_2}{\hat{d}} = \frac{-\varepsilon D V_g}{2} H_2(s) \frac{Z_{s1}}{Z_{i1} || R} \frac{(1 + k_1)}{(1 + k_2)(1 + k_3)} \tag{5.23}$$

where

$$(1 + k_1) = 1 + \frac{Z_{s2}}{Z_{s1}} \frac{(1 - D^2 Z_{s1}/R)}{(1 + Z_{i1}/R)}$$

$$(1 + k_2) = (1 + D^2 Z_{s1}/Z_{i1})$$

$$(1 + k_3) = (1 + D^2 Z_{s2}/Z_{i2})$$

$$H_2(s) = \frac{1}{1 + 2sL/R + 4s^2 LC}$$

This transfer function appears formidable, but it may be considerably simplified if the inequalities (5.21) hold. In this case, the $(1 + k_2)$ and $(1 + k_3)$ terms become nearly unity. The $(1 + k_1)$ term is of order unity for a reasonably damped system, but may be as high as 3 or 4 in magnitude at some frequencies. A reasonable procedure is to neglect all three terms for the first design, and to make any necessary corrections in later design iterations. Thus, if the inequalities of Eq. (5.21) are well-satisfied, then the second harmonic is given

approximately by

$$\frac{\hat{v}_2}{\hat{d}} \simeq - \frac{\varepsilon D \; V_g}{2} \; H_2(s) \; \frac{Z_{s1}}{Z_{i1} || R} \tag{5.24}$$

The steps necessary for the reduction of the second harmonic distortion are now apparent. The second harmonic transfer function may be made as small as desired by the choice of $|Z_{s1}|$ sufficiently less than $|Z_{i1} || R|$. This may involve choosing larger, more expensive values of L_f, C_f, and C_b however; therefore, it is advantageous to design the smallest input filter which meets the distortion and EMI specifications. As in the case of the bridge amplifier, an efficient design procedure involves the specification of reasonable distortion limits, followed by the intelligent choice of $Z_{s1}(s)$ and $Z_{i1}(s)$.

It is of interest to examine typical frequency dependencies of the quantities $H_2(s)$, $Z_{s1}(s)$ and $Z_{i1}(s)$ to determine peak distortion levels and the frequency ranges over which they occur. Bode plots of these quantities are constructed in Fig. 5.15. To satisfy Eq. (5.21), $|D^2 Z_{s1}|$ is chosen much smaller than $|Z_{i1}|$ and $|R|$, as shown. A first approximation for the second-harmonic response is thus Eq. (5.24). It is now a straightforward matter to construct the fundamental and second-harmonic response, plotted in Fig. 5.16 for the case when $\omega_f < \omega_c < \omega_0$. The second-harmonic response contains a zero at dc, rises to a maximum at some intermediate frequency, then falls off, eventually at a rate of 18 dB per octave.
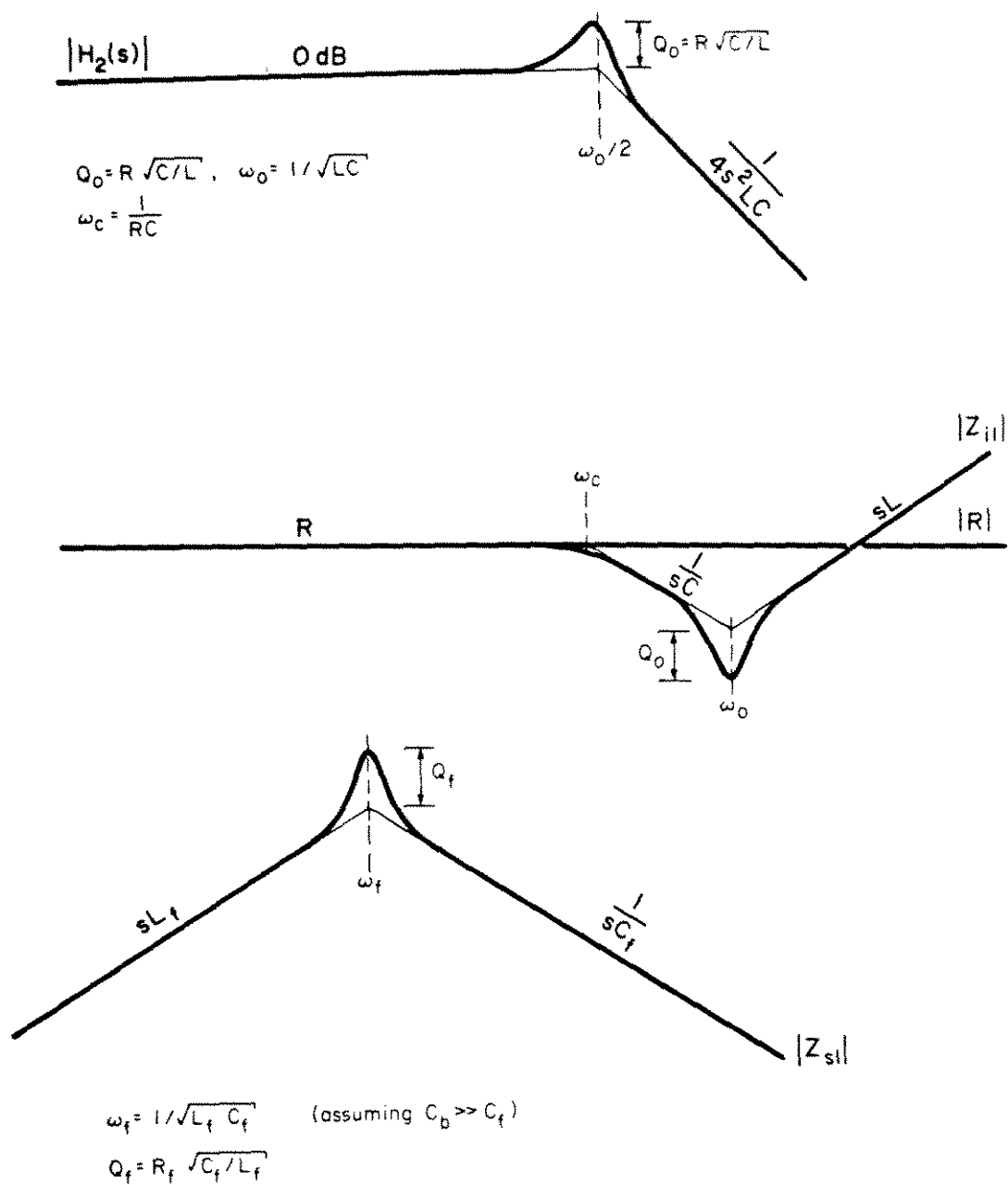
Fig. 5.15. Typical frequency dependencies of the relevant quantities $|Z_{sn}|$, $|Z_{in}|$, and $|H_n|$. The criterion $|Z_{s1}| << |Z_{i1}|| R|$ is well-satisfied in a low-distortion amplifier.
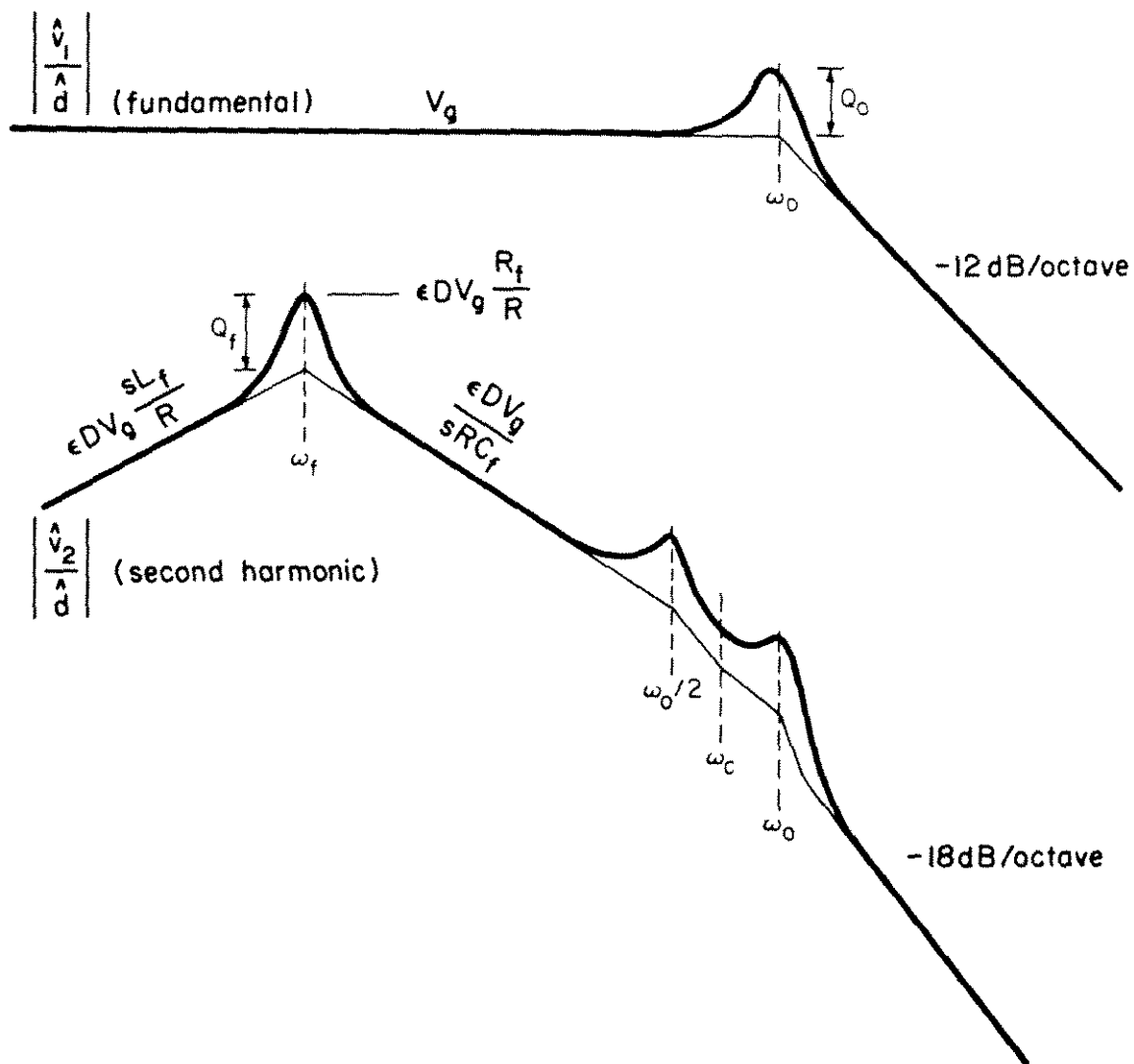
Fig. 5.16. Typical approximate frequency dependence of the fundamental response $|\hat{v}_1/\hat{d}|$ and second harmonic response $|\hat{v}_2/\hat{d}|$.

One now proceeds to design the input filter such that $\left|Z_{s1}\right|$ is sufficiently lower than $\left|Z_{i1}\right|\left|R\right|$, thereby ensuring that the approximate second-harmonic response given by Eq. (5.24) is acceptably low. It can be seen from Fig. 5.16 that the peak second harmonic response occurs at the input filter resonant frequency ω_f for the case drawn. The magnitude at this point is $\varepsilon DV_g R_f/R$. This peak may be lowered by proper input filter design, generally involving increased damping of the input filter (i.e., by decreasing the value of R_f). Again, the problem of properly designing an input filter under small-signal conditions has been discussed elsewhere, [6,7,8], and many of the results are applicable here. In particular, the corner frequencies ω_f and ω_0 should be well separated to avoid excessive peaking in the second-harmonic response. Next, the amount of damping necessary to reduce the second harmonic to an acceptable level is determined. Optimal values of R_f and C_b may be calculated [7], thereby avoiding the use of immoderate amounts of blocking capacitance for C_b. The result is the reduction of the second harmonic transfer function, thereby producing a satisfactorily linear amplifier.

The distortion modelling procedure has been demonstrated using two types of buck-derived amplifier configurations. Although the ideal buck converter in its simplest form is inherently linear, many practical implementations will be nonlinear. Specifically, the on-state resistance of the switches, the source impedance of the line, or the addition of an input filter cause distortion. The bridge

amplifier with input filter generates even harmonics in its input
filter and odd harmonics in its output filter. These harmonics may be
reduced to an arbitrarily low level by proper input filter design;
the criterion is that the output impedance of the input filter must
be sufficiently smaller than the input impedance of the output filter.
A similar situation occurs for the simple buck converter with input
filter. In this case, both even and odd harmonics appear at the input
and output. Again, the second harmonic is reduced by proper input
filter design. These examples show how the nonlinear distortion
processes in switching amplifiers may be analyzed in a design-oriented
manner using linear circuit models and Bode plots.

CHAPTER 6

OTHER SOURCES OF HARMONICS

6.1 Introduction

The previous chapters have considered only the nonlinearities
present in the ideal switching amplifier system. However, the
degradation of the large-signal performance of a practical switching
amplifier may occur in a number of other ways. Some of these problems
occur in all amplifiers, whether switched-mode or linear; others
arise from the peculiarities of the switching process itself. In
either event, it is useful to identify the various sources of
distortion and suggest possible remedies.

First, the open-loop bandwidth limits the maximum power
deliverable to the load at any given frequency; as a result, the
inductances and capacitances in the power circuit must be chosen with
special care if full output is to be obtained at high frequencies.
Second, the high-frequency ripple produced by the switching action is
a form of distortion but is normally considered separately since, in
most applications, the response of the load to excitations at the
switching frequency is negligible. Third, component nonidealities
such as long switching times or the nonlinearity of the ramp used in
the pulse-width-modulation process may cause additional distortion,
particularly when high switching frequencies are used. Finally, a
crossover distortion effect similar to the one found in class B

amplifiers can occur and must be corrected for in those cases where
its effect is significant.

6.2 Bandwidth Limitations

One of the most basic measures of the performance of an amplifier
is its bandwidth. In power amplifiers, the bandwidth must actually be
described in two ways. The first is the familiar small-signal
frequency response. A flat small-signal response ensures that low-
level signals of all frequencies within a given range are reproduced
uniformly. The second way is the "large-signal bandwidth" or
"maximum power frequency response". It measures the maximum
undistorted sinusoidal power deliverable as a function of frequency.
An insufficient power bandwidth leads to the familiar "slew-rate
limiting" effect, so-called because the maximum rate of change of the
output is limited. Both definitions of frequency response are
important in any power amplifier; the analysis procedure for switching
amplifiers is outlined below.

The small-signal frequency response measures the gain of the
amplifier for sinusoidal inputs, assuming that all harmonics are
negligible. It is valid only when the input is small enough that any
nonlinearities have no effect. Specifications regarding the small-
signal frequency response are usually met by the use of negative
feedback. This requires the employment of a small-signal model for
the nonlinear switching power converter [1,2,11], followed by the
application of standard linear feedback techniques.
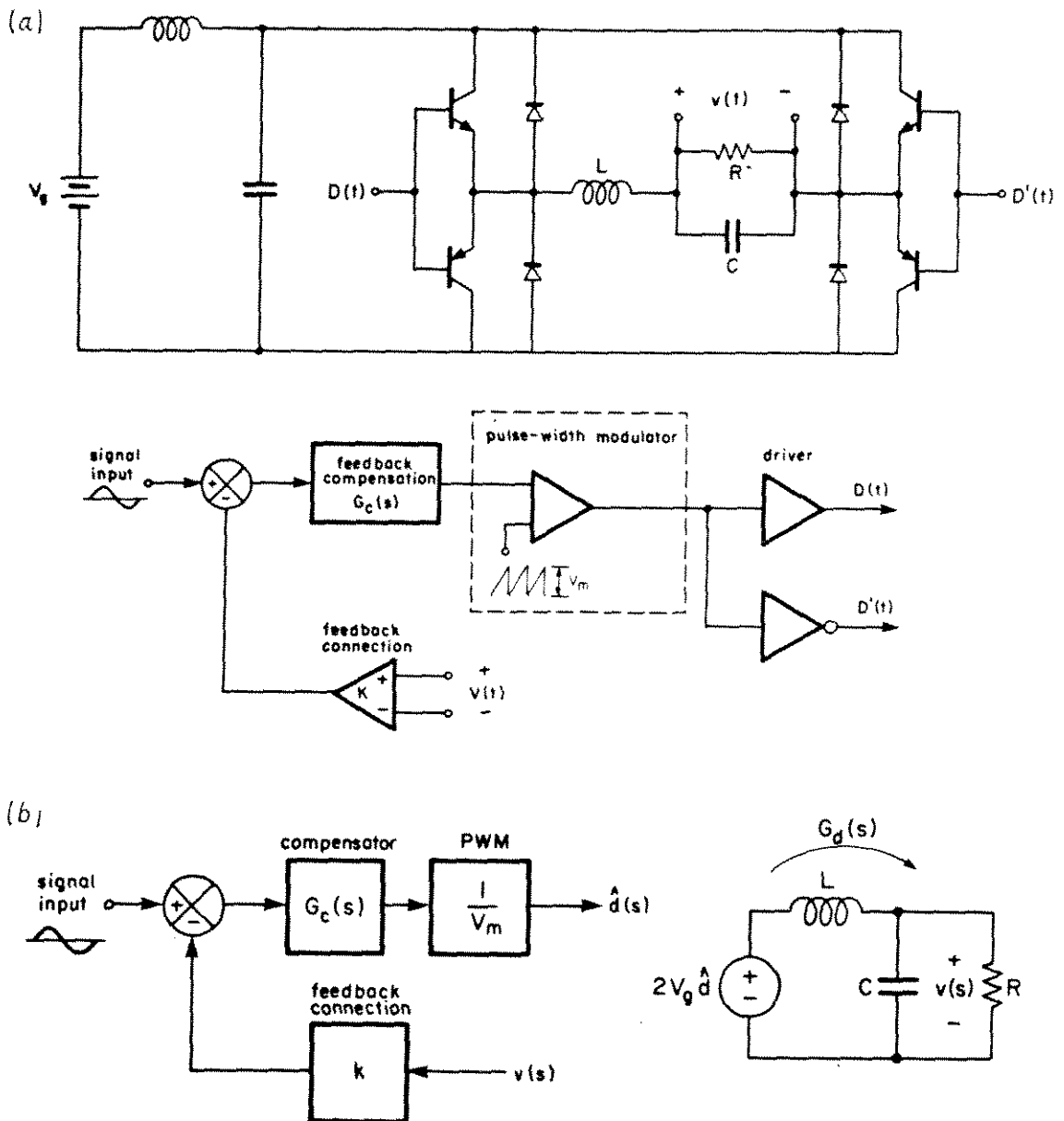
Fig. 6.1. *Small-signal modelling of a complete closed-loop switching amplifier: (a) the actual circuit; (b) the small-signal model.*

For example, consider the bridge converter of Fig. 2.4b. Usually, output voltage feedback is used, and the system is designed to provide a uniform small-signal response. A closed-loop system with compensation as in Fig. 6.1a is therefore designed, and the small-signal state-space averaged model of Fig. 6.1b applies. The relevant
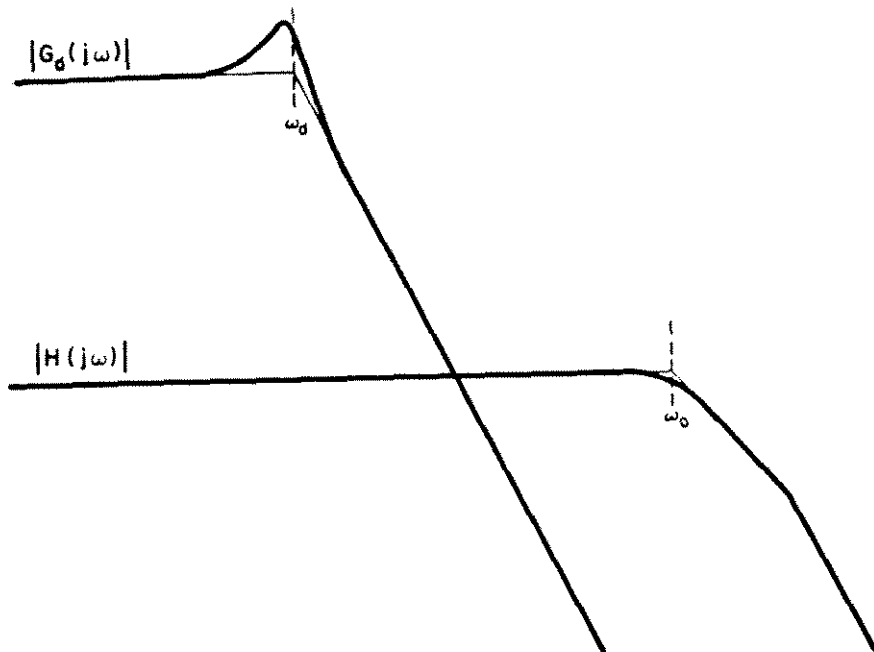
Fig. 6.2.   Typical power stage open-loop gain $|G_d(jw)|$, and complete amplifier closed-loop small-signal gain $|H(jw)|$, for the system of Fig. 6.1.

frequency responses are diagrammed in Fig. 6.2. The open-loop duty-ratio-to-output gain $G_d(s)$ of the power stage contains poles at some intermediate frequency ω_d, but the small-signal closed-loop frequency response of the entire amplifier $H(s)$ is unaffected until, at some high frequency ω_0, the loop gain becomes less than unity. Thus, the dynamics of the power stage have no effect on the small-signal frequency response at low and intermediate frequencies where the loop gain is large. Very desirable, robust small-signal characteristics can therefore be obtained.

The "maximum power frequency response" is a different matter. It is essentially unaffected by feedback, and occurs owing to the fact that the linear operating ranges of all electrical components are limited. Outside these ranges, the devices saturate or cut off, and the gain of the system is reduced. If the loop gain is reduced below

unity, then the feedback loop no longer functions, and the output is no longer undistorted. Hence, there is some maximum amplitude which the amplifier can produce, and this amplitude is a function of frequency.

The exact device which limits the output power varies from one design to another; however, this limit may often be expressed as a maximum and minimum duty ratio. Clearly, the duty ratio can never be outside the range [0,1]; often, the limit is more restrictive. In this case, the maximum sinusoidal output is obtained when the duty ratio is varied over this entire permissible range. Since the output is given by $\hat{v}(s) = G_d(s)\ \hat{d}(s)$ where $G_d(s)$ is the open-loop duty-ratio-to-output transfer function, the maximum-power frequency response is given by $G_d(j\omega)\ |\hat{d}|$ max. In other words, under the above assumptions, the large-signal bandwidth is limited by the open-loop frequency response of the power stage and is unaffected by feedback. For the bridge example, $G_d(s)$ contains two poles at frequency ω_d ascribable to the L-C output filter, as shown in Fig. 6.2. Hence, maximum sinusoidal power is obtainable only at frequencies below ω_d; at higher frequencies, the maximum power rolls off at a rate of 12 dB per octave.

A complete set of performance specifications for any power amplifier therefore includes the maximum power output obtainable at all frequencies of interest. To meet this spec, the circuit designer must place the open-loop poles in the power stage at a sufficiently high frequency; negative feedback does not change the large-signal bandwidth. Unfortunately, another type of distortion now becomes significant: the high-frequency switching ripple increases in

magnitude whenever the open-loop poles of the power stage are raised
in frequency. Thus, it is necessary to consider the effect of
increased switching ripple.

6.3 Switching Ripple and Component Nonidealities

Switching ripple is produced by almost every type of switching
converter and results from the incomplete attenuation of the high
frequency components of the pulse-width modulated waveform by an L-C
network. This form of distortion differs from other types in that the
major component of distortion occurs at the switching frequency ω_s and
its multiples and sidebands, rather than at simple multiples of the
fundamental. In most applications, the load contains an inherent
low-pass characteristic and thus has a negligible response at the
switching frequency; consequently, a moderate amount of high-frequency
switching ripple is tolerable.

Excessive ripple can degrade the performance of a switching
amplifier in a number of ways. Electromagnetic interference may
pollute the operating environment of the amplifier. Component stresses
within the converter increase. These considerations often impose a
stronger limitation on the ripple amplitude than does the response of
the load to high-frequency distortion components.

The ripple magnitude may be reduced by designing a larger L-C
filter; however, this reduces the large-signal bandwidth as discussed
in the previous section. The alternative is to increase the switching
frequency. Hence, the specification of the large-signal bandwidth
inherently sets a lower bound on the switching frequency, and values
well in excess of 20 kHz may be required. Unfortunately, component

nonidealities limit the maximum switching frequency; this is a major constraint on the performance attainable by present switching amplifiers. These nonidealities include long transistor and diode switching times, the various parasitic inductances and capacitances in the circuit, and nonlinearity of the clocked ramp waveform. These problems may be corrected by proper circuit design techniques; however, these techniques become expensive and difficult to apply at high switching frequencies. Therefore, reasonable specifications regarding the large-signal bandwidth and switching ripple amplitude are essential.

6.4 Crossover Distortion

It is well-known that class B amplifiers exhibit an effect known as "crossover distortion". This troublesome problem occurs when the output current passes through zero, and is a result of the dead zone in the gain characteristic of the amplifier caused by the base-emitter voltage drops of the output transistors.

Unfortunately, a similar effect occurs in switching amplifiers which is caused by the nonzero forward voltage drop across the transistors and diodes used to implement the switching function. This effect is most pronounced in low-voltage amplifiers using transistors having large on-state voltage drops.

For example, consider the bridge-configuration amplifier (without input filter) of Fig. 6.3. If the transistor and diode forward voltage drops are neglected, the dc gain is given by

$$\frac{V}{V_g} = (2D - 1) \qquad\qquad (6.1)$$
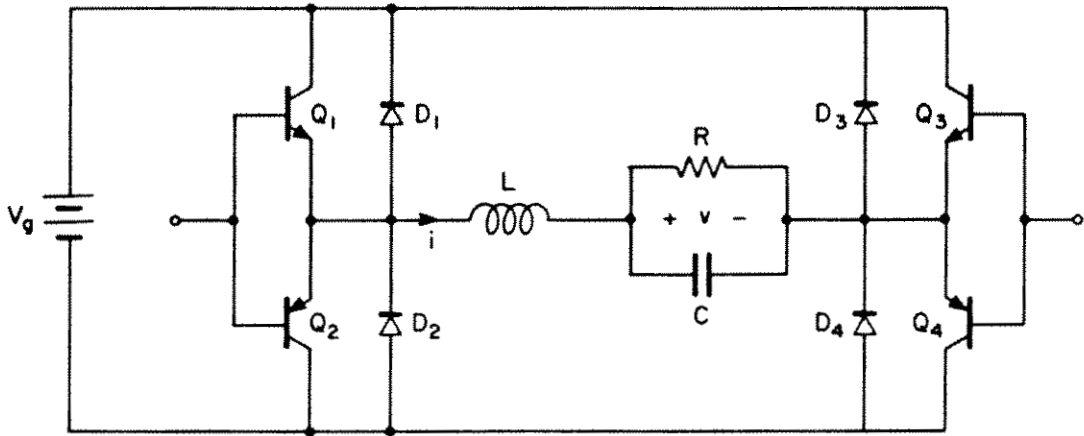
Fig. 6.3. A bridge amplifier which generates crossover distortion owing to the nonzero forward voltage drops across the switching transistors and diodes.
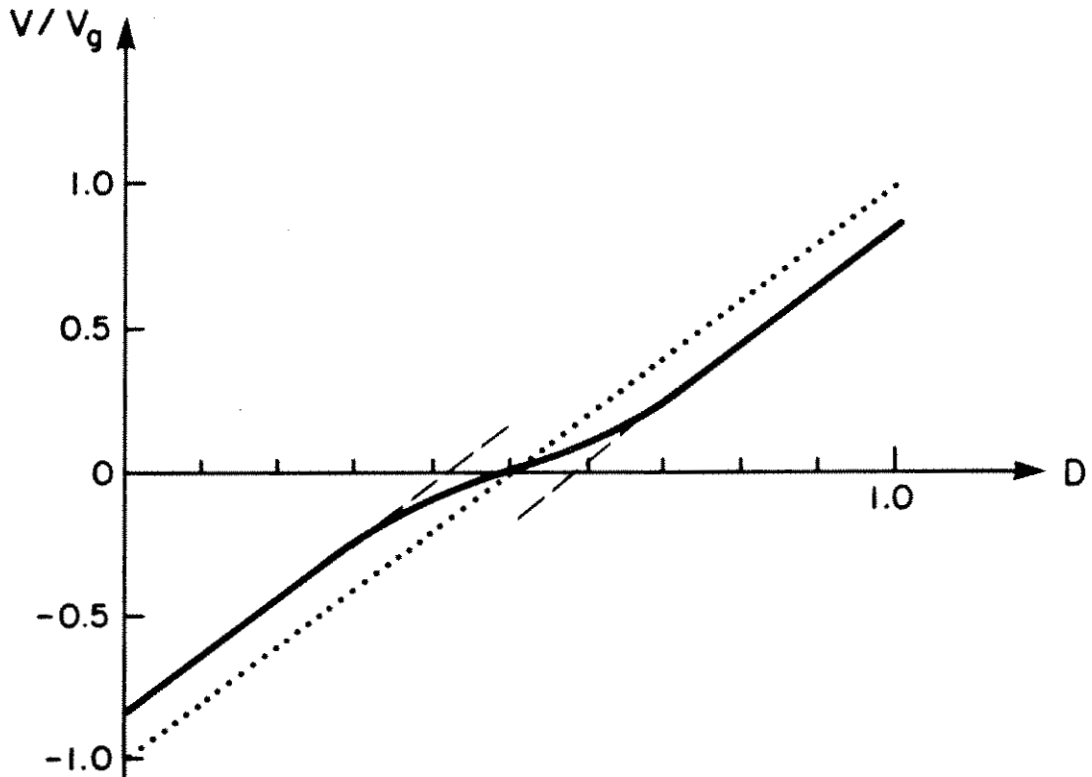
Fig. 6.4. Dc gain of the bridge amplifier of Fig. 6.3., degraded by crossover distortion.

This gain is a linear function of duty ratio D, as given by the dotted line in Fig. 6.4, and no dc distortion is predicted. However, when the transistor on-voltage V_T and diode on-voltage V_D are included, the gain is degraded as indicated by the solid line in Fig. 6.4. The gain may be divided into three regions of operation. First, for large positive values of inductor current i, Q_1 and Q_4 operate during switched interval DT_s, and D_2 and D_3 operate during interval $D'T_s$. The gain is given by Eq. (6.2).

$$\frac{V}{V_g} = (2D - 1) - 2(DV_T/V_g + D'V_D/V_g) \qquad (6.2)$$

Thus the dc gain of the amplifier depends on the ratios V_T/V_g and V_D/V_g. For large negative values of inductor current, D_1 and D_4 operate during interval DT_s, and Q_2 and Q_3 operate during interval $D'T_s$. The dc gain is then given by Eq. (6.3).

$$\frac{V}{V_g} = (2D - 1) + 2(DV_D/V_g + D'V_T/V_g) \qquad (6.3)$$

When the average inductor current is smaller than the peak current ripple, then the actual inductor current is sometimes positive and sometimes negative during each switching period. In this case, all four transistors and all four diodes operate at some time during one switching period. As a result, the gain lies somewhere between the values given by Eqs. (6.2) and (6.3), and is additionally a function of the current ripple.
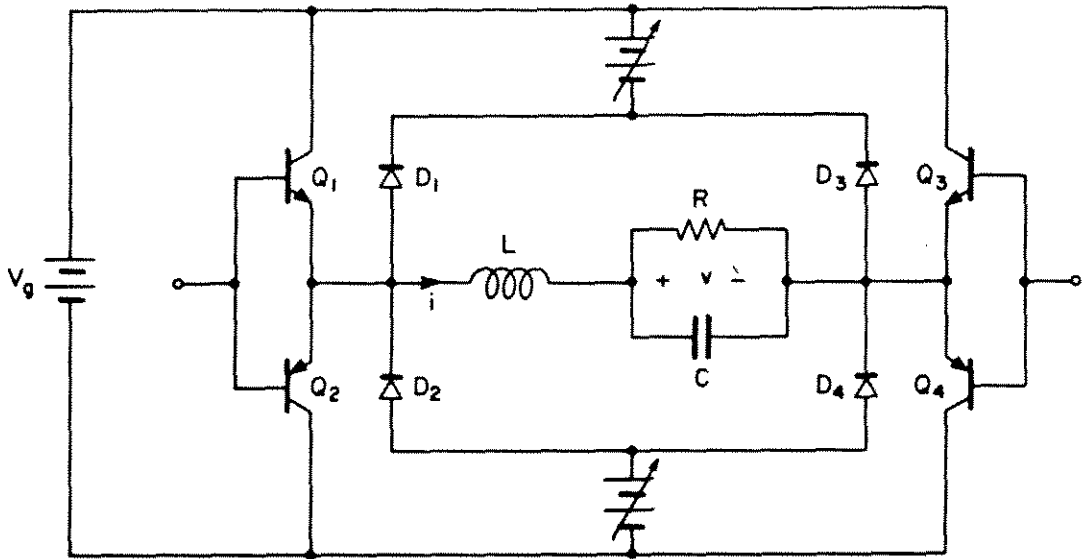
Fig. 6.5. Additional voltage bias is applied to null out the crossover distortion.

In class B amplifiers, crossover distortion is corrected by applying additional bias to counteract the effect of the base-emitter voltage drops of the output transistors. A similar scheme may be used for switching amplifiers. As shown in Fig. 6.5, one applies an additional voltage bias to the diodes to cancel out the effect of V_T and V_D. This bias must be adjusted to approximately $V_T + V_D$ to null out the crossover distortion.

A circuit similar to Fig. 6.5 was constructed using the values $V_g = 15V$, $V_T \simeq V_D \simeq 1V$, and with a large-signal bandwidth of 1 kHz. The open-loop response to a 100 Hz triangle wave and 100 Hz sine wave is shown in Fig. 6.6, first without the additional voltage bias and then with the bias included and properly adjusted. A substantial improvement can be seen for both waveforms.
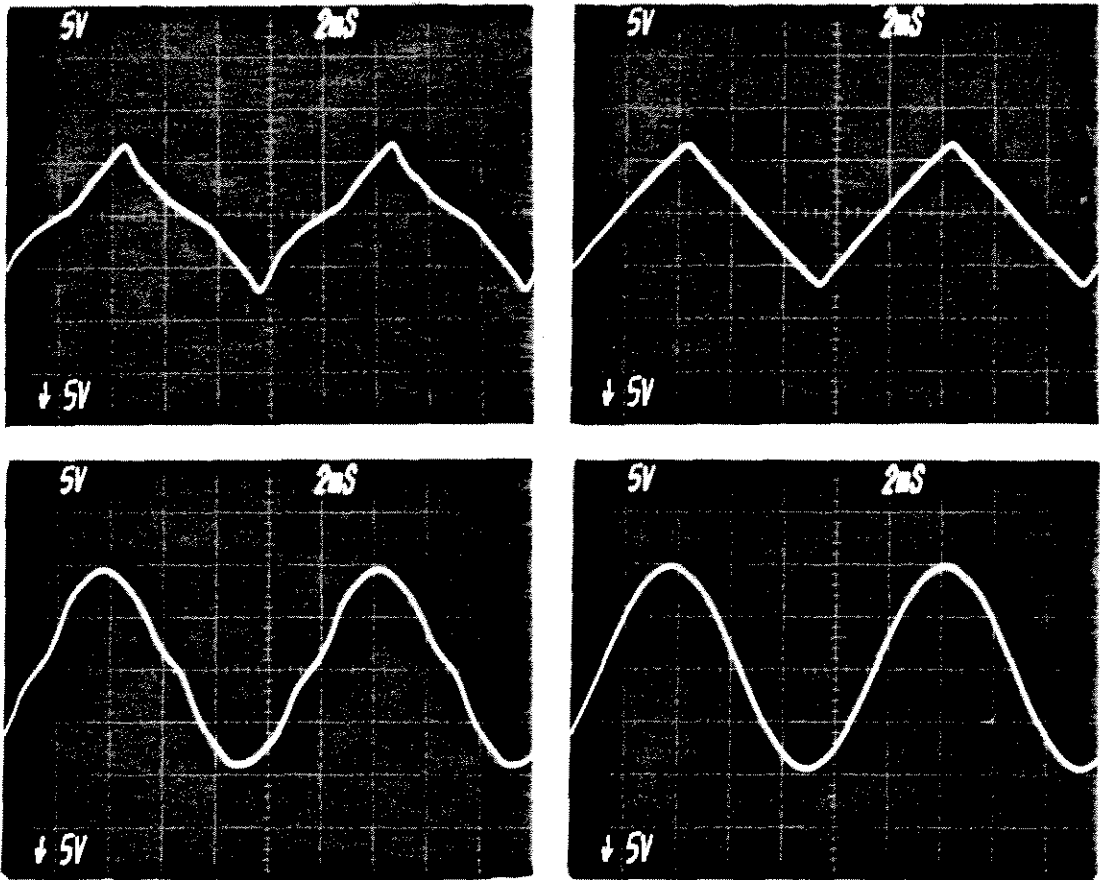
Fig. 6.6.   Output waveforms before and after the application of voltage bias to correct for crossover distortion. Top: response to triangle-wave excitation. Bottom: response to sine-wave excitation.

Thus, a crossover distortion effect caused by the forward voltage drop of the transistors and diodes used as switching elements can occur in switching amplifiers. It is particularly noticeable when the forward drops are large and the line voltage is low. The effect may be eliminated by the addition of voltage bias in series with the switching diodes or transistors.

CHAPTER 7

EXPERIMENTAL VERIFICATION

7.1 Introduction

Two different types of switching amplifiers were constructed and measured to provide quantitative verification of the distortion analysis method. First, the bridge-configuration buck amplifier with input filter analyzed in Section 5.3 was constructed, and the frequency dependence of the third harmonic was measured and correlated with the analytical predictions. The boost converter used as an example in Chapter 3 was also constructed, and the actual time-domain output waveforms are shown to coincide with the analytical series solution. Thus, the modelling method is verified in two independent ways.

7.2 Bridge-Type Buck Amplifier with Input Filter

The schematic of the bridge amplifier is given in Fig. 7.1, and a number of its features are of interest. First, the adjustable voltage sources V_1 and V_2 are necessary to reduce crossover distortion, as explained in Chapter 3. These voltage sources are actually small flyback converters, as detailed in Fig. 7.2, which were adjusted to provide approximately 2 volts output. The remaining third harmonic attributable to crossover distortion is negligible compared to the distortion arising from other sources. Second, the very large 25000 μF capacitor placed across V_g is necessary to reduce the output impedance
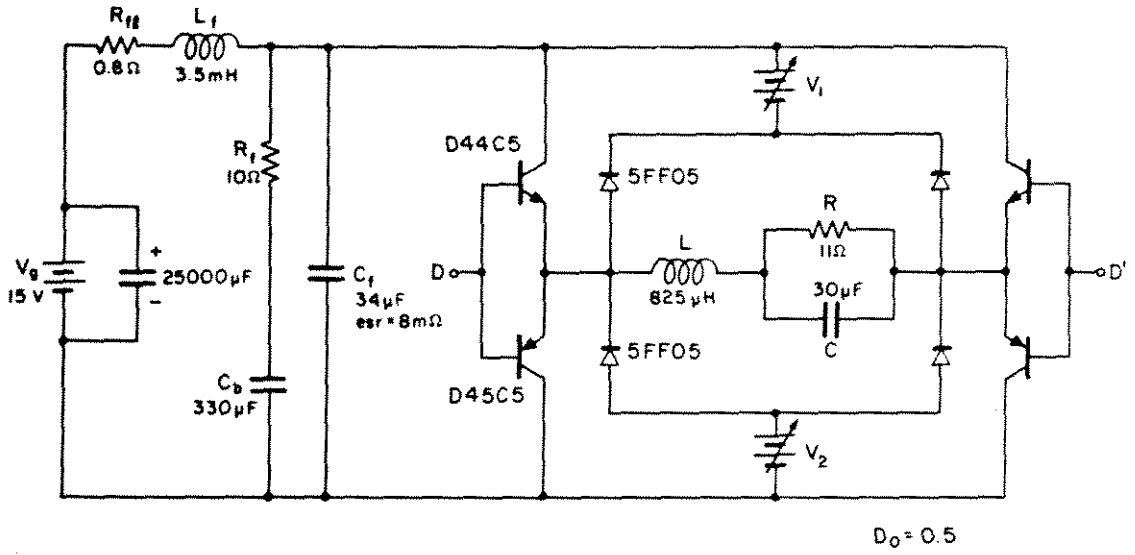
Fig. 7.1.   Schematic of the bridge amplifier test circuit.
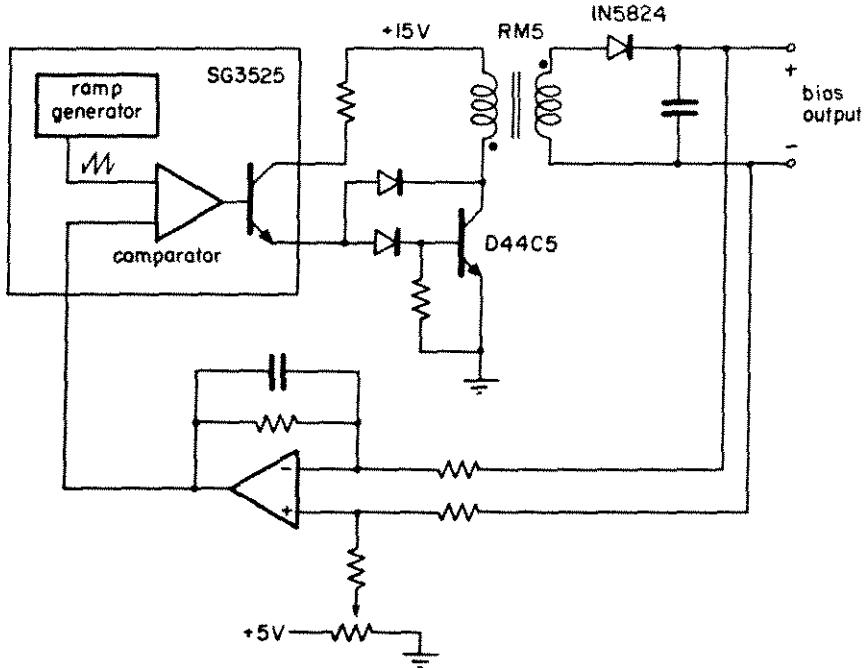
Fig. 7.2.   Simplified diagram of the flyback converter bias supplies.
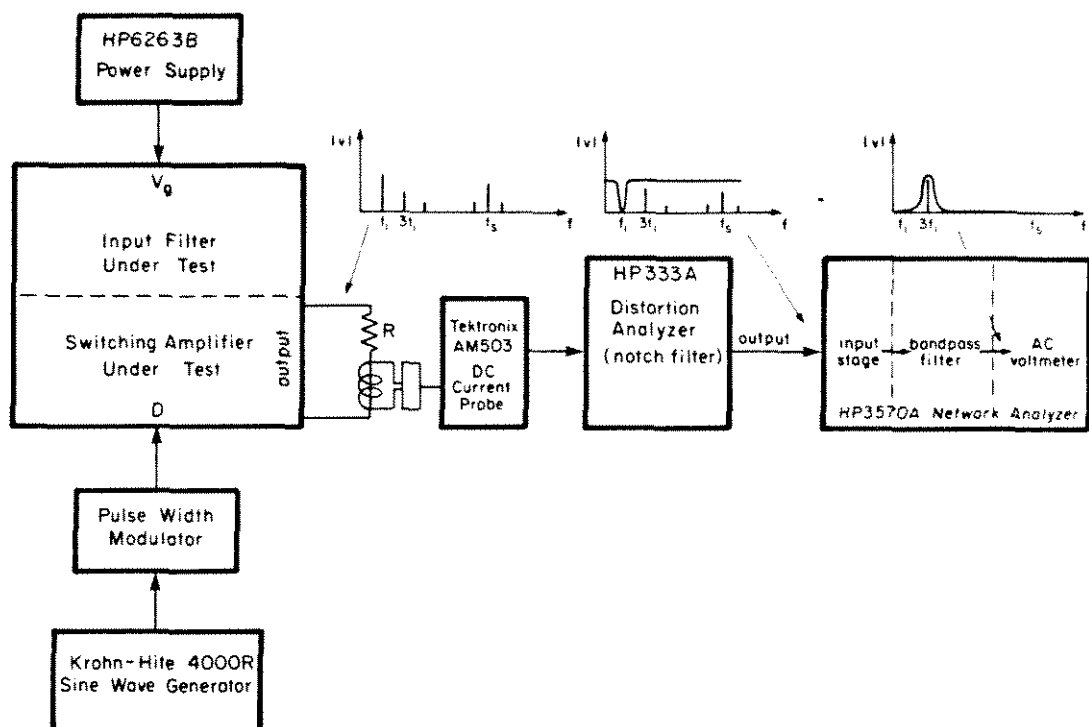
Fig. 7.3. The test setup used to measure the third harmonic response $|\hat{v}_3/d|$.

of the power supply and the connecting wires. This step ensures that the input filter is the only source impedance seen by the bridge. The distortion which remains is predominantly ascribable to the nonlinearity inherent in the bridge converter with input filter.

The test setup is diagrammed in Fig. 7.3. To make measurements of third harmonic distortion, it is necessary to use quite linear lab equipment. Therefore, the oscillator used was chosen because of the spectral purity of the sine wave it produces. Also, since the 11 Ω load is not referenced to ground, a current probe is used to measure the output current through the resistive load, thus avoiding the need to sense the output voltage differentially. It is necessary to set the probe to a high current scale to avoid the additional harmonics which would otherwise be introduced by the current probe amplifier.

Next, a distortion analyzer is used to null out the fundamental component of the output. At the output terminals of the distortion analyzer is a signal containing all of the harmonics generated by the amplifier under test but no fundamental. The use of this device greatly increases the accuracy of the measurements since the sensitivity of the network analyzer may then be increased without overloading its input stage with fundamental. Finally, the network analyzer is a device which contains a narrow bandpass filter followed by a voltmeter. This filter is tuned to the frequency of the desired harmonic, thus eliminating the other components of distortion. A reading is then made using the ac voltmeter.

Following the analysis of Section 5.3, Bode plots of the relevant quantities $|Z_{11}|$, $|Z_{s2}|$, and $|H_3|$ are constructed in Fig. 7.4 for the actual component values used. It can be seen that the linearity criterion $|Z_{s2}| \ll |Z_{11}|$ is not well satisfied in the range 100 Hz to 1 kHz. Consequently, substantial third harmonic is expected to occur over this interval (this problem could be remedied by increasing the value of C_f). Actually, as given by Eq. (5.10) the dominant component of the third harmonic response is

$$\left| \frac{\hat{v}_3}{\hat{d}} \right| = 2\varepsilon^2 V_g \left| \frac{Z_{s2}}{Z_{11}} \right| \left| H_3 \right| \tag{7.1}$$

The third harmonic has a nonzero amplitude at dc owing to the winding resistance of L_f. Over the frequency range of 10 Hz - 300 Hz, the third harmonic increases proportionally to the increase in $|Z_{s2}|$ caused by L_f. Above 300 Hz, both $|Z_{s2}|$ and $|H_3|$ decrease.
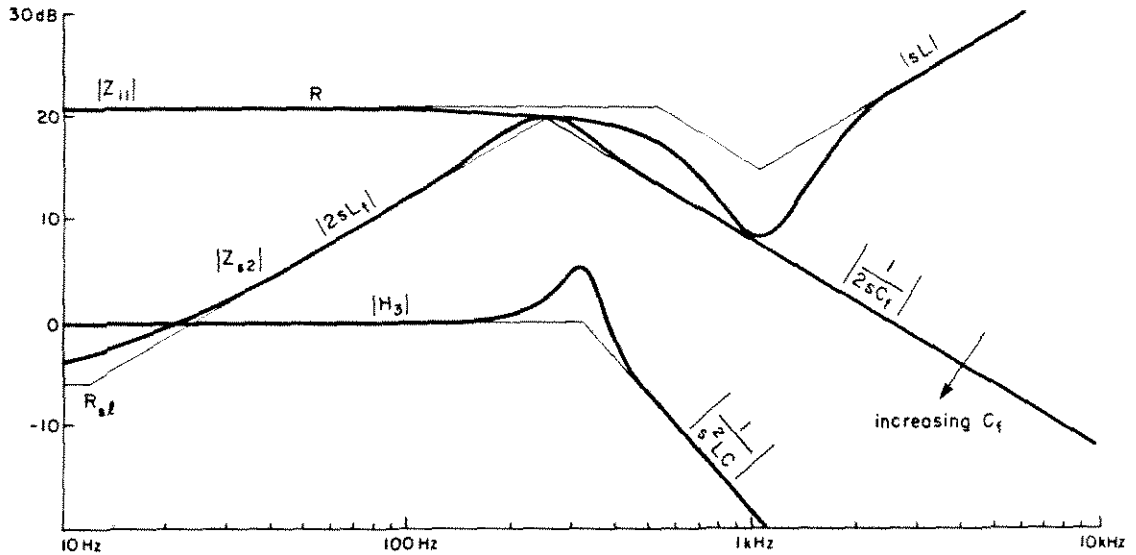
Fig. 7.4. Predicted frequency dependence of the quantities $|Z_{s2}|$, $|Z_{i1}|$, and $|H_3|$ for the actual test circuit.

Additionally, above 1 kHz $|Z_{i1}|$ increases. As a result, a peak occurs at 300 Hz, past which the amplitude of the third harmonic decreases.

The actual fundamental and third-harmonic measurements plotted against the computer-drawn predicted response are given in Fig. 7.5 for the input magnitude $\varepsilon = 0.2$. Satisfactory agreement is obtained over the entire range of frequencies measured, thus vindicating the procedure.
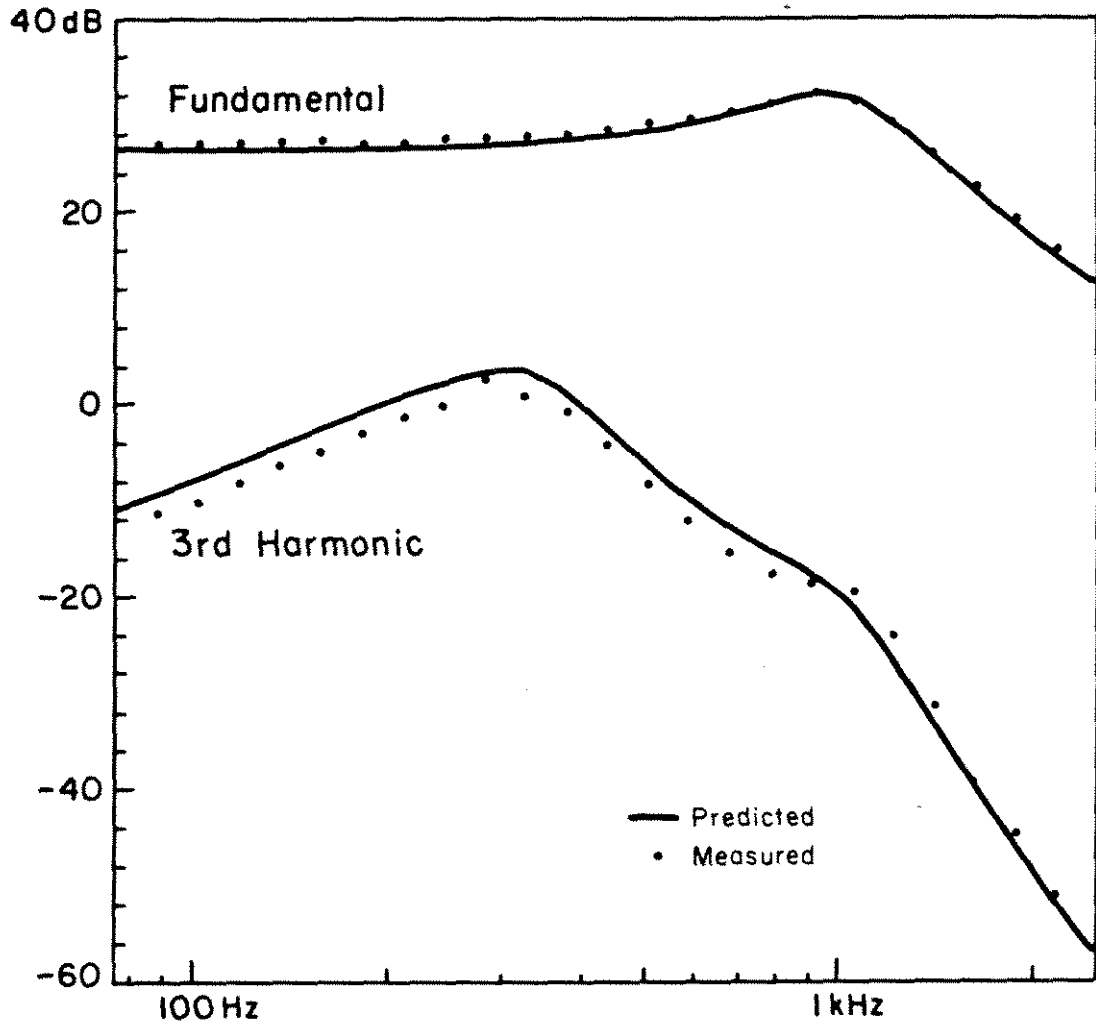
Fig. 7.5.   Experimental measurements of the bridge amplifier compared with theoretical predictions, for ε = 0.2.
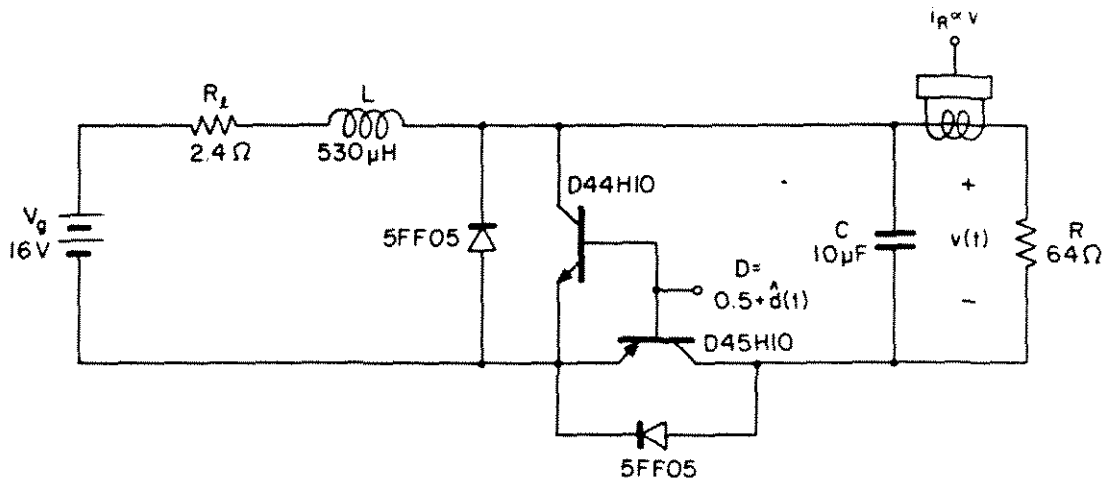
Fig. 7.6. *Schematic of the boost power stage test circuit.*

7.3 Boost Converter

The boost converter used as an example in Chapter 3 was also constructed, and the time-domain output waveforms were measured. A computer program was used to calculate each term in the series expansion of the output, and then to reconstruct the predicted output waveform by summing the series.

The power stage schematic is given in Fig. 7.6. This converter operates with a dc bias, and hence crossover distortion is not a problem for small enough ac signals. However, it is still possible for the inductor current to pass near or through zero. For this example, the inductor current ripple was approximately 10% of the quiescent current. For $R_\ell = 0.4\ \Omega$, it was found that this occurred at $\hat{d} = 0.03\ \sin(2\pi \cdot 1\ \text{kHz})t$. For this value of R_ℓ, the small-signal model predicts a resonance at 1.1 kHz with a Q of 8; hence, the gain is large enough to cause the inductor current to pass through zero during the cycle and generate crossover distortion. This problem could be corrected by the application of voltage bias in series with the diodes

or transistors, similar to the bridge example. The actual measurements were made with R_ℓ = 2.4 Ω. The circuit is much better damped with this value of R_ℓ, and no crossover problems occurred for $|\hat{d}|$ < 0.2. As a result, no voltage bias networks were necessary.

The pulse-width modulated signal for this and the previous examples was generated by an SG3525 switching regulator chip, running at 50 kHz. The internal amplifier was used at unity gain. The switching transistors, D44H10 and D45H10, were quite fast; the total delay and storage time was less than 70 nsec. As a result, for a pure sinusoidal input, the total second harmonic measured at the collector of the D44H10 was 70 dB below the fundamental, or .03%. It is apparent that the signal-processing and driver portions of the system are quite linear.

The duty ratio was modulated by a spectrally pure sine wave: $D(t) = 0.5 + 0.15 \sin(2\pi f_0 t)$ for the values f_0 = 100 Hz, 400 Hz, 1 kHz. Scope photos of the output voltage (actually the current in the load resistor R) are shown in Fig. 7.7. The computer-predicted waveforms are also given. To obtain the predicted waveforms, the computer first calculates the magnitude and phase of each term in the expansion to order (ϵ^n). The computer then reconstructs the predicted waveform by summing the series.

It can be seen that the measured and predicted waveforms agree quite well. Hence, the model correctly predicts both the magnitudes and the phases of the various components of the output waveform. The model has now been verified in two independent ways.

(a)
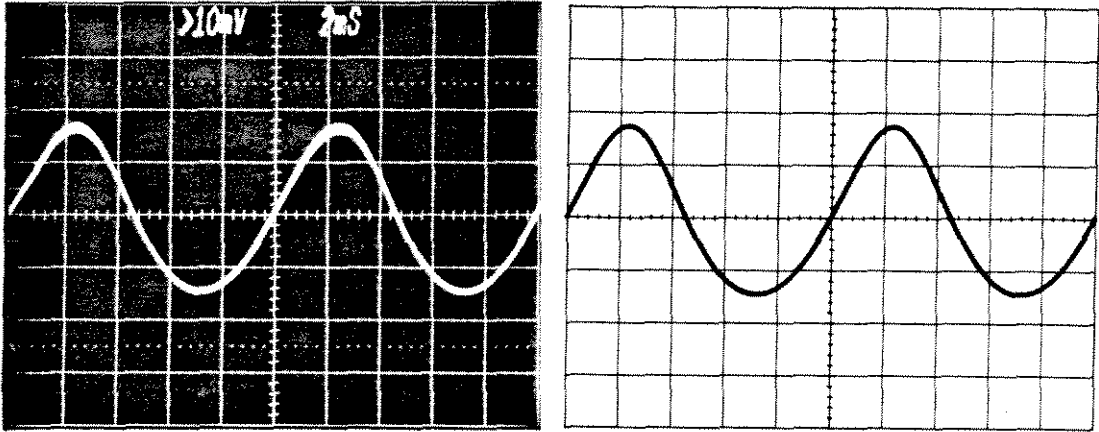
(b)
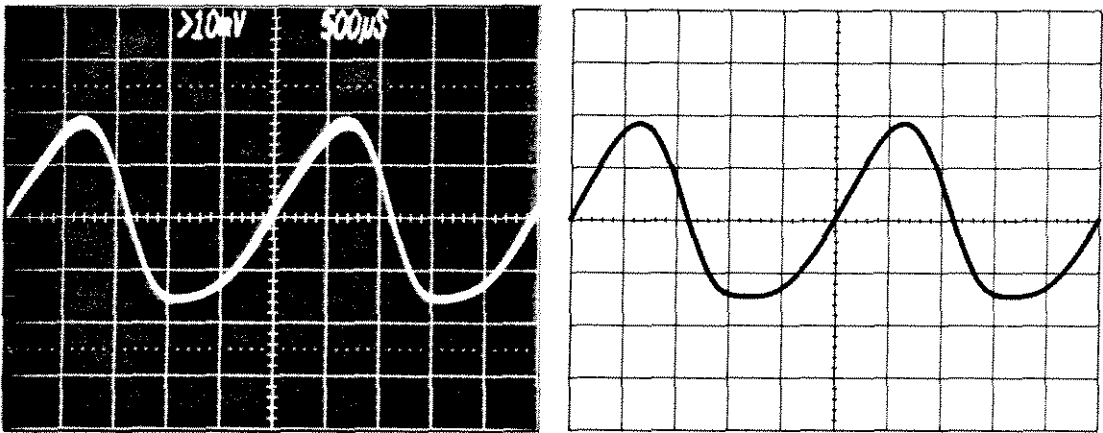
(c)
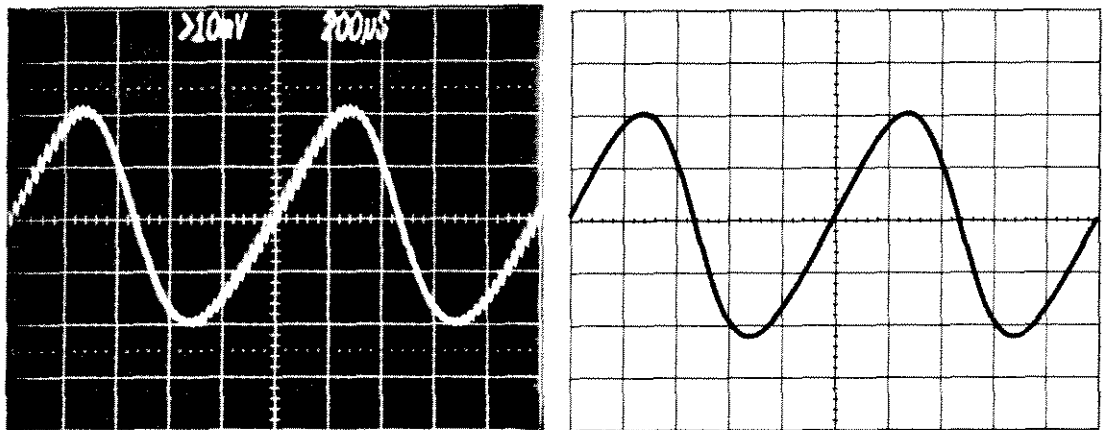
Fig. 7.7.   Experimentally measured output waveforms, left, and
predicted waveforms, right, for the boost converter excited
sinusoidally with ε = 0.15:   (a) 100Hz; (b) 400Hz; (c) 1kHz.

CHAPTER 8

CONCLUSIONS

A fundamental difference exists between the switching amplifier
and the switching power supply: the amplifier must reproduce continual
large-signal variations of a control signal, whereas the power supply
need only regulate a dc output against the occasional external
perturbations which may occur. Consequently, there is a need to
identify the features of the switching amplifier which limit its
large-signal performance, and to formulate a tractable procedure for
its large-signal analysis and design.

Switching amplifiers are in general nonlinear and usually generate
low-frequency harmonic distortion. Furthermore, the magnitude of this
distortion is a function of frequency which may attain a peak at some
intermediate frequency. Hence, a dc distortion analysis is not
sufficient; rather, it is necessary to construct ac models which
predict peak values and frequency ranges over which they occur.

A model which approximates the properties of interest is
described in Chapter 3. This model is especially well-suited for
amplifier design because it is *linear*; as a result, many of the
standard, familiar techniques of linear circuit theory may be applied,
and insight is gained into the large-signal operation of the entire
system.

The modelling procedure is extended in Chapter 4 for the case when two independent sinusoidal inputs are present; in this situation, intermodulation distortion occurs which is caused by the nonlinear interaction of the two inputs. Additional linear circuit models may be found which describe the intermodulation components of the output. Again, these models may be easily evaluated by the use of well-known linear techniques.

As an example of the procedure, two buck-type amplifiers with input filters are analyzed in Chapter 5, and are found to generate harmonics at their outputs. Bode plots of all relevant quantities are constructed, revealing the dependence of the harmonic distortion on the various element values in the circuit. For these examples, the relative distortion may be reduced to an arbitrarily low level by the design of $\left| Z_{s2}(s) \right|$ sufficiently smaller than $\left| Z_{11}(s) \right|$. This involves the proper choice of converter corner frequencies and associated Q-factors to avoid excessive peaking in the harmonic response. Thus, the distortion properties of the amplifier are easily related to familiar parameters of the system.

The above results are verified experimentally in Chapter 7. First, a bridge-type buck amplifier with input filter was measured to confirm the predicted frequency dependence of the fundamental and third harmonic components of the output. Next, a boost converter was measured to confirm the ability of the method to predict the actual time-domain waveforms present in the amplifier.

Other sources of distortion exist, each of which must be eliminated before sound large-signal performance is obtained. A crossover distortion effect similar to the one found in class B amplifiers can occur, and may be corrected for by the addition of an external voltage bias in series with the switching transistors or diodes. Slew-rate limitations can occur in any type of amplifier; however, this problem is particularly severe in high bandwidth switching amplifiers. To extend the large-signal bandwidth of a switching amplifier, one must tolerate either larger switching ripple or a higher switching frequency. This tradeoff is a fundamental limitation on the performance obtainable from a practical switching amplifier.

The various limitations on the large-signal performance of switching amplifiers are thus exposed, and some possible remedies have been suggested. The models developed allow the informed large-signal design of switched-mode amplifiers.

PART 2

TRANSIENTS IN SWITCHING REGULATORS

CHAPTER 9

INTRODUCTION

9.1 Introduction

Part 1 considered the effect of the switching converter
nonlinearity on the forced response of the converter. This problem
is of interest in large-signal ac applications such as in power
amplifiers. In Part 2, the effect of the nonlinearity on the *unforced*
response is investigated. This finds application in the design of dc
regulators, where it is necessary to ensure that the closed-loop
system is stable and well-behaved for all possible transients and
external perturbations.

Because of the inherently nonlinear behavior of switching
converters, it is very difficult to design a stable feedback loop using
exact methods since the resulting differential equations cannot
generally be solved. Instead, small-signal methods are commonly used,
where one linearizes the regulator model about a quiescent operating
point. These models are very useful to the practicing engineer since
he may apply all of the relatively simple techniques of linear circuit
theory such as Bode plots, root locus, etc. The physical insight
gained then allows the engineer to intelligently design his feedback
loop and to specify important small-signal specifications such as audio
susceptibility and output impedance.
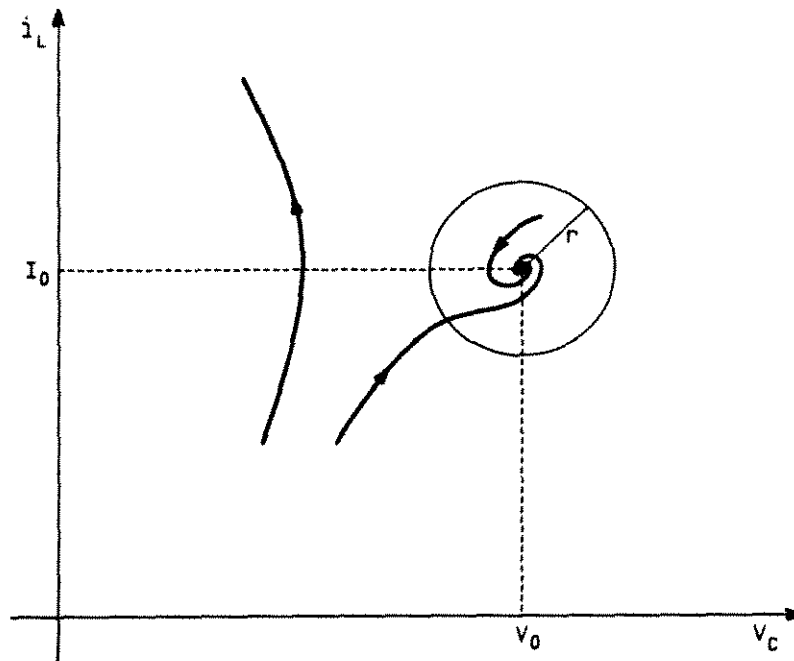
Fig. 9.1. Hypothetical trajectories of a switching regulator. Inductor current i_L is plotted vs. capacitor voltage v_c. A small-signal model was used to design the feedback loop; indeed, transient solutions within a radius r of the quiescent operating point (I_0, V_0) converge as desired. However, transient solutions outside this range may be unstable.

Unfortunately, because of the small-signal approximation, these methods do not ensure the complete large-signal stability of the quiescent operating point. One might conceive of a regulator which behaves as illustrated in Fig. 9.1. For small perturbations, less than some radius r from the quiescent operating point, the regulator behaves as predicted by the small-signal model, and transients converge as expected. However, for large perturbations, the nonlinear terms become significant, and some solutions do not converge to the desired quiescent point (i.e., some solutions are unstable). Other large transients do converge, but with a large, distorted waveform which may be much larger than predicted by the small-signal model and hence unacceptable.

A regulator which exhibits the hypothetical behavior illustrated
in Fig. 9.1 obviously is unreliable and unacceptable. The
investigation of the effects of switching regulator nonlinearities
and the exposition of some techniques for the avoidance of large-signal
instabilities are the subjects of Part 2.

9.2 The Large-Signal Stability Problem: An Example

Before embarking on a large-signal stability analysis, it is
necessary to determine whether the effect of the converter
nonlinearity is significant. Is it possible to design a regulator
whose response to large perturbations deviates substantially from the
response predicted by the small-signal model? Even worse, is it
possible for the response to be reasonably stable for small signals
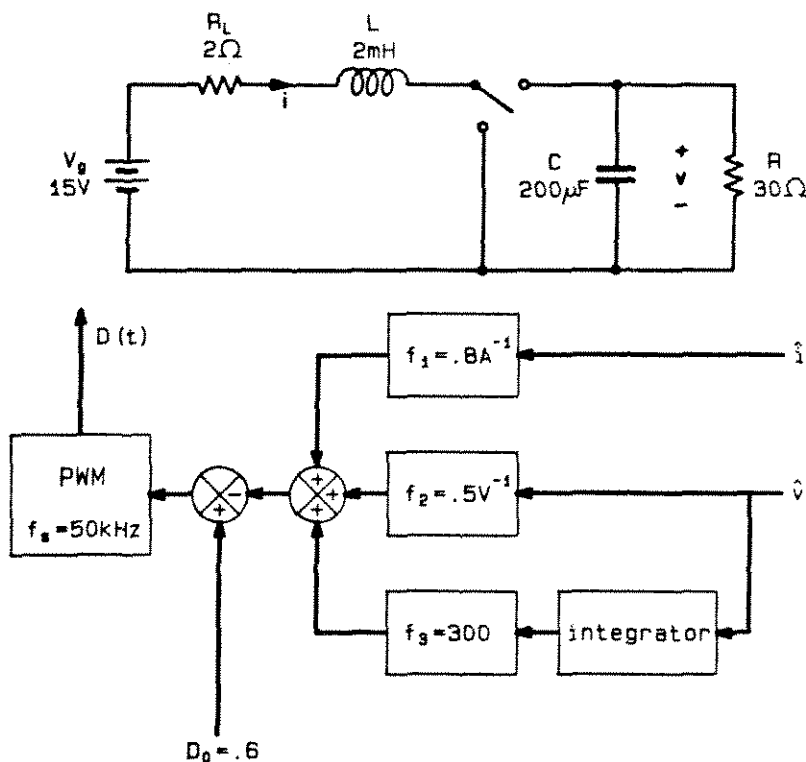
Fig. 9.2. Three-state boost regulator example.

but diverge for large transients? An example is given in this section which demonstrates that the answer to the above questions is *yes*; large-signal phenomena exist which can seriously degrade the performance of a switching regulator, and these phenomena are not predicted by small-signal models.

Consider the boost regulator shown in Fig. 9.2. The dc gain and efficiency curves are shown in Fig. 9.3. This regulator was designed to operate at a nominal duty ratio of .6 with an efficiency of 70.5%. The state-space-averaged small-signal model [1,11], is shown in Fig. 9.4. To stabilize the system in the presence of the right-half-plane zero which appears in the duty-ratio-to-output transfer function, the inductor current is fed back in addition to the output voltage. The integral of the output voltage is also fed back to improve regulation. For the values chosen, the closed-loop small-signal response contains one real pole and two complex poles with a Q of .6; thus, the system appears to be quite stable and well-damped. A computer program, detailed in Fig. 12.3 later in this thesis, was used to investigate the large-signal response of this regulator. The computer-predicted response to a small step change in inductor current and capacitor voltage is diagrammed in Fig. 9.5. It is indeed well-behaved; the waveforms appear linear, and a very small amount of overshoot occurs in the control $(\hat{d})$ waveform. The small-signal model is an excellent approximation in this case.

The response to a step change of intermediate proportions is shown in Fig. 9.6. The solid line is the nonlinear response, and the dotted line is the response predicted by the small-signal model. Although this response is stable, it is decidedly nonlinear. The peak

(a)

M

2

1

0

0 .1 .2 .3 .4 .5 .6 .7 .8 .9   D

(b)

η

.8

.6

.4

.2

0

0 .1 .2 .3 .4 .5 .6 .7 .8 .9   D
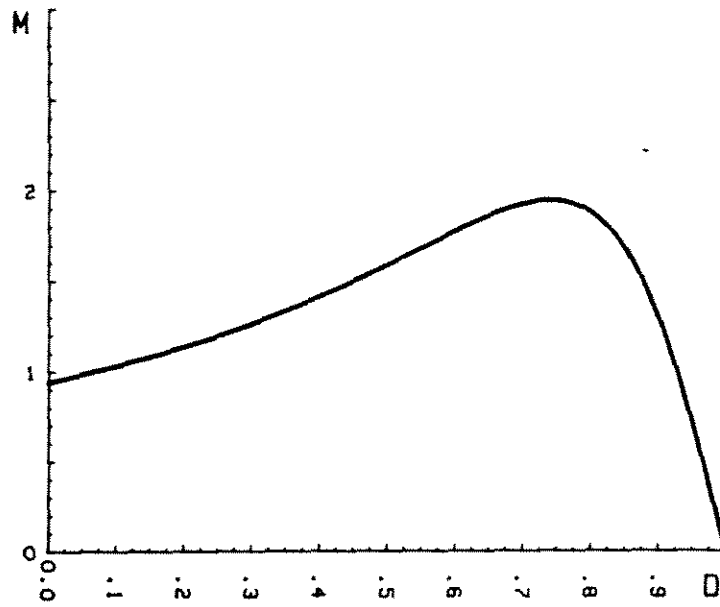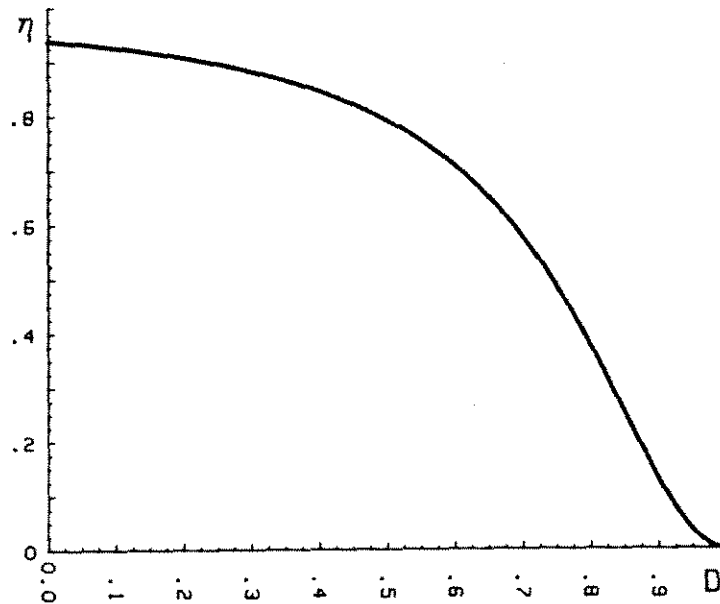
Fig. 9.3. Dc analysis of the boost example: (a) equilibrium gain
M = V_0/V_g; (b) equilibrium efficiency η.
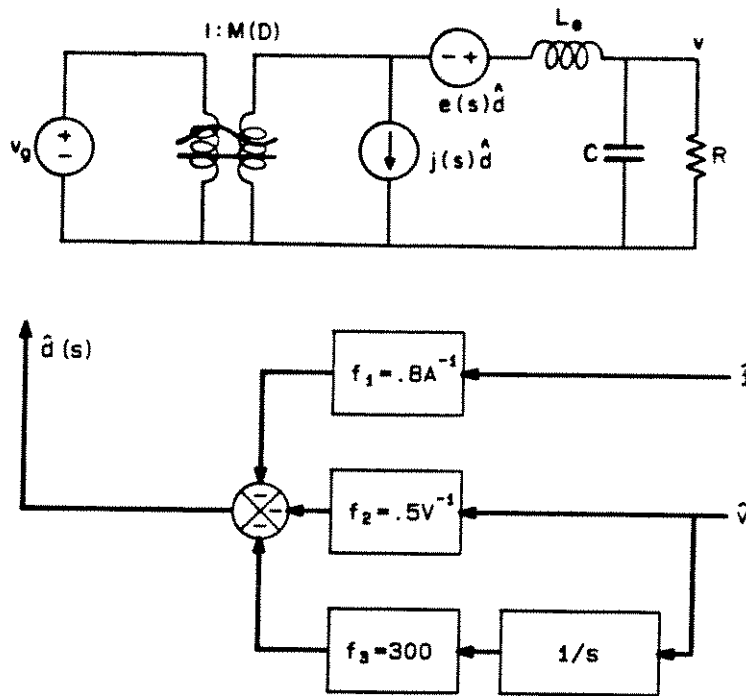
Fig. 9.4.   Small-signal state-space averaged model used to design the feedback loop of the three-state boost regulator example.
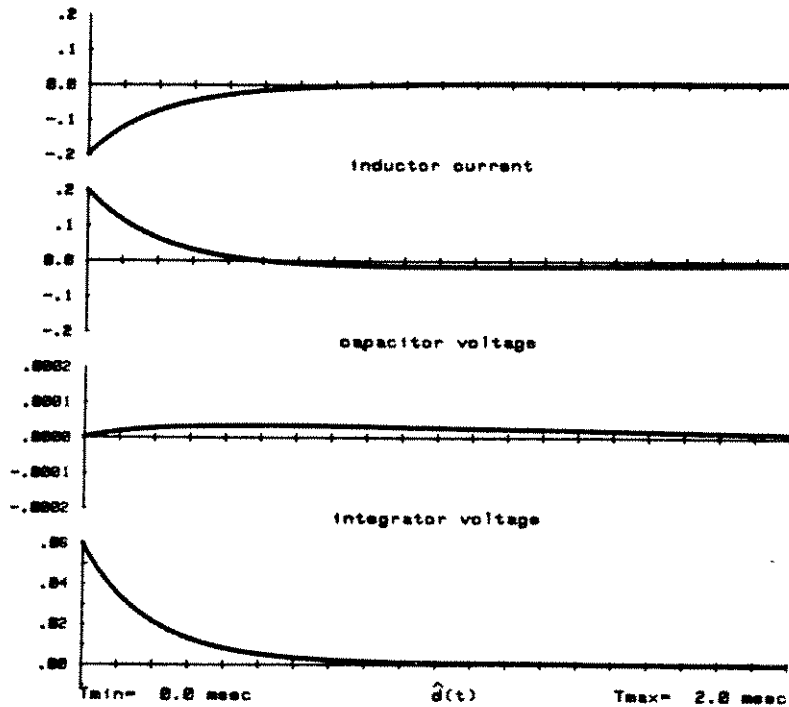
Fig. 9.5.   Computer-generated time-domain waveforms of the response to a small perturbation in capacitor voltage $\hat{v}$ and inductor current $\hat{i}$. The small-signal approximation is justified in this case, and the response converges as predicted.
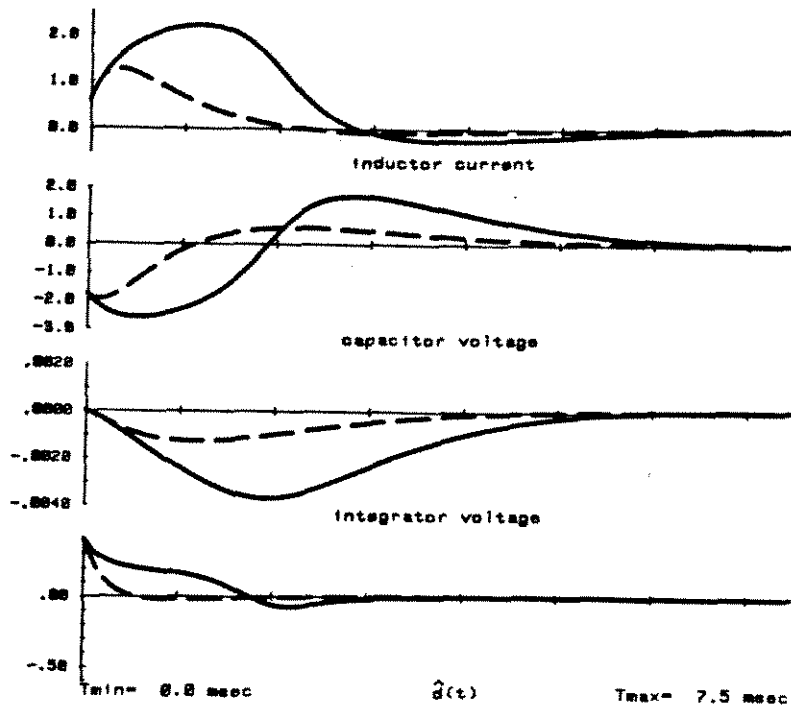
Fig. 9.6. Computer-generated waveforms of the response to a perturbation of intermediate proportions. Dashed line: as predicted by the small-signal model. Solid line: as predicted by the complete large-signal nonlinear model described in Fig. 12.3. Peak voltages and currents are significantly larger than the amounts predicted by the small-signal model.
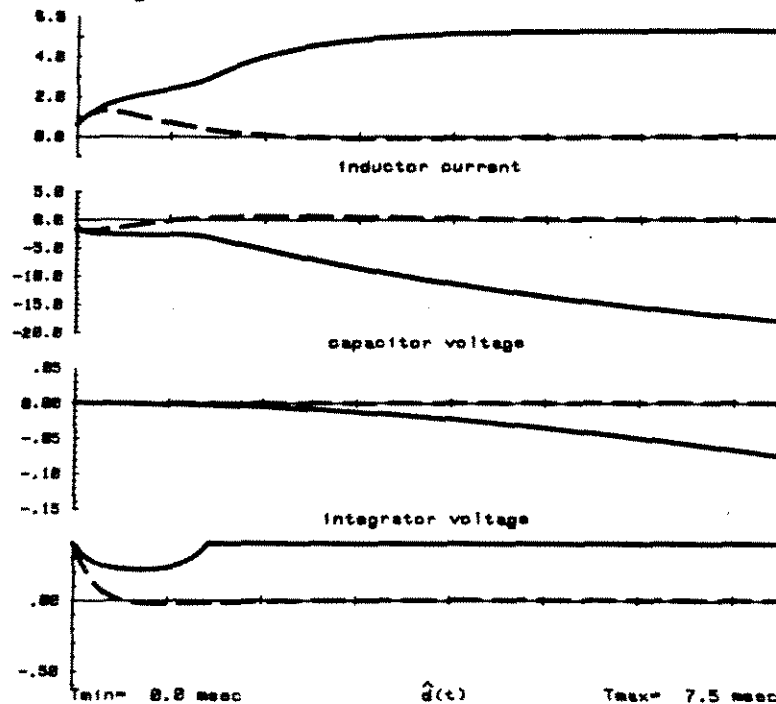
Fig. 9.7. Computer-generated waveforms of the response to a large perturbation. Dashed line: as predicted by the small-signal model. Solid line: as predicted by the large-signal nonlinear model. The response is unstable.

inductor current is larger than the amount predicted by the small-signal model, and the control ($\hat{d}$) waveform overshoots its nominal value much more than expected. The small-signal approximation is unjustified in this case.

The response to a yet larger step change in inductor current and capacitor voltage is shown in Fig. 9.7. The system is unstable in this case! The voltages and currents in the system become large, and the control signal saturates at its maximum value. Obviously, this design is unreliable.

In this example, the small-signal approximation is unjustified for moderate or large perturbations. Hence, even though the small-signal model predicts that the system response is well-damped, the effect of the nonlinearity can be of significance, causing larger overshoots than expected and possibly even instabilities.

9.3 Outline of Discussion

From the above example, it is apparent that small-signal switching regulator models do not necessarily include all features of importance. It is of interest, therefore, to model these additional large-signal effects. In Chapter 10, the basic tools necessary for the nonlinear analysis of Part 2 are reviewed. In Chapter 11, a nonlinear model is derived which predicts the behavior described in the boost example above. Two versions of this model are described. First, a discrete-time model is derived which is well-suited for computer simulations. Second, a continuous-time model is found which is sometimes more convenient for analytical calculations. Next, the saturation of the pulse-width modulator is accounted for. This

phenomenon has a significant effect on the large-signal response of
the regulator, and hence cannot be ignored. Models are derived which
describe the response of the regulator in the saturated regions.
Other modes of operation may occur, including current limiting modes
and transient discontinuous mode. The switching regulator is usually
rendered stable for large transients by the addition of extra modes
of operation which improve the large-signal response. It is
necessary to model each of these modes in order to understand the
operation of the regulator and to obtain a well-behaved system. The
transient discontinuous conduction mode is modelled in Section 11.4
and the effect of a current limiting mode is discussed in Section 13.9.

In Chapter 12, the implications of these models are examined.
First, the equilibrium points of the system are calculated. The
presence of real equilibrium points in addition to the desired
quiescent operating point indicates the existence of unstable
transient solutions; therefore, these additional real equilibrium
points must be eliminated. Next, the trajectories or transient
waveforms are calculated. Peak transient current and voltage levels
may then be determined, and the existence or absence of unstable
solutions verified.

In Chapter 13, a simple boost regulator example is solved. The
various modes of operation are determined, and analytical expressions
are found for their equilibrium points and boundaries in the state
plane. Approximate analytical expressions are also found for the
time-domain transient waveforms. A number of modifications are
suggested which improve the response, and yield a completely stable
regulator. This boost regulator example was constructed, and the

analysis of Chapter 13 was verified experimentally, as summarized in Chapter 14. The observed transient waveforms agree quite well with the predictions, and the existence of unstable solutions is confirmed.

As summarized in Chapter 15, this analysis points out the possibility of instabilities which occur owing to the nonlinear nature of the switching regulator. Insight may be gained into the large-signal behavior of the regulator, and the modifications necessary to obtain a well-behaved, globally stable regulator then become apparent. Thus, the informed large-signal design of switching regulators is now possible.

CHAPTER 10

FUNDAMENTALS OF STATE-PLANE ANALYSIS

10.1 Introduction

The plotting of transient waveforms in the state plane is a
well-known technique for the analysis and design of nonlinear
systems. Not only can the state plane portrait of a system illustrate
its stability regions, but also the transient peak currents and
voltages may be found. The various salient features of the response,
such as the positions of equilibrium points, may be determined, and in
many cases analytical expressions can be obtained which yield insight
into the dependence of these features on the various circuit element
values. The effect of various modifications such as the addition
of a current limiting mode is also easily seen. Thus, the state-plane
technique is a useful design tool.

The nonlinearity inherent in the converter power stage, whose
effect on the distortion generated by switching amplifiers is considered
in Part 1, is not the only nonlinear phenomenon of significance in a
switching regulator. A number of different modes of operation occur,
either unavoidably or by design. These modes include the saturation of
the pulse-width modulator, the transient discontinuous conduction mode,
and current limiting modes, all of which affect the stability and peak
transient current and voltage levels of the regulator. Consequently,
it is of interest to review the behavior of piecewise systems.

In this chapter, the fudamentals of the analysis of piecewise nonlinear systems in the state plane are reviewed. The various types of equilibrium points which can occur are listed, and their influence on the trajectories of the system is described. The applicability of tnese techniques to switching regulator analysis is illustrated by example. The large-signal regulator design problem is then examined in greater detail, and the strategy for the solution of this problem is formulated.

10.2 Review Of State-Plane Analysis And Piecewise Systems

The state-plane is used in Part 2 to display the transient inductor current and capacitor voltage waveforms of the switching regulator for various values of initial voltage $v_c(0)$ and current $i_L(0)$. For example, consider the boost regulator of Fig. 10.1. This system contains two independent states, the inductor current i_L and the capacitor voltage v_c. The state plane for this converter might appear as shown in Fig. 10.2. The transients which result from a few different initial conditions are plotted with time as an implicit variable; these are known as the "state-plane trajectories" of the system. It can be seen that some state-plane trajectories converge to the point (I_0, V_0) while others do not.

The equilibrium points of a system are prominent features of its state-plane portrait; they reveal a great deal of information regarding the large-signal response. The system is designed to regulate the capacitor (output) voltage at a quiescent level V_0. The quiescent
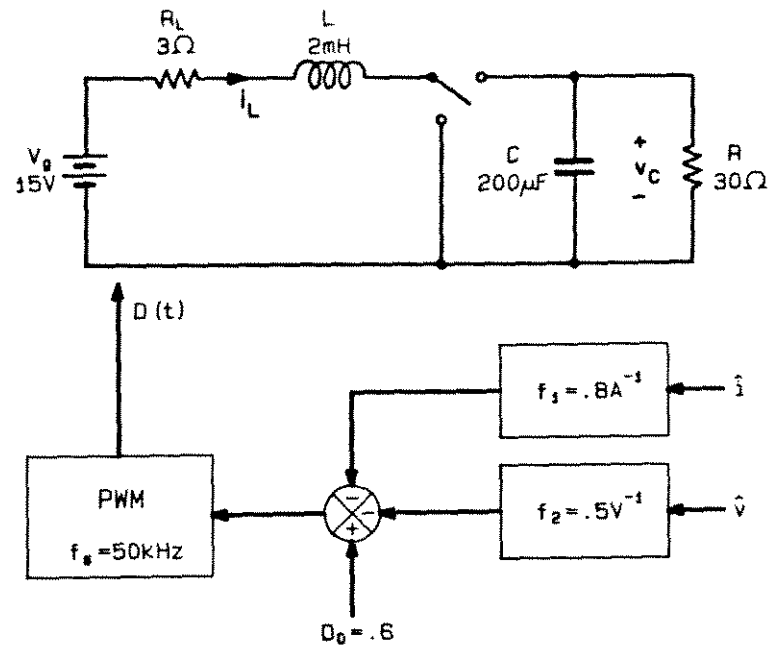
Fig. 10.1. A simple boost regulator.
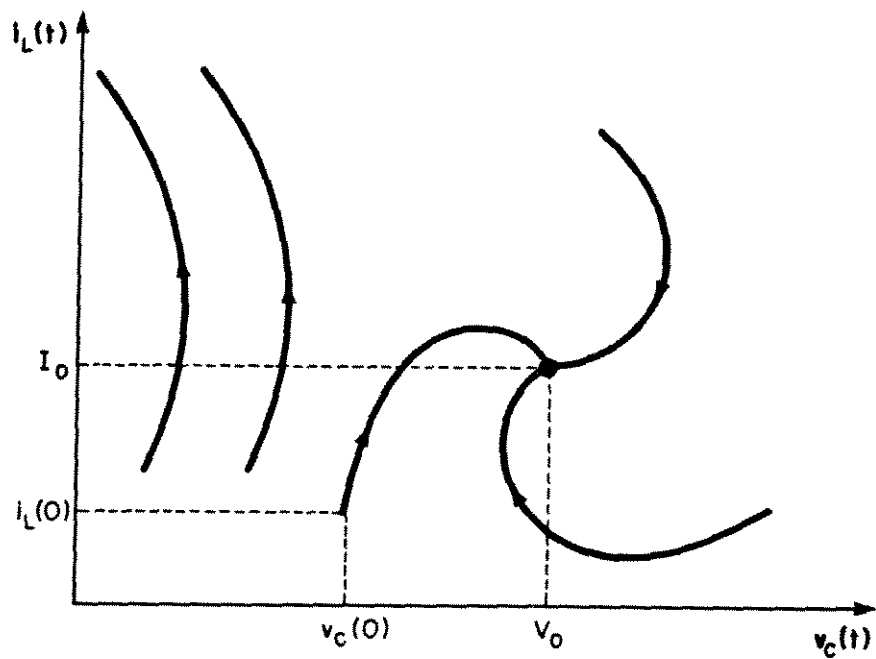
Fig. 10.2. Hypothetical state-plane trajectories for the boost regulator of Fig. 10.1.

inductor current I_0 is then determined by the output load. Thus, by design, the system contains an equilibrium point at (I_0, V_0).

In general, every equilibrium point of a system satisfies the continuous-time relation given in Eq. (10.1a) or its discrete counterpart Eq. (10.1b), given below:

$$\frac{dx(t)}{dt} = \underline{0} \qquad (10.1a)$$

$$\underline{x}_{n+1} = \underline{x}_n \qquad (10.1b)$$

where the vector $\underline{x}(t)$ contains the independent state variables of the system. As demonstrated in Chapter 12, Eq. (10.1) may be used to obtain analytical expressions for the positions of the equilibrium points. A nonlinear system may have more than one equilibrium point; indeed, the boost regulator example of Chapter 13 contains three. The presence of real equilibrium points in addition to the desired quiescent point indicates that the response for large signals deviates substantially from the small-signal predictions, and that unstable solutions may exist. Therefore, these unwanted real equilibrium points must be eliminated.

A classification of the different types of isolated real equilibrium points can be found in any nonlinear system textbook. If all trajectories in the neighborhood of a given equilibrium point diverge from the given point, then it is called an "unstable
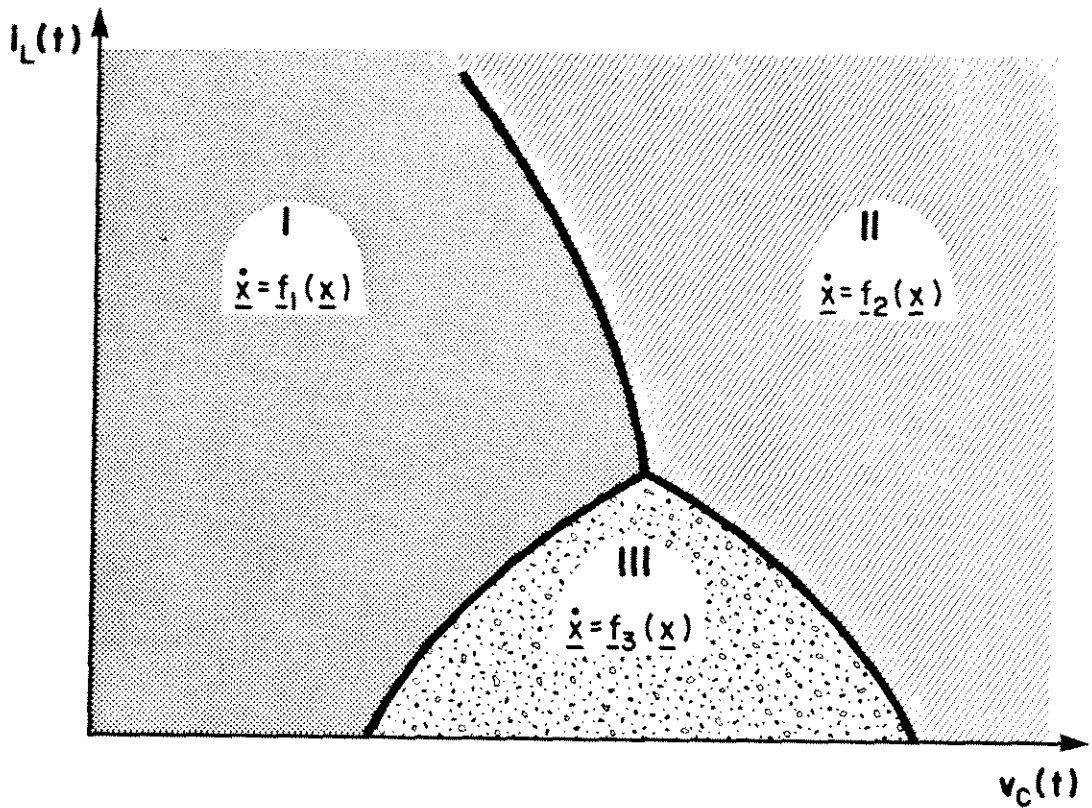
Fig. 10.3. A piecewise system is described by different (possibly nonlinear) state equations in each of several regions in the state plane.

equilibrium point". If some trajectories in the near vicinity converge and others diverge, then it is a "saddle point", while if all nearby trajectories converge then the point is a "stable equilibrium point". If all trajectories in the entire state plane converge to a single equilibrium point, then it is "globally stable". It is desired to ensure that the quiescent operating point of the regulator is globally stable, and furthermore that all trajectories converge in a well-behaved manner.

The typical switching regulator is a piecewise system. As illustrated in Fig. 10.3, one set of possibly nonlinear state equations describes the system in region I of the state plane, a different set of equations describes the system in region II, and so on. Associated

with each region is a separate set of trajectories and equilibrium points. The stability of the entire system depends not only on the equilibrium points and shapes of the trajectories in the various regions, but also on the boundaries between the regions.

For example, consider the system described by the following state equations:

$$
\left.
\begin{aligned}
\dot{x}_1 &= x_2 \\
\dot{x}_2 &= -x_1 - x_2 + 1
\end{aligned}
\right\} \quad \text{for } x_1 > 0 \tag{10.2a}
$$

$$
\left.
\begin{aligned}
\dot{x}_1 &= x_2 \\
\dot{x}_2 &= -x_1 - x_2 - 1
\end{aligned}
\right\} \quad \text{for } x_1 < 0 \tag{10.2b}
$$

The state equations change, depending on the sign of x_1; hence, the state plane for this system contains two regions whose boundary is the line $x_1 = 0$. As shown in Fig. 10.4, the state equations contain two real equilibrium points. For $x_1 > 0$, the equilibrium point occurs at $(1,0)$, and for $x_1 < 0$ the equilibrium point occurs at $(-1,0)$.

The system trajectories are constructed by considering each region separately. For $x_1 > 0$, the state equations (10.2a) are linear and can be solved exactly: the waveforms are damped sinusoids. These solutions are plotted in the state plane as shown in Fig. 10.5; they spiral into the stable focal point at $(1,0)$. The trajectories predicted by Eq. (10.2a) are shown as dotted lines in the left half-plane since Eq. (10.2a) is not valid for $x_1 < 0$.
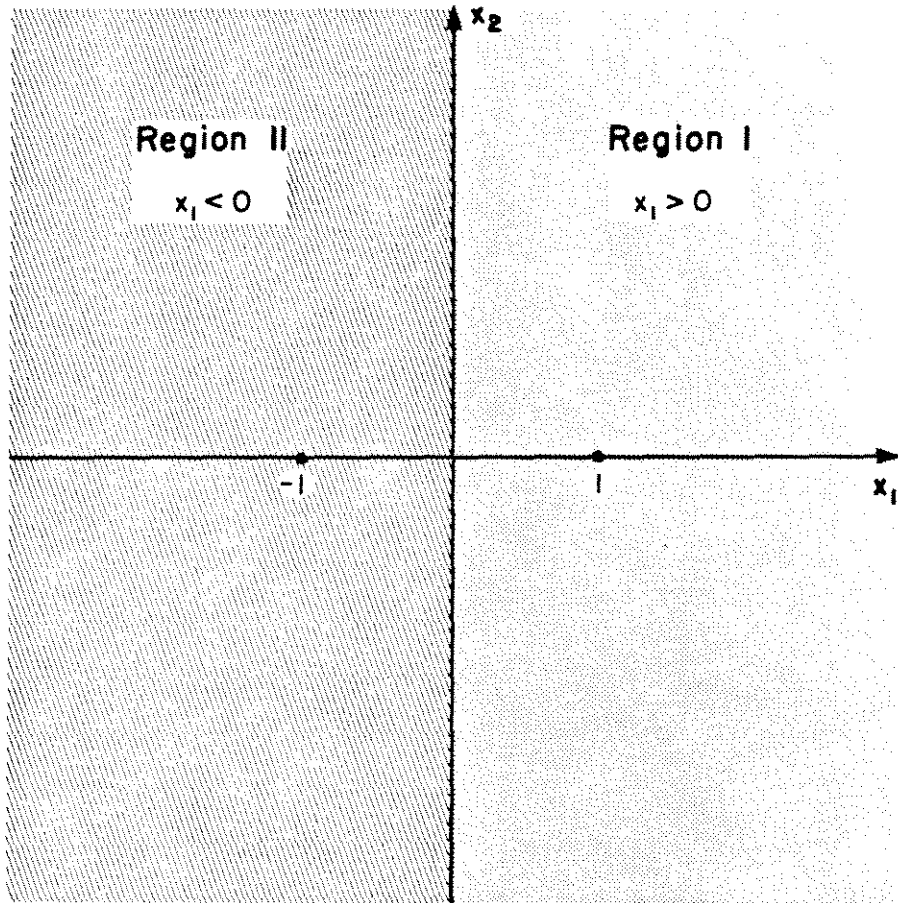
Fig. 10.4. The regions of the state plane for the system of Eq. (10.2). The right half-plane is described by Eq. (10.2a) and the left half-plane is described by Eq. (10.2b).
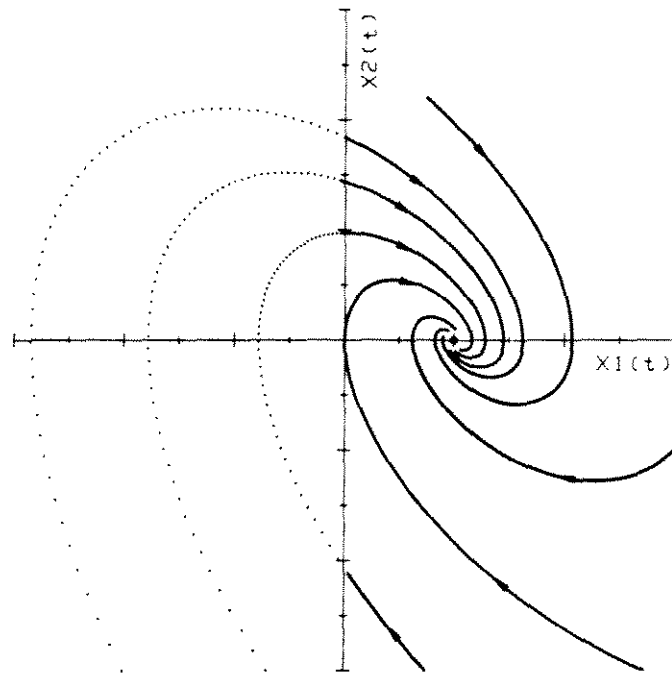
Fig. 10.5. The solutions of the state equations (10.2a) for the right half-plane are damped sinusoids; hence, the trajectories spiral into the stable focus at (1,0). These solutions are valid for $x_1 > 0$.
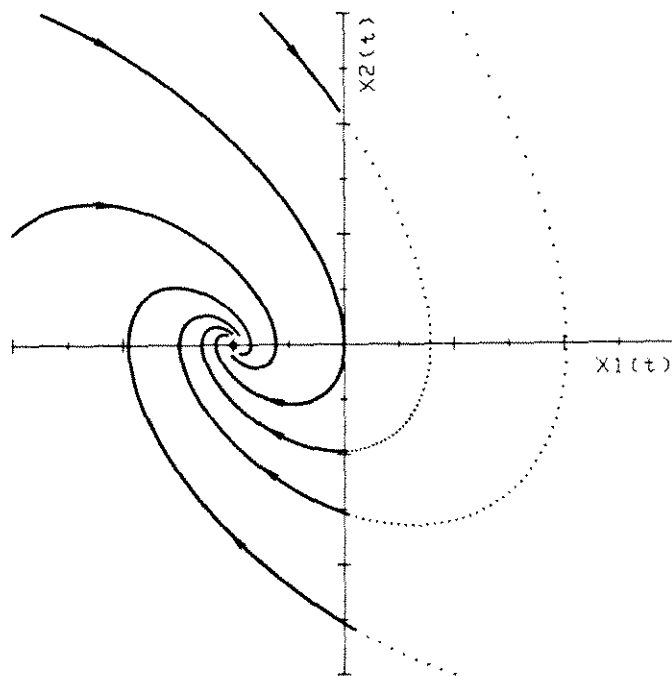
Fig. 10.6. The solutions of the state equations (10.2b) for the left half-plane are also damped sinusoids; the trajectories spiral into the stable focal point at (-1,0). These solutions are only valid for $x_1 < 0$.
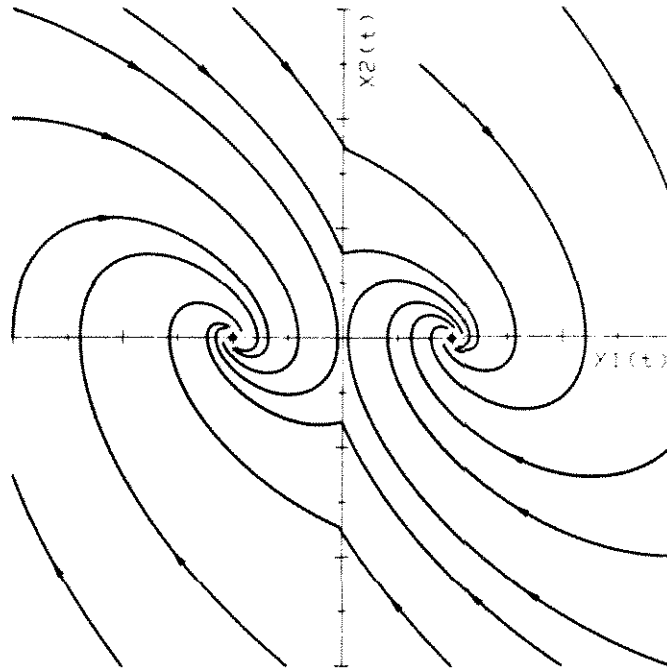
Fig. 10.7. *The complete state-plane portrait of the system of Eq. (10.2). Some trajectories converge to the stable equilibrium point (1,0), while the others converge to (-1,0).*

A similar analysis holds for $x_1 < 0$. In this case, Eq. (10.2b) is solved and the solutions plotted in the state plane as shown in Fig. 10.6. The trajectories spiral into the stable focal point at (-1,0). These solutions are not valid for $x_1 > 0$.

Figures 10.5 and 10.6 may now be combined as shown in Fig. 10.7 to obtain the state-plane portrait for the entire system. It can be seen that some trajectories converge to (1,0), while others converge to (-1,0). Thus, neither equilibrium point is globally stable.

As a second example, consider the system described by the following
state equations:

$$\dot{x}_1 = x_2$$
$$\dot{x}_2 = - x_1 - x_2 - 0.5 \qquad \text{for } x_1 > 0 \qquad (10.3a)$$

$$\dot{x}_1 = x_2$$
$$\dot{x}_2 = - x_1 - x_2 - 1 \qquad \text{for } x_1 < 0 \qquad (10.3b)$$

This system is similar to the system of Eq. (10.2), except the
equilibrium point at (1,0) has been moved to (-0.5,0).
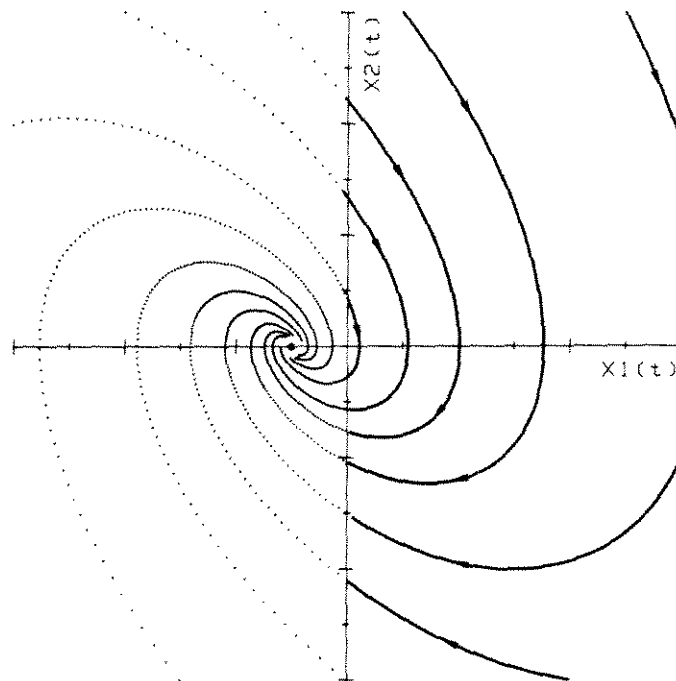
Fig. 10.8. The trajectories in the right half-plane for the second
example are described by Eq. (10.3a); they spiral towards
the virtual equilibrium point at (-0.5,0). These solutions
are only valid for $x_1 > 0$.

For $x_1 > 0$, the solutions are again damped sinusoids, and the trajectories tend to spiral into the focal point at (-0.5,0), as snown in Fig. 10.8. However, these trajectories leave the right half-plane where Eq. (10.3a) is valid before the focal point is reached; thus, the system is not actually in equilibrium at (-0.5,0). Instead, Eq. (10.3b) is invoked as x_1 becomes negative, and the solutions spiral into the stable equilibrium point at (-1,0) as shown in Fig. 10.9. It is apparent that this real equilibrium point (-1,0) is globally stable.

Because the point (-0.5,0) lies outside of the right half-plane where Eq. (10.3a) is valid, the system is not actually in equilibrium there. Such a point is called a "virtual equilibrium point". In this instance, the original system, described by Eq. (10.2), is not globally
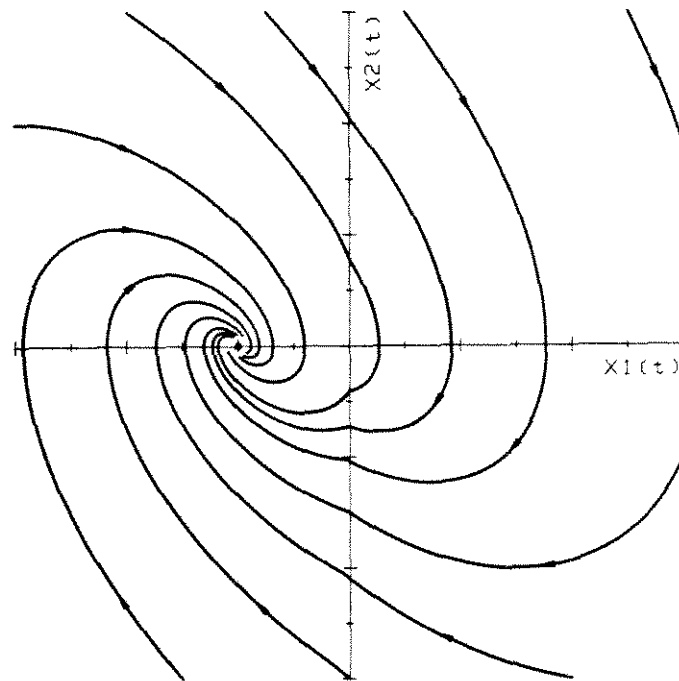
Fig. 10.9. The complete state-plane portrait of the system of Eq. (10.3). The real equilibrium point at (-1,0) is globally stable.

stable because it contains two real equilibrium points. However, movement of the equilibrium point of the right half-plane state equations into the left half-plane causes the system to contain one real equilibrium point and one virtual equilibrium point. The remaining real equilibrium point at (-1,0) then becomes globally stable.

Although it is necessary to eliminate all extra real equilibrium points before a well-behaved globally stable system is obtained, simply changing these extra real equilibrium points into virtual ones is not always sufficient. For example, consider the system

$$\left.\begin{array}{l} \dot{x}_1 = x_2 + 0.5 \\[2mm] \dot{x}_2 = - x_1 - 0.5 \, x_2 - 0.55 \end{array}\right\} \quad \text{for } x_1 > 0 \qquad (10.4a)$$

$$\left.\begin{array}{l} \dot{x}_1 = x_2 - 0.5 \\[2mm] \dot{x}_2 = - x_1 - 0.5 \, x_2 - 0.55 \end{array}\right\} \quad \text{for } x_1 < 0 \qquad (10.4b)$$

The state equations for the left half-plane now contain a real stable equilibrium point at (-0.3,0.5) and the state equations for the right half-plane contain a virtual equilibrium point at (-0.3,-0.5).

Equations (10.4) may be solved by the same procedure used for the previous two examples. The trajectories for the left half-plane spiral into the stable focal point at (-0.3,0.5), as shown in Fig. 10.10a, and the trajectories for the right half-plane tend to spiral into the virtual focal point at (-0.3,-0.5), as shown in Fig. 10.10b. Combination of Figs. 10.10a and 10.10b then yields the complete system trajectories shown in Fig. 10.11. It can be seen that solutions in the
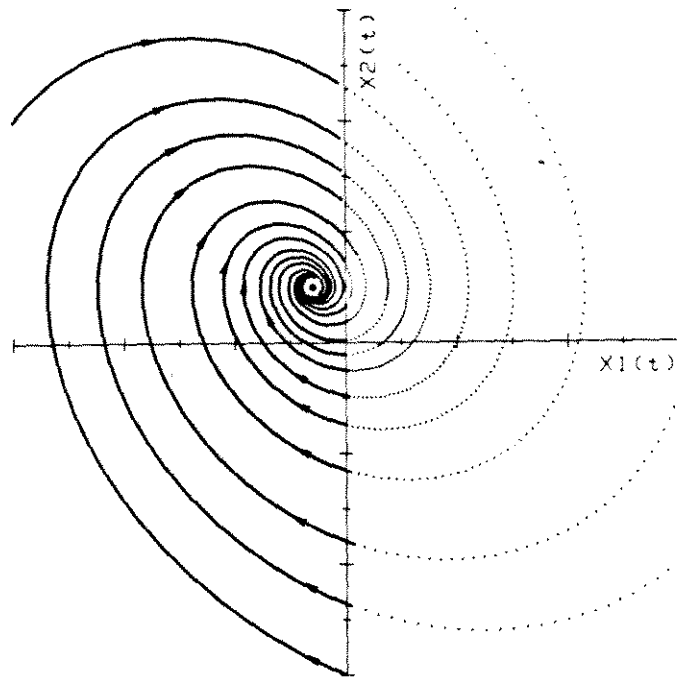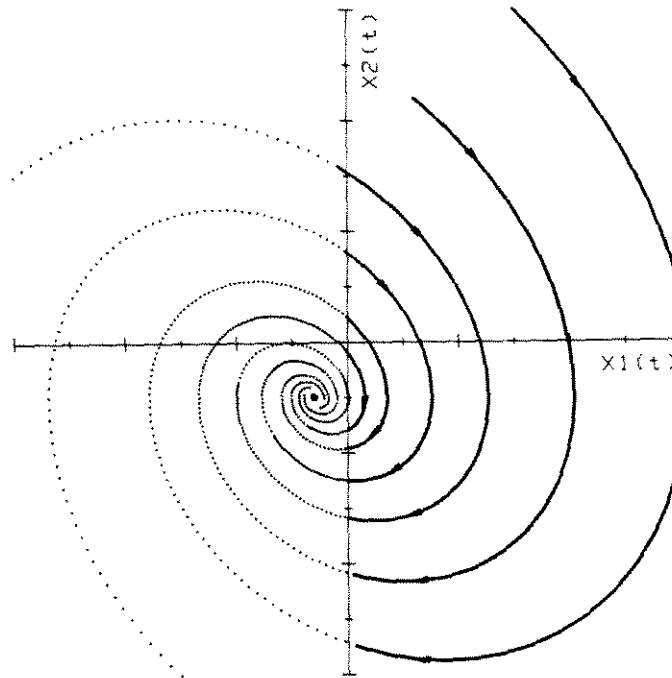
Fig. 10.10. The trajectories for the third example described by Eq. (10.4). (a) The solutions of the state equations which describe the left half-plane spiral into the stable focal point at (-0.3,0.5). These solutions are not valid for $x_1 > 0$. (b) The solutions of the state equations which describe the right half-plane spiral towards the virtual equilibrium point at (-0.3,-0.5). These solutions are not valid for $x_1 < 0$.
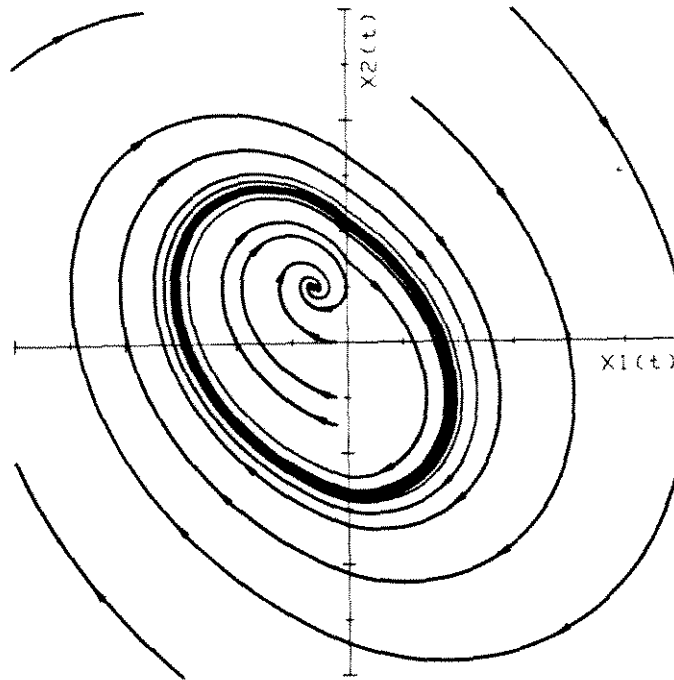
Fig. 10.11. The complete state-plane portrait of the system of Eq. (10.4). Some trajectories converge to the stable equilibrium point (-0.3,0.5), while others converge to a stable limit cycle. The real equilibrium point (-0.3,0.5) is not globally stable.

vicinity of the real equilibrium point at (-0.3,0.5) converge there, but all other solutions enter a stable limit cycle instead. Thus, this system is not globally stable.

It is evident that the fact that a piecewise system contains exactly one real equilibrium point, which is locally stable, is not sufficient to guarantee global stability. Nonetheless, it is necessary to eliminate all extra real equilibrium points in order to obtain a well-behaved system. Since it is fairly simple to obtain analytical expressions for the positions of the equilibrium points in the state plane, a reasonable design procedure is to first position the equilibrium points of the system such that all except the desired quiescent operating point are virtual. The system trajectories are

then constructed, either by computer as detailed in Chapter 12, or by approximate methods as described in Chapter 13. This either provides verification that all transient solutions are stable and well-behaved, or it reveals the presence of a limit cycle and indicates that further modifications are necessary.

10.3 The Switching Regulator Problem In More Detail

The regions of operation of a typical switching regulator are shown in Fig. 10.12. The particular configuration used in this example is the same simple boost regulator studied in detail in Chapter 13. The system operates in the usual unsaturated mode in the vicinity of the quiescent operating point (I_0, V_0) (region 1 in the figure). The state equations are nonlinear in this region, and more than one real equilibrium point may occur here. Next, the saturation of the pulse-width modulator causes the duty ratio to remain fixed, at its minimum value in region 2 and at its maximum value in region 3. The state equations are linear in both of these regions; hence, each region contains a single equilibrium point which may be real or virtual. Region 4 is the transient discontinuous conduction mode, described by yet another set of nonlinear differential equations. Regions 1, 2, 3, and 4 occur naturally in most switching regulators. A fifth region of operation is usually added as shown in an attempt to limit the peak current levels which the system must endure. The state equations which describe this region are usually nonlinear also. Thus, a typical system contains many regions of operation and is described by piecewise state equations.
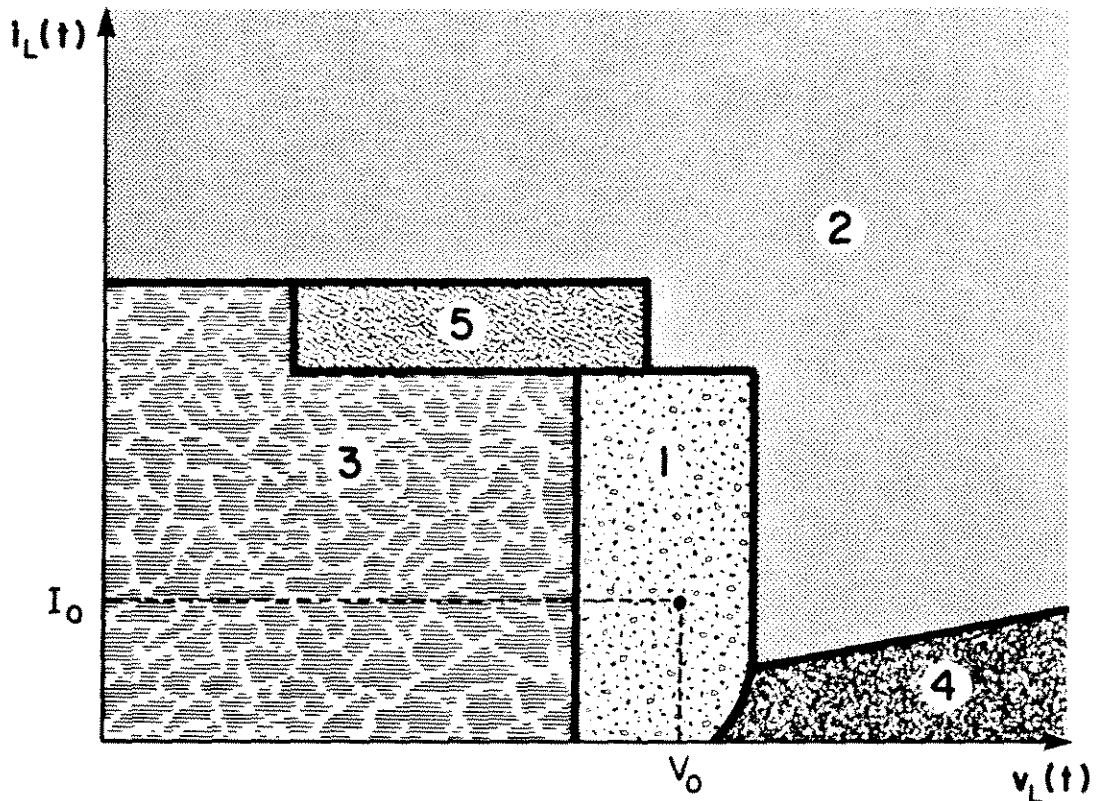
*Fig. 10.12. The regions of operation of a typical boost regulator:
(1) unsaturated region; (2) D = 0 saturated region;
(3) D = 1 saturated region; (4) transient discontinuous
conduction mode; (5) current limiting mode.*

It is apparent that a transient analysis of even the simplest
practical switching regulator may become very complex and involved.
To be effectively designed, the system must first be analyzed in a
systematic way. First, the various regions must be identified, their
boundaries constructed, and the state equations determined. This is
done in the next chapter. The key "linear ripple approximation" used
in previous small-signal analyses [1,2,41] is used here to obtain more
lucid results. The transient solutions should then be somehow
constructed, and analytic expressions found for all salient features
which allow the intelligent design of the system. Owing to the
piecewise nonlinear nature of the system, this is a difficult problem
in general. For second order systems, the state plane is an efficacious

tool and is employed in the chapters which follow. The trajectories
can be easily found, and the effect of modifications such as the
addition of a current limiting mode or limiting the maximum duty ratio
is apparent. Unfortunately, the general higher order system is much
more difficult to design. Analytical expressions for the locations
of the equilibrium points may still be determined and used to position
them properly; but, as noted in the previous section, this is not
sufficient to guarantee global stability. The solutions may, however,
be found by computer methods; this allows the verification of global
stability and the determination of peak transient voltages and currents.
The modifications necessary to obtain a well-behaved system then
become apparent.

CHAPTER 11

LARGE-SIGNAL MODELLING

11.1 Introduction

In this section, the nonlinear state equations which describe switching regulators operating in the continuous conduction mode are derived, and the regions of their validity are identified. Two versions of the model are useful. First, a discrete-time model is found which is suitable for computer simulation. Second, an additional approximation is made which yields a continuous-time model; this model is often more convenient for analytical calculations. Both models incorporate the key "linear-ripple approximation" used in previous small-signal methods [1,2,11,47,48]. However, no small-signal assumption is made; as a result, the method is valid for large signals.

Next, the saturation characteristics of the pulse-width modulator are accounted for. The duty ratio is always restricted to lie in a range no greater than [0,1], and the effect of this restriction on the stability of the regulator is so profound that no large-signal analysis can ignore it. Another mode may also occur, known as the discontinuous conduction mode [2,50]. This mode is modelled for transient conditions. The result of this section is the formulation of basic state equations which model the switching regulator and which are used in the subsequent sections to determine stability regions and peak transient component stress levels.

11.2 Unsaturated Region Model

The first step is to write the state equations of the regulator system during the two switched intervals DT_s and $D'T_s$. During each interval, the system may be described by a set of linear differential equations:

during interval DT_s (transistor ON)

$$K \frac{d\underline{x}(t)}{dt} = A_1 \underline{x}(t) + B_1 \underline{u} \tag{11.1}$$

during interval $D'T_s$ (transistor OFF)

$$K \frac{d\underline{x}(t)}{dt} = A_2 \underline{x}(t) + B_2 \underline{u} \tag{11.2}$$

where D = duty ratio $D' = 1 - D$.

T_s = time of one complete switching period.

K is a matrix usually containing values of inductance and capacitance.

$\underline{x}$ is a state vector, usually comprised of inductor currents and capacitor voltages.

$\underline{u}$ is a vector of independent sources.

These equations may be solved exactly; however, the subsequent analysis is greatly simplified if the "linear-ripple approximation" [1,2,11,47,48] is made. Specifically, if the natural frequencies ω_i of the converter power stage are all well below the switching

frequency, then Eqs. (11.1) and (11.2) above have approximately linear solutions. This is indeed the case in well-designed converters, in which the switching ripple is much smaller than the average value. In this case, only the terms to order $(\omega_i T_s)$ need be considered; higher-order terms are negligible. This corresponds to the approximation of the exponential matrix by the zero-order and first-order terms in its series expansion.

The result of this approximation is the following solutions for $\underline{x}(t)$ during the two switched intervals:

$$\underline{x}(t) = (I + K^{-1}A_1 t)\ \underline{x}(0) + K^{-1}B_1\underline{u}t \tag{11.3}$$

during $0 \le t \le DT_s$

$$\underline{x}(t) = (I + K^{-1}A_2(t - DT_s))\ \underline{x}(DT_s) + K^{-1}B_2\underline{u}\ (t - DT_s)$$

during $DT_s \le t \le T_s$ \hfill (11.4)

Combination of Eqs. (11.3) and (11.4) and elimination of the second-order terms which appear yields the following expression for $\underline{x}(T_s)$:

$$\underline{x}(T_s) = [I + T_s K^{-1}(DA_1 + D'A_2)]\underline{x}(0) + T_s K^{-1}(DB_1 + D'B_2)\underline{u} \tag{11.5}$$

Furthermore, after n + 1 switching intervals,

$$\underline{x}((n + 1)T_s) = \underline{x}_{n+1} = [I + T_s K^{-1}(D_n A_1 + D_n' A_2)]\underline{x}_n$$

$$+ T_s K^{-1}[D_n B_1 + D_n' B_2]\underline{u} \qquad (11.6)$$

This is the basic difference equation which describes the response of the system. It contains a constant term; hence, the system is not in equilibrium at the origin. It is convenient in the analysis which follows to redefine the axes so that the quiescent operating point of the regulator is at the origin. The quiescent operating point occurs at:

$$\underline{x}_{n+1} = \underline{x}_n = \underline{X}_0, \qquad D_{n+1} = D_n = D_0 \qquad (11.7)$$

Insertion of Eq. (11.7) into Eq. (11.6) and solution for $\underline{X}_0$ yields

$$\underline{X}_0 = - (D_0 A_1 + D_0' A_2)^{-1} (D_0 B_1 + D_0' B_2)\underline{u} \qquad (11.8)$$

The axes may now be shifted by use of the substitution below.

$$\underline{x}_n = \underline{X}_0 + \hat{\underline{x}}_n, \qquad D_n = D_0 + \hat{d}_n \qquad (11.9)$$

$$\hat{\underline{x}}_{n+1} = [I + T_s K^{-1}(D_0 A_1 + D_0' A_2)]\hat{\underline{x}}_n + T_s K^{-1}[(A_1 - A_2)\underline{X}_0 + (B_1 - B_2)\underline{u}]\hat{d}_n$$

$$+ T_s \hat{d}_n K^{-1}(A_1 - A_2)\hat{\underline{x}}_n \qquad (11.10)$$

Eq. (11.10) arises from the substitution of Eq. (11.9) into Eq. (11.6), and is the difference equation which describes the regulator while operating in the normal, unsaturated mode. No small-signal assumption has been made; hence, Eq. (11.10) is valid for large signals.

The duty ratio is usually a linear function of the regulator states. In this case,

$$\hat{d}_n = - \underline{f}^T \hat{\underline{x}}_n \qquad (11.11)$$

where $\underline{f}$ = feedback gain vector.

As a result of the linear dependence of $\hat{d}_n$ on $\hat{\underline{x}}_n$, the $T_s \hat{d}_n(A_1 - A_2)\hat{\underline{x}}_n$ term in Eq. (11.10) is quadratic, and the difference equation is nonlinear. This nonlinearity can seriously degrade the transient response of the regulator, possibly causing instabilities.

The discrete form of Eq. (11.10) and (11.11) makes them ideally suited for evaluation by computer. It is a simple matter to implement these equations on a small desktop computer and obtain the large-signal transient response of any switching regulator operating in the unsaturated region. In view of the difficulty of obtaining a closed-form analytical solution to Eq. (11.10) under transient conditions, this is an attractive alternative. Some of the time domain waveforms illustrated in this thesis were obtained in this manner.

Although the discrete equations above are well-suited for digital
computer evaluation, they are sometimes inconvenient for analytical
calculations. It is then preferred to obtain a continuous-time model
which contains familiar R's, L's, C's, and nonlinear devices, and hence
yields physical insight into the design problem. This has
previously been accomplished for the small-signal case [1,2,11], and the
same technique is applicable here. In particular, one uses a
forward-differencing approximation to estimate the continuous-time
derivative of the state vector, as below:

$$\frac{d\underline{x}(t)}{dt} \simeq \frac{\hat{\underline{x}}_{n+1} - \hat{\underline{x}}_n}{T_s} \tag{11.12}$$

This approximation is valid if all natural frequencies of the closed-
loop regulator are much less than the switching frequency. With this
approximation, Eq. (11.10) becomes

$$K \frac{d\hat{\underline{x}}(t)}{dt} = (D_0 A_1 + D_0' A_2)\hat{\underline{x}}(t) + [(A_1 - A_2)\underline{X}_0 + (B_1 - B_2)\underline{u}]\hat{d}(t)$$

$$+ \hat{d}(t) (A_1 - A_2)\hat{\underline{x}}(t) \tag{11.13}$$

with $\hat{d}(t) = - \underline{f}^T \hat{\underline{x}}(t)$

This is a continuous-time state equation which describes the
regulator while operating in the normal, unsaturated mode. It can be
used to infer the nature of the response to large perturbations and the
existence of instabilities. Owing to the presence of the $\hat{d}(A_1 - A_2)\hat{\underline{x}}$

term, this state equation contains quadratic nonlinear terms.

Thus, the equations which describe the response of switching regulators during large transients have been found for the case where the pulse-width modulator is unsaturated and the system operates in its usual mode. The linear-ripple approximation was made; this has the desirable effect of simplifying the analysis while ignoring the usually negligible effect of the high frequency switching ripple. A set of discrete state equations with quadratic nonlinearities is the result; these equations are well-suited for computer evaluation of the large-signal transient response. An additional approximation may be made which yields a continuous-time version of the state equations. This is often desirable for analytical design.

11.3 Saturated Region Models

So far, it has been assumed that the regulator always operates in its usual unsaturated mode. No account has yet been made of the inherent limits on the duty ratio: the duty ratio must always lie within the range [0,1]; often, the limit is even more restrictive. Outside the usual operating range, the duty ratio remains constant at its saturated value, and the regulator behaves as an open-loop linear system. This can significantly affect the large-signal stability of the regulator; in consequence, these additional modes of operation cannot be ignored. Some aspects of this effect have been previously considered [51,52,53]; the phenomenon is further investigated here.
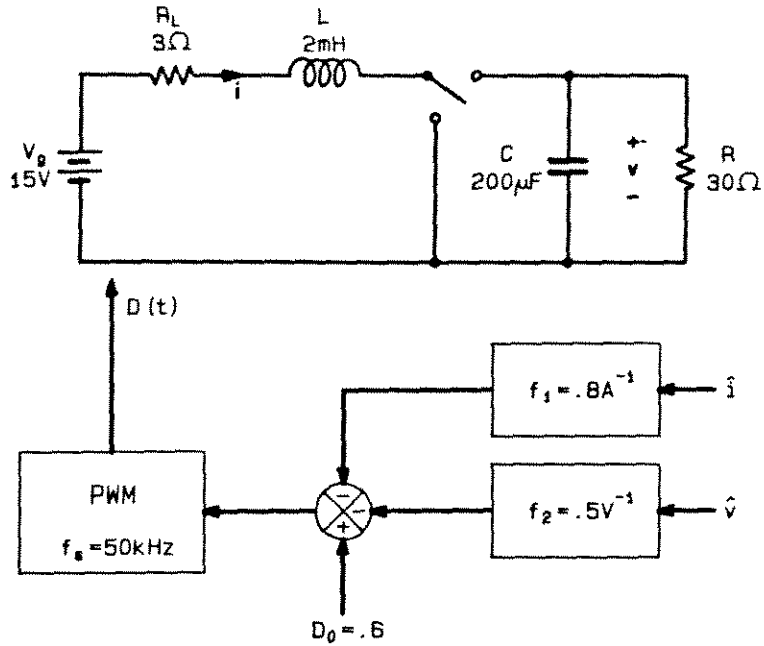
Fig. 11.1. Two-state boost regulator example.

As an example, consider the two-state boost regulator of Fig. 11.1.
In order to stabilize the system in the presence of the right-half
plane zero which appears in the small-signal duty-ratio-to-output
transfer function, the inductor current is fed back in addition to the
output voltage. The expression for the control signal (duty ratio) is
therefore

$$D(t) = D_0 + \hat{d}(t)$$

$$\hat{d}(t) = - f_1 \hat{i}_L - f_2 \hat{v}_c = - \underline{f}^T \underline{\hat{x}} \qquad (11.14)$$

where D_0 = quiescent duty ratio

f_1 = current feedback gain

f_2 = voltage feedback gain
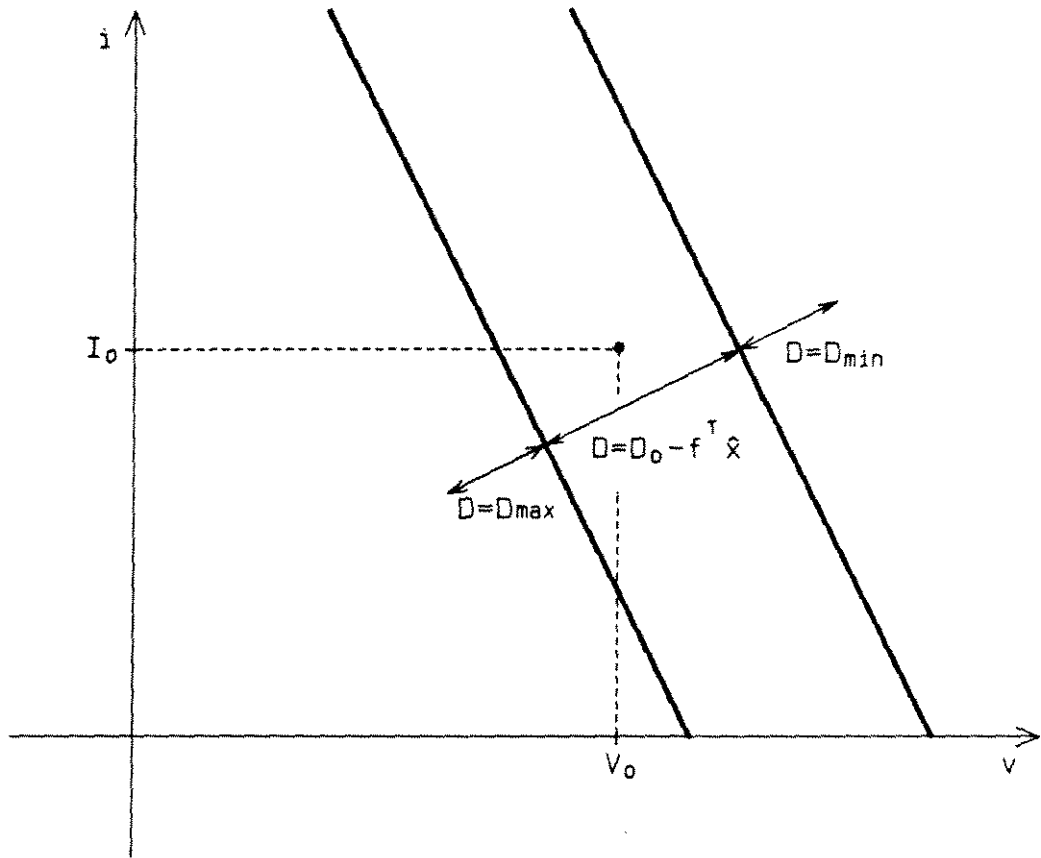
Fig. 11.2. The saturated and unsaturated regions of the state plane. I_0 and V_0 are the quiescent inductor current and capacitor voltage.

If $D(t)$ is limited to the range $[D_{min}, D_{max}]$ then the unsaturated region is the section of the plane where

$$D_{min} < D_0 - \underline{f}^T\underline{\hat{x}} < D_{max} \qquad (11.15)$$

To the left of this region, the duty ratio is fixed and equal to D_{max}, and to the right of this region, the duty ratio is fixed and equal to D_{min}. The situation is illustrated in Fig. 11.2.

The state equations in the saturated regions are easily found. When $-\underline{f}^T\underline{\hat{x}}$ is greater than $D_{max} - D_0$, then $D(t)$ is constant and equal to D_{max}. Likewise, $D(t)$ is constant and equal to D_{min} when $-\underline{f}^T\underline{\hat{x}}$ is less

than $D_{min} - D_0$. Substitution of $D_n = D_{sat}$ into (11.6) yields

$$\underline{x}_{n+1} = [I + T_s K^{-1}(D_{sat}A_1 + D'_{sat}A_2)]\underline{x}_n + T_s K^{-1}[D_{sat}B_1 + D'_{sat}B_2]\underline{u}$$

where D_{sat} = either D_{max} or D_{min} (11.16)

$$D'_{sat} = 1 - D_{sat}$$

This is a system of linear difference equations which describe the response of the system in the saturated regions.

The continuous-time state equations are again found by use of the forward-differencing approximation. The result for the $D = D_{sat}$ saturated region is

$$K \frac{d\underline{x}(t)}{dt} = [D_{sat}A_1 + D'_{sat}A_2]\underline{x}(t) + [D_{sat}B_1 + D'_{sat}B_2]\underline{u} \qquad (11.17)$$

This is a system of linear differential equations which describes the response in the $D = D_{sat}$ saturated region. Since the systems described by Eq. (11.16) and (11.17) are linear their solutions are exponential in nature. Furthermore, they contain exactly one equilibrium point. This point occurs at

$$\underline{x}_0 = - [D_{sat}A_1 + D'_{sat}A_2]^{-1}[D_{sat}B_1 + D'_{sat}B_2]\underline{u} \qquad (11.18)$$

This equilibrium point may or may not occur within the saturated region.

Thus, three modes of operation have been identified which occur in any ideal switching regulator. This change of operating mode is a result of the saturation of the pulse-width modulation process. The regions in the state plane in which each mode occurs have been found, and the relevant equations have been derived. In each saturated mode, the system state equations become linear.

11.4 Transient Discontinuous Conduction Region Model

The practical switching regulator exhibits a fourth mode of operation called the *transient discontinuous conduction mode*. It is a consequence of the nonideal realization of the switch by a single transistor and diode, as in Fig. 11.3. The diode does not allow the inductor current to become negative; instead, the diode becomes reverse-biased prematurely. As a result, three switched intervals occur, as in Fig. 11.4. As in the continuous conduction case, the transistor conducts during interval DT_s, and the diode conducts during interval $D_2 T_s$. However, when the inductor current reaches zero,
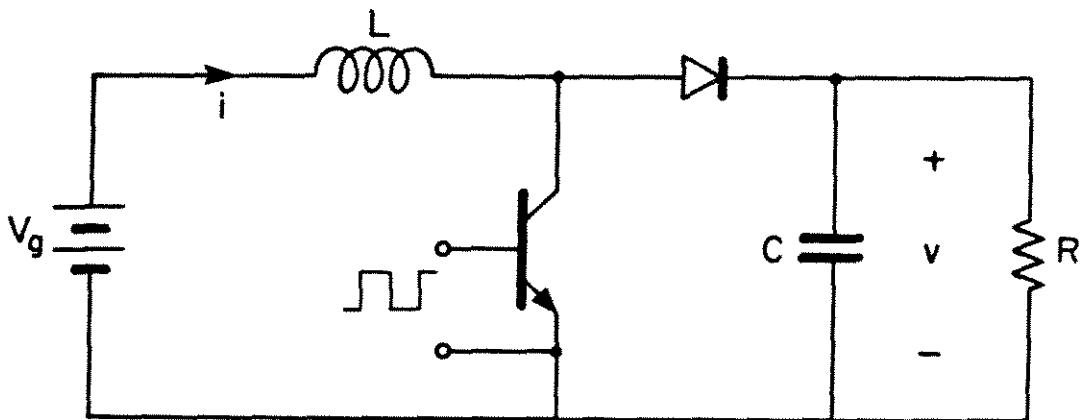
Fig. 11.3. The nonideal realization of the switch by a single transistor and diode causes the discontinuous conduction mode to occur.
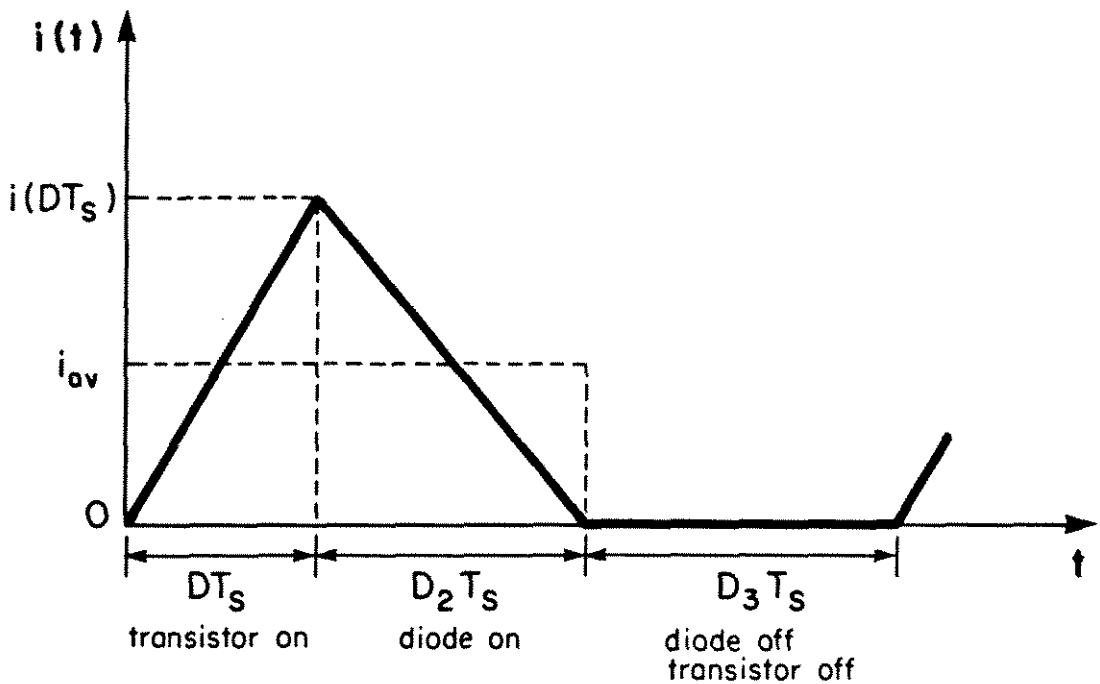
Fig. 11.4. *Inductor current waveforms during the discontinuous
conduction mode. An additional switched interval D_3T_s
occurs during which both transistor and diode are off.*

the diode ceases to conduct; hence, both transistor and diode remain

off during interval D_3T_s.

The discontinuous conduction mode has been previously modelled

under steady-state and small-signal conditions [2,42,50,54]. This

analysis can be extended without difficulty to include large-signal

phenomena. In essence, one follows all of the steps of the small-signal

state-space averaging procedure, including the modifications necessary

for the discontinuous conduction mode, with the exception of the

small-signal approximation itself.

As in the continuous conduction mode, the first step is to write
the state equations of the regulator system during the various
switched intervals. During each interval, the system is described by a
set of linear differential equations:

during interval DT_s (transistor ON, diode OFF)

$$\frac{d\underline{x}(t)}{dt} = A_1 \underline{x}(t) + B_1\underline{u} \tag{11.19}$$

during interval D_2T_s (transistor OFF, diode ON)

$$\frac{d\underline{x}(t)}{dt} = A_2 \underline{x}(t) + B_2\underline{u} \tag{11.20}$$

during interval D_3T_s (transistor OFF, diode OFF)

$$\frac{d\underline{x}(t)}{dt} = A_3 \underline{x}(t) + B_3\underline{u} \tag{11.21}$$

where D = duty ratio applied to transistor switch,

$$D + D_2 + D_3 = 1 \tag{11.22}$$

It is desired to solve the above equations by use of the
linear-ripple approximation, as was done for the continuous conduction
mode case. Unfortunately, a difficulty arises in that the inductor
current ripple is large compared to its average value; as a result,
the higher-order terms which arise from the inductor current ripple
are significant. This is dealt with in [2] by averaging the inductor
current over each switched interval. It is then a good approximation
to replace the instantaneous inductor current in the state equations
by this average current, provided that the switching ripples on the
other states in the system are much smaller than the average values.
This is a consequence of the requirement that the natural frequencies
of the system be much smaller than the switching frequency: if the
capacitor voltages change sufficiently slowly, then they react only
to the average inductor current rather than the instantaneous current.

Hence, one must treat the discontinuous variable, the inductor
current, differently from the other voltages and currents in the
system. This is accomplished by partitioning the state vector and
matrices as follows. Let

$$\underline{x}(t) = \begin{bmatrix} i(t) \\ --- \\ \underline{\xi}(t) \end{bmatrix} \qquad (11.23)$$

where $i(t)$ is the discontinuous state variable and $\underline{\xi}(t)$ is a vector
which contains the remaining state variables.

Also let

$$
A_i = \left[\begin{array}{c|c} a_i & \underline{\zeta}_i^T \\ \hline & \\ \underline{\gamma}_i & A_i \\ & \end{array} \right]
$$

$$
B_i = \left[\begin{array}{c} \underline{\beta}_i^T \\ \hline \\ B_i \end{array} \right]
\tag{11.24}
$$

Hence, with the approximation described above, the solution of Eq. (11.19) becomes

$$
i(DT_s) \cong (1 + DT_s a_1) \, i(0) + DT_s \underline{\zeta}_1^T \, \underline{\xi}(0) + DT_s \underline{\beta}_1^T \underline{u}
\tag{11.25}
$$

$$
\underline{\xi}(DT_s) \cong (I + DT_s A_1) \, \underline{\xi}(0) + DT_s \underline{\gamma} \, <i>_{DT_s} + DT_s B_1 \underline{u}
\tag{11.26}
$$

where $<i>_{DT_s}$ = inductor current averaged over interval DT_s

The average inductor current is found with the assumption of linear ripple:

$$
<i>_{DT_s} \cong (i(0) + i(DT_s))/2
\tag{11.27}
$$

Similar expressions result for interval D_2T_s:

$$i((D + D_2)T_s \cong (1 + D_2T_sa_2) \; i(DT_s) + D_2T_s \; \underline{\xi}_2^T \; \underline{\xi}(DT_s) + D_2T_s \; \underline{\beta}_2^T \underline{u}$$

$$(11.28)$$

$$\underline{\xi}((D + D_2)T_s \cong (I + D_2T_sA_2) \; \underline{\xi}(DT_s) + D_2T_s \; \underline{\gamma}_2 \; <i>_{D_2T_s} + D_2T_sB_2\underline{u}$$

$$(11.29)$$

with $<i>_{D_2T_s}$ = inductor current averaged over interval D_2T_s:

$$<i>_{D_2T_s} \cong (i(DT_s) + i((D + D_2)T_s))/2 \qquad (11.30)$$

The expressions for interval D_3T_s are simpler, since the inductor current is zero during this interval. Hence,

$$i(T_s) \equiv 0 \qquad (11.31)$$

$$\underline{\xi}(T_s) \cong (I + D_3T_sA_3) \; \underline{\xi}((D + D_2)T_s) + D_3T_sB_3\underline{u} \qquad (11.32)$$

$$<i>_{D_3T_s} \equiv 0 \qquad (11.33)$$

One final simplification can be made. During the first interval in which the system enters the transient discontinuous conduction mode,

the initial inductor current i(0) is not necessarily zero. However, for all subsequent switching cycles in the discontinuous mode, i(0) is necessarily zero. Also, since $i((D + D_2)T_s)$ is by definition zero, Eqs. (11.27) and (11.30) reduce to

$$<i>_{DT_s} = <i>_{D_2 T_s} = i(DT_s)/2 \triangleq i_{av} \tag{11.34}$$

Thus, the average inductor current during interval DT_s and $D_2 T_s$ is the same and is equal to i_{av}.

Combination of Eqs. (11.26), (11.29), and (11.32), and elimination of the second- and third-order terms which appear yields

$$\underline{\xi}(T_s) = [I + T_s(DA_1 + D_2 A_2 + D_3 A_3)]\underline{\xi}(0) + T_s[DB_1 + D_2 B_2 + D_3 B_3]\underline{u}$$

$$+ T_s[D\underline{\gamma}_1 + D_2\underline{\gamma}_2] \, i_{av} \tag{11.35}$$

with $\quad i_{av} = DT_s[\underline{\zeta}_1^T \, \underline{\xi}(0) + \underline{\beta}_1^T \underline{u}] \tag{11.36}$

Furthermore, after n + 1 switching intervals,

$$\underline{\xi}((n + 1)T_s) = \underline{\xi}(n + 1) = [I + T_s(D(n)A_1 + D_2(n)A_2 + D_3(n)A_3)]\underline{\xi}(n)$$

$$+ T_s[D(n)B_1 + D_2(n)B_2 + D_3(n)B_3]\underline{u} + T_s [D(n)\underline{\gamma}_1 + D_2(n)\underline{\gamma}_2] \, i_{av}(n)$$

$$\tag{11.37}$$

with $\qquad i_{av}(n) = D(n)T_s [\underline{\zeta}_1^T \underline{\xi}(n) + \underline{\beta}_1^T\underline{u}]/2$ $\qquad\qquad$ (11.38)

One additional constraint is required which reflects the fact that interval D_2T_s ends when the instantaneous inductor current falls to zero. Combination of equations (11.25) and (11.28), and elimination of second-order terms yields

$$i((D + D_2)T_s) = (1 + T_s(Da_1 + D_2a_2)) \, i(0) + T_s(D\underline{\zeta}_1^T + D_2\underline{\zeta}_2^T)\underline{\xi}(0)$$

$$+ \, T_s(D\underline{\beta}_1^T + D_2\underline{\beta}_2^T)\underline{u}$$

$$\equiv 0 \qquad\qquad (11.39)$$

Furthermore, after $n + 1$ switching intervals, $i(0) = 0$. One then obtains

$$0 = (D(n)\underline{\zeta}_1^T + D_2(n)\underline{\zeta}_2^T) \, \underline{\xi}(n) + (D(n)\underline{\beta}_1^T + D_2(n)\underline{\beta}_2^T)\underline{u} \qquad (11.40)$$

Equations (11.37), (11.38), and (11.40) are the basic difference equations which describe the response of the system in the transient discontinuous conduction mode. Because of their discrete form, they are well-suited for computer evaluation. As noted in [2], the system contains one less independent state than the usual in this mode because the inductor current is constrained to zero at the end of each switching cycle. This system is in general nonlinear.

It is sometimes preferred to obtain a continuous-time model for this mode of operation. This can be done by application of the same technique used for the continuous conduction mode model in Section 11.2.

In particular, one uses the Euler forward-differencing approximation to estimate the continuous-time derivative of the state vector, as follows:

$$\frac{d\underline{\xi}(t)}{dt} \cong \frac{\underline{\xi}_{n+1} - \underline{\xi}_n}{T_s} \tag{11.41}$$

With this approximation, Eqs. (11.37), (11.38), and (11.40) become

$$\frac{d\underline{\xi}(t)}{dt} = [DA_1 + D_2A_2 + D_3A_3]\underline{\xi}(t) + [DB_1 + D_2B_2 + D_3B_3]\underline{u}$$

$$+ [D\underline{\gamma}_1 + D_2\underline{\gamma}_2] \, i_{av}(t) \tag{11.41}$$

$$i_{av}(t) = \frac{D(t) \, T_s}{2} [\underline{\varsigma}_1^T\underline{\xi}(t) + \underline{\beta}_1^T\underline{u}] \tag{11.42}$$

$$0 = [D(t)\underline{\varsigma}_1^T + D_2(t)\underline{\varsigma}_2^T]\underline{\xi}(t) + [D(t)\underline{\beta}_1^T + D_2(t)\underline{\beta}_2^T]\underline{u} \tag{11.43}$$

These are the continuous-time equations which describe the regulator while operating in the transient discontinuous mode. The system is quite nonlinear in this region since the duty ratio $D(t)$ is, through the use of negative feedback, made dependent on the states of the system $\underline{\xi}(t)$ as well as on the inductor current $i(t)$.

The transient discontinuous conduction mode boundary can be easily found. The discontinuous mode occurs whenever the predicted length of interval D_2T_s is shorter than $(1 - D)T_s$. D_2 may be found by solution

of scalar equation (11.39); use of the criterion $D_2 < 1 - D$ then yields

$$i(0) < -T_s \frac{[D\underline{\zeta}_1^T + D'\underline{\zeta}_2^T]\underline{\xi}(0) + [D\underline{\beta}_1^T + D'\underline{\beta}_2^T]\underline{u}}{[1 + DT_s a_1 + D'T_s a_2]} \tag{11.44}$$

where $D' \triangleq 1 - D$

The system will operate in the transient discontinuous conduction mode during any switching cycle in which inequality (11.44) is satisfied. Note that this boundary is a function of all of the states of the system, $\underline{\xi}(0)$, as well as of the duty ratio D. Thus, the boundary may be a fairly complicated curve in the state plane. For example, it is shown in Chapter 13 for a boost regulator example that the boundary is parabolic in the unsaturated region and linear in the saturated regions.

Thus, the equations which describe the response of switching regulators during large transients have been found for the case where the system operates in the discontinuous conduction mode. The analysis is similar to the continuous conduction mode analysis, except that special care must be taken to reflect the fact that the inductor current ripple is large compared to its average value. This is dealt with by the use of the average inductor current, rather than the initial inductor current, in the state equations for each interval. A set of discrete nonlinear state equations is the result; these equations are well-suited for computer evaluation of the large-signal transient response. An additional approximation may be made which yields a continuous-time version of the state equations, as is sometimes

desired for analytical design. The region in the state plane in which this mode occurs has been found. In the next chapter, the models of this chapter are applied to the study of the large-signal transient waveforms and instabilities which are likely to occur in switching regulators.

CHAPTER 12

LARGE-SIGNAL ANALYSIS

12.1 Introduction

The objective of this chapter is the construction of the system response and the identification of sources of potential instability. First, the equilibrium points of the system are calculated. It is possible for more than one equilibrium point to exist, and this can lead to instability under large transient conditions. Second, the trajectories of the states of the regulator are determined, either by hand or by computer. The salient features are identified, and it then becomes apparent how to modify the system in order to obtain an acceptable response. The analysis is demonstrated on the boost regulator of Fig. 11.1.

12.2 Equilibrium Points in the Unsaturated Mode

The equilibrium points of a system are the most prominent features of the state-plane portrait of a nonlinear system. Calculation of the equilibrium points is a useful tool for pinpointing the source of instabilities and for constructing trajectories.

Two types of equilibrium points can exist for a given region of the state plane. The first type, known as a "real equilibrium point," is an equilibrium point which occurs inside the given region. The presence of real equilibrium points in addition to the desired quiescent operating point guarantees the presence of at least one unstable

solution. Hence, such points must be avoided. The second type is called a "virtual equilibrium point" and occurs outside the given region. The system is not actually in equilibrium at a virtual equilibrium point; nonetheless, these points can influence the transient response of the regulator. The presence of virtual equilibrium points guarantees neither the existence nor the absence of unstable transient responses.

Equilibrium points occur where

$$\hat{\underline{x}}^*_{n+1} = \hat{\underline{x}}^*_n \qquad \text{(discrete)} \qquad (12.1)$$

$$\frac{d\hat{\underline{x}}^*}{dt} = 0 \qquad \text{(continuous)} \qquad (12.2)$$

Since the forward differencing approximation, Eq. (11.12), has been used, Eqs. (12.1) and (12.2) are equivalent.

Insertion of Eq. (12.2) into Eq. (11.13) yields

$$\underline{0} = [A + d^*B]\hat{\underline{x}}^* \qquad (12.3)$$

where $A = D_0 A_1 + D_0' A_2 - (A_1 - A_2)\underline{x}_0 \underline{f}^T - (B_1 - B_2)\underline{u}\,\underline{f}^T$

$B = A_1 - A_2$

$d^* = - \underline{f}^T \hat{\underline{x}}^*$

$\hat{\underline{x}}^* = $ the value of $\hat{\underline{x}}$ at the desired equilibrium point

A is the small-signal continuous-time closed-loop system matrix, and B is a matrix which describes the nonlinear term. Equation (12.3) describes the positions of the equilibrium points in the unsaturated region. In addition to the trivial solution $\hat{\underline{x}}* = \underline{0}$ (the desired quiescent operating point), a number of extra solutions may exist. One may easily find these other equilibrium points by the following procedure:

First, notice that if Eq. (12.3) is satisfied for some $\hat{\underline{x}}* \neq 0$, then necessarily $\hat{\underline{x}}*$ lies in the nontrivial null space of $[A + d*B]$. In other words, $[A + d*B]$ must have a zero eigenvalue, $\hat{\underline{x}}*$ must be an eigenvector corresponding to that zero eigenvalue, and

$$\det[A + d*B] = 0 \tag{12.4}$$

A relatively simple procedure, then, is to first find which values of d* satisfy Eq. (12.4). Once the values of d* are known, the solution of Eq. (12.3), together with the constraint $d* = - \underline{f}^T\hat{\underline{x}}*$, is straightforward. One can then see how to design the regulator such that these additional equilibrium points are correctly positioned outside of the unsaturated region. Their influence on the transient response of the regulator can then be made small.

For the boost example of Fig. 11.1, the quantities in Eq. (12.3) are

$$\hat{\underline{x}}^* = \begin{bmatrix} \hat{i}^* \\ \\ \hat{v}^* \end{bmatrix} \qquad\qquad A = \begin{bmatrix} -R_1 & -n_1 \\ \\ n_2 & -1/R_2 \end{bmatrix}$$

$$\underline{f} = \begin{bmatrix} f_1 \\ \\ f_2 \end{bmatrix} \qquad\qquad B = \begin{bmatrix} 0 & 1 \\ \\ -1 & 0 \end{bmatrix}$$

$$(12.5)$$

where $R_1 = R_L + V_0 f_1$ $\qquad\qquad n_1 = D_0' + V_0 f_2$

$\qquad n_2 = D_0' + I_0 f_1$ $\qquad\qquad R_2 = R \mid\mid (-1/I_0 f_2)$

$\qquad I_0$ = quiescent inductor current

$\qquad V_0$ = quiescent output voltage

Eq. (12.4), the expression for the control (d*) at the equilibrium points, then becomes

$$d^{*2} - d^*(n_1 + n_2) + n_1 n_2 + \frac{R_1}{R_2} = 0 \qquad\qquad (12.6)$$

This equation is quadratic and has two roots; hence, two equilibrium points may exist for the unsaturated region in addition to the quiescent operating point $\hat{\underline{x}} = \underline{0}$. For the values specified in Fig. 11.1, the two roots are

$$d^* = .236, \quad 13.64 \tag{12.7}$$

The equilibrium point at $d^* = .236$ is well within the unsaturated region. It causes the large-signal transient response to differ significantly from that predicted by small-signal models; in fact, some solutions are unstable.

The root $d^* = 13.64$ represents a virtual equilibrium point. It lies outside the unsaturated region where Eq. (12.6) is valid; in consequence, the system is not actually in equilibrium at this point. Nonetheless, it is possible for a virtual equilibrium point to influence the response of a nonlinear system. In this case, however, the distance it lies away from the unsaturated region is sufficiently large that its effect on the trajectories is negligible.

The positions in the state plane of the equilibrium points are now found by solution of Eq. (12.3). For this example, one obtains

$$\hat{i}^* = -\frac{d^*}{f_1 + R_2 f_2 (n_2 - d^*)}$$

$$\hat{v}^* = -\frac{d^*}{f_2 + \frac{f_1}{R_1}(d^* - n_1)} \tag{12.8}$$
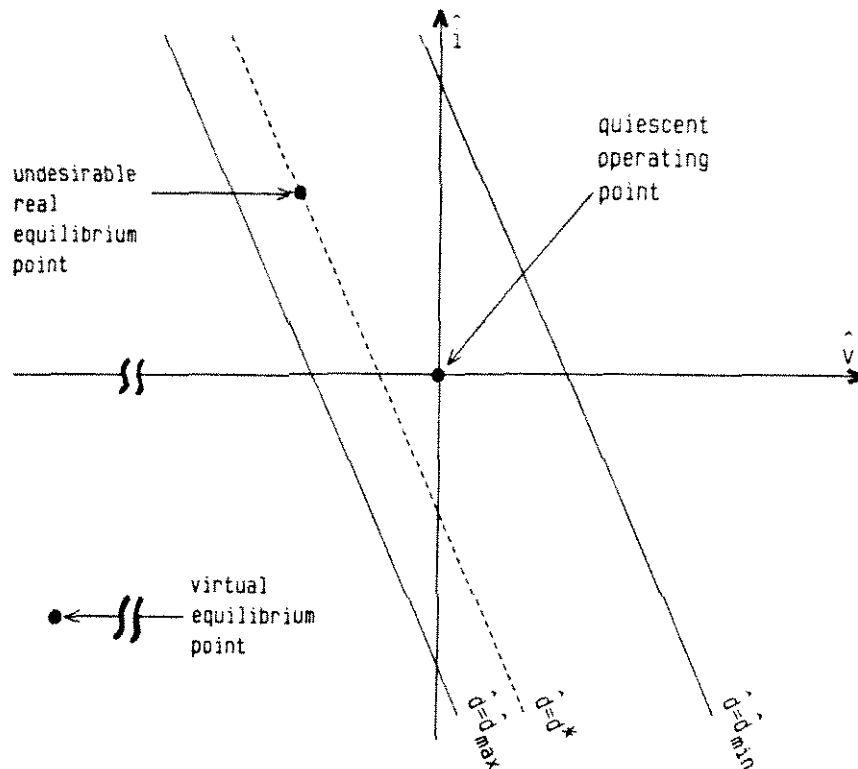
Fig. 12.1. *Summary of the unsaturated region equilibrium points for the boost example of Fig. 11.1. In addition to the usual quiescent operating point, a real equilibrium point exists at d* = .236. A (insignificant) virtual equilibrium point occurs at d* = 13.64.*

For the values specified in Fig. 11.1, these expressions yield

$$\hat{i}^* = 2.0A, \quad \hat{v}^* = -3.7V \qquad \text{at } d^* = .236$$

$$(12.9)$$

$$\hat{i}^* = 1.9A, \quad \hat{v}^* = -24.2V \qquad \text{at } d^* = 13.64$$

The unsaturated region equilibrium points are summarized in Fig. 12.1. Two real equilibrium points exist: in addition to the desired quiescent operating point at $\hat{\underline{x}} = \underline{0}$, an unwanted real equilibrium point occurs as shown; hence, unstable responses are expected to occur. A virtual equilibrium point also occurs, but has little effect on the response of the system.

The nature of each equilibrium point and the approximate trajectories in the vicinity of these points may be found by perturbation and linearization of the nonlinear state equations, Eq. (11.6) or (11.13). Let

$$\underline{x}(t) = \underline{X}_0 + \underline{x}^* + \underline{\tilde{x}}(t)$$

$$D(t) = D_0 + d^* + \tilde{d}(t) \tag{12.10}$$

$\underline{\tilde{x}}(t)$ and $\tilde{d}(t)$ are the state vector and duty ratio perturbations with respect to the equilibrium values $(\underline{X}_0 + \underline{x}^*)$ and $(D_0 + d^*)$, respectively. Upon insertion of Eq. (12.10) into the continuous-time state equation, and upon elimination of higher-order nonlinear terms, one obtains

$$K \frac{d\underline{\tilde{x}}(t)}{dt} = [A + d^*B - B\underline{x}^*\underline{f}^T] \, \underline{\tilde{x}}(t) \tag{12.11}$$

where A and B are defined as in Eq. (12.3). Eq. (12.11) describes the response of the system in the vicinity of $\underline{x}(t) = \underline{X}_0 + \underline{x}^*$. Since the nonlinear terms have been discarded, it is valid only for small signals. The nature of the equilibrium point at $\underline{x}(t) = \underline{X}_0 + \underline{x}^*$ may now be determined by calculation of the eigenvalues (poles) of the system in Eq. (12.11). For this boost example, the characteristic equation of Eq. (12.11) becomes

$$\det[sK - (A + d^*B - B\underline{x}^*\underline{f}^T)] = s^2 LC + s[(R_1 + v^*f_1)C + (\frac{1}{R_2} - i^*f_2)L]$$

$$+ i^*(f_1(n_1 - d^*) - f_2 R_1) + v^*(f_1/R_2 + f_2(n_2 - d^*)) = 0$$

$$\tag{12.12}$$

For the equilibrium point at $d* = .236$, the roots of Eq. (12.12) are

$$s_1 = -2600 \qquad s_2 = 3000 \qquad \text{rad/sec} \qquad (12.13)$$

Since one root is in the right half-plane, and the other is in the left half-plane, the real equilibrium point at $d* = .236$ is a saddle point. Thus, by perturbation and linearization of the system state equations about each equilibrium point, one may determine the nature of the solutions in the vicinity of these points.

12.3 Equilibrium Points In The Saturated Modes

The next step is the investigation of the equilibrium points of the saturated regions. Since in these regions the response is linear, exactly one equilibrium point occurs for each region. If either of these points is real, then unstable responses exist. Therefore, the equilibrium points of both saturated regions must be virtual in a globally-stable regulator.

The equilibrium points for the saturated regions are given by Eq. (11.18). This equation is now solved in a straightforward manner to find the positions of the saturated region equilibrium points. For the boost example, one obtains

$$V_{sat} = \frac{V_g}{D'_{sat}} \cdot \frac{1}{1 + R_L/D'^2_{sat} R} \qquad (12.14)$$

$$I_{sat} = \frac{V_{sat}}{D'_{sat} R} \qquad (12.15)$$

where

V_{sat} = equilibrium output voltage for $D = D_{sat}$ saturated region

I_{sat} = equilibrium inductor current for $D = D_{sat}$ saturated region.

One possible design strategy is to limit the duty ratio to a range sufficiently smaller than $[0,1]$, thereby improving the response by moving the saturated region equilibrium points well outside of their respective regions. Hence, it is of interest to determine the locus of V_{sat} and I_{sat} in the state plane for various values of D_{sat}. Combination of Eqs. (12.14) and (12.15) yields

$$I^2_{sat} RR_L - I_{sat} RV_g + V^2_{sat} = 0 \qquad (12.16)$$

Thus, the locus is an ellipse. Eq. (12.16) is plotted in Fig. 12.2. It can be seen that the $D = 0$ point is well outside of the $D = D_{min}$ saturated region; consequently, the choice of $D_{min} = 0$ poses no apparent problems. However, the $D = 1$ point lies inside the $D = D_{max}$ saturated region for the case illustrated. As a result, unstable solutions are guaranteed to exist for the choice of $D_{max} = 1$.

One way to avoid obtaining a real equilibrium point in the $D = D_{max}$ saturated region is to choose D_{max} sufficiently less than one, thereby moving the equilibrium point outside the region. A second way is to lower the ratio f_2/f_1 (i.e., increase the amount of current feedback in relation to the output voltage feedback). This moves the $D = D_{max}$
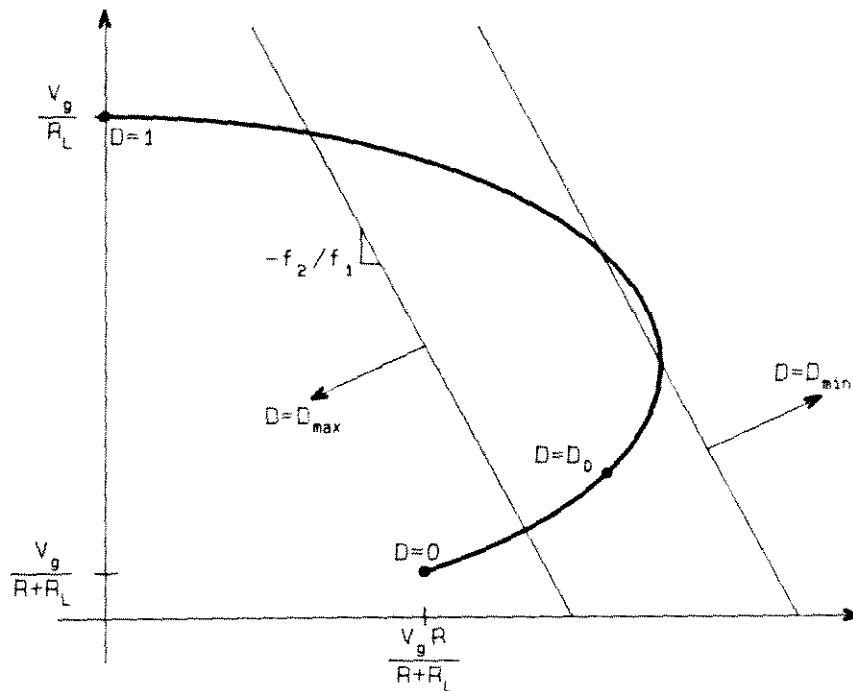
Fig. 12.2. The locus of saturated region equilibrium points in the state plane is a portion of an ellipse. The saturated region boundaries are superimposed. The regulator must be designed such that both saturated region equilibrium points are virtual.

saturated region boundary to the left, past the equilibrium point. Both strategies are effective in eliminating the presence of unstable transient solutions.

The nature of the saturated region equilibrium points and trajectories is easily found by evaluation and solution of the linear state equations, Eq. (11.16) or (11.17). First, the nature of the equilibrium point of the $D = D_{sat}$ region is determined by calculation of tne eigenvalues of the system in Eq. (11.17). For this boost example, the characteristic equation of the $D_{max} = 1$ saturated region becomes

$$\det[sK - (D_{max}A_1 + D'_{max}A_2)] = (1 + sL/R_\ell) (1 + sRC) = 0 \qquad (12.17)$$

Since both roots are in the left half-plane, the real equilibrium point in the $D_{max} = 1$ saturated region is stable.

Since Eq. (11.17) is linear, its solution is straightforward, and hence the time domain waveforms in the saturated regions are easily calculated. Since the equilibrium point in the $D = D_{max}$ region is stable, the solutions in this region are decaying exponentials or damped sinusoids which tend towards this stable equilibrium point. A similar result holds for the $D = D_{min}$ saturated region: the (virtual) equilibrium point is stable, and hence the solutions are decaying exponentials or damped sinusoids which tend towards the virtual equilibrium point, but the solutions leave the $D = D_{min}$ saturated region before this virtual equilibrium point is reached. A further example of the solutions in the saturated regions is given in the next chapter, where the actual waveforms are calculated for a specific boost regulator example.

Thus, the positions of the equilibrium points can be calculated without difficulty. The presence of real equilibrium points in addition to the desired quiescent operating point indicates that the regulator is not globally stable; therefore, these points must be eliminated. As an example, the equilibrium points of a two-state boost regulator were found. In addition to the quiescent operating point, one real equilibrium point existed in the unsaturated region and another in the $D = 1$ saturated region. Hence, this design was not globally stable. The response could be improved by moving these equilibrium points well outside of their respective regions; they would then become virtual equilibrium points.

12.4 Construction Of Trajectories

Knowledge of the existence and positions of the equilibrium points of the regulator yields a great deal of insight into the large-signal operation of the system; however, this knowledge is not complete. It is also necessary to calculate peak transient currents and voltages, to show that no limit cycles exist, and to verify that all possible responses are well-behaved and stable. Therefore, it is desirable to construct the system trajectories.

A number of methods exist for the analytical construction of trajectories [5,44], such as the vector-field method or the method of isoclines. For second-order systems, these methods work well. However, since the dimension of the state space is equal to the number of states of the system, these analytical methods become impractical for regulators with many states. In some cases such as the boost example of the next chapter, various approximations may be made which allow the analytical calculation of the nonlinear system response. Unfortunately, none of these techniques are completely general; as a result, it may become necessary to resort to computer simulation. The state equations describing the transient response of the regulator, Eq. (11.10), are easily implemented on most computers. Most of the state-plane trajectories illustrated in this thesis were plotted by a small desktop computer programmed in BASIC.

Figure 12.3 contains the flowchart of the program. The initial state $\hat{\underline{x}}_0$ of the system is given as input, and then the computer iteratively calculates $\hat{\underline{x}}_n$, the values of the state variables at the
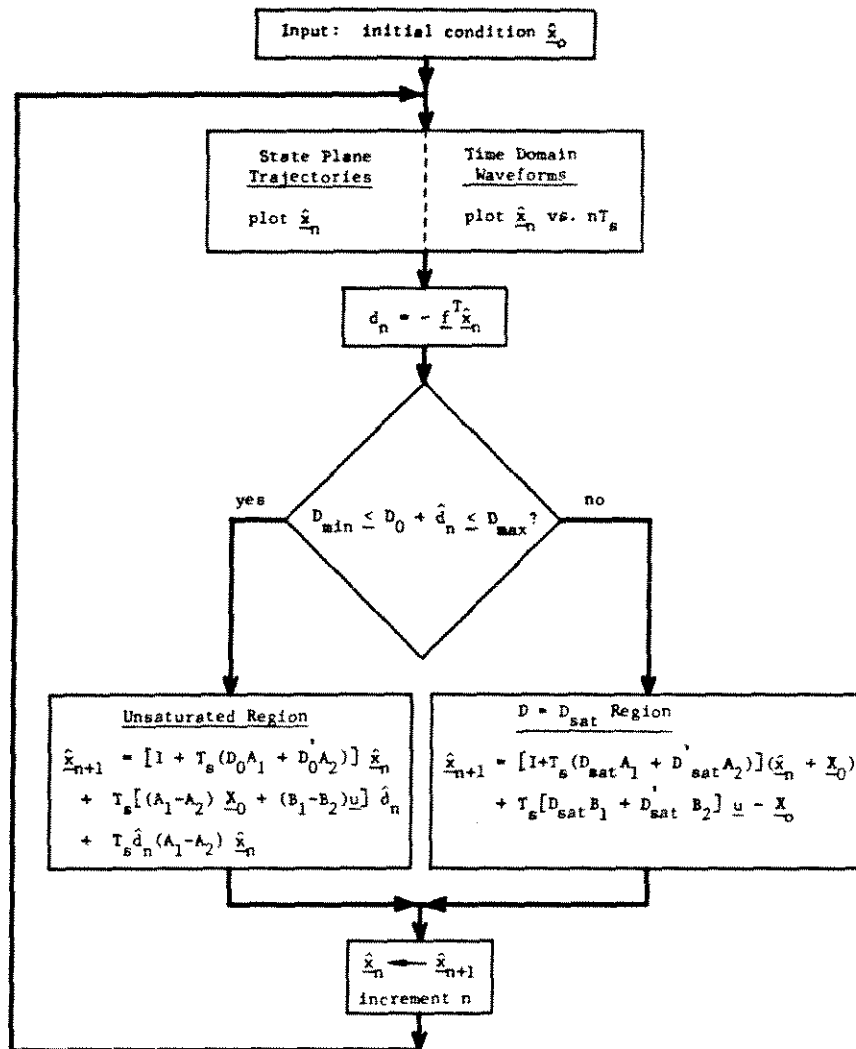
Fig. 12.3.   Flowchart of the computer program for the calculation of the trajectories and time domain transient waveforms.

switching instants $t = nT_s$, as follows: at the n-th switching interval, the duty ratio $\hat{d}_n$ is evaluated from Eqs. (11.14) and (11.15). The region of operation is determined by use of Eqs. (11.15) and (11.44). If the system is in the unsaturated region, then Eq. (11.6) is used to find $\hat{\underline{x}}_{n+1}$. If the system is in one of the saturated regions, then Eq. (11.16), is used to determine $\hat{\underline{x}}_{n+1} = (\underline{x}_{n+1} - \underline{X}_0)$, with D_{sat} taken

to be either D_{max} or D_{min} depending on the region. Other modes of operation, such as current limiting or saturation of devices in the feedback path, could be added here if desired. The program then increments n and repeats the procedure. State-plane trajectories may be obtained, where the values of two of the states are plotted in a plane, or time domain waveforms may be found.

The computer-drawn state plane trajectories for the two-state boost regulator example are shown in Fig. 12.4. The peak values of inductor current and output voltage during any given transient are apparent. The effect of the unsaturated region real equilibrium point at i* = 2.0A, v* = -3.7V can also be seen: some unstable solutions occur which bend away in the vicinity of the equilibrium
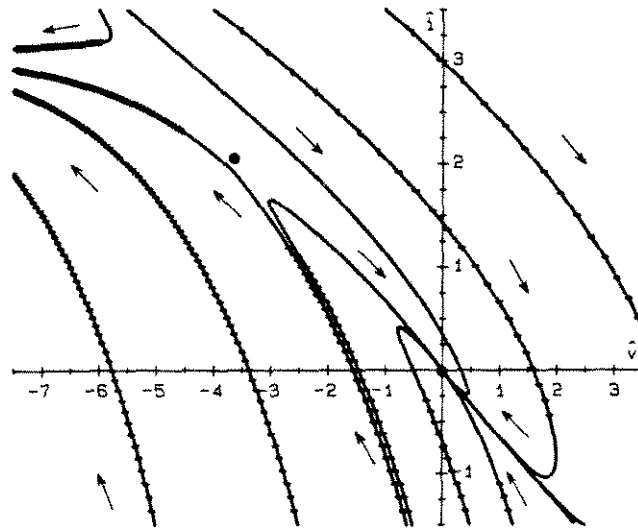
Fig. 12.4. Computer-predicted state-plane trajectories for the two-state boost example. Some transients converge to the desired quiescent operating point $\hat{x}$ = 0, while others converge to the unwanted real equilibrium point in the D = D_{max} saturated region. The real equilibrium point at d* = .236 is a saddle point.

point and head towards a large negative value of $\hat{v}$. This equilibrium point is a saddle point. As explained in the previous section, another real equilibrium point exists in the D = 1 saturated region. This point is a stable equilibrium point, and all solutions which do not converge to the desired quiescent operating point converge to this additional equilibrium point.

This system may be made globally stable by sufficient increase of the ratio of current feedback to voltage feedback. The system then has four virtual equilibrium points in addition to the real quiescent operating point. The trajectories are plotted in Fig. 12.5 for the values f_1 = 0.8, f_2 = 0.08. It can be seen that all solutions converge to the point $\hat{i}$ = 0, $\hat{v}$ = 0, and a well behaved, globally stable response is obtained.
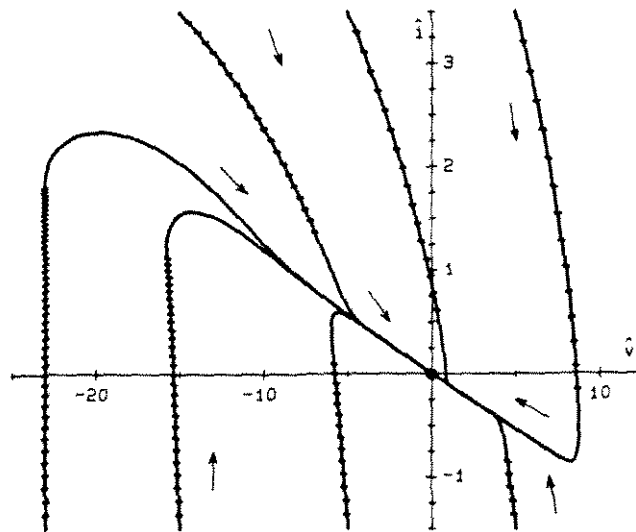
Fig. 12.5. The quiescent operating point of the two-state boost regulator example becomes globally stable when the ratio of f_1 to f_2 is increased a sufficient amount.

Transient waveforms may also be plotted vs. time. This was done for the boost with integrator example in Figs. 9.5, 9.6, and 9.7. In this way, the actual response of systems with more than two states may be predicted, the existence or absence of unstable solutions verified and peak currents and voltages determined.

Thus, the nonlinear models of Chapter 11 may be used to investigate the large-signal response of a switching regulator. Equilibrium points may be calculated analytically, and positioned properly to obtain a well-behaved response. The actual state-plane trajectories or time-domain waveforms may be calculated easily by a small desktop computer; this allows the informed design of the regulator and ensures a globally stable system.

CHAPTER 13

EXAMPLE: TRANSIENT ANALYSIS OF ˙

A SIMPLE BOOST REGULATOR

13.1 Introduction

The relevance of the general analysis of the previous chapters is
best illustrated by a specific example. In this chapter, the complete
large-signal behavior of the simple boost regulator of Fig. 13.1 is
determined, its salient features are identified, and some ways to
improve the response are suggested.
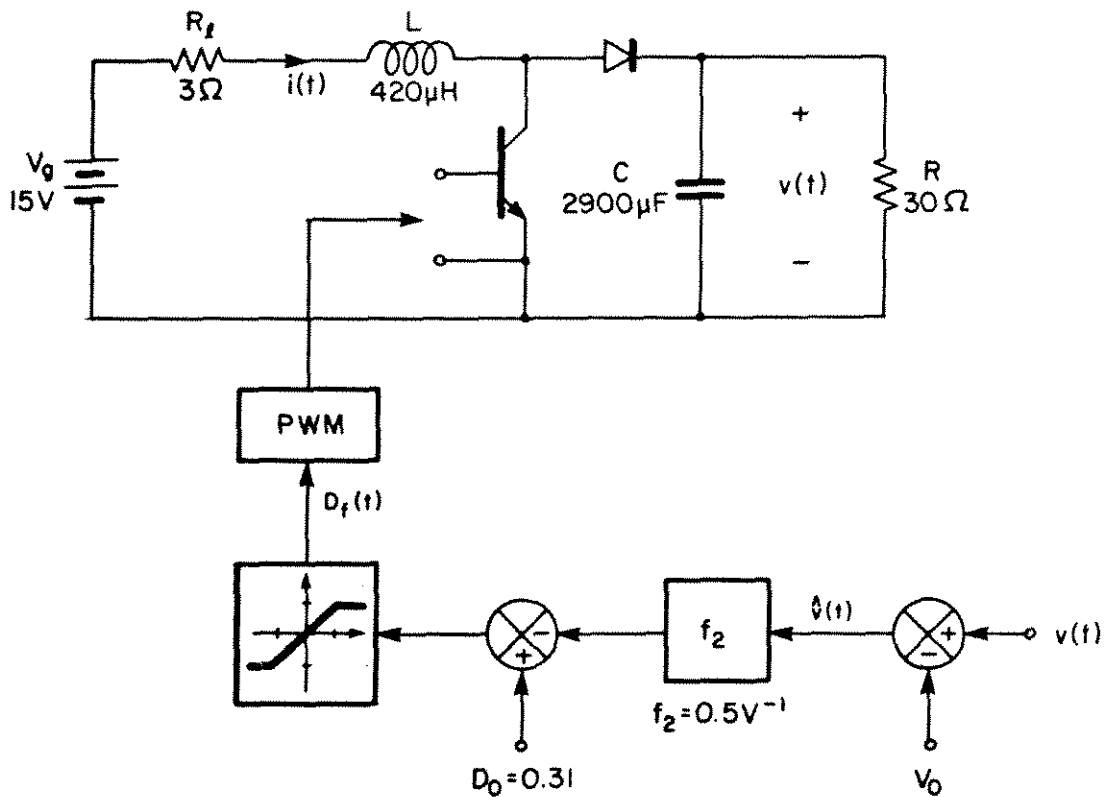
Fig. 13.1. Boost regulator example.

First, the small-signal characteristics of the regulator are designed. The feedback loop contains pure voltage feedback, without compensation networks or current feedback; this simplifies the large-signal analysis and results in a more lucid example. Next, the usefulness of the equilibrium output voltage curves is discussed, emphasizing the fact that these curves cannot be used to determine transient voltages or currents. The different modes of operation are then identified, and analytical expressions are found for their boundaries in the state plane. Each region is studied in detail, revealing the positions of the equilibrium points for each region and their effect on the large-signal stability of the system. Suitable approximations are then made which yield simple expressions for the time-domain transient waveforms. The complete transient behavior of the system, as well as some possible strategies for the improvement of its response, then becomes apparent.

13.2 Small-Signal Design

The quiescent operating point of the regulator must be stabilized for small perturbations before the large-signal behavior is considered. This is accomplished here using the techniques described in [1,2].

The small-signal loop gain may be found by use of the state-space averaging technique; it contains two poles and a right-half-plane zero:

$$T = T_0 \frac{(1 - s/\omega_a)}{(1 + s/\omega_1)(1 + s/\omega_2)} \qquad (13.1)$$

where

$$f_1 = \omega_1/2\pi \cong 10 \text{ Hz} \cong 1/2\pi C(R_\ell||D_0'^2 R)$$

$$f_2 = \omega_2/2\pi \cong 1 \text{ kHz} \cong R_\ell/2\pi L$$

$$f_a = \omega_a/2\pi \cong 4 \text{ kHz} \cong (D_0'^2 R - R_\ell)/2\pi L$$

Eq. (13.1) is plotted in Fig. 13.2. It is apparent that the open-loop system is overdamped; owing to the large value of capacitance used, the output capacitor dominates the open loop response.

A moderate amount of dc loop gain is used, such that the loop gain reaches unity at 100 Hz with a phase margin of 90^0.
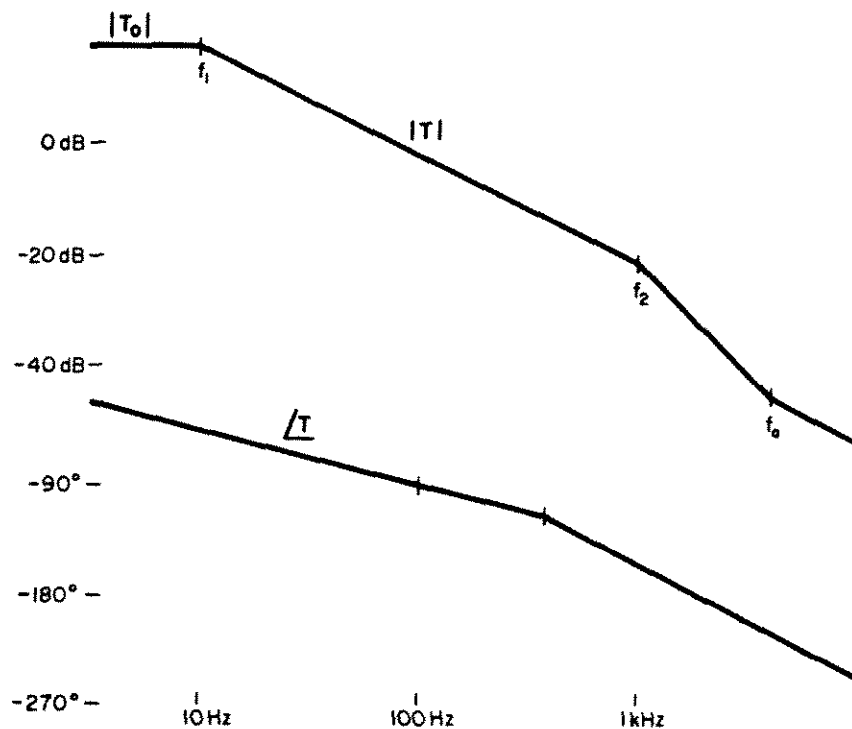
Fig. 13.2. Small-signal analysis: the system is overdamped, with a phase margin of approximately 90^0.

Hence, the closed-loop response is also overdamped and is dominated by a low-frequency pole at 100 Hz. A high frequency pole occurs at 1 kHz. Thus, the poles of the closed-loop system are well separated, and the two modes do not interact. The small-signal design is very conservative.

13.3 Equilibrium Output Voltage Curves

The familiar expression for the open-loop equilibrium output voltage as a function of applied constant duty ratio may be found by use of Eq. (11.8). For the boost example, one obtains Eq. (13.2); this relation is plotted in Fig. 13.3.

$$V = \frac{V_g}{D'} \cdot \frac{1}{1 + R_\ell/D'^2 R} \tag{13.2}$$

This expression is derived with the assumption that the system is in steady-state; consequently, one cannot deduce nonequilibrium properties such as transient voltages or incremental gains. Eq. (13.2) can only be used to determine the output voltage in equilibrium.

The boost regulator of Fig. 13.1 is in equilibrium at more than one value of output voltage V_0; these points may be found graphically by use of Fig. 13.3, as follows: If the system is in equilibrium at a given duty ratio D (read along the horizontal axis of Fig. 13.3), then the output voltage V is given by the equilibrium gain curve (read along the left-hand vertical axis of Fig. 13.3). The feedback circuit senses this voltage and determines a new duty ratio D_f according to the
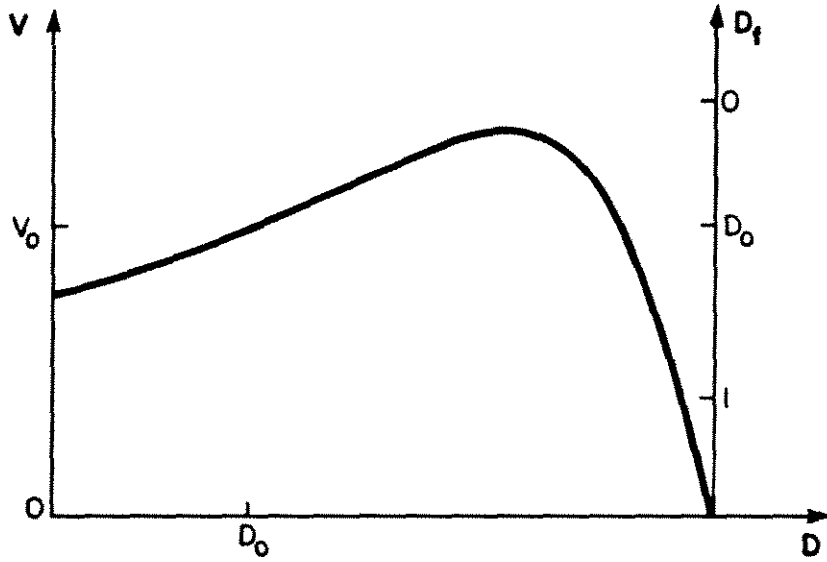
Fig. 13.3.   Equilibrium output voltage V as a function of applied duty ratio D.   The system is designed to operate at quiescent duty ratio D_0 and output voltage V_0.
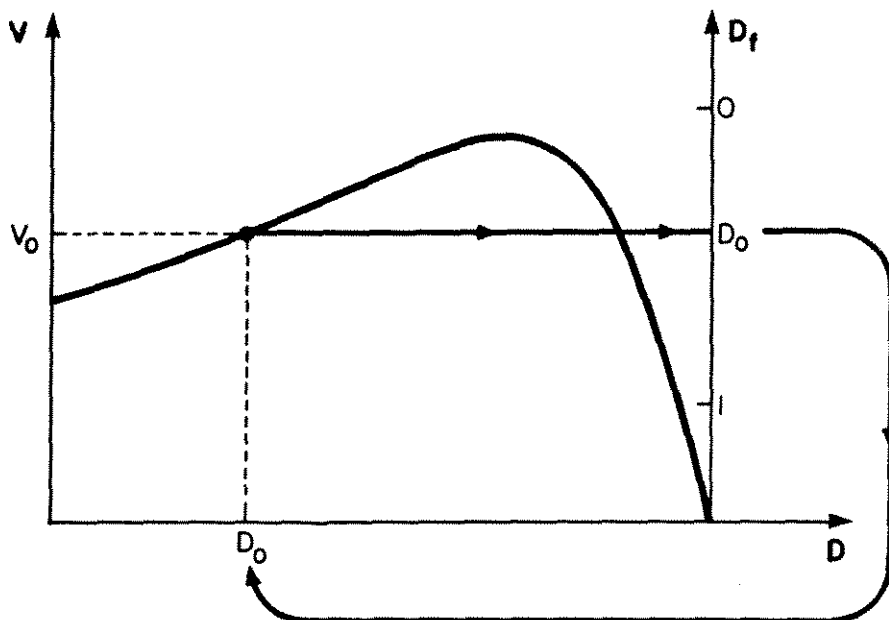
Fig. 13.4.   The system is in equilibrium at duty ratio D_0 (D_f axis scale is exaggerated).

linear voltage feedback law $D_f = D_0 - f_2(V - V_0)$, as read along the right-hand vertical axis of Fig. 13.3. The system is in equilibrium if and only if $D = D_f$.

For example, the system is in equilibrium at duty ratio D_0; this is the usual quiescent operating point. Referring to Fig. 13.4, at this point the converter produces output voltage V_0 in equilibrium. As a result, the feedback circuit returns duty ratio D_0 (read along right-side vertical axis), and applies this value to the converter (along horizontal axis). Since this is the original duty ratio, this point is indeed an equilibrium point.

We must avoid the temptation to say, "the slope of the equilibrium voltage curve reverses sign for high duty ratios; therefore, the incremental loop gain under transient conditions reverses sign, positive feedback is applied, and the system becomes unstable. A saddle point therefore occurs at the inflection point;
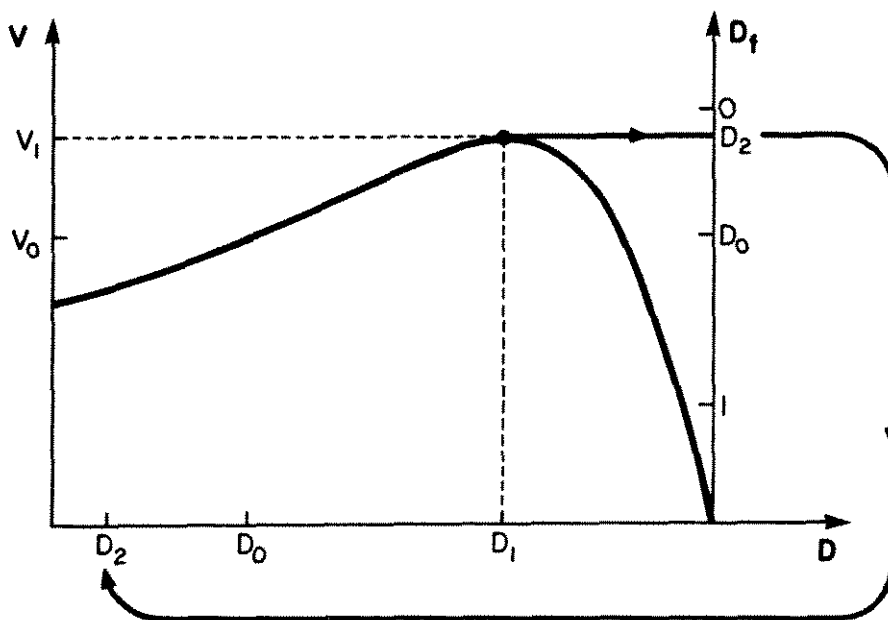
Fig. 13.5. The system cannot be in equilibrium at duty ratio D_1; hence, this is not a saddle point.

i.e., at the duty ratio which produces peak equilibrium output voltage." The fallacy lies in the attempt to predict the output voltage under transient conditions by use of the equilibrium gain curve. The curve can, however, be used to determine whether the inflection point is a saddle point. Referring to Fig. 13.5, equilibrium voltage V_1 is predicted when duty ratio D_1 is applied to the converter. The feedback circuit then returns duty ratio D_2. Since $D_2 \neq D_1$, the system is not in equilibrium, and hence no saddle point can occur for $D = D_1$.

The correct position of the saddle point is at $D = D^*$, illustrated in Fig. 13.6. If the system is in equilibrium at $D = D^*$, then the output voltage is V^*. The feedback circuit therefore returns duty ratio D^*. Since this is the original duty ratio, the system is in equilibrium.
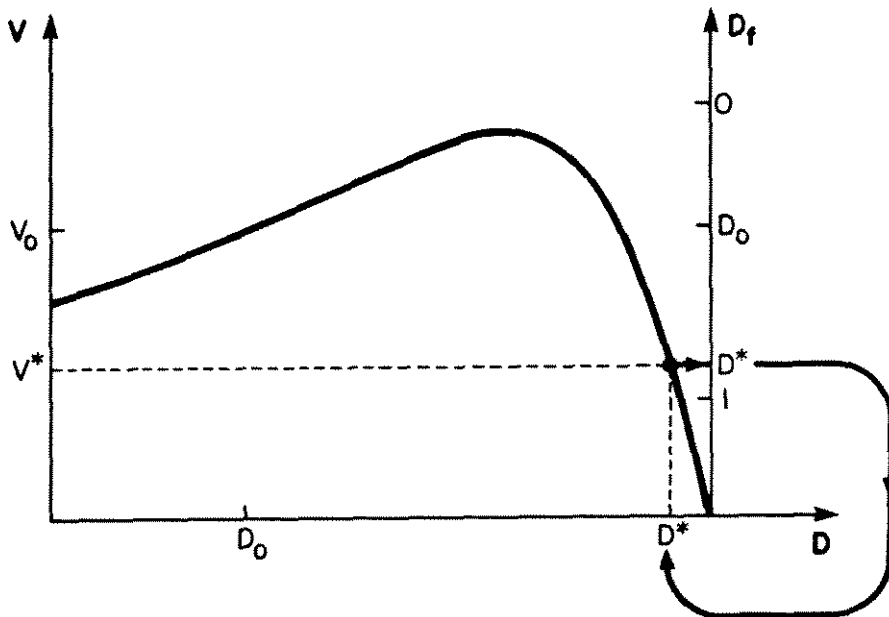
Fig. 13.6. The system can be in equilibrium at duty ratio D^*. This is the correct position of the saddle point.
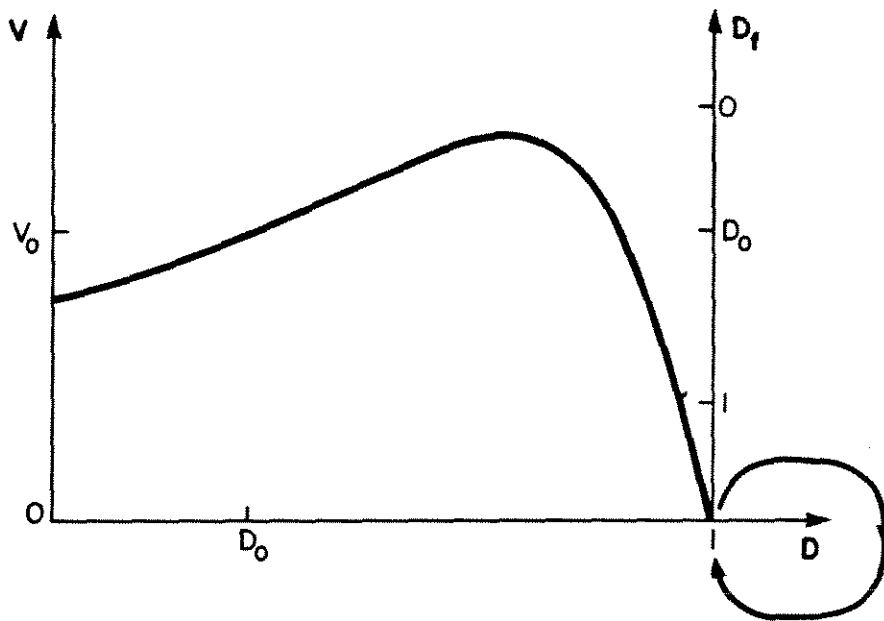
Fig. 13.7. A third equilibrium point occurs at D = 1; this is an undesired stable equilibrium point.

A third equilibrium point occurs at D = 1, as shown in Fig. 13.7. The duty ratio cannot be larger than unity; as the output voltage is decreased, the duty ratio increases until it saturates at D = 1. Past this point, the duty ratio remains constant. If the system is in equilibrium at D = 1, then the output voltage is 0. The feedback circuit returns duty ratio 1, and hence the system is in equilibrium. This equilibrium point is stable.

This graphical procedure can be refined so that all equilibrium points are found at once. The requirement that $D = D_f$ yields an expression which, along with the equilibrium output voltage Eq. (13.2), constitute two equations which must be satisfied simultaneously. Hence, one can plot both equations on the same graph; they intersect at each equilibrium point.

The feedback relation for this system is linear with saturation, as in Eq. (13.3):

$$
D_f = \begin{cases} D_{min} & , & v \geq V_{max} \\ D_0 - f_2(v - V_0) & , & V_{max} \geq v \geq V_{min} \\ D_{max} & , & v \leq V_{min} \end{cases} \quad (13.3)
$$

where

$$
V_{max} = V_0 + (D_0 - D_{min})/f_2
$$

$$
V_{min} = V_0 + (D_0 - D_{max})/f_2
$$

With the requirement that $D = D_f$ in equilibrium, Eq. (13.3) becomes

$$
D = \begin{cases} D_{min} & , & V \geq V_{max} \\ D_0 - f_2(V - V_0) & , & V_{max} \geq V \geq V_{min} \\ D_{max} & , & V \leq V_{min} \end{cases} \quad (13.4)
$$

The equilibrium points of the system occur where Eqs. (13.2) and (13.4) are satisfied simultaneously. These two equations are plotted in Fig. 13.8a for the case $D^* < D_{max} < 1$; the three equilibrium points are readily apparent. It can be seen that the two undesired equilibrium points could be eliminated by choosing $D_{max} < D^*$, as in Fig. 13.8b. Although the elimination of these undesired equilibrium points does not guarantee global stability, it is nonetheless a necessary condition. In many cases, the choice of D_{max} sufficiently less than D^* yields an acceptable response.

(a)
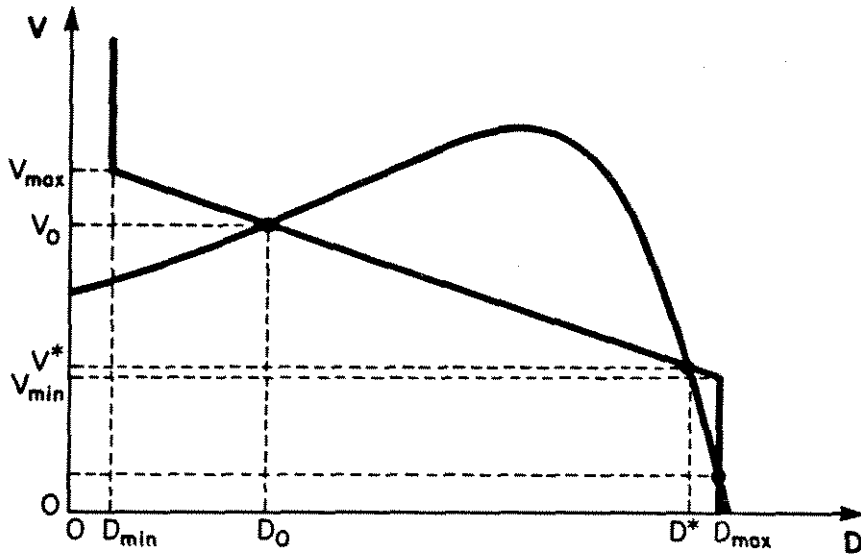
(b)
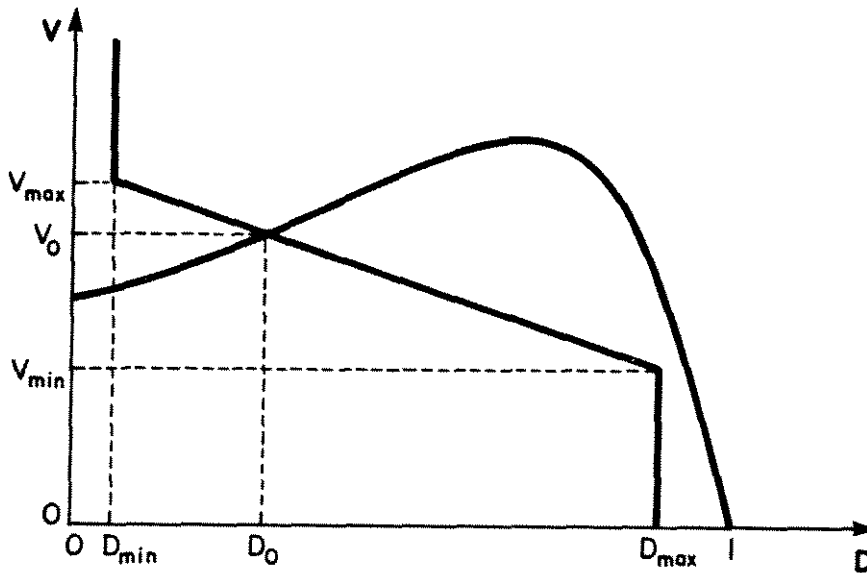
Fig. 13.8. Graphical construction to find the positions of the equilibrium points. The equilibrium output voltage curve, Eq. (13.2), and the feedback relation, Eq. (13.4), are plotted simultaneously; they intersect at each equilibrium point. (a) the case when D* < D_max < 1 contains three real equilibrium points; (b) the case when D_max < D* contains only one real equilibrium point.

In summary, the equilibrium output voltage curve is derived with the assumption that the system has reached steady-state. Transient information has been discarded; in consequence, one cannot deduce nonequilibrium properties from this curve. However, the positions of all equilibrium points can be found; for this example, in addition to the usual quiescent operating point of $D = D_0$, a saddle point occurs at $D = D^*$ and a stable equilibrium point occurs at $D = 1$.

13.4 Modes of Operation

In this section, the various modes of operation are identified. Analytical and numerical expressions are found for their boundaries in the state plane. There are a total of four modes of operation in this example. In addition to the normal unsaturated operating range, the feedback control may saturate at the maximum duty ratio ($D_{max} = 1$), or at the minimum duty ratio ($D_{min} = 0$). For inductor currents near zero, the system may enter the discontinuous mode, where the diode becomes reverse-biased prematurely. The boundaries of each region are plotted in the state plane, providing quantitative knowledge of each mode.

As described in Section 11.3, the duty ratio must always lie in the interval $[0,1]$; sometimes the limit is even more restrictive: $[D_{min}, D_{max}]$. Outside the usual operating range, the duty ratio remains constant at its saturated value, and the regulator behaves as an open loop system.

For the boost example considered here, linear voltage feedback
is employed. Inside the usual unsaturated operating range of the
converter, the duty ratio, determined by the feedback loop, is a linear
function of the output voltage as given below:

$$D(t) = D_0 - f_2(v(t) - V_0) \tag{13.5}$$

If the output voltage is decreased, the duty ratio increases until,
at some voltage V_{min}, the duty ratio reaches its maximum limit D_{max}.
Past this limit, the duty ratio remains saturated. V_{min} may be
calculated by use of Eq. (13.5), with the result given below:

$$V_{min} = V_0 + (D_0 - D_{max})/f_2 \tag{13.6}$$

A similar phenomenon occurs as the output voltage is increased beyond
the voltage V_{max} which causes the duty ratio to saturate at its
minimum value D_{min}:

$$V_{max} = V_0 + (D_0 - D_{min})/f_2 \tag{13.7}$$

Hence, three operating modes have been identified so far, as
summarized in Fig. 13.9. For $V_{max} > v(t) > V_{min}$, the system operates
in its usual unsaturated mode, with the duty ratio varying linearly
with the output voltage. For $v(t) > V_{max}$, the pulse-width modulator
saturates, and hence the duty ratio remains constant at $D = D_{min}$.
Finally, the pulse-width modulator also saturates when $v(t) < V_{min}$;
in this case, the duty ratio remains fixed at $D = D_{max}$. For the circuit
values specified in Fig. 13.1, the quantities of Eq. (13.6) and (13.7)
are
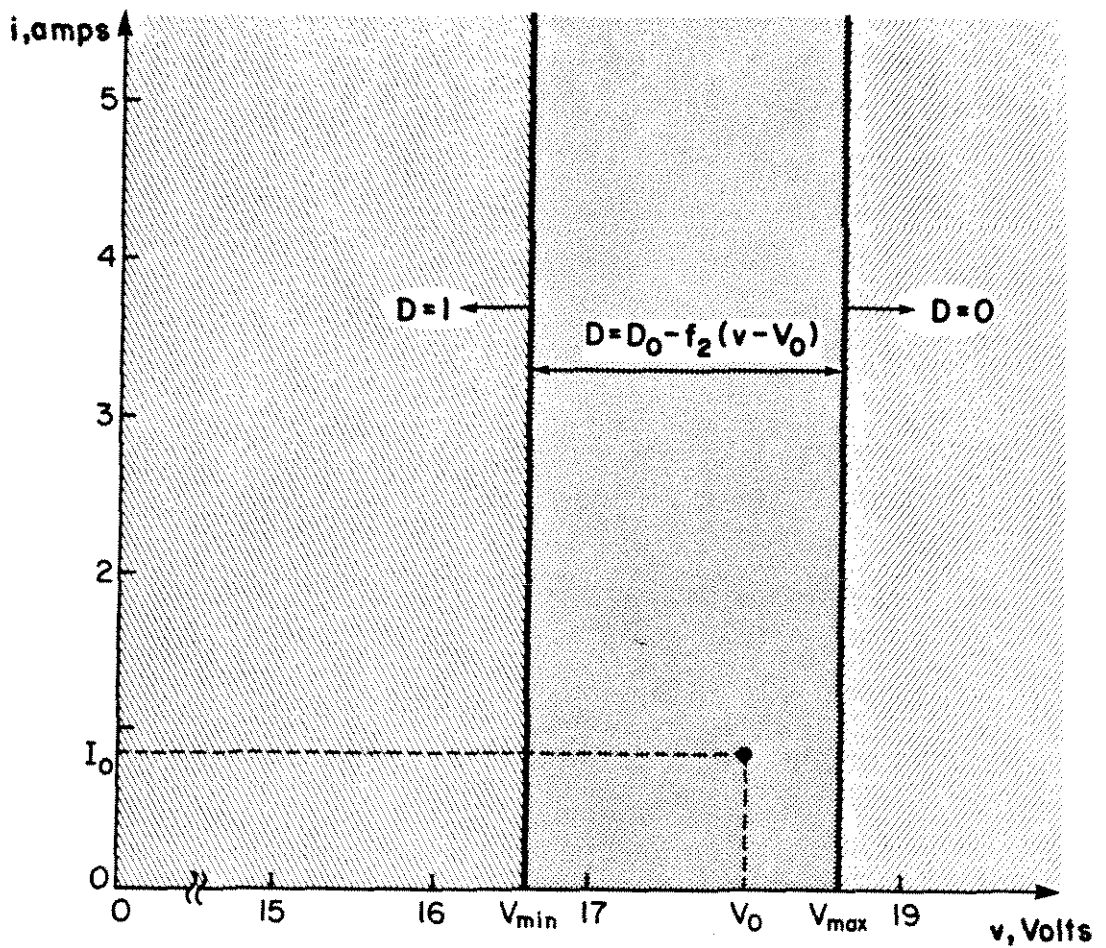
Fig. 13.9. *The boundaries in the state plane of the three modes of operation which have been identified so far: the D = 1 saturated region, the unsaturated region, and the D = 0 saturated region.*

$D_0 = 0.31$ $\qquad$ $D_{min} = 0$ $\qquad$ $D_{max} = 1$

$V_0 = 18.0$ Volts

$I_0 = 0.87$ Amps $\hfill$ (13.8)

$V_{min} = 16.6$ Volts

$V_{max} = 18.6$ Volts

A fourth mode which occurs in this example is the transient discontinuous conduction mode. As described in Section 11.4, it arises because of the nonideal realization of the switch by a single transistor and diode; rather than allow the inductor current to become negative, the diode becomes reverse-biased prematurely. This alters the system state equations; consequently, this mode must be considered separately.

The region of the state plane in which the transient discontinuous mode occurs is found by use of Fig. 13.10. During interval DT_s, when the transistor conducts, the inductor current rises approximately linearly, with slope V_g/L. The current at the end of this interval is therefore

$$i(DT_s) = i(0) + \frac{V_g}{L} DT_s \qquad (13.9)$$

During interval $D'T_s$, when the transistor does not conduct, the current decays approximately linearly, with slope $(V_g - v)/L$.
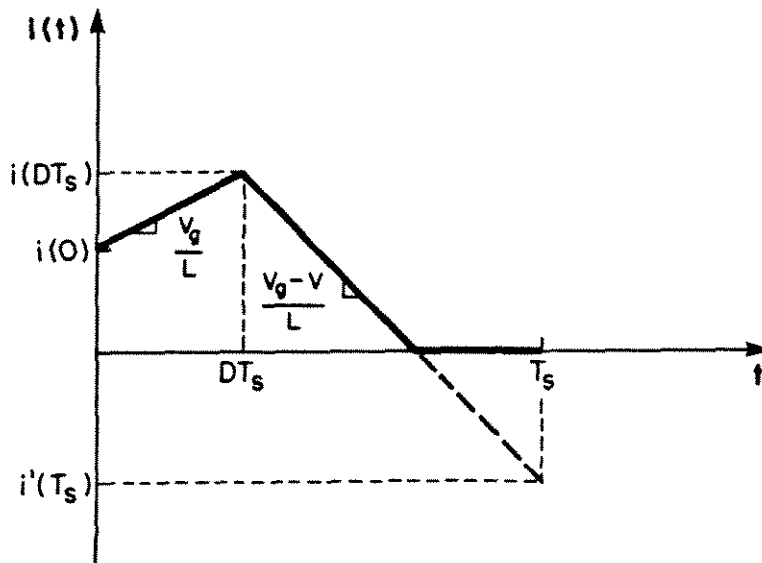
Fig. 13.10. Inductor current waveforms for determination of the transient discontinuous conduction mode boundary. The discontinuous conduction mode occurs if $i'(T_s) < 0$.

The system enters the discontinuous mode if the inductor current falls to zero before the end of the cycle, in other words, if $i'(T_s) < 0$. $i'(T_s)$ is easily calculated from Fig. 13.10:

$$i'(T_s) = i(DT_s) + \frac{V_g - v}{L} D'T_s = i(0) + \frac{T_s}{L}(V_g - D'v) \qquad (13.10)$$

Therefore, the transient discontinuous conduction mode occurs whenever

$$i(0) \leq \frac{T_s}{L}(D'v - V_g) \qquad (13.11)$$

This is the basic relation which describes the discontinuous mode boundary for the boost converter. It depends on both the duty ratio and the output voltage.

For $v \geq V_{max}$, when the duty ratio is saturated at $D = D_{min}$, the discontinuous mode boundary becomes

$$i(0) \leq \frac{T_s}{L}(D'v - V_g)\bigg|_{D = D_{min}} = \frac{T_s}{L}((1 - D_{min})v - V_g) \qquad (13.12)$$

which is a linear function of the output voltage v. For the values specified in Fig. 13.1, one obtains

$$i(0) \leq 0.17 \text{ Amps} \quad \text{at } v = V_{max} \qquad (13.13)$$

For $V_{min} \leq v \leq V_{max}$, when the system operates in the unsaturated mode, the duty ratio is a linear function of v as given by Eq. (13.5). Combination of Eqs. (13.5) and (13.11) yields

$$i(0) \leq \left. \frac{T_s}{L} (D'v - V_g) \right|_{D = D_0 - f_2(v - V_0)}$$

$$= \frac{T_s}{L} (f_2 v^2 + v(D_0 - f_2 V_0) - V_g) \tag{13.14}$$

which is a quadratic function of the output voltage v. This relation coincides with the value given in Eq. (13.13) at $v = V_{max}$, and crosses the i(0) = 0 axis at

$$V_b = 18.2 \quad \text{Volts} \tag{13.15}$$

The boundary predicted by Eq. (13.14) is negative for voltages less than this value. Of course, i(0) cannot be negative; therefore, the transient discontinuous mode does not occur when the output voltage is less than the value specified by Eq. (13.15).

For $v \leq V_{min}$, when the system operates in the $D = D_{max}$ saturated mode, the discontinuous mode boundary becomes

$$i(0) \leq \left. \frac{T_s}{L} (D'v - V_g) \right|_{D = D_{max}} = \frac{T_s}{L} ((1 - D_{max})v - V_g) \tag{13.16}$$
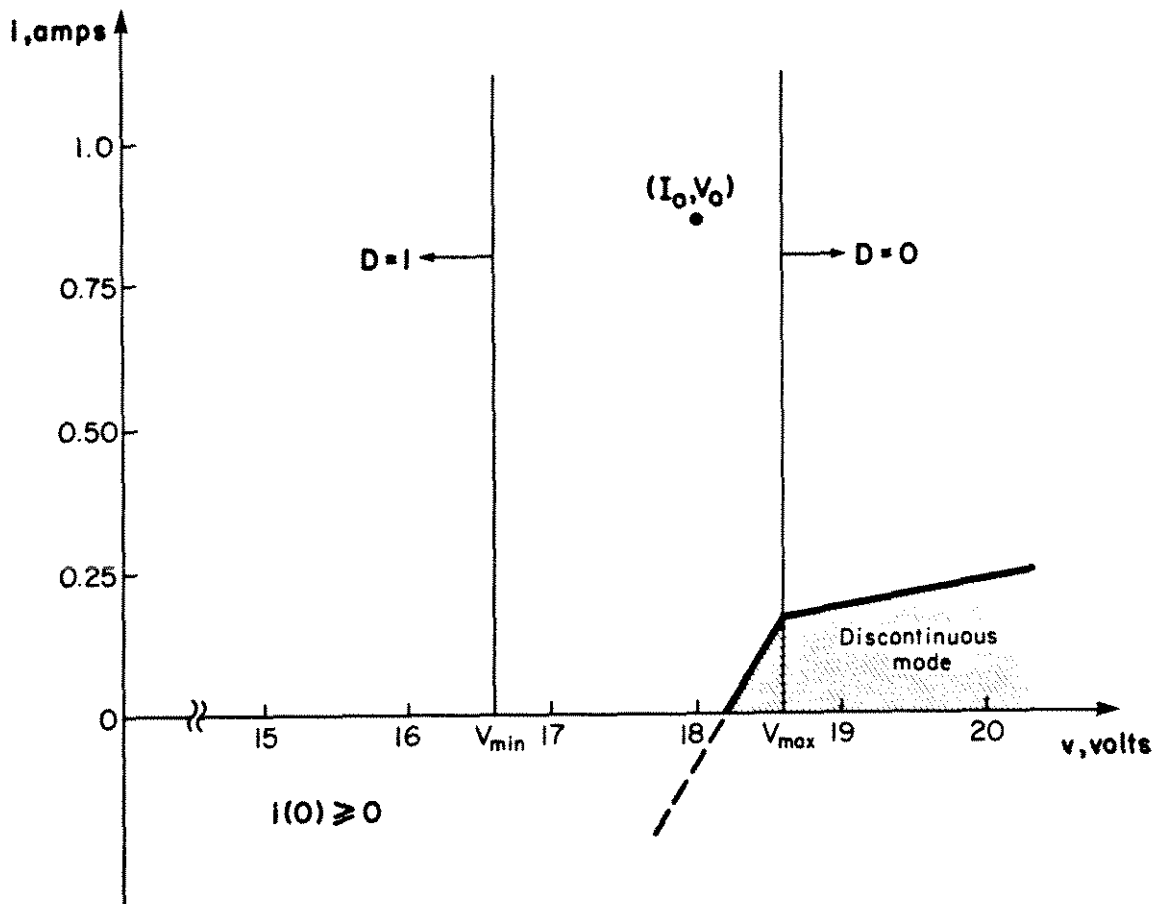
Fig. 13.11. Discontinuous conduction region boundaries in the state plane.

For the values specified in Fig. 13.1, one obtains

$$i(0) \leq - \frac{T_s}{L} V_g = - 0.71 \quad \text{Amps} \tag{13.17}$$

Again, since i(0) cannot be negative, the transient discontinuous mode does not occur while the duty ratio is saturated at its maximum limit.

The region in the state plane where the transient discontinuous conduction mode occurs is summarized in Fig. 13.11.

Thus, the simple boost regulator exhibits four modes of operation. In addition to the usual unsaturated mode, the system may operate with the duty ratio control saturated at its maximum or minimum limits. For small inductor currents, the regulator may enter the transient discontinuous conduction mode. A fifth mode, current limiting, is usually added; the implementation of this mode is discussed later in this chapter. We will next calculate the detailed response of the system in each region.

13.5 Unsaturated Region Waveforms

The state equations in the unsaturated region are nonlinear; an exact closed-form solution is not known. In this section, a number of approximations are made which yield an accurate analytical expression for the transient response in this region. This expression correctly predicts the presence of unstable solutions and the positions of the equilibrium points.

As noted in Section 13.2, a large value of capacitance was chosen for this example; as a result, the system is overdamped and the closed-loop small-signal poles are well-separated. Under these conditions, the system contains two natural modes:

(1) A fast mode, in which the inductor current changes rapidly while the capacitor voltage remains nearly constant, and

(2) a slow mode, in which the capacitor voltage changes slowly and is followed by the inductor current.

This suggests solving the two modes separately and assuming that any interaction is negligible.

The unsaturated region continuous-time state equations are found by evaluation of Eq. (11.13). For this example, one obtains

$$L \frac{d\hat{i}(t)}{dt} = -R_1 \hat{i}(t) - n_1 \hat{v}(t) + \hat{d}(t) \hat{v}(t) \qquad (13.18a)$$

$$C \frac{d\hat{v}(t)}{dt} = n_2 \hat{i}(t) - \hat{v}(t)/R_2 - \hat{d}(t) \hat{i}(t) \qquad (13.18b)$$

where $\hat{d}(t) = -f_2 \hat{v}(t)$

$R_1 = R_\ell = 3 \ \Omega$

$R_2 = R||(-1/I_0 f_2) = -2.5 \ \Omega$

$n_1 = D_0' + V_0 f_2 = 9.7$

$n_2 = D_0' = .69$

$$V_0 = \frac{V_g}{D_0'} \ \frac{1}{1 + R_\ell/D_0'R} = 18.0 \ \text{Volts}$$

$$I_0 = \frac{V_0}{D_0'R} = .88 \ \text{Amps}$$

valid for $D_{min} \leq D_0 + \hat{d}(t) \leq D_{max}$

Fast Mode

With the assumption that the fast mode occurs in a time interval sufficiently short, the capacitor voltage is essentially constant. Eq. (13.18a) then becomes

$$L \frac{d\hat{i}(t)}{dt} \cong - R_1 \hat{i}(t) - n_1 \hat{v}(0) + \hat{d}(0) \; \hat{v}(0) \tag{13.19}$$

with $\quad \hat{d}(0) = - f_2 \; \hat{v}(0)$

$\quad\quad \hat{i}(0) \;$ is given

This is a linear differential equation. Its solution is

$$\hat{i}(t) \cong i(0) \; e^{-\omega_L t} + \frac{\hat{v}(0)}{R_1} (\hat{d}(0) - n_1)(1 - e^{-\omega_L t}) \tag{13.20}$$

where $\quad \omega_L = R_1/L \quad , \quad \tau_L = L/R_1$

Note that the fast mode is stable when $\omega_L > 0$. After the fast mode has decayed,

$$i(t) \rightarrow \frac{\hat{v}}{R_1} \; (\hat{d} - n_1) \; = \; - \frac{\hat{v}}{R_1} \; (f_2 \; \hat{v} + n_1) \tag{13.21}$$

valid for $t >> \tau_L$

As shown in Fig. 13.12, the inductor current decays exponentially during the fast mode, and eventually reaches the quasi-equilibrium value given in Eq. (13.21). By assumption, the capacitor voltage remains essentially constant. Hence, the state-plane trajectories, plotted in Fig. 13.13, are nearly vertical lines. They end at the parabola described by Eq. (13.21).
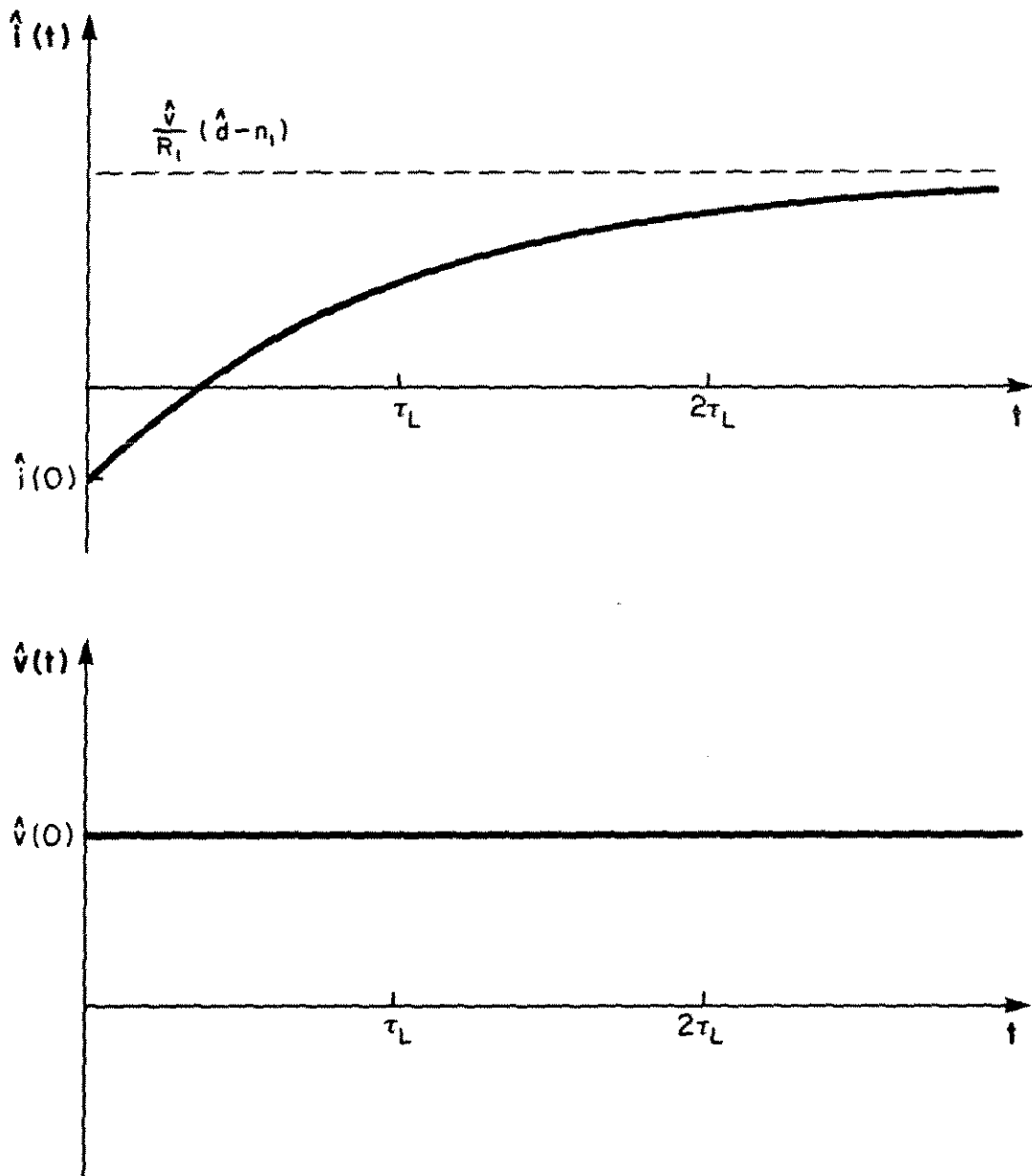
Fig. 13.12. Unsaturated region fast mode waveforms. The inductor current decays exponentially and reaches quasi-equilibrium, while the capacitor voltage remains essentially constant.
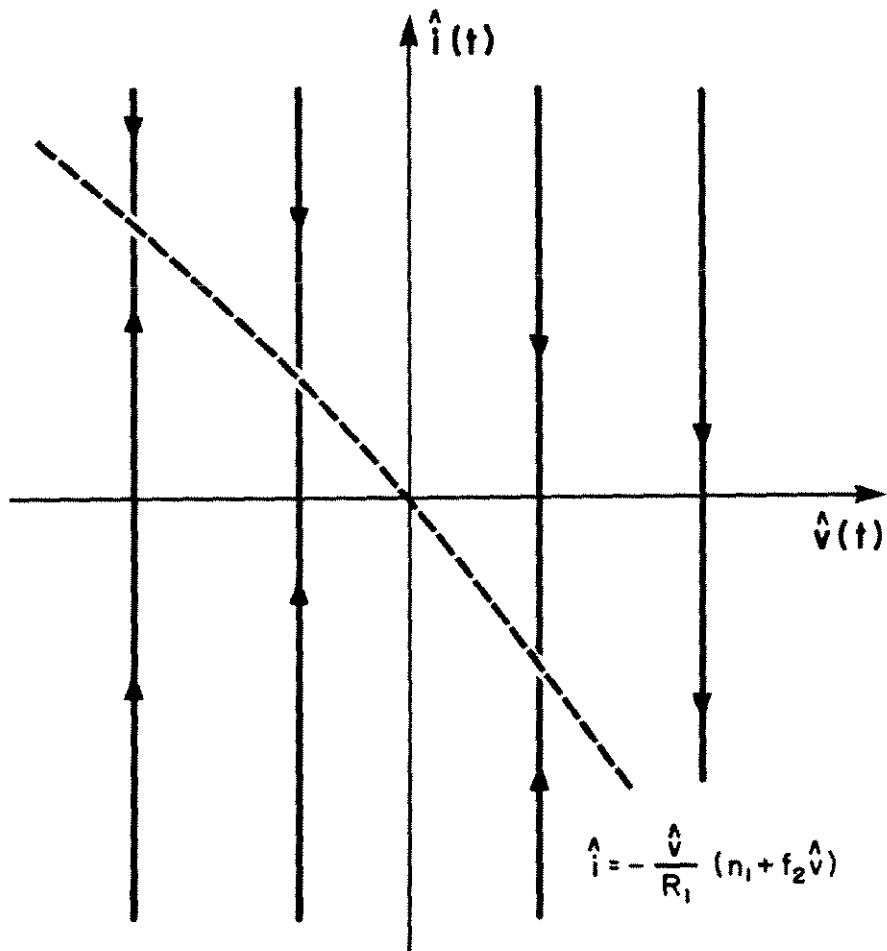
Fig. 13.13. *The unsaturated region fast mode state-plane trajectories are nearly vertical lines which end at the parabola described by Eq. (13.21).*

Slow Mode

For times much greater than τ_L, the fast mode has decayed and hence the inductor current is at the quasi-equilibrium value given by Eq. (13.21). Substitution of Eq. (13.21) into Eq. (13.18b) yields

$$C \frac{d\hat{v}(t)}{dt} = - \frac{\hat{v}(t)}{R_1 C} [\hat{d}^2(t) - (n_1 + n_2)\hat{d}(t) + n_1 n_2 + \frac{R_1}{R_2}] \qquad (13.22)$$

with $\hat{d}(t) = - f_2 \hat{v}(t)$

Eq. (13.22) is the basic differential equation which describes the slow mode. Since $\hat{d}(t)$ is linearly proportional to $\hat{v}(t)$, Eq. (13.22) contains cubic and parabolic nonlinear terms as well as a linear term. This equation could be integrated immediately; however, it is preferred to first employ an additional approximation which yields more lucid results.

Note that the quantity in brackets in Eq. (13.22) is identical to Eq. (12.6), with d* replaced by $\hat{d}(t)$; this is the expression for the additional unsaturated region equilibrium points. Evaluation of this expression yields

$$d*^2 - (n_1 + n_2) d* + n_1 n_2 + \frac{R_1}{R_2} = 0 \qquad (13.23)$$

$$d* = .56 \quad , \quad 9.8$$

The equilibrium point d* = .56 is significant; it is a saddle point. However, the equilibrium point at d* = 9.8 lies well outside the unsaturated operating range of the system, and hence has little effect on the transient waveforms. Unfortunately, its presence complicates the analytical expressions severely.

Notice that the two roots of Eq. (13.23) are well-separated. This suggests that one may factor Eq. (13.23) analytically, as follows:

$$\hat{d}^2 - (n_1 + n_2)\, \hat{d} + n_1 n_2 + R_1/R_2$$

$$\cong (n_1 n_2 + \frac{R_1}{R_2} - (n_1 + n_2)\hat{d})\,(1 - \hat{d}/(n_1 + n_2)) \qquad (13.24)$$

valid provided $(n_1 + n_2)^2 >> \left| n_1 n_2 + R_1/R_2 \right|$

Eq. (13.24) predicts that the unsaturated region equilibrium points occur at

$$d^* \cong .53, \ 10.4 \qquad (13.25)$$

Hence, Eq. (13.24) appears to be an accurate approximation of Eq. (13.23).

Furthermore, if

$$\left| \frac{\hat{d}(t)}{n_1 + n_2} \right| = \left| \frac{f_2\, \hat{v}(t)}{n_1 + n_2} \right| << 1 \qquad (13.26)$$

everywhere inside the unsaturated operating range of the regulator, then the virtual equilibrium point at $d^* \cong (n_1 + n_2)$ may be neglected entirely. This is indeed the case here, where $(n_1 + n_2) = 10.4$, and $\left| \hat{d}(t) \right| \leq .69$. This is a useful approximation for many systems.

With these approximations, Eq. (13.22) becomes

$$\frac{d\hat{v}(t)}{dt} + \omega_c\, \hat{v}(t)\, [1 - \hat{v}(t)/\hat{v}^*] \cong 0 \qquad (13.27)$$

where

$$\omega_c = \frac{1}{C(R_2 \| \frac{R_1}{n_1 n_2})} = 2\pi(100 \ Hz)$$

$$\hat{v}* \cong - \frac{n_1 n_2 + R_1/R_2}{f_2(n_1 + n_2)} = -1.12 \ Volts$$

Eq. (13.27) is the basic state equation which describes the slow mode, with the effect of the virtual equilibrium point at d* = 10.4 neglected. It is now easily solved by integration:

$$\int_{\hat{v}(0)}^{\hat{v}(t)} \frac{du}{u(1 - u/\hat{v}*)} \cong - \int_{0}^{t} \omega_c \ d\tau \tag{13.28}$$

Evaluation of the integrals and solution for $\hat{v}(t)$ yields

$$\hat{v}(t) \cong \frac{\hat{v}(0) \ e^{-\omega_c t}}{1 + \frac{\hat{v}(0)}{\hat{v}*}(e^{-\omega_c t} - 1)} \tag{13.29}$$

Eq. (13.29) is the basic result of this section; it is the approximate large-signal response of the slow mode. Note that, for $|\hat{v}(0)| << |\hat{v}*|$, the denominator becomes nearly unity and the response approaches the small-signal result:

$$\hat{v}(t) \cong \hat{v}(0) \ e^{-\omega_c t} \tag{13.30}$$

valid for $|\hat{v}(0)| << |\hat{v}*|$
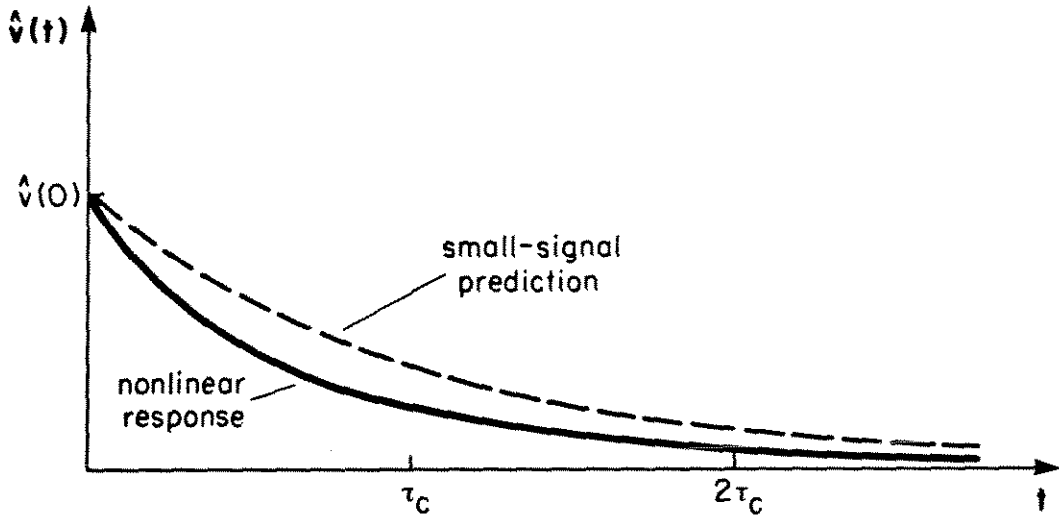
Fig. 13.14. Unsaturated region slow mode waveforms for the case
$\hat{v}(0) > 0$. The solutions are stable, and decay more
rapidly than the small-signal result.

It is of interest to sketch the response for larger values of
$\hat{v}(0)$. The first case considered is when $\hat{v}(0) > 0$. In this case, the
denominator of Eq. (13.29) is greater than 1:

$$1 + \frac{\hat{v}(0)}{\hat{v}^*} (e^{-\omega_c t} - 1) \geq 1 \qquad (13.31)$$

for $\hat{v}(0) > 0$

since $\hat{v}^*$ is negative. As a result, the response given by Eq. (13.29)
decays more rapidly than the small-signal response of Eq. (13.30), as
shown in Fig. 13.14. It is clear that the system is stable for all
$\hat{v}(0) > 0$.
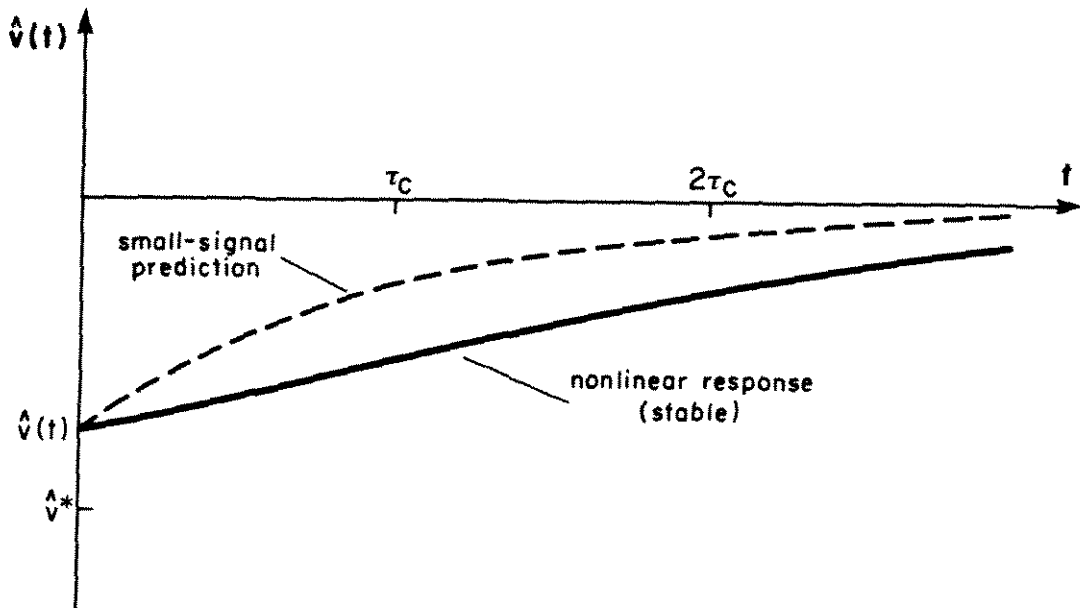
Fig. 13.15. Slow mode waveforms for the case $0 > \hat{v}(0) > v*$. The solutions are stable but decay slower than the small-signal result.

The next case is $\hat{v}(0) = 0$, where the system is started at the quiescent operating point. The solution is trivial, given by $\hat{v}(t) = 0$ for all t.

For $0 > \hat{v}(0) > \hat{v}*$, the denominator of Eq. (13.29) is less than one but greater than zero:

$$0 < 1 + \frac{\hat{v}(0)}{\hat{v}*} (e^{-\omega_c t} - 1) < 1 \qquad (13.32)$$

for $0 > \hat{v}(0) > \hat{v}*$

again since $\hat{v}*$ is negative. The response given by Eq. (13.29) decays slower than the small-signal response of Eq. (13.30), as shown in Fig. 13.15. Nonetheless, the solution is stable and eventually reaches the quiescent point $\hat{v} = 0$.
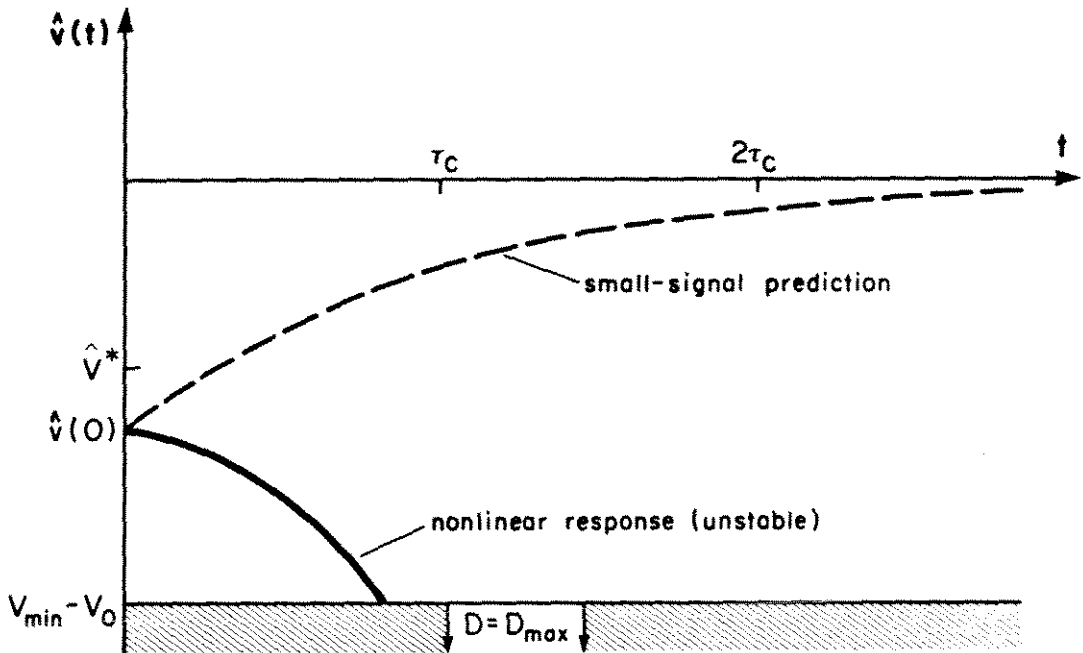
Fig. 13.16. Slow mode waveforms for the case v* > v̂(0). The solutions are unstable.

The fourth case is $\hat{v}(0) = \hat{v}*$. The solution then becomes

$$v(t) = \hat{v}* \qquad \text{for all } t \qquad\qquad (13.33)$$

for $\hat{v}(0) = \hat{v}*$

In this case, the system is started exactly at the (unstable) saddle point at $\hat{v} = \hat{v}*$.

The final case is where $\hat{v}(0)$ is more negative than $\hat{v}*$. The denominator of Eq. (13.29) is then negative at $t = 0$, passes through zero after some finite time, and goes to +1 as $t \to \infty$. Hence, the system diverges in finite time, as shown in Fig. 13.16. Of course, for $\hat{v}(t) + V_0 < V_{min}$, the system leaves the unsaturated region where Eq. (13.29) is valid; the model for the $D = D_{max}$ saturated region (given later in this chapter) must then be used. Nonetheless, the behavior for $\hat{v}(0) \leq \hat{v}*$ is undesirable and must be corrected before

a sound design can be obtained. Some methods for achieving this are discussed later in this chapter.

The complete inductor current waveform may now be calculated; it is the combination of Eqs. (13.20) and (13.29). The complete capacitor voltage waveform is given by Eq. (13.29) alone. Thus, the complete unsaturated mode response is as summarized below:

$$\hat{v}(t) \cong \frac{\hat{v}(0)\, e^{-\omega_c t}}{1 + \frac{\hat{v}(0)}{\hat{v}^*}(e^{-\omega_c t} - 1)}$$

$$\tag{13.34}$$

$$\hat{i}(t) \cong \hat{i}(0)\, e^{-\omega_L t} - \frac{\hat{v}(t)}{R_1}\,(n_1 + f_2\,\hat{v}(t))\,(1 - e^{-\omega_L t})$$

The state plane trajectories in the unsaturated region can now be plotted, as in Fig. 13.17. As noted before, the fast mode trajectories are approximately vertical lines, and end at the parabola described by Eq. (13.21). The slow mode trajectories move along this parabola, and end at the quiescent operating point for $\hat{v}(0) > \hat{v}^*$. They diverge and end at the $D = D_{max}$ region boundary for $\hat{v}(0) < \hat{v}^*$.

Thus, simple, approximate analytical expressions are found for the response of this boost regulator example in the unsaturated mode. Two key approximations are made. First, the occurrence of two approximate natural modes of the system is assumed, and the interaction which actually takes place between them is neglected. This is justified because their time constants are widely separated.
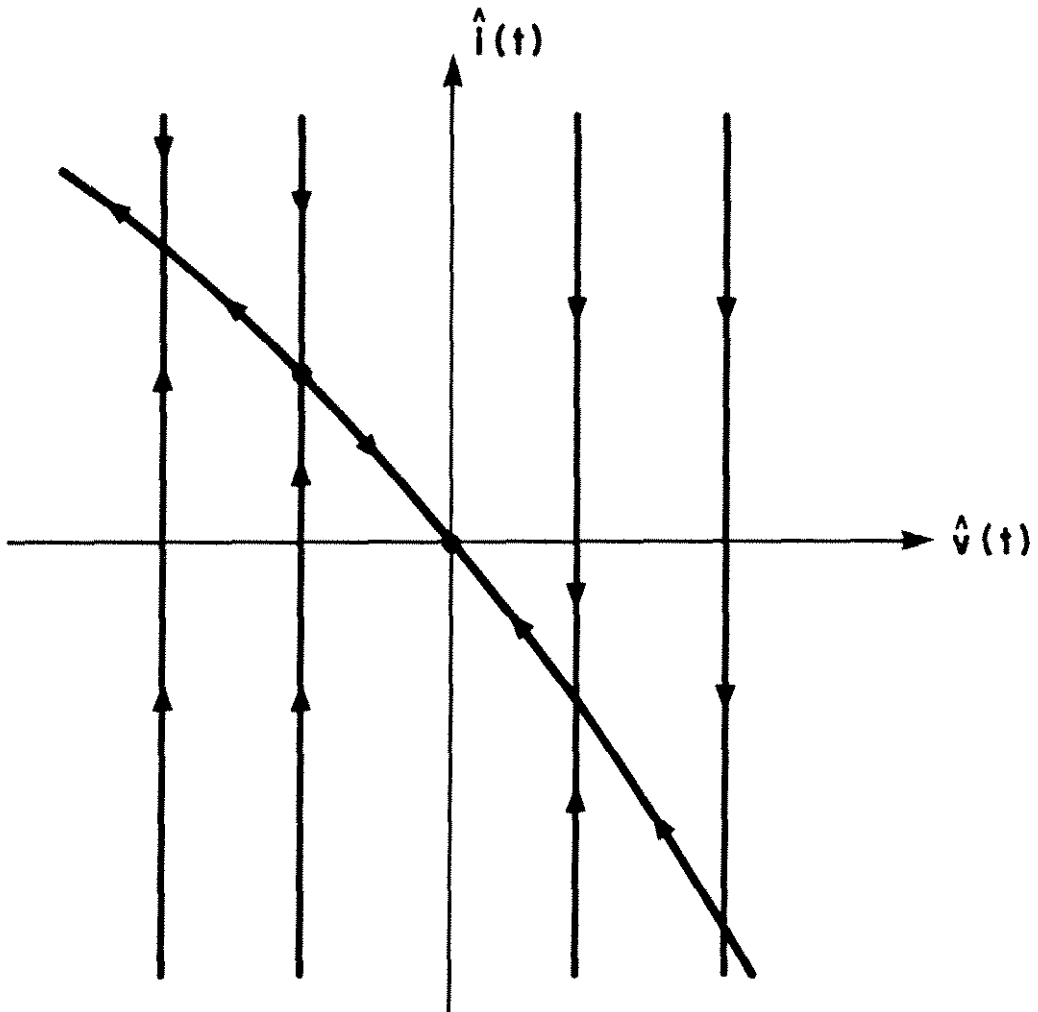
Fig. 13.17. Complete unsaturated region state-plane portrait. A saddle point occurs along the parabola which describes the slow mode at $\hat{v} = \hat{v}^{\star}$. Solutions are stable for $\hat{v}(0) > \hat{v}^{\star}$, and unstable for $\hat{v}(0) < \hat{v}^{\star}$.

Second, the influence of the virtual equilibrium point which occurs at $d^{\star}$ = 9.8 is neglected; this simplifies the analytical expressions with little loss of accuracy. The predicted waveforms exhibit the correct qualitative behavior, including the presence of a saddle point and unstable solutions. It is shown in Chapter 14 that the results are quantitatively correct also.

13.6 $D = D_{min}$ Saturated Region Waveforms

It is desired to calculate the trajectories and waveforms in the other regions as well. In this section, the equilibrium point and transient waveforms for the $D = D_{min}$ saturated region are found. Since the duty ratio is constant, the state equations become linear in this region, and hence are easily solved.

Eq. (11.17) is the general continuous-time state equation for the saturated regions. Evaluation of this expression for the boost regulator example yields

$$L \frac{di(t)}{dt} = - R_\ell \, i(t) - D'_{min} \, v(t) + V_g \qquad (13.35a)$$

$$C \frac{dv(t)}{dt} = D'_{min} \, i(t) - v(t)/R \qquad (13.35b)$$

valid for $v(t) \geq V_{max}$

$$i(t) \geq \frac{T_s}{L} (D'_{min} \, v(t) - V_g)$$

Since these state equations are linear, their solution is straight-forward. The waveforms in this region are decaying exponentials or damped sinusoids.

The same type of approximation used in the unsaturated region may be used here if desired. Owing to the large value of output capacitance used, the natural frequencies of the system in the $D = D_{min}$ region are well-separated, and the system is overdamped. Under these conditions,

the system again contains the following natural modes:

    (1) a fast mode, in which the inductor current changes rapidly while the capacitor voltage remains nearly constant, and

    (2) a slow mode, in which the capacitor voltage changes slowly and is followed by the inductor current.

This suggests solving the two modes separately, as before.

With the assumption that the fast mode occurs in a time interval sufficiently short, the capacitor voltage remains essentially constant. Eq. (13.35a) then becomes

$$L \frac{di(t)}{dt} \cong - R_\ell \, i(t) - D'_{min} \, v(0) + V_g \tag{13.36}$$

$$i(0) \text{ is given}$$

The solution of this linear differential equation is

$$i(t) \cong i(0) \, e^{-\omega_3 t} + \frac{V_g - D'_{min} v(0)}{R_\ell} (1 - e^{-\omega_3 t}) \tag{13.37}$$

where $\quad \omega_3 = \dfrac{R_\ell}{L} = 2\pi(1.1 \text{ kHz})$

$$\tau_3 = L/R_\ell$$

after the fast mode has decayed,

$$i(t) \rightarrow \frac{V_g - D'_{min} V}{R_\ell} \tag{13.38}$$

valid for $t >> \tau_3$

The inductor current decays exponentially during the fast mode, and eventually reaches the quasi-equilibrium value given in Eq. (13.38). By assumption, the capacitor voltage remains essentially constant.

For times much greater than τ_3, the fast mode has decayed, and hence the inductor current is at the quasi-equilibrium value given in Eq. (13.38). Substitution of this expression into Eq. (13.35b) yields

$$C \frac{dv(t)}{dt} \cong - \frac{v(t)}{R||R_\ell/D_{min}^{'2}} + \frac{D_{min}' V_g}{R_\ell} \tag{13.39}$$

The solution of this linear differential equation is

$$v(t) \cong v(0) e^{-\omega_4 t} + \frac{V_g}{D_{min}'} \frac{1}{1 + R_\ell/D_{min}' R} (1 - e^{-\omega_4 t}) \tag{13.40}$$

where $\omega_4 = \dfrac{1}{R||R_\ell/D_{min}^{'2} C} = 2\pi \ (20 \ Hz)$

For large t, Eqs. (13.40) and (13.37) predict that the system reaches the $D = D_{min}$ saturated region equilibrium point (I_{min0}, V_{min0}), where

$$V_{min0} = \frac{V_g}{D_{min}'} \frac{1}{1 + R_\ell/D_{min}^{'2} R} = 13.6 \ Volts$$

$$\tag{13.41}$$

$$I_{min0} = \frac{V_g}{R_\ell + D_{min}^{'2} R} = .45 \ Amps$$
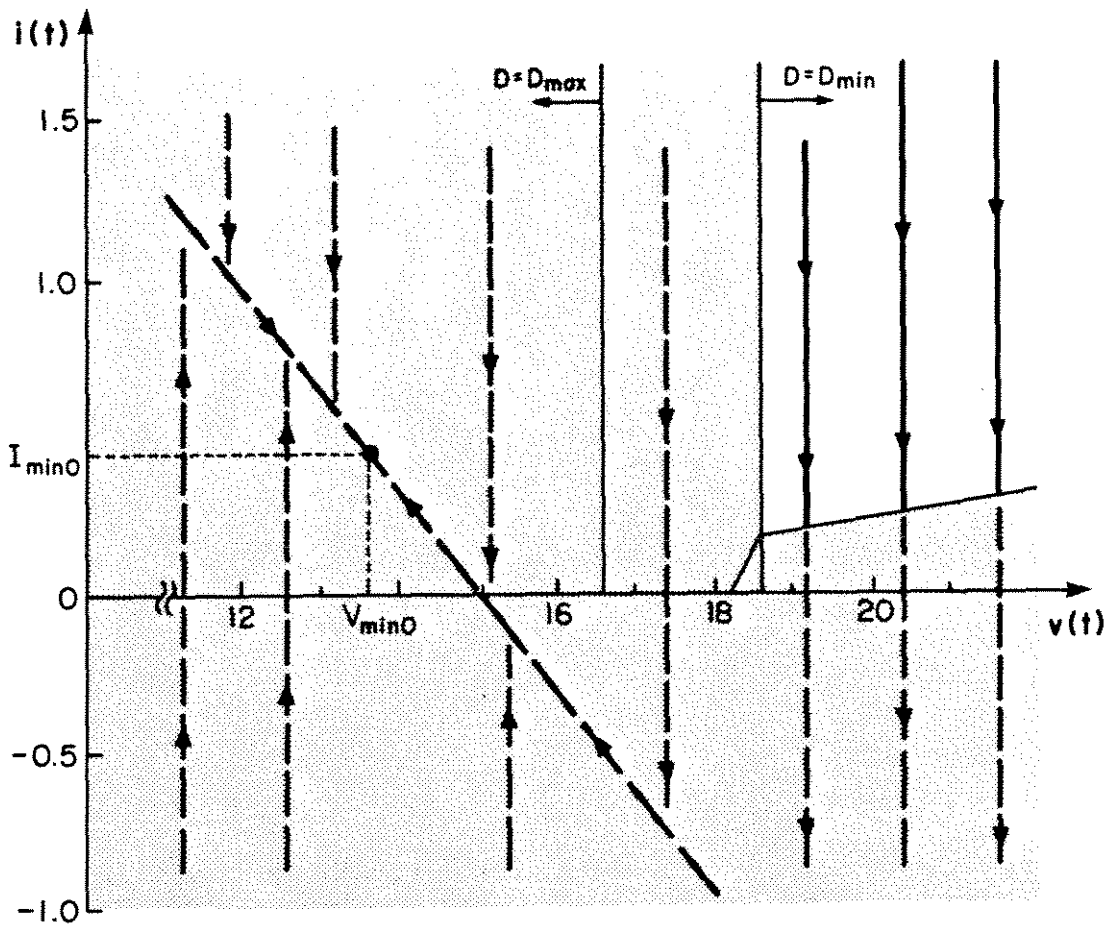
Fig. 13.18. The trajectories predicted by the $D = D_{min}$ saturated region state equations. These solutions are not valid outside of the $D = D_{min}$ saturated region (shaded area).

These relations could also be found by evaluation of Eqs. (12.10) and (12.11).

The $D = D_{min}$ saturated region state plane trajectories are plotted in Fig. 13.18. The fast mode trajectories are nearly vertical lines, since the capacitor voltage remains essentially constant during this time. The slow mode trajectories lie along the line described by Eq. (13.38), and end at the (virtual) equilibrium point (I_{min0}, V_{min0}).
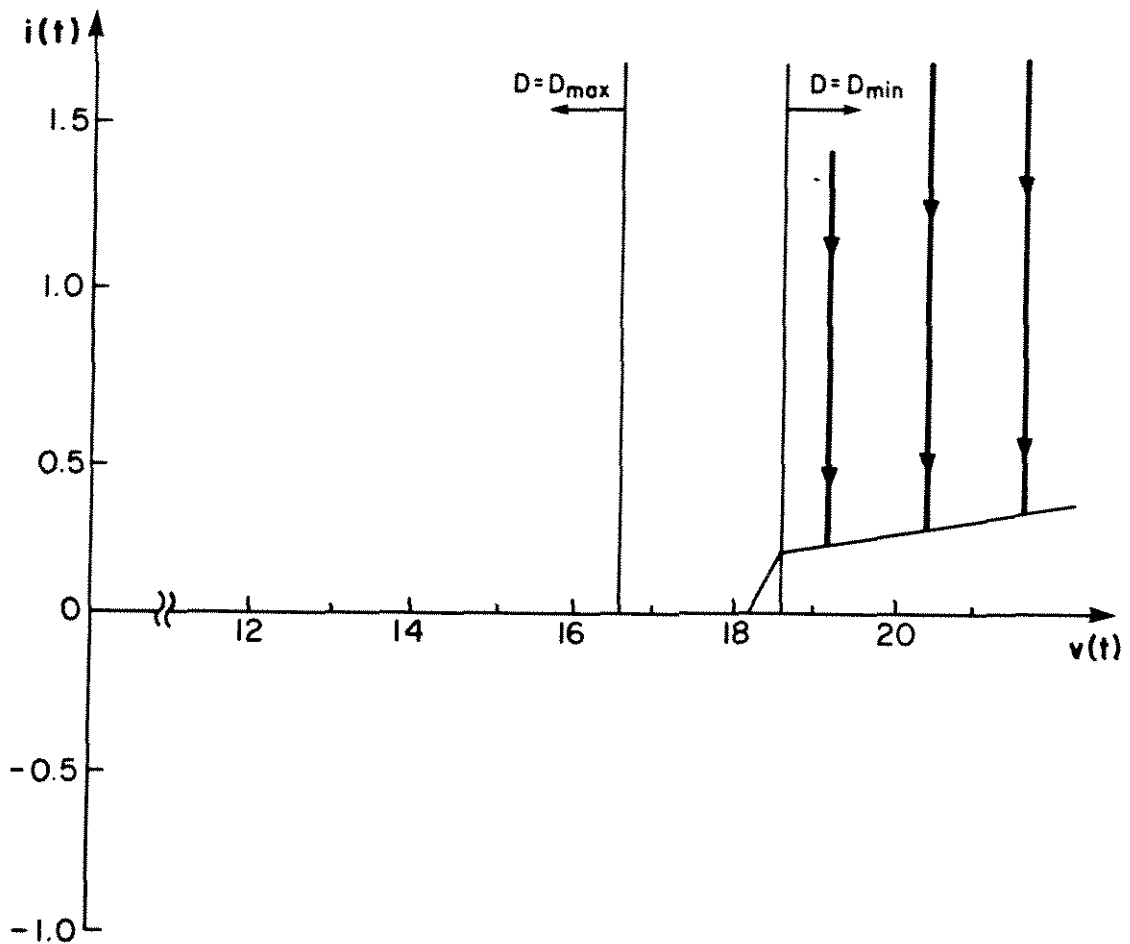
Fig. 13.19. The trajectories in the D = D_min saturated region are nearly vertical lines which end at the transient discontinuous conduction region boundary.

Note that the slow mode and the equilibrium point lie outside the $D = D_{min}$ saturated region where Eq. (13.35) is valid. As a result, the system leaves the $D = D_{min}$ saturated region before the slow mode or virtual equilibrium point is reached. As shown in Fig. 13.19, only the fast mode trajectories inside the region are valid.

Thus, in the $D = D_{min}$ saturated region, the output voltage remains essentially constant while the inductor current decays exponentially. As shown in Fig. 13.19, the trajectories are nearly vertical lines which end at the transient discontinuous conduction mode boundary.

13.7 $D = D_{max}$ Saturated Region Waveforms

The analysis for this region is similar to the analysis of the
previous section. The system is again described by a fast mode and a
slow mode, and contains one equilibrium point. The major difference
lies in the fact that the slow mode trajectories occur inside the
$D = D_{max}$ saturated region, and the equilibrium point may be real
rather than virtual. The presence of a real equilibrium point inside
this region indicates that solutions which do not converge to the
desired quiescent operating point occur.

The continuous-time state equations for this region may be found
by evaluation of Eq. (11.17); the result is

$$L \frac{di(t)}{dt} = - R_\ell \, i(t) - D_{max}' \, v(t) + V_g \tag{13.42a}$$

$$C \frac{dv(t)}{dt} = D_{max}' \, i(t) - v(t)/R \tag{13.42b}$$

where $D_{max}' = 1 - D_{max}$

valid for $v(t) \leq V_{min}$

$\qquad\quad i(t) \geq 0$

The state equations are again linear in this region, and their
solutions are decaying exponentials or damped sinusoids. For this
example, the time constants of the two modes of the system are again
well-separated, and the response may be approximated if desired by
the same procedure used for the $D = D_{min}$ saturated mode. The result
for the fast mode is

$$i(t) \cong i(0) \, e^{-\omega_3 t} + \frac{V_g - D'_{max} v(0)}{R_\ell} (1 - e^{-\omega_3 t}) \qquad (13.43)$$

where $\omega_3 = \dfrac{R_\ell}{L} = 2\pi \ (1.1 \ \text{kHz})$

$\tau = 1/\omega_3$

After the fast mode has decayed,

$$i(t) \cong \frac{V_g - D'_{max} V}{R_\ell} \qquad (13.44)$$

valid for $t >> \tau_3$

Insertion of Eq. (13.44) into Eq. (13.42b) and solution for $v(t)$ then yields the slow mode response:

$$v(t) \cong v(0) \, e^{-\omega_5 t} + \frac{V_g}{D_{max}} \frac{1}{1 + R_\ell/D_{max}^{'2} R} (1 - e^{-\omega_5 t}) \qquad (13.45)$$

where $\omega_5 = \dfrac{1}{R||R_\ell/D_{max}^{'2} \ C} = 2\pi \ (1.8 \ \text{Hz})$

After both modes have decayed, the system reaches the $D = D_{max}$ saturated region equilibrium point, given by

$$V_{max0} = V_g \frac{D'_{max} R}{R_\ell + D_{max}^{'2} R} = 0 \ \text{Volts}$$

$$\qquad (13.46)$$

$$I_{max0} = \frac{V_g}{R_\ell + D_{max}^{'2} R} = 5 \ \text{Amps}$$
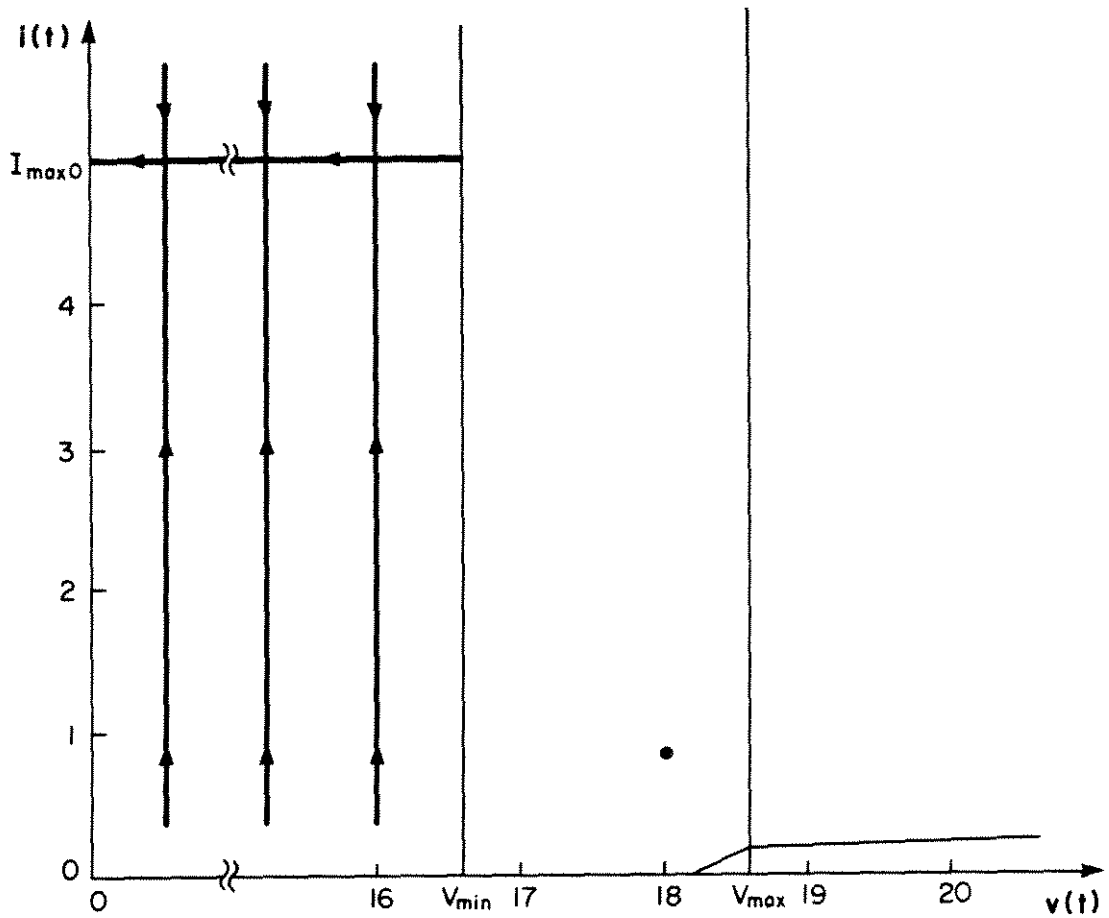
Fig. 13.20. The trajectories in the $D = D_{max}$ *saturated region. All solutions in this region converge to the undesired real equilibrium point at* (5A,0V).

The $D = D_{max}$ saturated region trajectories are plotted in Fig. 13.20. The fast mode trajectories are again nearly vertical lines since the capacitor voltage reamins nearly constant during this time. The slow mode trajectories lie along the line given by Eq. (13.44), and end at the real stable equilibrium point (I_{max0}, V_{max0}).

This behavior is very undesirable; all solutions in the $D = D_{max}$ saturated region converge to the unwanted real equilibrium point (I_{max0}, V_{max0}) rather than the quiescent operating point. Thus, it is possible for the system to "hang up". This situation may be rectified by the addition of current feedback or current limiting (discussed in Section 13.9), or by decreasing D_{max} (discussed next).

Perhaps the simplest way to render this system globally stable is to limit the maximum duty ratio. For an overdamped system such as this one, the system becomes globally stable for $D_{max} < D_0 + d^*$ (d^* is given by Eq. (13.23)). As an example of this, the trajectories are plotted in Fig. 13.21 for the case $D_{max} = .825$. The fast mode trajectories are again vertical lines, and the slow mode trajectories again lie along the line described by Eq. (13.44), but the equilibrium point no longer lies inside the saturated region. Evaluation of Eq. (13.46) for this value of D_{max} yields

$$V_{max0} = 20.1 \text{ Volts}$$

$$I_{max0} = 3.8 \text{ Amps}$$

(13.47)

Hence, the $D = D_{max}$ saturated region equilibrium point now becomes virtual. Rather than hanging up inside the saturated region, the slow mode trajectories now enter the unsaturated region as shown.

Although this is a stable response, it may still be unacceptable. The peak transient current may be as much as five times the quiescent inductor current of .87 Amps. A very large inductor may be required to handle this current.
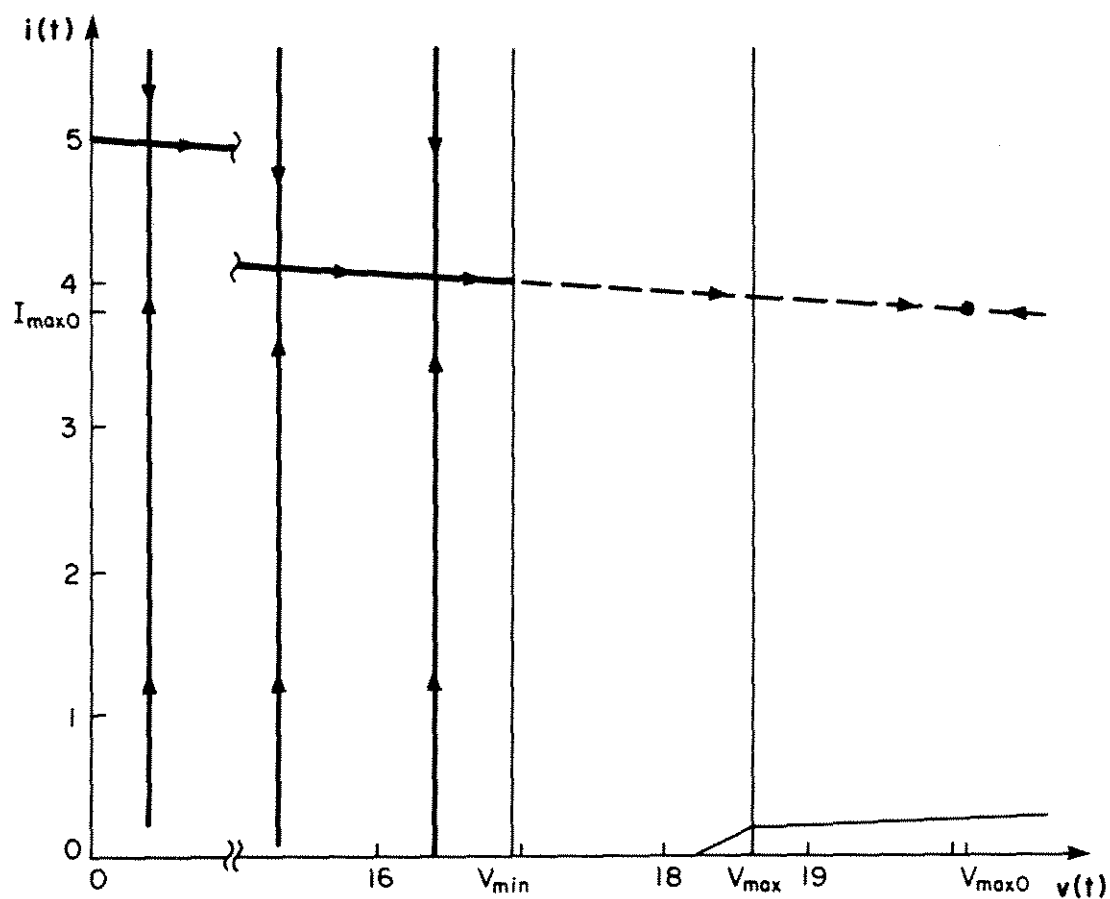
Fig. 13.21. The trajectories in the D = D$_{max}$ saturated region for the case when D$_{max}$ is limited to 0.825. All solutions inside this region now tend towards the unsaturated region.

13.8   Transient Discontinuous Conduction Mode Waveforms

The final region of operation is the transient discontinuous conduction mode. The state equations are nonlinear inside this region; however, the nonlinear terms are very small in magnitude. As a result, their effect is negligible, and the transient waveforms are very nearly decaying exponentials.

There are actually two subregions inside this region: (1) for $v(t) > V_{max}$, the duty ratio is saturated at $D = 0$, and (2) for $v(t) < V_{max}$, the duty ratio varies linearly with $v(t)$. The response in the saturated subregion is trivial; both the diode and the transistor remain off during the entire switching cycle. As a result, the inductor current is zero and the capacitor voltage decays through the load R. The waveforms can be written by inspection:

$$i(t) = 0$$
$$v(t) = v(0) \, e^{-\omega_6 t} \qquad\qquad (13.48)$$

where $\omega_6 = 1/RC = 2\pi(1.8 \text{ Hz})$

valid for $i = 0$ and $v \geq V_{max}$

For $v(t) < V_{max}$, the state equations are nonlinear; however, the solution is numerically very close to Eq. (13.48). The state equations may be found as described in Section 11.4; evaluation of Eqs. (11.41), (11.42), and (11.43) yields
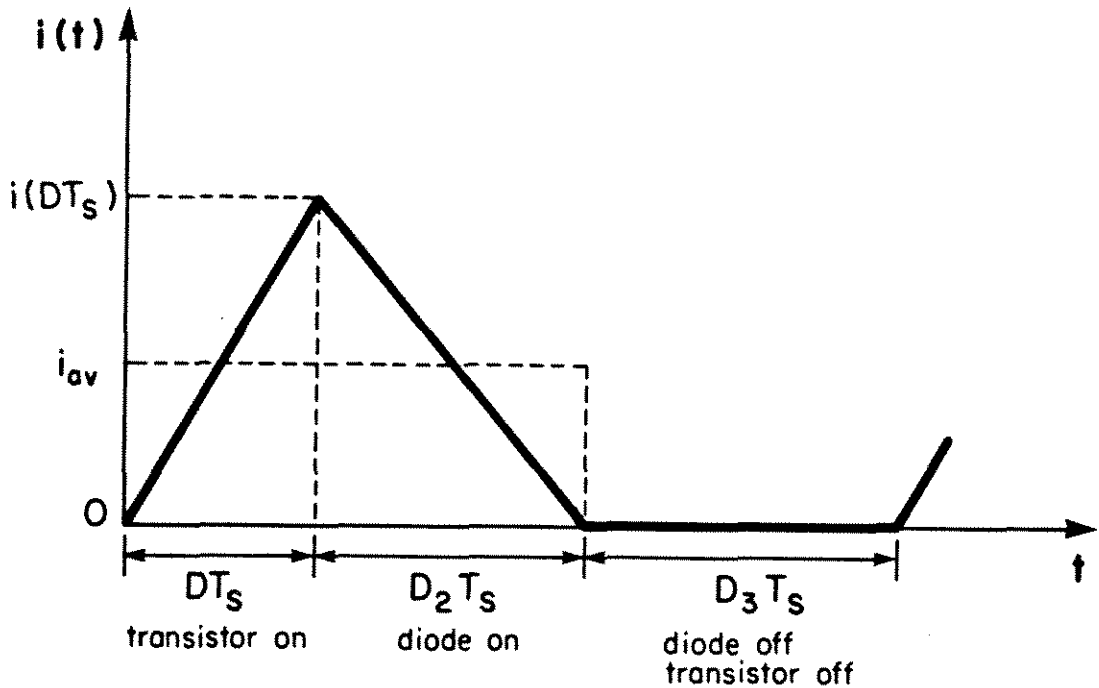
Fig. 13.22. The inductor current waveform for the transient discontinuous mode.

$$i_{av}(t) = \frac{V_g\, D(t)\, T_s}{2L} \qquad\qquad (13.49a)$$

$$0 = \frac{D(t) + D_2(t)}{L}\, V_g - \frac{D_2(t)}{L}\, v(t) \qquad\qquad (13.49b)$$

$$\frac{dv(t)}{dt} = -\frac{v(t)}{RC} + \frac{i_{av}(t)}{C}\, D_2(t) \qquad\qquad (13.49c)$$

The inductor current ceases to be an independent state since it is constrained to be zero at the beginning and end of each switching cycle. i_{av} is the value of the inductor current averaged over interval $(D + D_2)T_s$, as in Fig. 13.22. The system is nonlinear because i_{av} is a linear function of duty ratio $D(t)$ and hence of $v(t)$ also, and $D_2(t)$ is a nonlinear function of $v(t)$. These two terms appear multiplied together in Eq. (13.49c). Since Eq. (13.49 abc) represents a first-

order system, it could be integrated in a straightforward manner to yield an expression for $v(t)$. However, this is unnecessary because the amplitude of the linear term in Eq. (13.49c) is more than an order of magnitude larger than the nonlinear term everywhere inside the discontinuous conduction region. This can be seen as follows: From Eq. (13.49a),

$$\left|i_{av}\right|_{max} \leq \frac{V_g T_s}{2L} \cdot \max D(t) = .062 \quad \text{Amps} \tag{13.50}$$

From Eq. (13.49b),

$$\left|D_2\right|_{max} \leq \max \frac{D V_g}{(V - V_g)} = .825 \tag{13.51}$$

Hence, the magnitude of the nonlinear term is less than

$$\left|i_{av}\right|_{max} \left|D_2\right|_{max} / C = 17.6 \text{ V/sec} \tag{13.52}$$

The magnitude of the linear term is bounded below by

$$\frac{\left|v(t)\right|_{min}}{RC} = 209 \text{ V/sec} \tag{13.53}$$

Hence, the effect of the nonlinear term is of second order. To a good degree of approximation,

$$\frac{dv(t)}{dt} \cong - \frac{v(t)}{RC} \tag{13.55}$$

$$v(0) \text{ given}$$

everywhere inside the transient discontinuous conduction region. The solution is then given by

$$v(t) \cong v(0) \; e^{-\omega_6 t} \tag{13.56}$$

for all i,v inside the discontinuous conduction region. This is a valid approximation whenever expression (13.53) is much larger than (13.52) in the worst case. This can be expressed as

$$\frac{V_b}{R} >> i_{av} D_2 \bigg|_{v = V_b} \tag{13.57}$$

where V_b is the output voltage at the edge of the discontinuous conduction region, as given by Eq. (13.15). Note that Eq. (13.57) is a measure of how far the system is from equilibrium in the region since, if the "much greater than" sign is replaced by an equal sign, then the right hand side of Eq. (13.49c) becomes zero at V_b, and hence the system is in equilibrium there. Therefore, one expects the above approximation to be valid as long as the quiescent operating point of the system lies sufficiently far from the discontinuous mode.

Thus, the state equations are nonlinear and first-order in the discontinuous conduction region. Although these equations could be integrated directly to obtain an expression for the voltage waveform in this mode, it is much simpler to approximate the solution by a decaying exponential. This approximation is valid whenever Eq. (13.57) is well-satisfied.
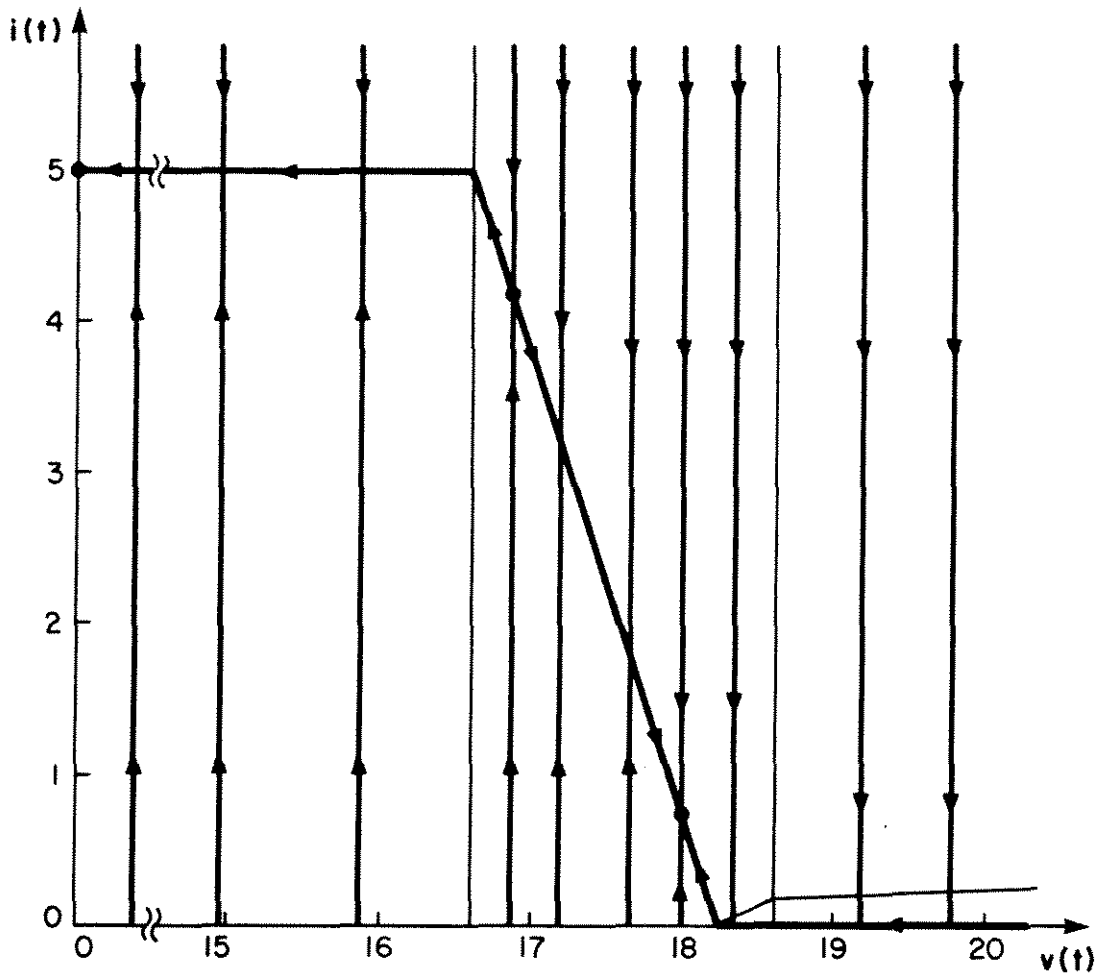
Fig. 13.23. State-plane trajectories of the entire system. Solutions converge to the quiescent operating point for v(0) > V*, but converge to the unwanted equilibrium point (5A,0V) for v(0) < V*. A saddle point occurs along the slow mode locus for v = V*.

13.9 Discussion

The complete state-plane portrait of the system can now be drawn, as in Fig. 13.23. The fast mode trajectories follow nearly vertical lines in all regions. The slow mode trajectories follow the i = 0 axis in the discontinuous conduction region, the parabola described by Eq. (13.21) in the unsaturated region, and the line given by Eq. (13.44) in the D = 1 saturated region. It is apparent that the solutions converge to the desired quiescent operating point (I_0, V_0)
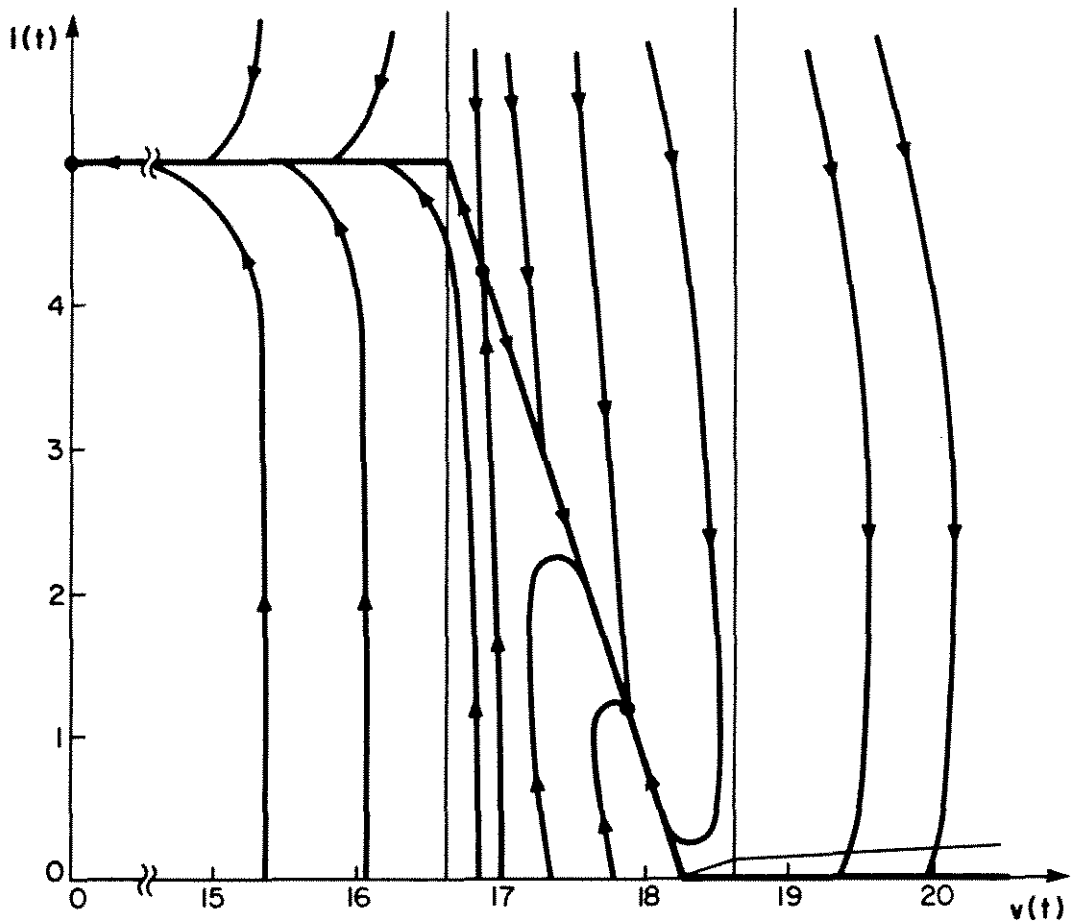
Fig. 13.24. The qualitative effect of a reduction in output capacitance C on the state-plane trajectories. The capacitor voltage increases for large values of D'i, and the trajectories become rounded for currents near quasi-equilibrium.

for v(0) > v*, but end at the unwanted equilibrium point in the D = 1 saturated region at (5A, 0v) for v(0) < v*. Peak transient currents and voltages can be found; in particular, the peak inductor current is larger than the quiescent value I_0 for v(0) < V_0.

The qualitative effect of a reduction in output capacitance C or increase in inductance L can also be deduced. In this case, since the time constants of the fast and slow modes are not as well-separated, the trajectories no longer follow vertical lines during a fast mode. Instead, one expects the capacitor voltage to increase for large values of D'i, the average diode current, as shown in the upper
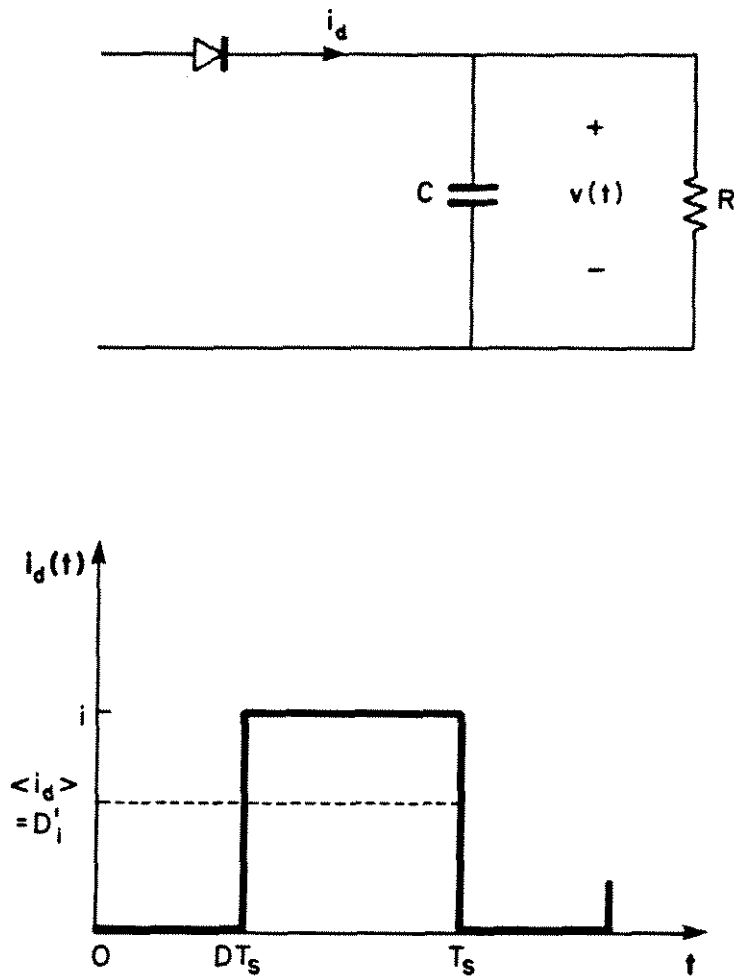
Fig. 13.25. *The average diode current is related to the inductor current by the duty ratio:* $\langle i_d \rangle = D'i$. *If the average diode current is greater than the load current in a given switching cycle, then the net output voltage increases over the given cycle.*

right-hand portion of Fig. 13.24. Also, one expects the slow mode to start before the fast mode has finished; hence, the trajectories become rounded for currents near quasi-equilibrium. The time domain waveforms for this case can be calculated exactly in the saturated regions since the state equations become linear there. The waveforms may also be calculated analytically in the discontinuous conduction mode since, although the state equations are nonlinear, they are

separable and of first order and hence can be integrated directly. Unfortunately, it is not known how to solve the second-order nonlinear state equations which describe the unsaturated region when the time constants of the modes are not widely separated. One must resort to the computer methods described in Section 12.4 for this case. Nonetheless, the qualitative argument presented above allows one to sketch the approximate state plane trajectories.

It is desired to ensure that all solutions converge to the quiescent operating point (I_0, V_0), and that peak current levels do not exceed some maximum value I_{lim}. One way to accomplish this is through the addition of a current limiting mode. A number of different current limiting modes are possible; probably the most useful one is known as the "current-programmed mode", where the converter duty ratio is determined by the times at which the instantaneous switch current reaches the maximum value I_{lim}. This has the effect of shortening the duty ratio when the inductor current is near I_{lim}, and it often is effective in limiting the peak inductor current. This mode has been previously modelled under steady-state and small-signal conditions [47,48,55,56].

The basic strategy employed in most current limiting modes is to reduce the duty ratio such that the switch or inductor current is regulated at the maximum level I_{lim}. Therefore, the trajectories follow a horizontal line at $i = I_{lim}$, as shown in Fig. 13.26, when the system operates in a properly functioning current limiting mode. Note that the unsaturated region saddle point and the $D = 1$ saturated region equilibrium point now become virtual. Furthermore, if the
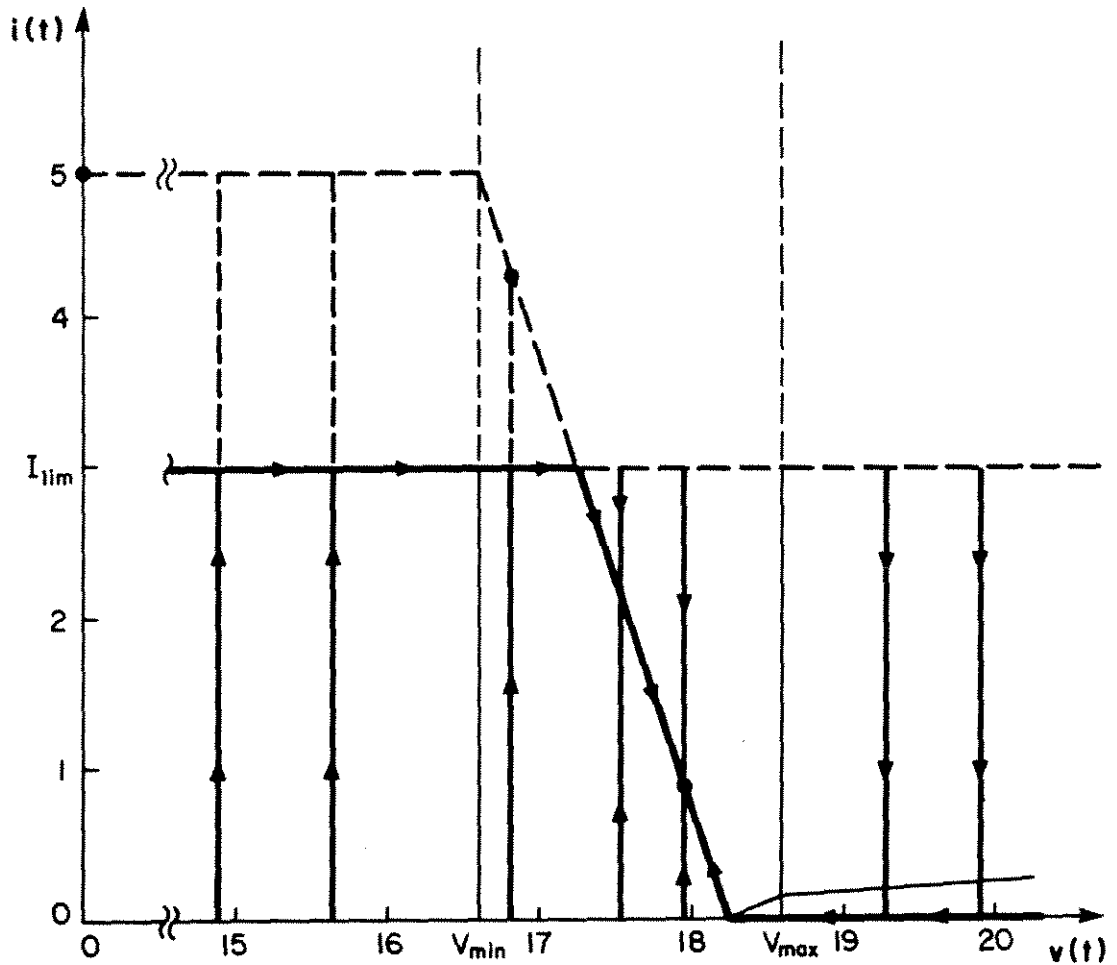
Fig. 13.26. *The effect of the addition of a properly designed current limiting mode. The trajectories follow the horizontal line* i = I_{lim}. *The system becomes globally stable.*

average diode current $<i_d>$ = D'i is greater than the load current v/R, then the net capacitor charge increases over each switching cycle, and hence the output voltage v increases. The current limiting mode trajectories then move towards the right as shown. It is apparent that the addition of a current limiting mode can render the boost example globally stable.
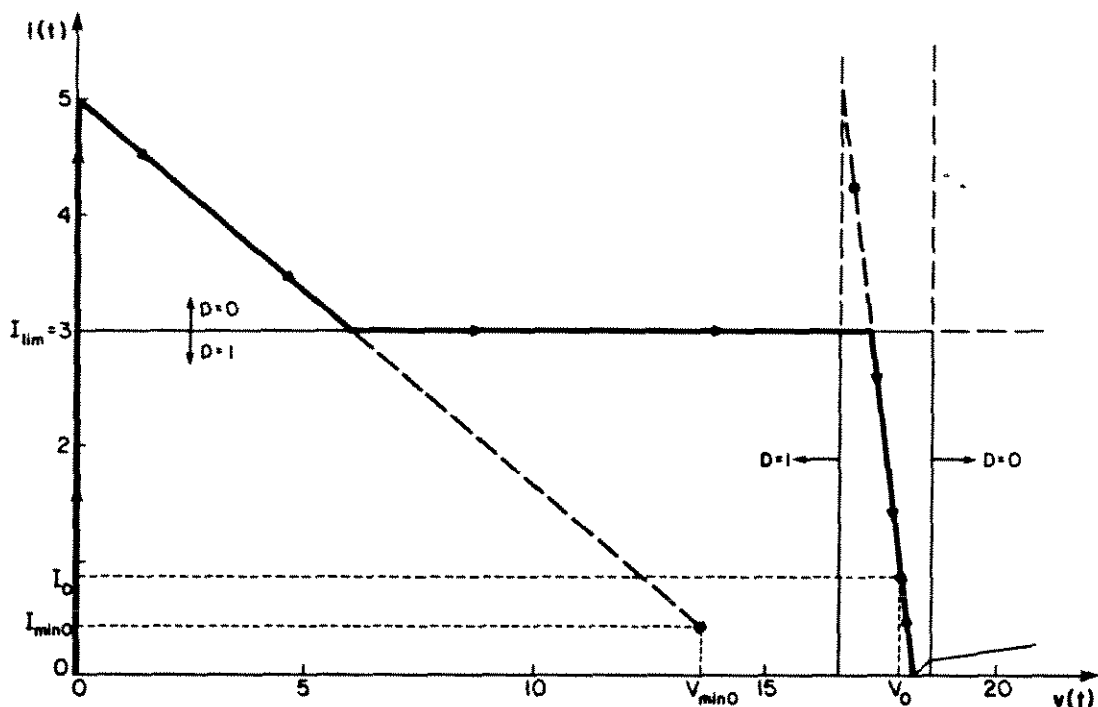
Fig. 13.27. The saturation of the pulse-width modulator affects the current limiting mode also. In this case, the D = 0 saturated mode occurs for all currents greater than I_{lim}. The trajectory at turn-on is shown.

The saturation of the pulse width modulator may affect the current limiting mode also. For example, consider the turn-on transient of the boost example with current limiting, where $i(0) = 0$ Amps and $v(0) = 0$ Volts. As shown in Fig. 13.27, the system begins in the D = 1 saturated region, the fast mode occurs, and the inductor current increases rapidly. When the inductor current reaches I_{lim}, the current limiting mode is invoked, and the duty ratio is decreased in an attempt to restrict the current below I_{lim}. However, since the output voltage is approximately zero, the current continues to rise independently of the duty ratio. This can be seen from the basic fast mode differential equation, repeated below:

$$L \frac{di(t)}{dt} \cong - R_{\ell} \, i(t) - D'(t) \, v(0) + V_g \Big|_{v(0) \, = \, 0}$$

$$= V_g - R_{\ell} \, i(t)$$

(13.58)

wnich is independent of $D(t)$. In consequence, the duty ratio is decreased to its minimum value of zero, where it remains as long as $i > I_{lim}$. During this time, the $D = D_{min}$ saturated region model of Section 13.6 applies. In particular, the current continues to rise until it reaches the quasi-equilibrium value of 5 Amps, given by Eq. (13.38). The slow mode described by Eq. (13.40) then occurs. Eventually, the inductor current again reaches I_{lim} and the current limiting mode functions properly.

Thus, it is apparent that the addition of a current limiting mode does not necessarily guarantee that peak current levels are always below the desired level I_{lim}. For the boost regulator example, it is impossible to control the duty ratio such that the peak current at start-up is only three Amps. Nonetheless, the addition of a current limiting mode is an effective means of obtaining global stability.

As discussed in Section 13.7, global stability may also be obtained by limiting the maximum duty ratio. However, since the slow mode inductor current is controlled by the parasitic inductor dc resistance R_{ℓ}, as given by Eq. (13.44), the peak current levels may be much larger than desired. As a result, the current limiting mode is usually preferred.

Thus, a simple boost regulator has been analyzed and is found to be stable for small signals but not globally stable. In particular, all transients for $v(0) < v^*$ converge to the undesired equilibrium point at zero voltage and high current. Approximate analytical expressions have been found for the nonlinear response of the converter, subject to key assumptions which require that the time constants of the system are well-separated, and that the third equilibrium point of the unsaturated region is extraneous and may be neglected. The various regions of operation in the state plane have been identified; in addition to the usual unsaturated mode, $D = D_{min}$ and $D = D_{max}$ saturated modes may occur, as well as a transient discontinuous conduction mode. The system may be rendered globally stable by the addition of a current limiting mode. Approximate analytical expressions may be found for the system trajectories; transient peak current levels then become apparent. In this way, the large-signal transient behavior of the boost regulator example may be understood, and the system may be intelligently designed.

CHAPTER 14

EXPERIMENTAL VERIFICATION

A boost regulator was constructed and measured to provide verification of the analysis of Chapter 13.

The schematic of the power stage is shown in Fig. 14.1. It is necessary to overdesign the system so that it can tolerate the large currents which occur when the quiescent operating point is not globally stable. Thus, the inductor, transistor, and diode must handle five Amps. This is also why the somewhat large value of 3 Ω is chosen for R_ℓ; since the peak currents are limited by R_ℓ, they would be even larger and more difficult to verify if a smaller value of R_ℓ were used.
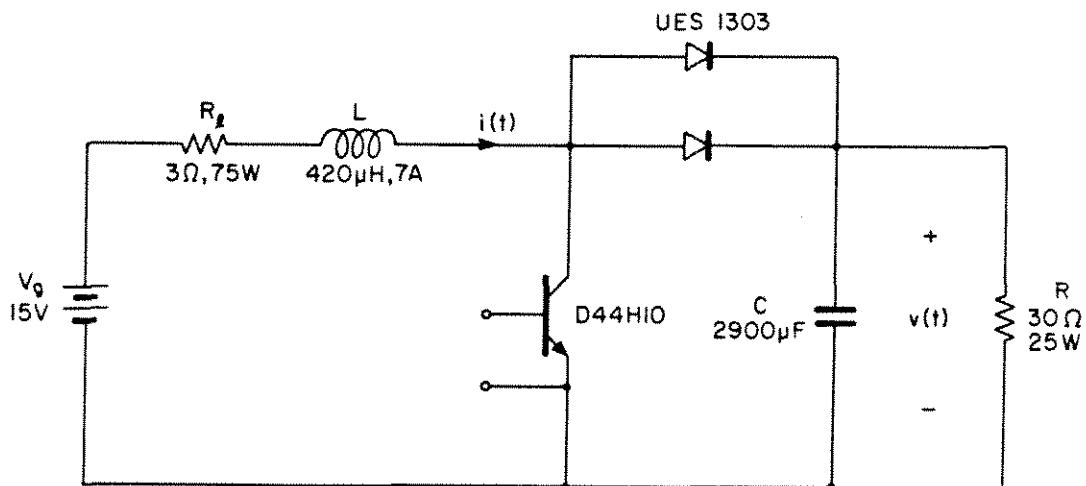
Fig. 14.1. Boost power stage used to experimentally verify the analysis of Chapter 13.
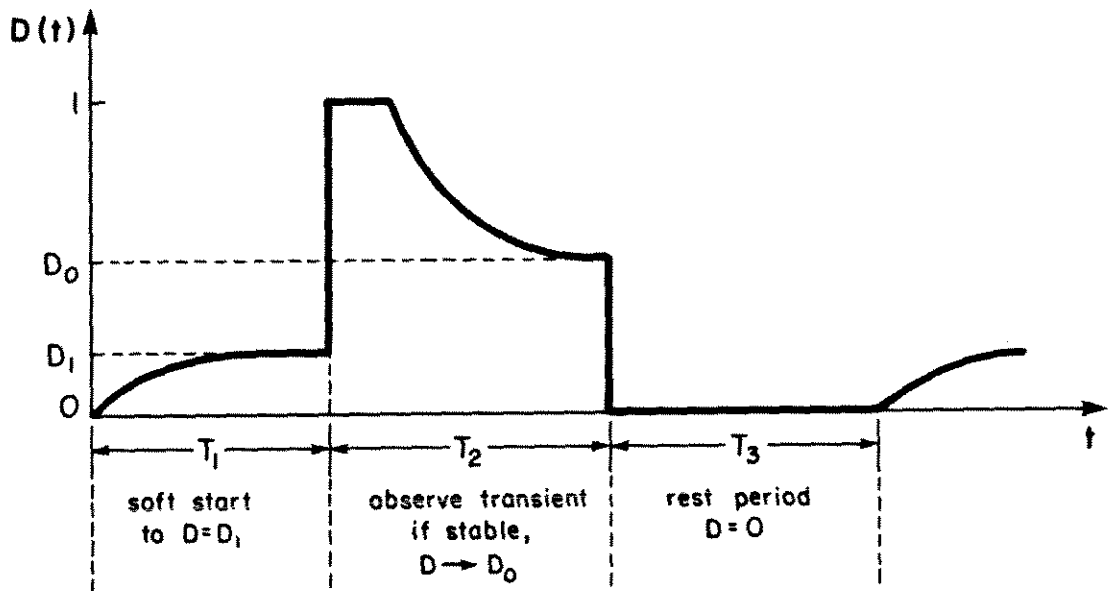
Fig. 14.2. So that the transient response may be observed on an oscilloscope, the system is excited repetitively.

It is desired to repetitively excite the circuit so that the transient response may be observed on an oscilloscope. This is done by cycling the system through the states shown in Fig. 14.2, as follows: During T_1, the system soft starts to a given perturbation duty ratio D_1. The feedback loop is disabled. During T_2, the feedback loop is enabled, and the resulting transient is observed on the oscilloscope. The system either converges to the desired quiescent operating point corresponding to $D = D_0$, or an unstable response occurs. During T_3, the feedback loop is disabled, the duty ratio is set to zero, and the power stage is allowed to cool off. The entire sequence then repeats.
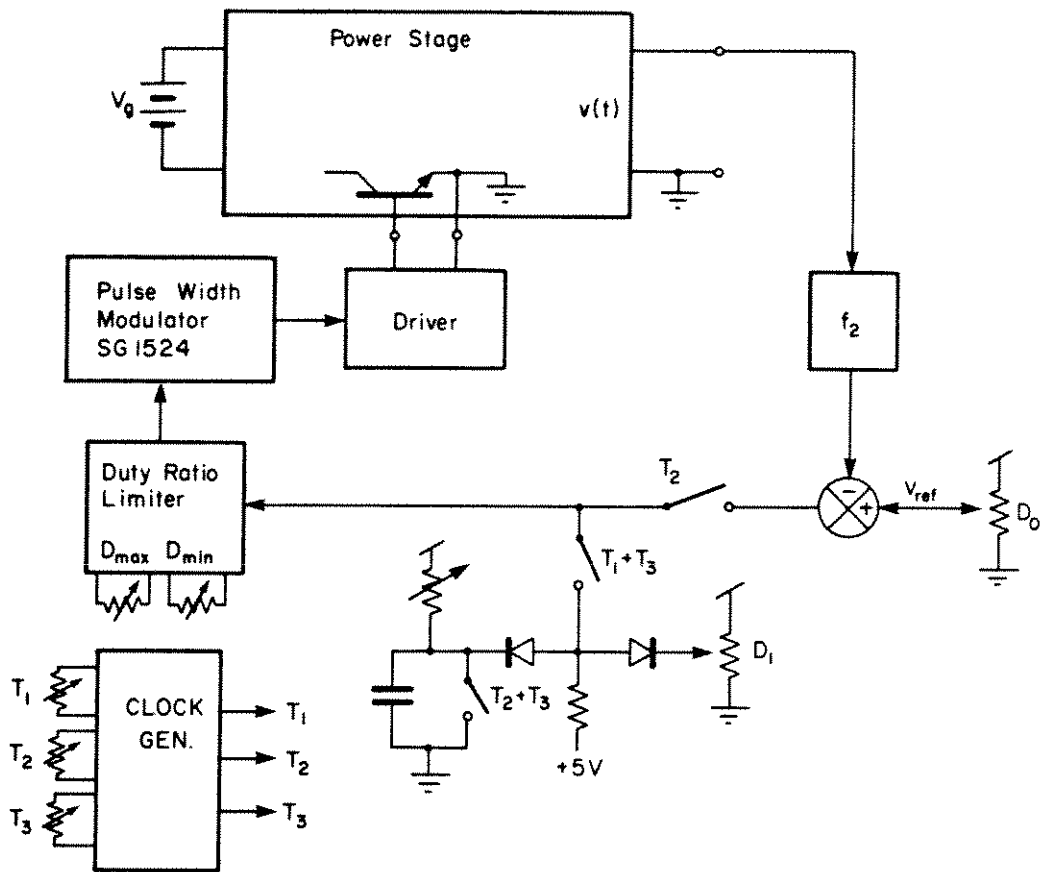
Fig. 14.3. Block diagram of the control circuit.

The block diagram of the control circuit is given in Fig. 14.3. A clock circuit generates the timing signals T_1, T_2, and T_3. These signals control analog switches which connect the input of the pulse width modulator to a soft-start circuit during interval T_1, to the voltage feedback during interval T_2, and to ground during interval T_3. A limiting circuit allows D_{max} and D_{min} to be artificially set to any level. A z-axis signal is provided so that the oscilloscope may be blanked during intervals T_1 and T_3; in this way, only the desired transients which occur during interval T_2 are seen on the oscilloscope.
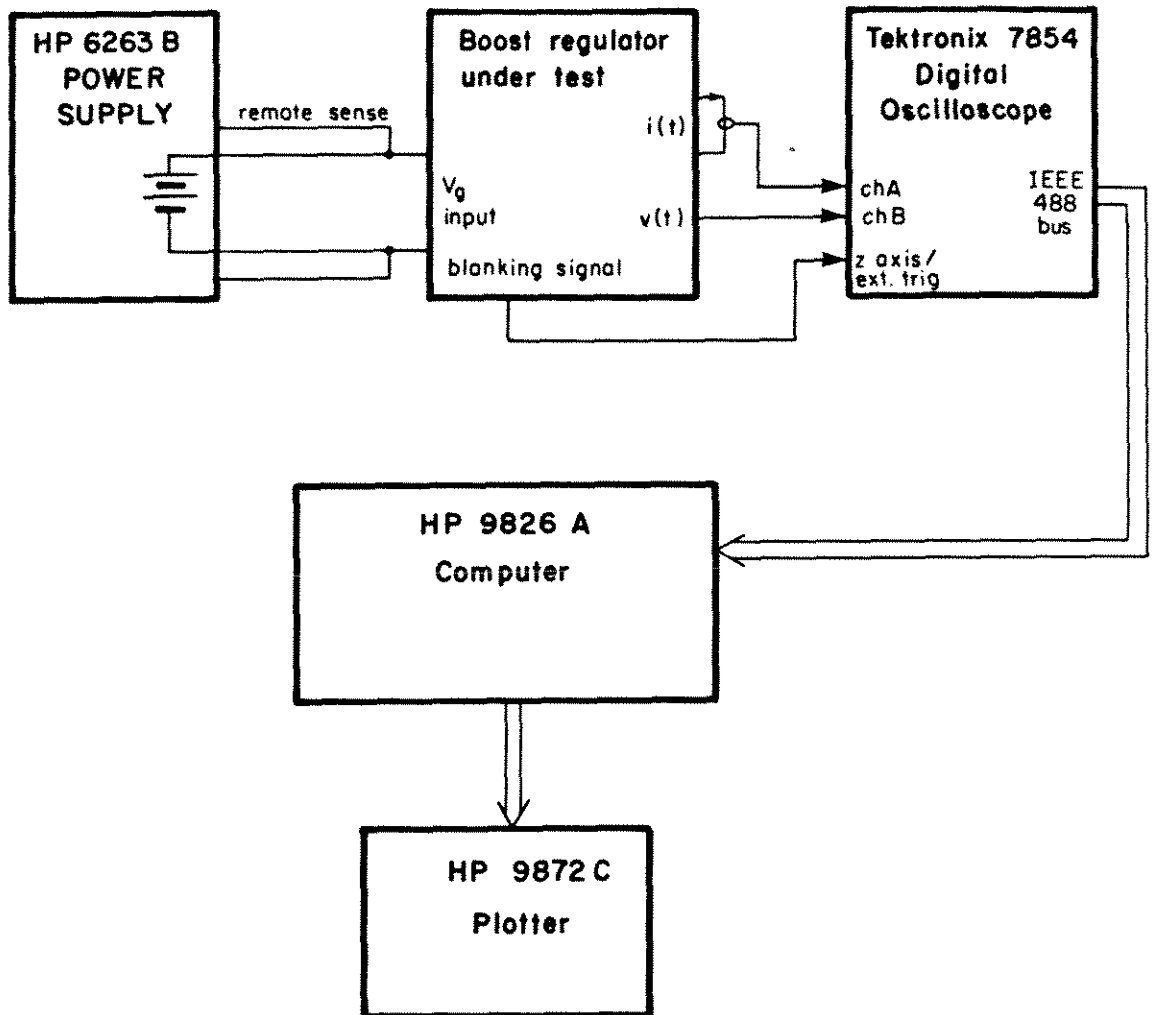
Fig. 14.4. *The test setup. The trajectories are acquired and stored by a computer, which can then plot several different trajectories on the same graph.*

The test setup is diagrammed in Fig. 14.4. A dc current probe measures the inductor current and a voltage probe measures the output voltage; the two signals are displayed on the oscilloscope in x-y mode to obtain the state plane trajectories. The use of a digital oscilloscope allows one to send the data to a computer. The computer stores the trajectories generated from several different initial conditions and then plots them on the same graph.
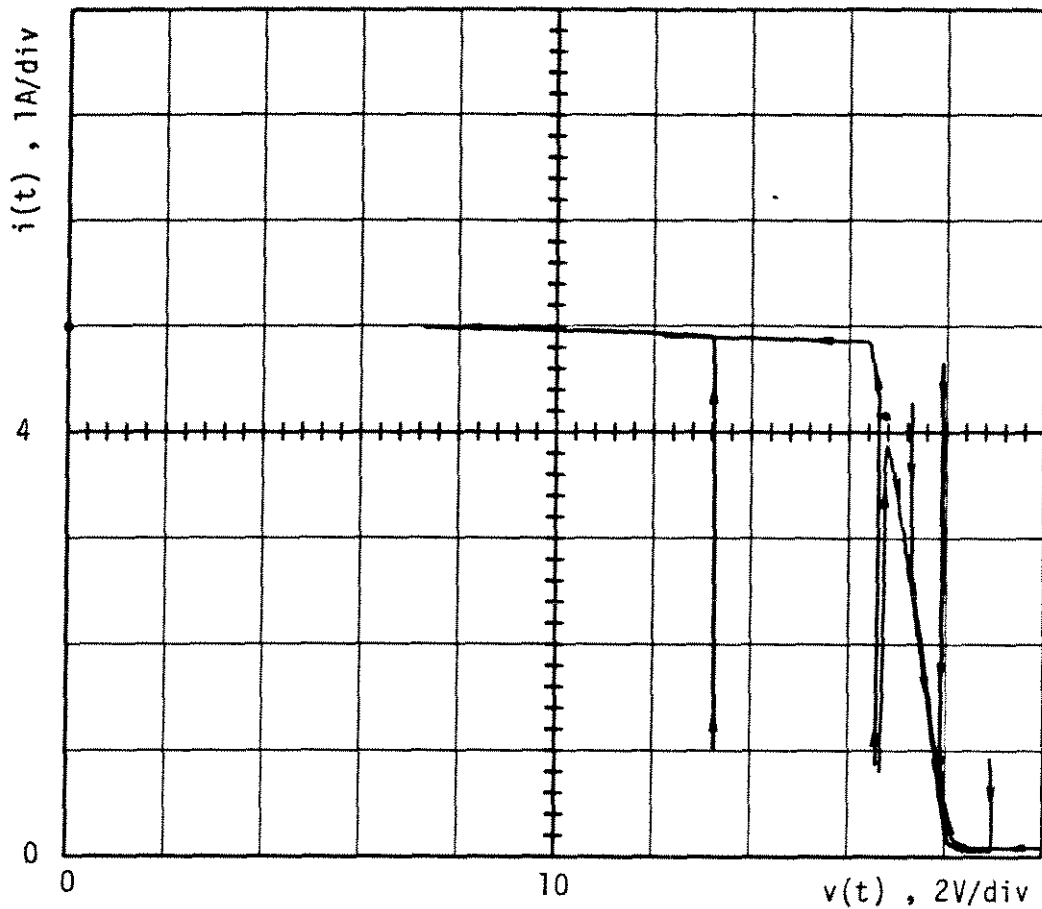
Fig. 14.5. Experimental data for the basic boost regulator. The results agree quite well with the predicted trajectories of Fig. 13.23.

The experimental data obtained for the basic boost regulator of Chapter 13 are shown in Fig. 14.5. The presence of unstable solutions for $v(0) < 16.8V$ is apparent. Also, the approximation of the fast mode by nearly vertical lines appears correct. The discontinuous conduction region can be seen along the horizontal axis for $V(t) > 18.25V$. The quiescent operating point at $v \cong 18V$, $i = 0.9A$ is stable since all solutions in its vicinity converge there, but the equilibrium point at $v = 16.8V$, $i = 4.25A$ is a saddle point because the fast mode trajectories in its vicinity converge but the slow mode trajectories diverge. The unstable trajectories tend towards the
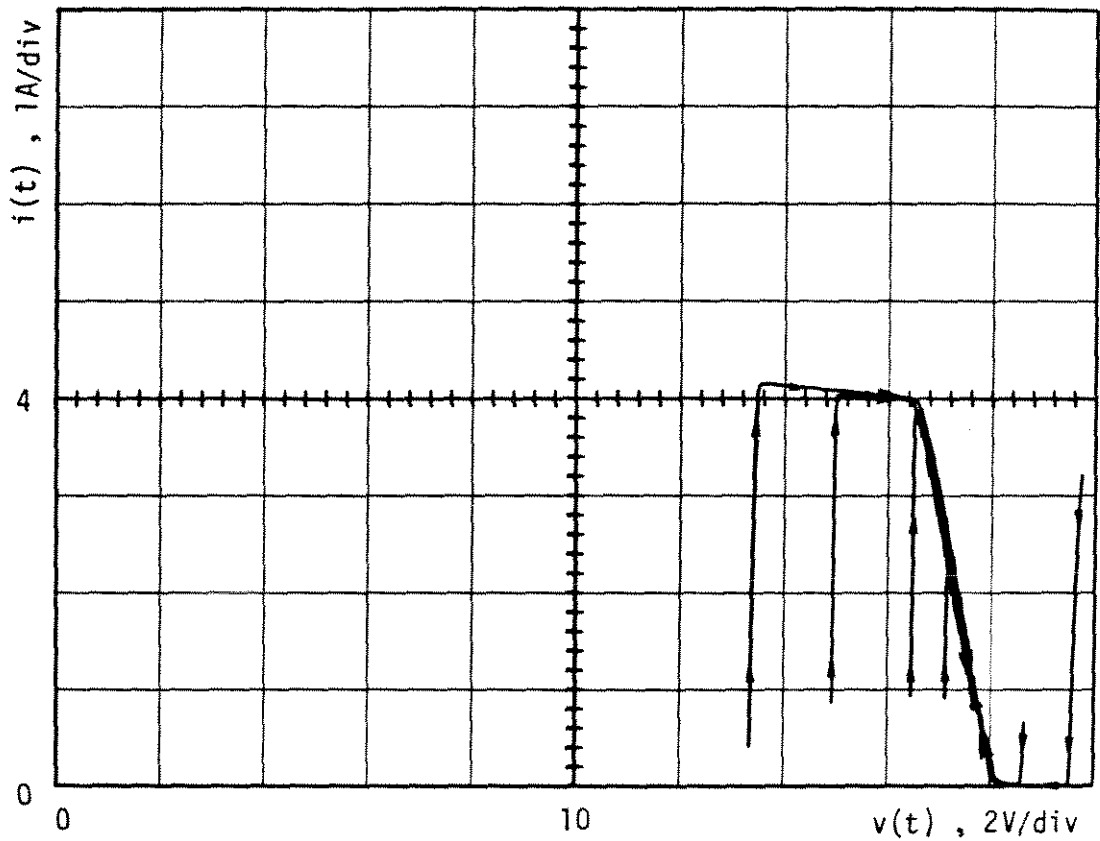
Fig. 14.6. Experimental data for the boost regulator with D_{max} reduced to 0.825.

stable equilibrium point in the $D = D_{max} = 1$ saturated region at (5A,0V). Thus, the experimental data agree quite well with the predictions of Chapter 13.

The case where D_{max} is reduced to .825 is shown in Fig. 14.6. The saddle point and $D = D_{max}$ region equilibrium point now become virtual. It can be seen that peak current levels may still be as large as 4 Amps. Nonetheless, all trajectories are stable. The measurements agree quite well with the predicted response of Fig. 13.21.
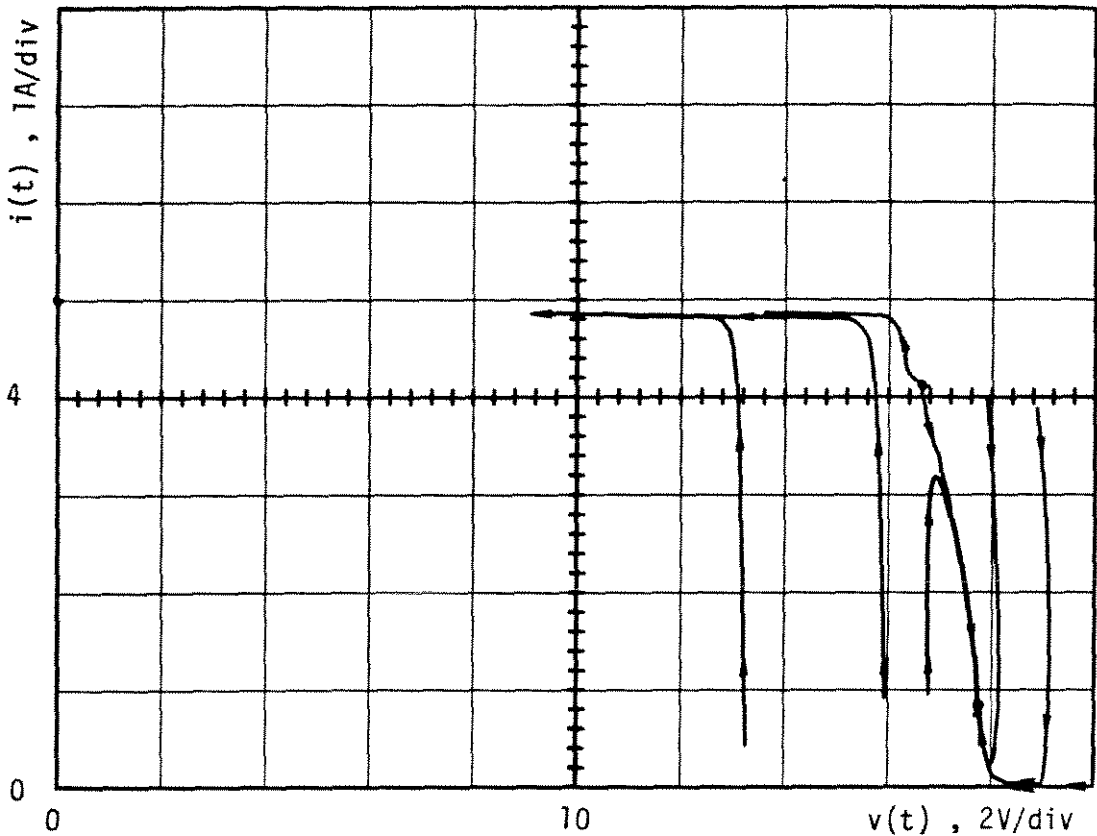
Fig. 14.7. Experimental data for the boost regulator with C reduced from 2900μF to 450μF.

The third set of measuremnts made is for the case when D_{max} is again 1, but the capacitor is reduced from 2900 μF to 450 μF. As predicted in Section 13.9, the fast mode trajectories are no longer perfectly straight vertical lines. Instead, the capacitor voltage increases for large values of D'i, as seen in the trajectories with initial capacitor voltages of 18 and 19 Volts. Also, the trajectories become rounded for currents near quasi-equilibrium. Hence, the qualitative predictions for this case are also verified.

Thus, the boost regulator example of Chapter 13 is shown in three instances to behave as predicted. In consequence, the validity of the analysis of Chapter 13, as well as of the models of Chapter 11, is established.

CHAPTER 15

CONCLUSIONS

Because the small-signal switching regulator models are linear
and hence easily applied to most practical design problems, and
because of the insight they afford into the operation of the regulator,
they are indispensable tools for the design of a switching regulator.
However, because of the small-signal assumption, these models do not
describe the behavior of the regulator during large transients. As
evinced by the example in Section 9.2, it is possible for a
regulator to be stable for small perturbations but not for all large
perturbations. A design of this type is unreliable.

It is of interest, therefore, to formulate models which are valid
for large signals and to determine the nature of these large-signal
instabilities. It would then be possible to ensure that the large-
signal transient response is well-behaved. A set of large-signal
models is described in Chapter 11. The key linear-ripple approximation
of the small-signal state-space averaging method [1,2,11] is employed,
but no small-signal assumption is made. The resulting nonlinear state
equations correctly predict the large-signal behavior of the system
while it operates in the usual unsaturated mode.

The effects of other nonlinearities in the system must be
included as their influence is substantial. The saturation of the
pulse-width modulator can have a stabilizing effect on the system.

The transient discontinuous conduction mode prevents the inductor

current from becoming negative. A current-limiting mode may be

purposely added; this too can help stabilize the system.

The equilibrium points of a system are prominent features of its

state plane portrait, and the knowledge of their number and positions

can yield a great deal of insight into the large-signal system

behavior. The equilibrium points of switching regulators are studied

in Chapter 12.

Analytical expressions are found which may be used to place the

equilibrium points at suitable locations in the state plane, thereby

improving the large-signal transient response. This is first

demonstrated for the example of a two-state boost regulator with total

state feedback. It is found that this regulator has four equilibrium

points in addition to the quiescent operating point. Only two of these

points may have a serious detrimental effect on the response, however.

With proper circuit design, this example may be rendered globally

stable.

The actual state-plane trajectories or time-domain transient

response may be found. This is easily accomplished by the computer

evaluation of the models of Chapter 11. In this way, the existence

of unstable solutions may be observed, and peak values of transient

response waveforms calculated.

A simple boost regulator example is analyzed in Chapter 13. The

modes of operation are identified, and their boundaries in the state

plane are determined. The models of Chapter 11 are evaluated, and

approximate analytical solutions are found for the actual time domain transient waveforms. It is found that some transients converge as desired to the quiescent operating point, while others are unstable and result in large inductor current. This situation may be corrected by the addition of a current limiting mode or by limiting the maximum duty ratio. The predicted behavior of this sytem is verified experimentally in Chapter 14.

A number of effects have been neglected here. Additional modes of operation may exist, such as other types of current limiting modes or the saturation of other devices in the system. Also, more analysis is possible, such as the prediction of limit cycles and the analytical estimation of stability regions. Nonetheless, the most basic aspects of the nonlinear phenomena which occur have now been described, and the informed large-signal design of most switching regulators is now possible.

REFERENCES

[1] R. D. Middlebrook and Slobodan Ćuk, "A General Unified Approach to Modelling Switching-Converter Power Stages," IEEE Power Electronics Specialists Conference, 1976 Record, pp. 18-34 (IEEE Publication 76CH1084-3 AES); also International J. of Electronics, vol. 42, no. 6, pp. 521-550, June 1977.

[2] Slobodan Ćuk, "Modelling, Analysis, and Design of Switching Converters," PhD thesis, California Institute of Technology, November 1976.

[3] Richard Bellman, *Perturbation Techniques in Mathematics, Physics, and Engineering*, Holt, Rinehart, and Winston, 1964.

[4] Ali Nayfeh, *Perturbation Methods*, John Wiley and Sons, 1973.

[5] J. J. Stoker, *Nonlinear Vibrations*, John Wiley and Sons, 1950.

[6] R. D. Middlebrook, "Input Filter Considerations in Design and Application of Switching Regulators," IEEE Industry Applications Society Annual Meeting, 1976 Record, pp. 366-382 (IEEE Publication 76CH1122-1-IA).

[7] R. D. Middlebrook, "Design Techniques for Preventing Input-Filter Oscillations in Switched-Mode Regulators," Proc. Fifth National Solid-State Power Conversion Conference (Powercon 5), pp. A3.1-A3.16, May 1978.

[8]   T. K. Phelps and W. S. Tate, "Optimizing Passive Input Filter
        Design," Proc. Sixth National Solid-State Power Conversion
        Conference (Powercon 6), pp. G1.1-G1.10, May 1979.

[9]   Slobodan Ćuk and Robert W. Erickson, "A Conceptually New High-
        Frequency Switched-Mode Amplifier Technique Eliminates Current
        Ripple," Proc. Fifth National Solid-State Power Conversion
        Conference (Powercon 5), pp. G3.1-G3.22, May 1978.

[10]   Slobodan Ćuk and R. D. Middlebrook, "Advances in Switched-Mode
        Power Conversion," Robotics Age, vol. 1, no. 2, pp. 6-18, Winter
        1979.

[11]   Farhad Barzegar, Slobodan Ćuk, and R. D. Middlebrook, "Using
        Small Computers to Model and Measure Magnitude and Phase of
        Regulator Transfer Functions and Loop Gain," Proc. Eighth
        International Solid-State Power Conversion Conference (Powercon 8),
        pp. H-1.1-28, April 1981.

[12]   Robert W. Erickson and R. D. Middlebrook, "Origins of Harmonic
        Distortion in Switching Amplifiers," Proc. Fourth Annual
        International PCI'82 Conference, pp. 567-582, March 1982.

[13]   Robert W. Erickson and R. D. Middlebrook, "Large-Signal
        Modelling and Analysis of Distortion in Switching Amplifiers,"
        Technical Report, Caltech Power Electronics Group, January 1982.

[14]   Slobodan Ćuk and R. D. Middlebrook, "A New Optimum Topology
        Switching Dc-to-Dc Converter," IEEE Power Electronics Specialists
        Conference, 1977 Record, pp. 160-179 (IEEE Publication
        77CH1213-8 AES).

[15]   R. D. Middlebrook and Slobodan Ćuk, "Isolation and Multiple
       Output Extensions of a New Optimum Topology Switching Dc-to-Dc
       Converter," IEEE Power Electronics Specialists Conference,
       1978 Record, pp. 256-264 (IEEE Publication 78CH1337-5 AES).

[16]   Slobodan Ćuk, "Switching Dc-to-Dc Converter with Zero Input or
       Output Current Ripple," IEEE Industry Applications Society Annual
       Meeting, 1978 Record, pp. 1131-1146 (IEEE Publication 78CH1346-6IA).

[17]   R. D. Middlebrook, "Modelling and Design of the Ćuk Converter,"
       Proc. Sixth National Solid-State Power Conversion Conference
       (Powercon 6), pp. G3.1-G3.14, May 1979.

[18]   Loman Rensink, Art Brown, Shi-Ping Hsu, and Slobodan Ćuk, "Design
       of a Kilowatt Off-Line Switcher Using a Ćuk Converter," Proc.
       Sixth National Solid-State Power Conversion Conference
       (Powercon 6), pp. H3.1-H3.26, May 1979.

[19]   Slobodan Ćuk and R. D. Middlebrook, "Dc-to-Dc Switching Converter,"
       U.S. Patent 4,184,197, January 15, 1980. Foreign patents
       pending.

[20]   Slobodan Ćuk, "Push-pull Switching Power Amplifier," U.S. Patent
       4,186,437, January 29, 1980. Foreign patents pending.

[21]   J. Tal and E. K. Persson, "Pulse-Width Modulated Amplifiers for
       Dc Servo Systems," Proc. Third Annual Symposium on Incremental
       Motion Control Systems and Devices, pp. Q1-Q15, May 1974.

[22]   R. Schmidt, "The Rengenerative Energy Phenomenon in Pulse-Width
       Modulated Dc Servo Systems," Proc. Sixth Annual Symposium on
       Incremental Motion Control Systems and Devices, pp. 261-269,
       May 1977.

[23] D. T. Phan and J. Tal, "Analysis and Design of the Paper Advance and Hammer Shift Servo Systems in High-Speed Line Printers," Proc. Seventh Annual Symposium on Incremental Motion Control Systems and Devices, pp. 203-218, May 1978.

[24] D. Hipkins, "An Analysis of Nonlinearities in Pulsewidth Modulated Bridge Amplifiers," Proc. Seventh Annual Symposium on Incremental Motion Control Systems and Devices, pp. 249-255, May 1978.

[25] D. F. Geiger, "Advances in Switching Servo Amplifiers," Proc. Seventh Annual Symposium on Incremental Motion Control Systems and Devices, pp. 137-152, May 1978.

[26] D. J. Becker, "Designing Microprocessor-Controlled PWM Inverters," Proc. Fifth National Solid-State Power Conversion Conference (Powercon 5), pp. D3-1-D3-6, May 1978.

[27] W. Rippel and D. Edwards, "A New High Efficiency Polyphase SCR Inverter Topology Using FET Commutation," Proc. Eighth National Solid-State Power Conversion Conference (Powercon 8), pp. D1-3.1-75, April 1981.

[28] P. U. Lind, "Four Quadrant Bilateral Power Converter," Proc. International PCI/MOTORCON '82 Conference, pp. 142-150, March 1982.

[29] R. Hayward, "Programmable L.F. Function Generator Using High Frequency P.W.M. Techniques," International Telecommunications Energy Conference, 1979 Record, (Intelec '79), pp. 472-475 (IEEE Publication 79CH1502-4).

[30] Farhad Barzegar and Slobodan Ćuk, "A New Switched-Mode Amplifier
      Produces Clean Three-Phase Power," Proc. Ninth International
      Solid-State Power Conversion Conference (Powercon 9),
      pp. E3.1-E3.15, July 1982.

[31] Farhad Barzegar and Slobodan Ćuk, "A Polyphase Switching Sine
      Amplifier and Unity Power Factor Converter," U.S. Patent applied
      for, California Institute of Technology.

[32] Farhad Barzegar and Slobodan Ćuk, "Solid-State Drives for
      Induction Motors: Early Technology to Current Research,"
      IEEE Region 6 Conference, 1982 Record, pp. 92-102 (IEEE
      Publication 82CH1738-4).

[33] H. A. Nienhaus, J. C. Bowers, and J. L. Brooks, "An Active Power
      Bandpass Filter," IEEE Power Electronics Specialists Conference,
      1978 Record, pp. 307-316 (IEEE Publication 78CH1337-5 AES).

[34] J.C. Bowers, S.J. Garrett, H.A. Nienhaus, and J.L. Brooks,
      "A Solid-State Transformer," IEEE Power Electronics Specialists
      Conference, 1980 Record, pp.253-264, (IEEE Publication
      80CH1529-7).

[35] H.A. Nienhaus, J.C. Bowers, and J.L. Brooks, "A Power Frequency
      Converter," International Telecommunications Energy Conference,
      1979 Record (Intelec '79), pp. 360-367 (IEEE Publication
      79CH1502-4).

[36] B. Berman, "Techniques for Optimizing Solar Array Power Systems,"
      Proc. Seventh National Solid-State Power Conversion Conference
      (Powercon 7), pp. C4-1 - C4-14, March, 1980.

[37] A. Kernick, D.L. Stechschulte, and D.W. Shireman, "Static
      Inverter with Synchronous Output Waveform Synthesized by Time-
      Optional-Response Feedback," IEEE Power Electronics Specialists
      Conference, 1976 Record, pp. 148-156, (IEEE Publications
      76CH1084-3 AES).

[38] M.F. Schlecht, "A Line Interfaced Inverter with Active Control of
      the Output Current Waveform," IEEE Power Electronics Specialists
      Conference, 1980 Record, pp. 234-241, (IEEE Publication
      80CH1529-7).

[39] M.F. Schlecht, "Time-Varying Feedback Gains for Power Circuits
      with Active Waveshaping," IEEE Power Electronics Specialists
      Conference, 1981 Record, pp. 52-59, (IEEE Publication
      81CH1652-7).

[40] G.W. Wester and R.D. Middlebrook, "Low-Frequency Characterization
      of Switched Dc-to-Dc Converters," IEEE Power Processing and
      Electronics Specialists Conference, 1972 Record, pp. 9-20
      (IEEE Publication 72 CHO 652-8 AES); also IEEE Trans. Aerospace
      and Electronic Systems, vol. AES-9, pp. 376-385, May 1973.

[41] R.D. Middlebrook and Slobodan Ćuk, "Modelling and Analysis
      Methods for Dc-to-Dc Switching Converters," invited review paper,
      IEEE International Semiconductor Power Converter Conference,
      1977 Record, pp. 90-111 (IEEE Publication 77CH1183-3IA).

[42] R.D. Middlebrook, Slobodan Ćuk, and W. Behen, "A New Battery Charger/Discharger Converter," IEEE Power Electronics Specialists Conference, 1978 Record, pp. 251-255 (IEEE Publication 78CH1337-5 AES).

[43] R.D. Middlebrook, "Power Electronics: Topologies, Modelling, and Measurement," IEEE International Symposium on Circuits and Systems 1981 Record, Chicago, April 1981. pp. 230-238, (IEEE Publication 81CH1635-2).

[44] M. Vidyasagar, *Nonlinear Systems Analysis*, Prentice-Hall, 1978.

[45] N. Krylov and N.N. Bogoliubov, *Introduction to Nonlinear Mechanics*, Princeton University Press, Princeton, N.J., 1947.

[46] N.N. Bogoliubov and Y.A. Mitropolski, *Asymptotic Methods in the Theory of Nonlinear Oscillations*, Gordon and Breach, N.Y., 1961.

[47] Arthur R. Brown and R. D. Middlebrook, "Sampled-Data Modeling of Switching Regulators," Power Electronics Specialists Conference, 1981 Record, Boulder, Colorado, June 1981, pp. 349-369, (IEEE Publication 81CH1652-7).

[48] A. R. Brown, "Topics in the Analysis, Measurement, and Design of High-Performance Switching Regulators," PhD thesis, California Institute of Technology, May 1981.

[49] D. J. Packard, "Discrete Modelling and Analysis of Switching Regulators," PhD thesis, California Institute of Technology, May 1976; also, Report No. M76-43 Hughes Aircraft Co., Aerospace Groups, Culver City, California.

[50]   Slobodan Ćuk and R. D. Middlebrook, "A General Unified Approach
       to Modelling Switching Dc-to-Dc Converters in Discontinuous
       Conduction Mode," IEEE Power Electronics Specialists Conference,
       1977 Record, pp. 36-57, (IEEE Publication 77CH 1213-8 AES).

[51]   K. Harada and T. Nabeshima, "Large-Signal Transient Response of a
       Switching Regulator," IEEE Power Electronics Specialists
       Conference, 1981 Record, pp. 388-394 (IEEE Publication
       81CH1652-7).

[52]   D. B. Edwards and T. K. Caughey, "Global Analysis of a Buck
       Regulator," IEEE Power Electronics Specialists Conference,
       1978 Record, pp. 12-16 (IEEE Publication 78CH1337-5 AES).

[53]   D. B. Edwards, "Time Domain Analysis of Switching Regulators,"
       PhD thesis, California Institute of Technology, March, 1977.

[54]   Slobodan Ćuk, "Discontinuous Inductor Current Mode in the
       Optimum Topology Switching Converter," IEEE Power Electronics
       Specialists Conference, 1978 Record, pp. 105-123 (IEEE
       Publication 78CH1337-5 AES).

[55]   C. W. Deisch, "Simple Switching Control Method Changes Power
       Converter into a Current Source," IEEE Power Electronics
       Specialists Conference, 1978 Record, pp. 300-306, (IEEE
       Publication 78CH1337-5 AES).

[56] Shi-Ping Hsu, Art Brown, Loman Rensink, and R. D. Middlebrook, "Modelling and Analysis of Switching Dc-to-Dc Converters in Constant-Frequency Current-Programmed Mode," IEEE Power Electronics Specialists Conference, 1979 Record, pp. 284-301, (IEEE Publication 79CH1461-3 AES).